UNIVERSITÀ
DEGLI STUDI
DI PADOVA

UNIVERSITÁ DEGLI STUDI DI PADOVA

DIPARTIMENTO DI TECNICA E GESTIONE

DEI SISTEMI INDUSTRIALI

SCUOLA DI DOTTORATO DI INGEGNERIA INDUSTRIALE

INDIRIZZO: MECCATRONICA E SISTEMI INDUSTRIALI

CICLO XXV

EXPERIMENTAL ANALYSIS AND MULTI-SCALE ANALYTICAL AND NUMERICAL MODELLING OF NANOMODIFIED COMPOSITE MECHANICAL PROPERTIES

Direttore della Scuola : Ch.mo Prof. Paolo Colombo

Coordinatore d'indirizzo: Ch.mo Prof. Alberto Trevisani

Supervisore :Ch.mo Prof. Marino Quaresimin

Dottorando : Marco Salviato

To my better half...

Summary

Nanocomposites represent a new class of materials which, thanks to the outstanding functional and mechanical properties are endowed with, is earning more and more interest from the scientific community and the industry. As a matter of facts, results available in the literature indicate the possibility to obtain exceptional performance increments even at low nanofiller volume fraction.

To effectively exploit the huge potential of nanocomposites it is of primary concern that with the experimental analysis, abundantly developed in the literature among the rest, comes an adequate modeling activity. Of course, the creation of models, either analytical or numerical, is a milestone for the comprehension and prediction of the mechanical behavior of this kind of materials and their successive application in engineering design.

One of the most critical issues in modeling macro-mechanical properties of nanostructured materials is their *hierarachical structure* which spans from nano to macro length-scales. A good model should take into account the characteristic phenomena of each length-scale and bridge their effects from the “smaller” scale to the macroscale. As a consequence, a different way of thinking from traditional approaches is needed and a completely new class of models is required.

In this work an extensive review on the main approaches available in the literature for mechanical properties modeling of polymeric-based nanocomposites is proposed. The importance of a multiscale approach either hierarchical or concurrent is discussed and a classification of the models based on the scale level used to address the model (micro-, nano and molecular) is introduced as well.

Then, a comprehensive study on interfacial effects on nanoparticle debonding is presented. The analysis is developed within the frame of Finite Fracture Mechanics and Surface Elasticity. It accounts, contemporaneously, for the

emergence of an interphase zone around the nanoparticle and for surface stresses on the nanoparticle periphery.

Afterwards, a unique multiscale analytical procedure useful to evaluate the overall fracture toughness of a polymer/nanoparticle nanocomposite is proposed. The models developed for each damaging mechanism are introduced, highlighting the most important parameters. All models are finally integrated and comparison is carried out between the predicted nanocomposite fracture toughness and some experimental data taken from the literature.

In the second part of the work, the experimental investigations carried out by the author are described and discussed. The effects of nanomodification by nanoclays on polymers and composite laminates in terms of quasi-static and cyclic fracture properties are investigated. In case of nanomodified polymers, it is found that nanomodification significantly enhances the fracture behaviour of the system either in quasi-static or cyclic regime and for different loading modes. In the case of nanomodified laminates, due to the nanofiller morphology, the behaviour of clay-modified laminates is still almost comparable to that of the base laminates.

Sommario

I nanocompositi, ottenuti mediante modificazione di resine polimeriche con cariche di dimensioni nanometriche, rappresentano una classe di materiali che sta riscuotendo un notevole interesse da parte della comunità scientifica e del mondo industriale.

Combinando infatti, in maniera opportuna, rinforzi su scala nanometrica con polimeri tradizionali è possibile ottenere dei nuovi materiali dalle eccezionali proprietà fisiche e di resistenza.

I risultati finora disponibili in letteratura indicano la possibilità di ottenere incrementi prestazionali molto elevati già con frazioni di nanocarica limitate, dell'ordine di qualche percento.

Al fine di poter sfruttare l'enorme potenziale di questo tipo di materiali è necessario che l'attività sperimentale sia accompagnata da un'adeguata attività di modellazione, così da mettere a punto dei modelli comportamentali capaci di prevedere le proprietà meccaniche del nanocomposito, includendo la struttura gerarchica e la peculiarità dei meccanismi di rinforzo.

In questo lavoro viene proposta una panoramica e un'analisi critica delle principali metodologie di modellazione finora disponibili in letteratura, con riferimento alle proprietà meccaniche e in particolare alla tenacità a frattura.

Per ciascun modello analizzato vengono descritti gli aspetti maggiormente significativi, le ipotesi di base e le conseguenze che tali ipotesi hanno sul risultato finale. Viene delineata l'importanza di un approccio multi-scala, gerarchico o concorrente, alla modellazione e viene introdotta una classificazione dei principali approcci basata sulla scala di lunghezza investigata per affrontare il problema (micro-, nano- e molecolare).

Successivamente, viene presentato uno studio approfondito degli effetti interfacciali sul meccanismo di debonding di nanoparticelle. L'analisi è stata condotta nell'ambito della teoria della Finite Fracture Mechanics e della Surface Elasticity. Vengono tenuti in considerazione, contemporaneamente, gli effetti di un'interfase che circonda la nanoparticella e di tensioni superficiali agenti all'interfaccia con la matrice.

L'analisi del meccanismo di debonding rappresenta la base di una procedura multiscala per il calcolo della tenacità a frattura di nanocompositi particellari. L'approccio proposto in questo lavoro unisce i modelli di danneggiamento sviluppati dall'autore. Vengono discussi il funzionamento del modello e l'influenza dei principali parametri e le previsioni sono confrontate con risultati sperimentali provenienti da letteratura.

Nella seconda parte del lavoro vengono presentati e discussi i risultati delle campagne sperimentali condotte dall'autore con particolare enfasi agli effetti della nanomodificazione sul comportamento a frattura, quasi-statico e ciclico, sia di polimeri nanomodificati che di laminati nanomodificati con nanoclay. Nel caso di polimeri nanomodificati, viene mostrato come l'aggiunta di nanorinforzi comporti un miglioramento significativo del comportamento a frattura del sistema sia in regime quasi-statico che ciclico e per diversi modi di sollecitazione. Nel caso di laminati nanomodificati, a causa della morfologia del nanofiller, il comportamento a frattura è risultato ancora confrontabile a quello dei laminati base.

Acknowledgements

I would like to express gratitude to my supervisor Prof. Marino Quaresimin and to Prof. Michele Zappalorto, for their kind suggestions and support.

This research has been realized thanks to the support of Veneto Nanotech, the Italian Cluster of Nanotechnology (Padova, Italy). I would like to express my sincere gratitude for having sponsored my Doctoral course throughout the tree years.

Ringraziamenti

Quando, tre anni fa, decisi d'intraprendere la strada del dottorato lo feci con un obbiettivo preciso in mente: crescere, imparare, migliorarmi. Questo non significa solo lavorare con passione e con impegno ma anche attingere il meglio dal prossimo. Molte sono le persone che durante questo percorso mi sono state vicine. Alcune le conosco da tutta una vita, altre ho avuto modo d'incontrarle durante il mio cammino.

Per prima cosa ringrazio il Professor Quaresimin per la fiducia che ha sempre dimostrato nei miei confronti e per tutte le opportunità che mi ha offerto e che ho cercato di cogliere con impegno e dedizione. Lo ringrazio per tutti i suoi consigli e insegnamenti e per l'ottimo rapporto che si è instaurato in questi anni.

Voglio ringraziare in modo speciale Michele, prima di tutto un caro amico oltre che un esempio da seguire. Ricorderò sempre con affetto le nostre lunghe discussioni sulla meccanica della frattura e sulla vita così come i periodi di scoramento quando i conti "non tornavano" e gli "spuntini" di festeggiamento quando si raggiungeva un risultato. In particolare, rammenterò con un sorriso la faccia della gente che udendo le nostre conversazioni mi sentiva chiamarlo "il Maestro". Per me è sempre stato naturale chiamarlo così, perché così l'ho sempre considerato.

Desidero ringraziare il mio amico Paolo con cui, durante questo percorso di crescita, ho condiviso periodi di lavoro intenso ma anche di grande divertimento. E' stato bellissimo lavorare con un vero amico prima che con un collega che stimo moltissimo e a cui auguro una grande carriera nel mondo della ricerca.

Un ringraziamento va anche a tutti i miei amici Christian, Dario, Alessandro, Pippo, Giorgia, Reza, Alberto, Massimiliano, Matteo, Lucio, Nicola, Walter e Alex.

Voglio ringraziare in modo particolare la mia famiglia. Mio padre per dedicare ogni giorno della sua vita a me e i miei fratelli affrontando da solo difficoltà spesso insormontabili. Mi ha insegnato l’importanza dello studio e da lui ho imparato ad aver sempre fiducia nei miei mezzi. Mia madre, mia nonna Teresa,

mia nonna Marialuisa e i miei fratelli per avermi sostenuto e per essermi stati sempre vicino. Inoltre, desidero ringraziare Ricky, Romolo, Silvano e Anna per avermi accolto come in una famiglia e in particolare Catia per i suoi saggi consigli.

Voglio infine dedicare il ringraziamento più importante a Rossella, la donna della mia vita, il mio tesoro, il "mio mare". La ringrazio per tutti i preziosi momenti passati assieme, per il suo sostegno e la complicità nei momenti di gioia ma sopratutto la ringrazio per avermi donato la felicità. Con semplicità, come deve essere. Così, mentre il vento spazza il cielo di questa freddissima notte di Chicago e guardo il mio amore che mi sorride, mi piace concludere questo lavoro con la consapevolezza che in questi anni siamo cresciuti insieme e insieme cresceremo per sempre.

... "Quando tu guarderai il cielo, la notte, visto che io abiterò in una di esse, visto che io riderò in una di esse, allora sarà per te come se tutte le stelle ridessero. Tu avrai, tu solo, delle stelle che sanno ridere!"

Contents

There is nothing noble about
being superior to another man.
True nobility lies in being
superior to your previous self.

Introduction

Nanocomposites represent a new class of materials which, thanks to the outstanding functional and mechanical properties are endowed with, is earning more and more interest from the scientific community and the industry. As a matter of facts, results available in the literature indicate the possibility to obtain exceptional performance increments even at low nanofiller volume fraction.

To effectively exploit the huge potential of nanocomposites it is of primary concern that with the experimental analysis, abundantly developed in the literature among the rest, comes an adequate modeling activity. Of course, the development of models, either analytical or numerical, is a milestone for the comprehension and prediction of the mechanical behavior of this kind of materials and their successive application in engineering design.

In Chapter 1, the main nanocomposites properties and industrial applications are described and some up-to-date data about commercial products are given as well. Chapters 2 deals with some important modeling issues that must be addressed in order to obtain reliable predictions. As a matter of facts, the reduction in filler length scale, on the one hand is the key of the extraordinary properties of nanocomposites thanks to which the exploitation of matter in its molecular state is possible, on the other hand takes to the limit many important drawbacks already known for traditional composites. Moreover, one of the most critical issue in modeling macro-mechanical properties of nanostructured materials is their *hierachical structure* which spans from nano to macro length-scales. A good model should take into account the characteristic phenomena of each length-scale and bridge their effects from the “smaller” scale to the macroscale. As a consequence, a different way of thinking from traditional approaches is needed and a completely new class of models is required. The importance of a multiscale

approach either hierarchical or concurrent is discussed and a classification of the models based on the scale level used to address the model (micro-, nano and molecular) is introduced as well.

Afterwards, Chapter 3 gives a comprehensive study on interfacial effects on nanoparticle debonding. The analysis is developed within the frame of Finite Fracture Mechanics and Surface Elasticity. It accounts, contemporaneously, for the emergence of an interphase zone around the nanoparticle and for surface stresses on the nanoparticle periphery.

In Chapter 4 a unique multiscale analytical procedure useful to evaluate the overall fracture toughness of a polymer/nanoparticle nanocomposite is proposed. The models developed for each damaging mechanism are introduced, highlighting the most important parameters. All models are finally integrated and comparison is carried out between the predicted nanocomposite fracture toughness and some experimental data taken from the literature.

In the second part of the work, the experimental investigations carried out by the author are described and discussed. In Chapter 5 the effects of nanomodification by nanoclays on polymers in terms of quasi-static fracture properties under mixed mode loading are investigated. It is found that nanomodification significantly enhances the fracture behaviour of the system for different loading modes the increment being dependent on the mode mixity. The results are compared to some fracture criteria available in the literature and an insightful discussion is made.

Finally, in Chapter 6, the effects of nanomodification by nanoclay on composite laminates made by vacuum infusion are investigated. Mode I fracture toughness and crack propagation resistance for neat and clay-modified epoxy, interlaminar shear strength, mode I delamination resistance for base and clay-modified epoxy laminates are analysed. Available results indicate a significant improvement in the fracture toughness and crack propagation threshold of clay-modified epoxy. However, due to the nanofiller morphology, the behaviour of clay-modified laminates is still almost comparable to that of the base laminates.

1

Nanocomposites: an overview

1.1 Introduction

The recent advance in nanofabrication techniques has made it possible to manufacture composite materials containing nanoscale fillers giving rise to a new class of materials termed "nanocomposites". Although nanotechnology has emerged only in recent times in the field of advanced materials, its conception goes back to the end of fifties when Nobel Laureate Richard P. Feynman gave a talk at the Annual meeting of the American Physical Society that has become one classic science lecture of the 20th century ("There's Plenty of Room at the Bottom", Feynman, 1959). Since the 1980s, many inventions and discoveries in fabrication of nanoobjects have been a testament to his idea, however, only in the last decade it has been acknowledged that nanomaterials can cause a technological revolution comparable to the coming of electronics or informatics. To understand how concrete are the expectations, it can be considered that the funding for research and development on nanomaterials in the USA passed only in the three years between 1997 and 2000 from 116 to 270 millions of dollars and it was estimated to have reached 961 millions in 2004. Analogous investments have been done in Europe and Japan (Carati et al., 2004, Wood, 2004).

The promise of nanotechnology is to create revolutionary material combinations preventing from classic material trade-offs between desired performances, mechanical properties, cost and processibility (Vaia and Wagner, 2002). As a matter of facts, experimental results available in the literature witness the possibility of creating materials of outstanding chemical and physical properties by adding only a small amount of nanofiller (Adebahr et al., 2001, Becker et al., 2002, Ajayan et al., 2002, Becker et al., 2002, Ray and Okamoto, 2003, Wetzel et al., 2003, Zhang and Sing, 2004, Thostenson et al., 2005, Liu et al., 2006, Fiedler

et al., 2006, Wichmann et al., 2006a, Wichmann et al., 2006b, Quaresimin and Varley, 2008, Battistella et al., 2008, Quaresimin et al. 2012).

1.2 Main applications and market

Thanks to their enhanced physical, thermal and other unique properties, which are often superior to conventional microscale composites, nanocomposite market volume is rapidly increasing in many engineering applications. In the short term, the most rapid gains will be seen in high-level applications where the additional cost of nanomaterials is not a critical factor. By 2025, it is expected that nanocomposites will be a US$9 bln market, with volumes nearing 5 mln tons and the 20% of the market constituted by nanocomposites based on thermoset resins.

US NANOCOMPOSITES DEMAND (thousands tons)				
	2005	2010	2020	% Annual Growth 2005-2020
Nanocomposites Demand	70	156	3196	29
Thermoplastic	69	150	2546	27
Thermoset	1	6	650	55

Table 1.1. Nanocomposites' US market forecast from 2005 to 2020 (www.plastemart.com)

Among thermosets, nanofillers will make the strongest impact in reinforced polyester and epoxy compounds. Packaging and motor vehicles, two key early markets for nanocomposites, are supposed to account for nearly the 40% of demand in 2020. However, by 2025, electrical and electronics applications will gain in prominence, as nanotube-based composites will penetrate a sizable portion of the market as a substitute for other conductive materials. Construction will emerge as a significant market as nanocomposites begin to replace fiber-reinforced plastics in a number of applications. In 2006, nearly all nanomaterial demand consisted of carbon black in conductive composites. However, as material and production costs of clay-based nanocomposites fall, clays will rise to account for over half of all nanomaterials demand by volume in 2025.

Supplier & Tradename	Matrix Resin	Nano-Filler	Target Market
Bayer AG (Durethan LPDU)	Nylon 6	Organo-clay	Barrier films
Clariant	PP	Organo-clay	Packaging
Creanova (Vestamid)	Nylon 12	Nano-tubes	Electrically conductive
GE Plastics (Noryl GTX)	PPO/Nylon	Nano-tube	Automotive painted parts
Honeywell (Aegis)	Nylon 6 Barrier Nylon	Organo-clay Organo-clay	Multi-purpose Bottles and film
Hyperion	PETG, PBT PPS, PC, PP	Nano-tube	Electrically conductive
Kabelwerk Eupen of Belgium	EVA	Organo-clay	Wire & cable
Nanocor (Imperm)	Nylon 6 PP Nylon MDX6	Organo-clay Organo-clay Organo-clay	Multi-purpose Molding PET beer bottles
Polymeric Supply	Unsaturated polyester	Organo-clay	Marine, transportation
RTP	Nylon 6, PP	Organo-clay	Multi-purpose, electrically conductive
Showa Denko (Systemer)	Nylon 6 Acetal	Clay, mica Clay, mica	Flame retardance Multi-purpose
Ube (Ecobesta)	Nylon 6, 12 Nylon 6, 66	Organo-clay Organo-clay	Multi-purpose Auto fuel systems
Unitika	Nylon 6	Organo-clay	Multi-purpose
Yantai Haili Ind. & Commerce of China	UHMWPE	Organo-clay	Earthquake-resistant pipe

Table 1.2. Main application of some of today commercial clay nanocomposites (Source: Bins & Associates, Sheyboygan, Wis.).

Similarly, a decline in price will enable the rapid commercialization of carbon nanotubes, which will eventually gain over 60% of the nanocomposite materials market in value terms (Source: www.plastemart.com).

Identifying potential markets, intensifying research activities, and government funding for R&D operations constitute major factors in the commercialization of

Product	Characteristics	Applications	Producer
Nylon Nanocomposites	improved modulus, strength, heat distort temperature, barrier properties	automotive parts (e.g. timingbelt cover, engine cover, barrier, fuel line), packaging , barrier film	Bayer Honeywell Polymer RTP Company Toyota Motors Ube Unitika
Polyolefin nanocomposites	stiffer, stronger, less brittle, lighter, more easily recycled, improved flame retardancy	step-assist for GMC Safari and chevrolet Astro vans, heavy-duty electrical enclosure	Basell, Blackhawk Automotive, Plastics Inc, General Motors, Gitto Global Corporation, Southern Clay Products
M9	High barrier properties	Juice or beer bottles, multi-layer films, containers	Mitsubishi Gas Chemical Company
Durethan KU2-2601 (nylon 6)	Doubling of stiffness, high gloss and clarity, reduced oxygen transmission rate, improved barrier properties	Barrier films, paper coating	Bayer
Aegis NC (nylon 6/barrier nylon)	doubling of stiffness, higher heat distort temperature, improved clarity	medium barrier bottles and films	Honeywell Polymer
Aegis TM OX	Highly reduced oxygen transmission rate, improved clarity	High barrier beer bottles	Honeywell Polymer
Forte nanocomposite	improved temperature resistance and stiffness, very good impact properties	automotive furniture appliance	Noble Polymer

Table 1.3. Commercial polymer nanocomposites and applications (Source: www.nanocompositech.com).

nanocomposites. A few nanocomposites have already reached the marketplace, while a few others are on the verge, and many continue to remain in the laboratories of various research institutions and companies. Tables 1.2 and 1.3 summarize some commercial nanocomposites of today.

1.3 A new definition of the synergistic effect

Composite materials are based on the principle of obtaining new enhanced properties than those of the original constituents through the exploitation of synergistic interactions. While in conventional composites, the reinforcement is on the order of microns, in nanocomposites the reinforcement can encompass different length scales: from the order of a few nanometers to the macroscale. Indeed, nanotechnology has been defined as ‘‘the creation, processing, characterization, and utilization of materials, devices, and systems with dimensions on the order of 0.1–100 nm, exhibiting novel and significantly enhanced physical, chemical, and biological properties, functions, phenomena, and processes due to their nanoscale size’’ (Thostenson et al., 2005) putting a new light to the concept of synergistic effect. Accordingly, in this work, a nanocomposite is defined as a multi-phase material which, thanks to its *hierarchical structure* promoting the interaction of different time and length scales, is endowed with properties that are not just a synergistic combination of whose of the singular bulk constituents, rather, a set of new ones coming from the exploitation of matter at its molecular state (Quaresimin et al., 2012).

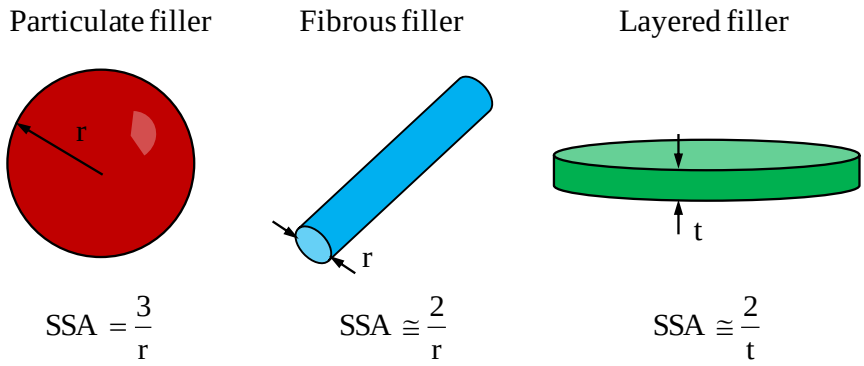

Figure 1.2. Specific surface area (SSA) for varying reinforcement geometries.

1.4 The "Nano-effect"

The extraordinary physical and chemical properties of nanocomposites can be related to the so called "nano-effect", a phenomena linked to the hierarchical structure of this kind of materials.

Reducing the size of particles from the micro- to the nano-scale produces an enormous interfacial area per unit volume between the filler and the matrix polymer (Figure 1.2. shows the surface area/volume (SSA) relations for varying reinforcement geometries). For instance, an interfacial area of about 700 m^2/cm^3 (comparable to the surface of a football field within a raindrop) occurs in dispersions of layered silicates in polymer. Figure 1.3. displays the ratio between particle surface and volume for spherical and fibrous fillers as a function of particle diameter (Fiedler et al., 2006). It can be seen that carbon nanotube (single-wall carbon nanotube, SWCNT, double-wall carbon nanotube, DWCNT, and multi-wall carbon nanotube, MWCNT) and spherical nanoparticles, like fumed silica (FS) and carbon black (CB) have specific surface areas orders of magnitude higher than traditional micro-sized fillers, as carbon fibers (CF), glass fibers (GF) and glass beads (GB). These dimensions imply that the distance between the particles is comparable to their size. For a 1 nm-thick plate, the distance between plates approaches 10 nm at only 7 vol% of plates.

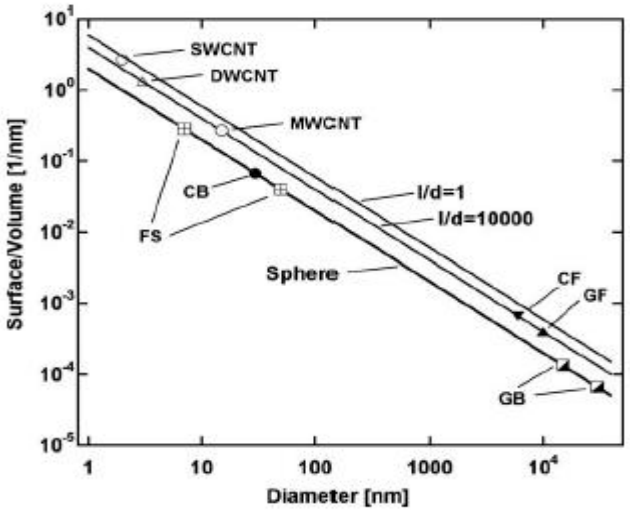

Figure 1.3. Surface/ volume ratio of nano- and micro-sized fillers as a function of particle diameter. The measure unit [1/nm] corresponds to 1000 m^2/cm^3 (Fiedler at al., 2006).

The use of nanofillers can induce a considerable improvement not only in the mechanical properties of the composite material, like high tensile strength and high elastic modulus, but also other interesting properties like thermal stability, fire retardancy, gas permeability, resistance to abrasion and to solvents, modifications of the optical and electrical properties. A very interesting aspect of the use of nanofillers is that they offer exceptional improvements already at filler concentrations much lower than traditional (micro-sized) fillers. An example is shown in Fig.1.4, where nanoplatelets of aluminosilicate can double the modulus of nylon 6 already at 6.5 wt%, while three times this amount of glass fibres is required to achieve the same increase. This is a considerable advantage since lower filler contents translate into lighter composites, which is a desirable feature in many applications, and in addition, it induces smaller sacrifices in matrix properties, such as ductility, impact strength and surface finishing.

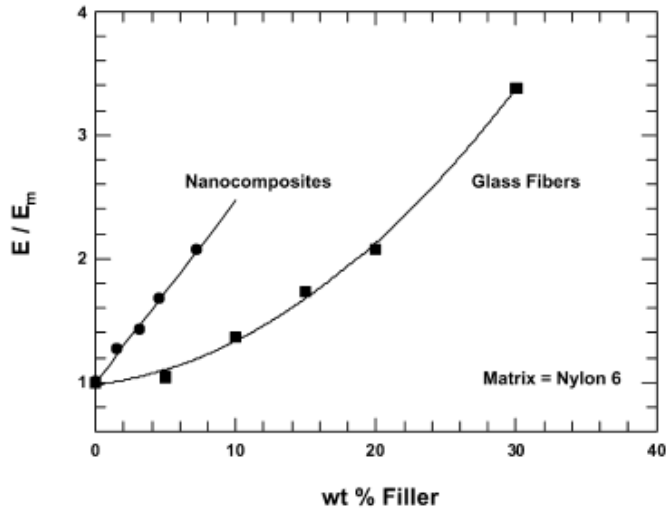

Figure. 1.4. Comparison of the reinforcement of nylon-6 by organically modified montmorillonite (nanocomposites) and glass fibers (Fornes and Paul, 2003).

Another aspect to take into consideration is that being reinforcement's dimensions of the same length scale as the radius of gyration of polymeric chains, it can make molecular interactions with the matrix causing the formation of a interphase whose properties can be very different from the constituent's ones. According to Ajayan et al., already at low volume fractions, even entire matrix is essentially part of the interfacial region (Ajayan et al., 2004). Figure 1.6 shows a Molecular

Dynamics simulation of the interactions between a CNT and polymeric chains (Lordi and Yao, 2000).

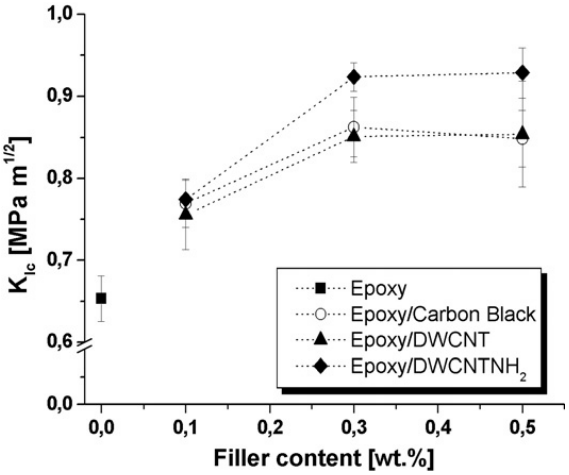

Figure 1.5. Fracture toughness K_{Ic} of carbon black/epoxy and DWCNT/epoxy composites vs. nanofiller content (Gojny et al., 2004).

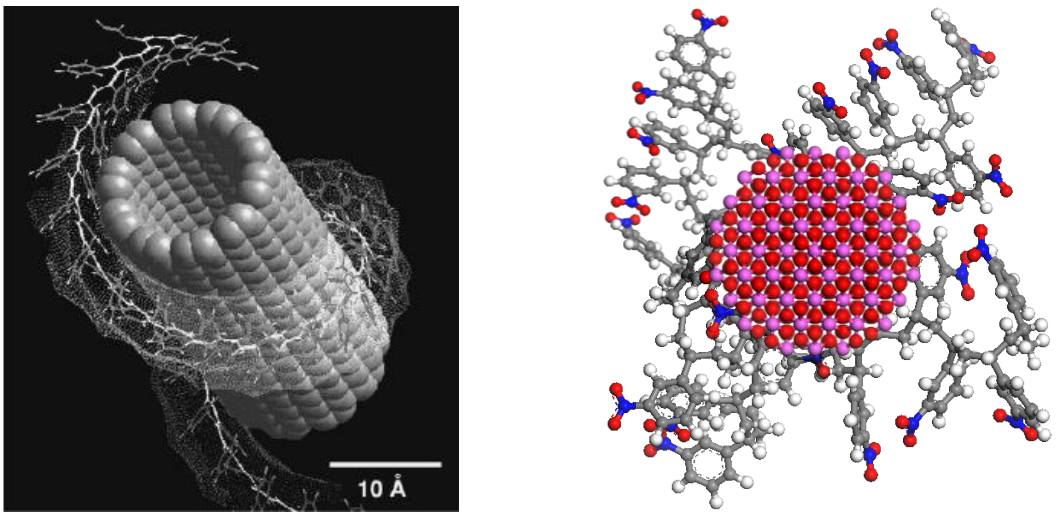

a) b)

Figure 1.6. a) molecular dynamics simulation of the interactions between a CNT and polymeric chains (Lordi and Yao, 2000) and b) a molecular dynamics simulation of an Al_2O_3 nanoparticle within an epoxy polymer.

1.5 Nanofiller typologies

Depending on how many dimensions of the filler are in the nanometer range three types of nanocomposites can be distinguished (Figure 1.7):

- *Isodimensional particles* have all three dimensions in the order of nanometers, examples are spherical silica nanoparticles or semiconductor

clusters.

- *Nanotubes and whiskers,* when two dimensions are in the nanometer range and the third is longer forming elongated structures, such as carbon nanotubes or cellulose whiskers;
- *Layered crystal nanofillers,* when only one dimension is in the nanoscale, the nanofiller assumes the form of sheets of one to few nanometers thick and of hundreds to thousands of nanometers long and large. The most investigated in this class are clay and layered silicates.

1.6 Isodimensional nanoparticles

Equi-axed nanoparticles have been available for more than a century. Well established processes have been used for years to produce carbon black and silica particles.

1.6.1 Production processes

Plenty of production processes exist for nanoparticles. Aerosol methods form nanoparticles by condensation from a gas phase. A successful aerosol process is in *flame hydrolysis*, where a vapour precursor is burned in an hydrogen/oxygen fuel mixture to produce a metal oxide and the specific surface area (SSA) can be controlled adjusting the temperature. Titania, aluminia, zirconium oxide and silica particles are synthesized by flame hydrolysis. The size for silica range from 7 to 27 nm and the SSA from 100 to 380 m^2/g.

Pyrolysis is also an aerosol method and it's used for carbon black, with a size range of 20-300 nm and surface areas of 20-300 m^2/g.

Gas condensation forms a metal vapour in an oxygen atmosphere or in an inert gas, then the gas is cooled down and the nanoparticles are collected. The oxygen atmosphere is used for metal oxides (like TiO_2, Al_2O_3, ZrO_2, etc.), while with inert gas metal particles are obtained. Beside these, there are many other processes: laser ablation, plasma and chemical vapor condensation, wet-chemistry methods, sonication chemistry and hydrodynamic cavitation are only some examples (Ajayan et al., 2004).

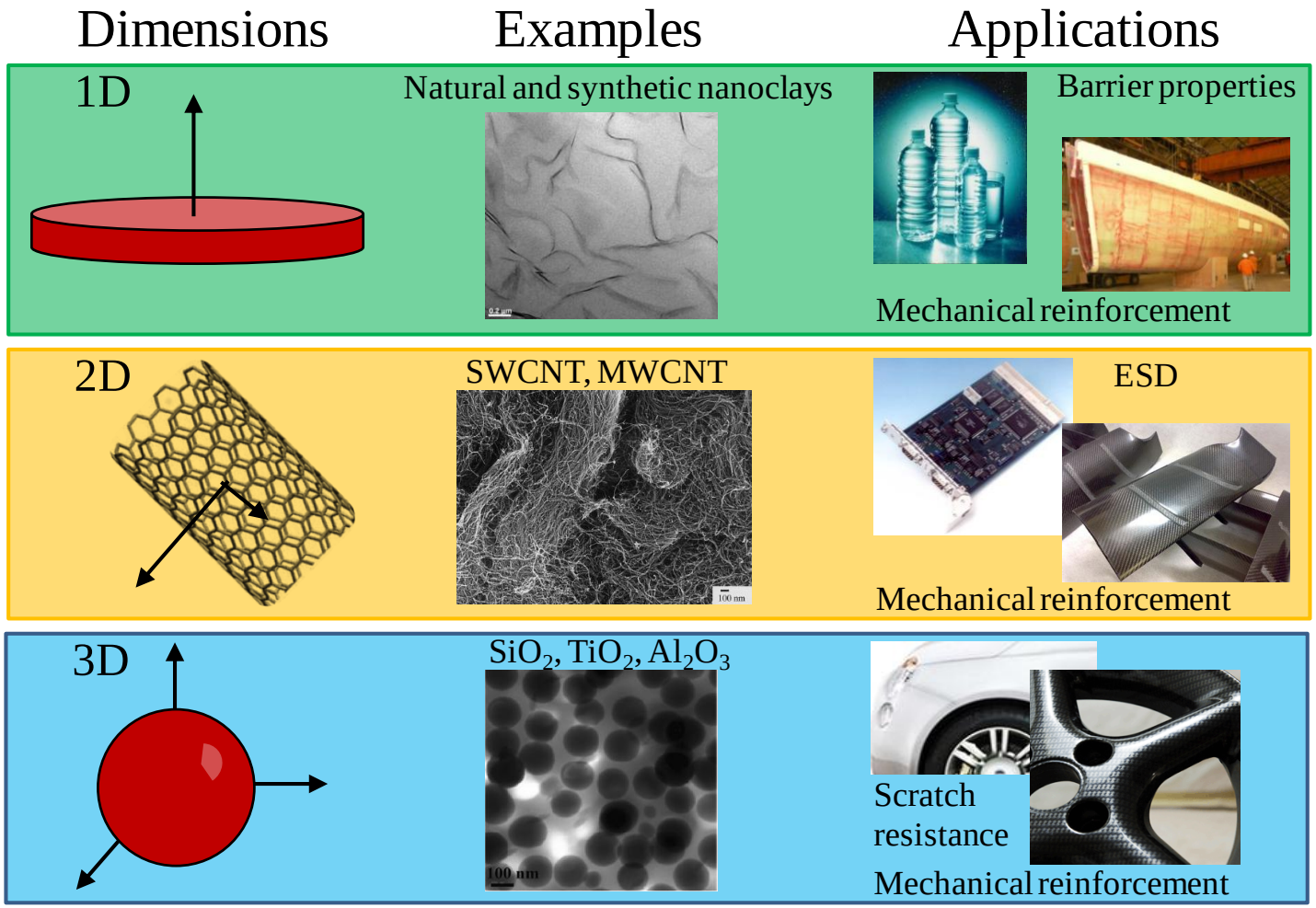

Figure 1.7. Comparison between the main nanofiller typologies.

1.6.2 Properties and applications

Carbon black and silica particles have found applications in the reinforcement of rubbers, in catalysis, chemical-mechanical polishing, water treatment, in thickening coatings and paints, for printing inks (Chan et al., 2002).

Nanoparticle-filled polymers can lead to increases in modulus and strength, maintaining the polymer's ductility. For example, Table 1.3 reports the improvement in properties obtained by introducing calcium carbonate nanoparticles in polypropylene. Besides, Zhang et al. (Zhang et al., 2004) measured an improvement in fracture toughness with the introduction of nanoparticles: the addition 4.5 vol% of silane-treated Al_2O_3 particles led to an increase of nearly 100% in the fracture toughness of unsaturated polyester.

	Impact strength [J/m]		Ultimate stress [MPa]		Ultimate strain [%]		Modulus [MPa]		Yield stress [MPa]		Yield strain [%]	
	mean	SD	mean	SD	mean	SD	mean	SD	mean	SD	mean	SD
PP	55.2	2	27.4	0.4	50.9	3.9	1.6	0.2	34.6	0.3	15.5	0.2
PP/4.8wt%	110.2	6.8	25.7	0.2	48.5	0.2	3.0	0.1	31.1	0.1	9.7	0.3
PP/9.2wt%	128.6	9.9	24.3	0.2	48.8	0.6	2.6	0.1	29.2	0.3	7.7	0.1

Table 1.3. Polypropylene (PP) /calcium carbonate ($CaCO_3$) nanocomposites (Chan et al., 2002).

1.7 Polymer layered silicate nanocomposites

Layered silicates were the first kind of nanoscale fillers to be used to produce nanocomposites for commercial applications.

In 1988, a group of researchers of Toyota started to systematically study nanocomposites formed by montmorillonite dispersed in nylon 6, which are now used in transmission belts in Toyota's engines.

1.7.1 Phyllosilicates

Phyllosilicates are aluminium or magnesium silicate idrates characterized by a lamellar structure which eventually can host other elements in their ionic state. The term phyllosilicates comes from the greek word *phyllon* , i.e. leaf, and states

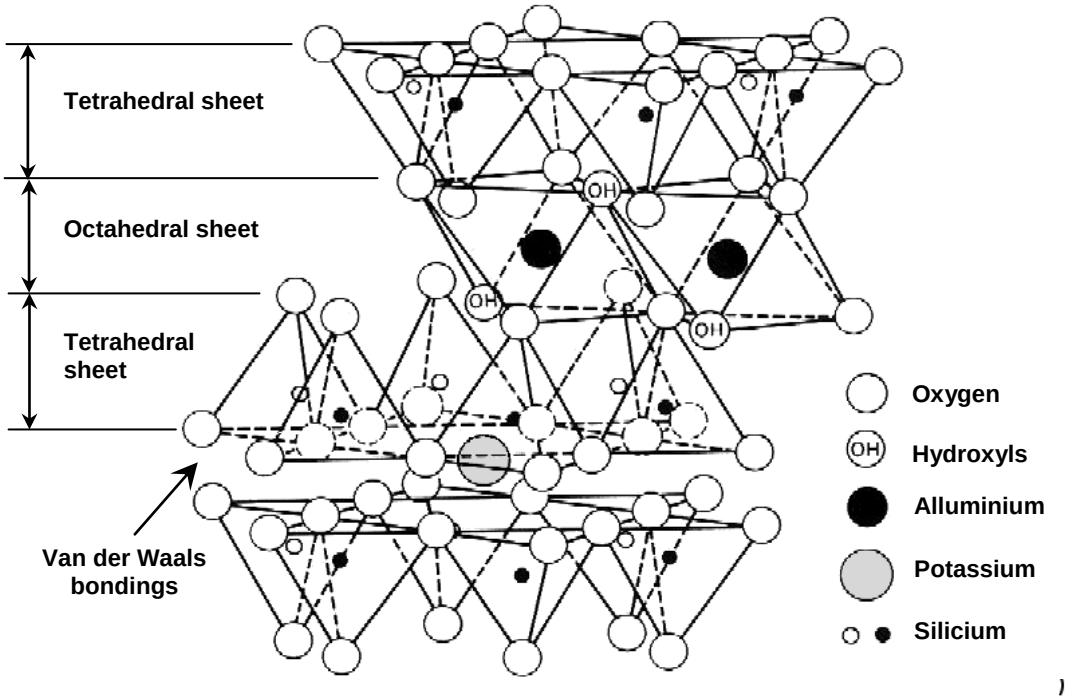

Figure 1.8. Schematic representation of montmorillonite structure.

for the typical planar structure of this kind of silicates.

The layered silicates commonly used in nanocomposites belong to the structural family known as the 2:1 phyllosilicates the most common of which are *montmorillonite*, *hectorite* and *saponite*. Their crystal lattice consists of two-dimensional layers where a central octahedral sheet of alumina or magnesia is fused to two external silica tetrahedron by the tip (SiO_4^{-4}), so that the oxygen ions of the octahedral sheet do also belong to the tetrahedral sheets.

The layer thickness is around 1 nm and the lateral dimensions of these layers may vary from 300 Å to several microns and even larger depending on the particular

Silicate	Isomorphous substitution position	Chemical formula
Montmorillonite	Octahedral	$M_x(Al_{4-x}Mg)(Si)_8O_{20}(OH)_4$
Hectorite	Octahedral	$M_x(Mg_{6-x}Li)(Si)_8O_{20}(OH)_4$
Saponite	Tetrahedral	$M_x(Mg_6)(Si_{8-x}Al_x)O_{20}(OH)_4$

Table 1.4. Chemical formula and characteristic parameter of commonly used 2:1 phyllosilicates. M, monovalent cation; x, degree of isomorphous substitution (between 0.5 and 1.3) (Ray and Okamoto, 2003).

silicate. These layers organize themselves to form stacks with a regular van der Walls gap in between them, called *interlayer* or *gallery*. Isomorphic substitution within the layers (for example, Al^{3+} replaced by Mg^{2+} or by Fe^{2+}, or Mg^{2+} replaced by Li^{+}) generates negative charges that are counterbalanced by alkali or alkaline-earth cations situated in the interlayer (Ray and Okamoto,2003). In Figure 1.8 the structure of a 2:1 phillosilicate is shown (montmorillonite).

1.7.2 Clay compatibilization

The lamellar crystals are characterized by the presence of an interlayer of ions and water molecules (H_2O) kept together by ion-dipole links. The presence of these ions is due to the fact that the clay layers are not neutral, rather, there is an accumulation of residual negative charges generated by the isomorphous substitution of Al^{3+} in place of Si^{4+}, Mg^{2+} or Fe^{2+} in place of Al^{3+} in the lattice. To reestablish electric neutrality, alkaline metallic and alkaline-earth ions (mainly Na^{+}, Ca^{2+} e K^{+}) and H_2O molecules, intercalates between the phyllosilicate layers (Figure 1.9).

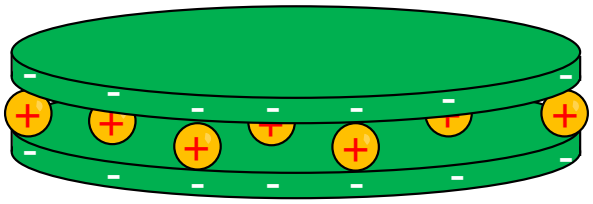

Figure 1.9: Cations intercalation to reestablish electric neutrality.

The metallic ions and H_2O molecules interlayer makes the clay layers mechanical delamination very difficult. On the other hand, cations and water are not intimately part of the crystal lattice and can be easily substituted by other cations or molecules. This aspect is the basis of the production of modified clays for nanocomposites production.

The clay surface is hy*drophilic* which would make the polymer intercalation a very complex operation. For this reason, it is necessary to organically modify or compatibilize the clay surface making it *lipophilic* (or *organophilic*). Phyllosilicates compatibilization is realized by ionic exchange reactions in order

to substitute the metallic cations, generally Na^+ e Ca^{2+}, with others endowed with higher affinity to the polymeric matrix (Figure 1.10).

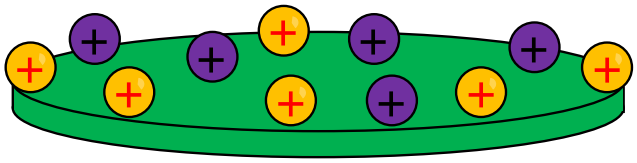

Figure 1.10 Metallic cations substitution by compatilizers.

The maximum amount of cations that can be substituted is constant for a given clay and is quantified by the *cation exchange capacity* (*CEC*); *CEC* is measured in mequiv/g or, more frequently, in mequiv/100gm. For example, montmorillonite *CEC* ranges usually between 80 and 150 meq/100g, depending on the number of isomorphous substitution in the lattice.

The compatibilizing agents are composed of an *idrophilic* group which interacts with polar groups like H_2O or clay and an *organophil* group. The most common are *amino acids*, *silanes* and *alkylammonium ions*. The former are constituted by an amino basic group ($-NH_2$) and by an acid carboxylic group (-COOH); Amino acids are ionized by means of acids transfering a proton to the aminic group in order to promote the ionic exchange to the intercalated cations. Silanes are charactherized by the general chimica formula $R-SiX_3$, where R stands for an organophil group linked to silicon with an hydrolytically stable bond, while X represents a generic group substitutiong *hydroxyl* (–OH) by *hydrolysis*. This way, silanes are able to react with the inorganic surfaces containing (–OH) groups. Alkylammonium ions mainly come from primary alkylammine which are protonated to give $R-NH_3^+$ ions where R is an alkylic group composed by 1 to 18 carbon atoms.

At present, due to the complexity of the compatibilization process, there is a lot of commercial already modified clays, *organoclays*. Once compatibilized, as a matter of facts, the clay is ready to be filed in the polymeric matrix which, in case of structural nanocomposites, is usually an epoxy resin.

1.7.3 Classification and morphology

Polymer layered silicate nanocomposites can be classified in different ways, according to matrix, clay typologies, the production process, functional properties, *etc*. In this work, a morphological classification is proposed to take into account the interaction level between matrix and nanoclays phases as illustrated in figure 1.11. In general, layered silicates have layer thickness on the order of 1 nm and a very high aspect ratio (e.g. 10–1000). A few weight percent of layered silicates that are properly dispersed throughout the polymer matrix thus create much higher surface area for polymer/filler interaction as compared to conventional composites.

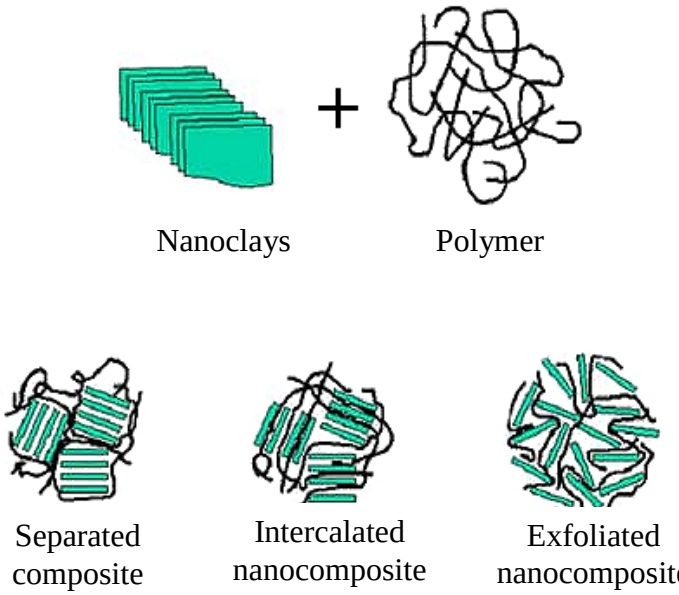

Figure 1.11. Possible polymer/layered silicate composites: separated composite; intercalated nanocomposite; exfoliated nanocomposite.

Depending on the strength of interfacial interactions between the polymer matrix and layered silicate (modified or not), three different types of polymer layered silicates (PLS) nanocomposites are thermodynamically achievable (Ray and Okamoto, 2003, Luo and Daniel, 2003):

- a *separated composite*, when the polymer is unable to intercalate between the silicate sheets and it is comparable to a conventional microcomposite (nanoclays cluster dimensions usually belong to micro length scale);
- an *intercalated nanocomposite*, when one or more extended polymer chain is

intercalated between the silicate layers resulting in a well ordered multilayer morphology built up with alternating polymeric and inorganic layers;

- an *exfoliated or delaminated nanocomposite*, when the silicate layers lose their parallelism and they are completely and uniformly dispersed in a continuous polymer matrix.

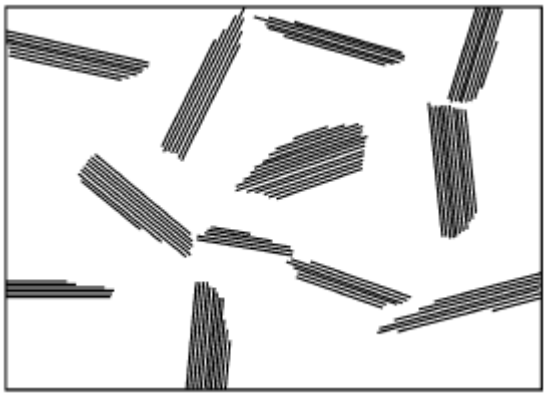

Figure 1.12. Schematic representation of a separated composite (Luo and Daniel, 2003).

In a *separated composite* the clay particles (tactoids) exist in their original aggregated state with no insertion (intercalation) of polymer matrix between the layers (Figure 1.12). In this state the particles can inpart only marginal enhancement of properties to the matrix (Luo and Daniel, 2003).

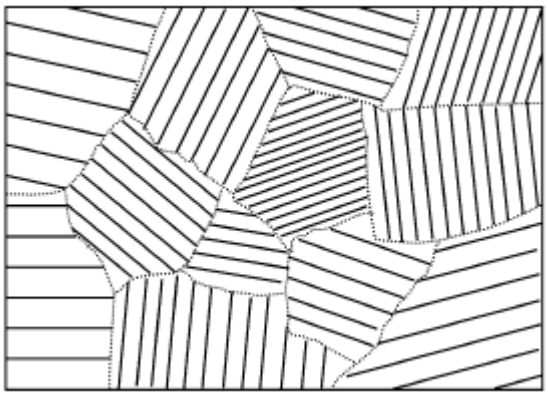

Figure 1.13. Schematic representation of a fully intercalated PLS nanocomposite (Luo and Daniel, 2003).

In *Intercalated nanocomposites* the polymer is inserted (intercalated) into the clay structure between the layers in a crystallographically regular fashion (Figure 1.13

and 1.16). The nanocomposite is interlaid by only a few molecular layers of polymer and the properties of the particle resemble those of the ceramic host are composed by single polymeric chains.

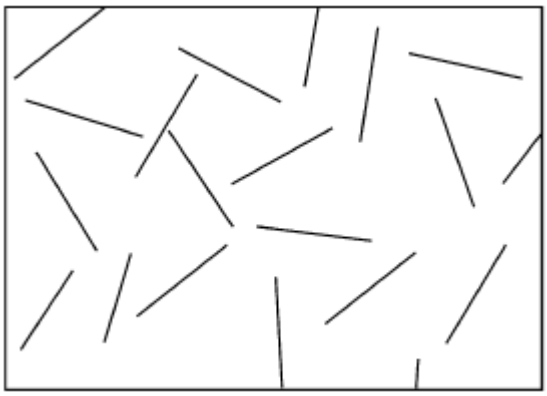

Figure 1.14. Schematic representation of a fully exfoliated PLS nanocomposite (Luo and Daniel, 2003).

In an *exfoliated nanocomposite* the individual 1 nm thick clay layers are separated and dispersed in a continuous polymer matrix with average distances between layers depending on the clay concentration (Figure 1.14). An exfoliated nanocomposite has properties governed primarily by the matrix. Generally, exfoliated nanocomposites exhibit better properties than intercalated ones of the same particle concentration.

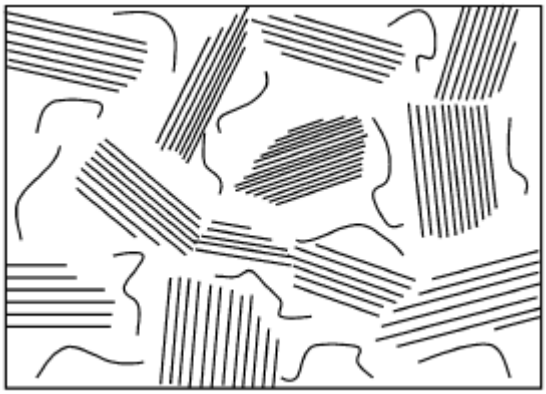

Figure 1.15. Schematic representation of a partially intercalated and exfoliated PLS nanocomposite (Luo and Daniel, 2003).

Actually, full intercalation and exfoliation are extreme cases: usually PLS nanocomposites present an intermediate situation of partial intercalation and

exfoliation (Figure 1.15).

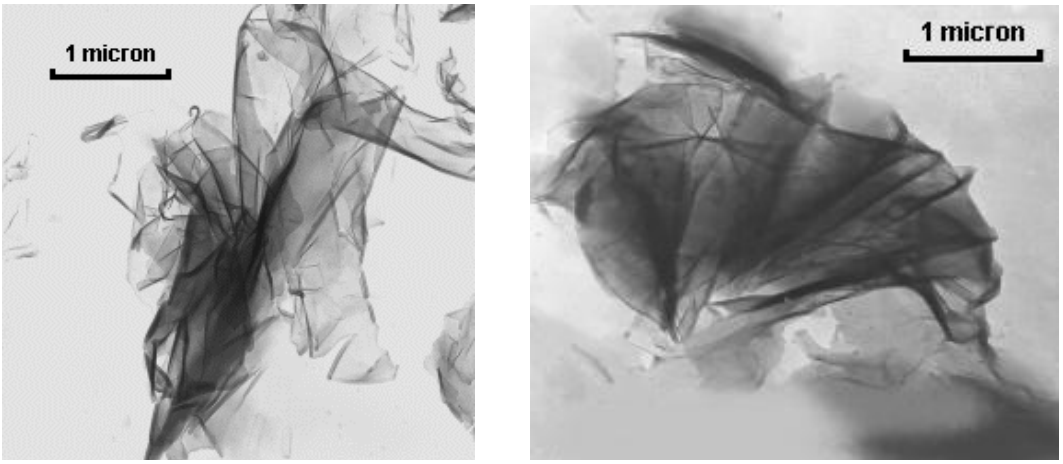

Figure 1.16. TEM images of Intercalated montmorillonite (Source: www.scprod.com).

1.7.4 Production processes

There are three main strategies used to prepare polymer/layered silicate nanocomposites:

- *Exfoliation - adsorption*
- *In - situ intercalative polymerization*
- *Melt intercalation*
- *Template synthesis*

In the *Exfoliation – adsorption* the layered silicate is exfoliated into single layers using a solvent, in which the polymer is soluble. The polymer then adsorbs onto the delaminated sheets and when the solvent is evaporated, the sheets reassemble, sandwiching the polymer to form, in the best case, an ordered multilayer structure. Under this process are also gathered the nanocomposites obtained through *emulsion polymerization*, where the layered silicate is dispersed in the aqueous phase.

However, this method has some important drawbacks concerned not only with the identification of adequate nanofiller-polymer-solvent systems but, above all, the solvent extraction; in facts the solvent thermal stability usually improves after intercalation causing expensive and time consuming thermal treatments to the elimination. This fact makes this process unapplicable to industrial production.

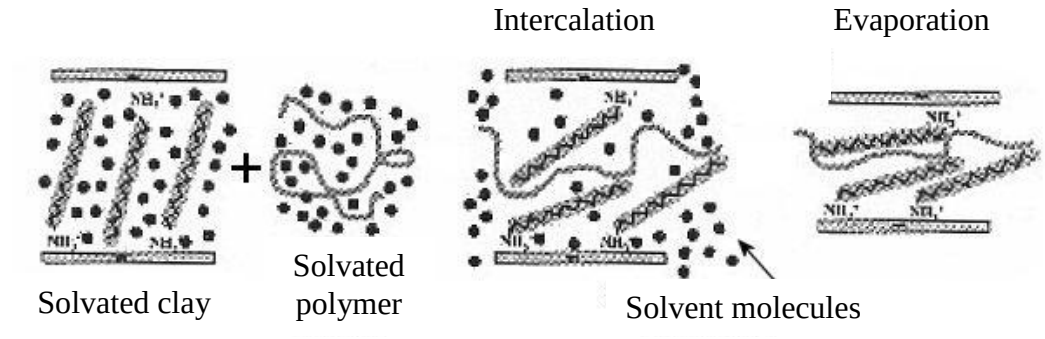

Figure 1.17. Schematic representation of the Exfoliation-adsorption process (Ray and Okamoto, 2003).

In the *In - situ intercalative polymerization* technique, the layered silicate is swollen within the liquid monomer, or a monomer solution, so as the polymer formation can occur in between the intercalated sheets. Polymerization can be initiated either by heat or radiation, by the diffusion of a suitable initiator or by a catalyst fixed through cationic exchange inside the interlayer before the swelling step by the monomer.

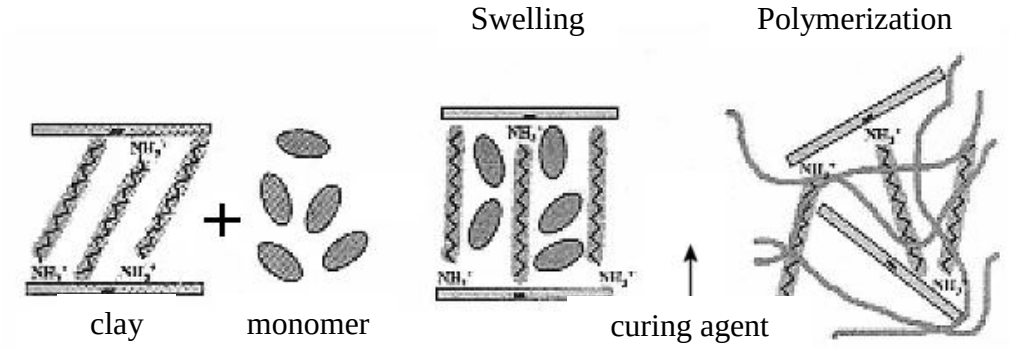

Figure 1.18. Schematic representation of the in - situ intercalative polymerization process (Ray and Okamoto, 2003).

One of the drawbacks of this method, is the effect of the high temperatures required for polymerization to the phyllosilicate morphology. As a matter of facts, the modifier, usually an alkylammonium salt, can break down diminishing the affinity of the clay with the matrix. This can hinder the penetration and the growth of the polymeric chains in the intragallery causing the formation of micrometric instead of nanometric sized agglomerates.

In *Melt intercalation* the layered silicate is mixed with the polymer matrix in the molten state. Under these conditions and if the layer surfaces are sufficiently

compatible with the chosen polymer, the polymer can crawl into the interlayer space and form either an intercalated or an exfoliated nanocomposite. In this technique, no solvent is required.

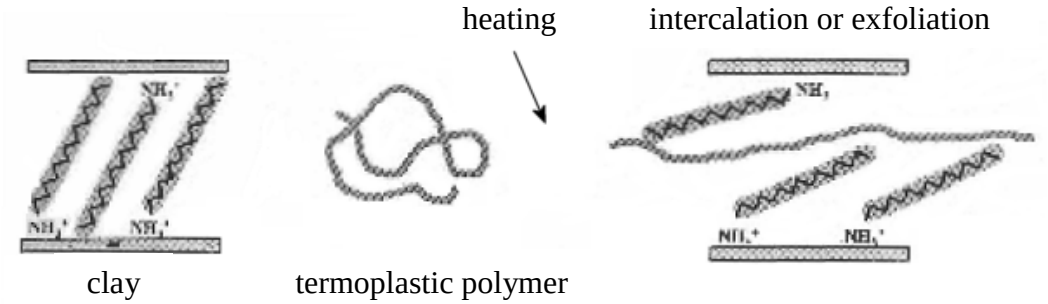

Figure 1.19. Schematic representation of the melt intercalation process (Ray and Okamoto, 2003).

In *template synthesis* the silicates are formed in situ in a aqueous solution containing the polymer and the silicate building blocks, but this technique is far less developed for layered silicates.

1.7.5 Properties

Nanocomposites consisting of a polymer and a layered silicate frequently exhibit remarkably improved mechanical and material properties when compared to those of pristine polymers, even if they contain small amounts (< 5 wt%) of layered silicate. Improvements include a higher modulus, increased strength and heat

Properties	Nylon 6	4%MMT/nylon6	Improvement
Tensile modulus [GPa]	11	21	+ 91 %
Tensile strength [MPa]	69	107	+ 55 %
Glass transition temp[°C]	65	145	+ 123 %
Impact strength [KJ/m^2]	23	28	+ 22 %
Water absorption [%]	0.87	0.51	- 41 %
Thermal expansion	13*10^{-5}	6.2*10^{-5}	- 51 %

Table 1.5. Improvement of properties for nylon 6 reinforced with 4 wt% of montmorillonite.

resistance, decreased gas permeability and flammability, and increased biodegradability. An example of the properties which can be achieved is shown in

Table 1.5. The main reason for these improved properties in nanocomposites is attributed to the stronger interfacial interaction between the matrix and the layered silicate, compared with conventional filler-reinforced systems. The main reason for the drastic improvement in tensile modulus in N6 nanocomposites, for instance, is the strong interaction between matrix and silicate layers via formation of hydrogen bonds, as shown in Figure 1.20 (Ray and Okamoto, 2003).

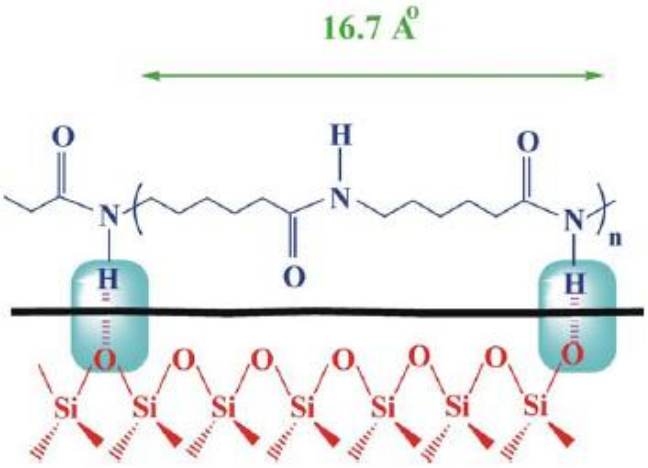

Figure 1.20. Schematic illustration of formation of hydrogen bonds in N6/MMT nanocomposites (Ray and Okamoto, 2003).

Young's modulus: the ability of silicates to improve elastic modulus depends on the length of the silicate layers, as shown in Figure 1.21, and it seems that exfoliated layers are the main factor responsible for the stiffness improvement,

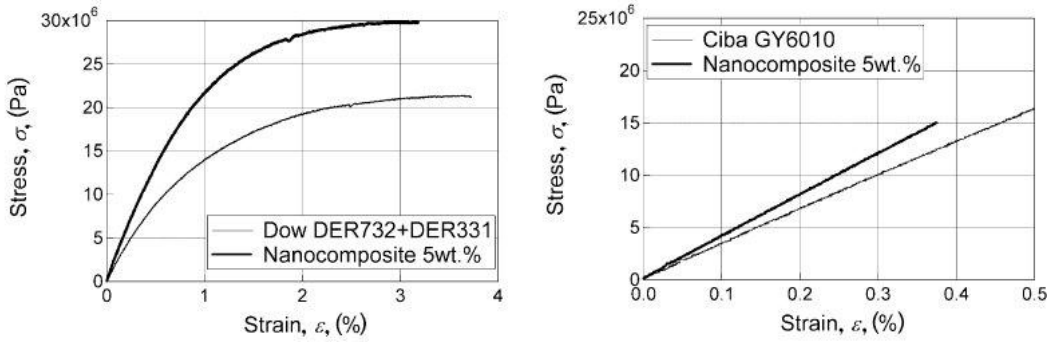

Figure 1.21. Stress/strain curves for epoxy resin a) DOW DER331/732 and b) Ciba-Geigy GY 6010 (Luo and Daniel, 2003).

N6/$(HE)_2M_1R_1$ nanocomposites	Modulus [GPa]	Yield strength [MPa]	Strain[a] (%)	Elongation at break (%) Crosshead speed		Izod impact strength [J/m]
				0.51 cm/min	5.1 cm/min	
LMW						
0.0 wt% MMT	2.82	69.2	4.0	232	28	36.0
3.2 wt% MMT	3.65	78.9	3.5	12	11	32.3
6.4 wt% MMT	4.92	83.6	2.2	2.4	4.8	32.0
MMW						
0.0 wt% MMT	2.71	70.2	4.0	269	101	39.3
3.1 wt% MMT	3.66	86.6	3.5	81	18	38.3
7.1 wt% MMT	5.61	95.2	2.4	2.5	5	39.3
HMW						
0.0 wt% MMT	2.75	69.7	4.0	3.4	129	43.9
3.2 wt% MMT	3.92	84.9	3.3	119	27	44.7
7.2 wt% MMT	5.70	97.6	2.6	4.1	6.1	46.2

Table 1.6. N6/$(HE)_2M_1R_1$ nanocomposites main mechanical properties (Fornes and Paul, 2003).
[a] Strain at yield point measured during modulus and yield strength testing using a crosshead speed of 0.51 cm/min.

while intercalated particles, with a lower aspect ratio, play a minor role. In various polymer matrixes (not only Nylon 6, but also PMMA or EVA and thermosets) exfoliation is a key factor in improving the Young's modulus, while this is not necessary in pure elastomers.

The *tensile strength*, in thermoplastic-based nanocomposites, is usually improved and this is explained by the presence of polar and even ionic interactions between the polymer and silicate layers. Also epoxy thermosets with the T_g under room temperature increase their tensile strength with layered silicates independently from the aspect ratio of the layers. Indeed, thermosets with an high T_g do not lead to improvements in the tensile stress at break.

The *elongation at break* can be dramatically reduced in thermoplastic nanocomposites (like PMMA, PS or PP), while the addition of nanoclays in cross-linked matrixes triggers an increase of the elongation at break and again an exfoliated structure is preferable on an intercalated composites.

It can happen that *impact strength* can be reduced in exfoliated nanocomposites, but this decrease is not very pronounced: Alexandre and Dubois (Alexandre and Dubois, 2000) reported to drop from 6.21 kJ/m^2 of neat nylon-6 to 6.06 kJ/m^2 of the 4.7 wt% clay/nanocomposite.

The *thermal stability* of polymeric materials is usually studied by thermogravimetric analysis (TGA). The weight loss due to the formation of volatile products after degradation at high temperature is monitored as a function

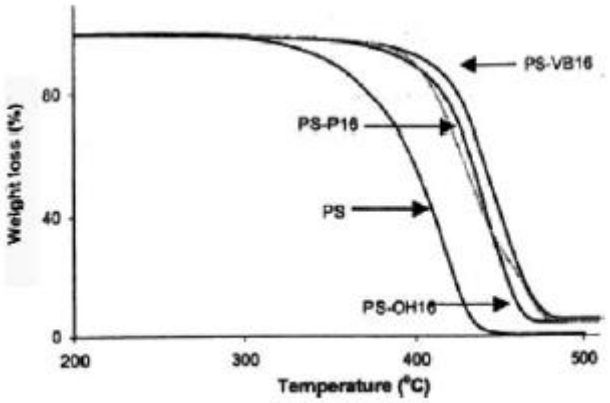

Figure 1.22. TGA curves for polystyrene, PS and the nanocomposites. Increase of thermal stability in montmorillonite nanocomposites (Zhu et al., 2001).

of temperature. Generally, the incorporation of clay into the polymer matrix was found to enhance thermal stability. An example is given in Figure 1.22.

Flame retardancy: The Cone calorimeter is one of the most effective bench-scale methods for studying the fire retardant properties of polymeric materials. Fire-relevant properties such as the heat release rate (HRR), heat peak HRR, smoke production, and CO_2 yield, are vital to the evaluation of the fire safety of materials. In 1976 Unitika Ltd, Japan, first presented the potential flame retardant properties of N6/layered silicate nanocomposites (Fujiwara and Sakamoto, 1976). Then in 1997 Gilman et al. reported detailed investigations on flame retardant properties of N6/layered silicate nanocomposite (Gilman et al., 1997). Recently, Gilman reviewed the flame retardant properties of nanocomposites in detail (Gilman, 1999). Since the decreased flammability of nanocomposites is one of the most important properties, the results of some of the most recent studies on flame retardant properties of nanocomposites are reported in the following. Table 1.7 represents the cone calorimeter data of three different kinds of polymer and their nanocomposites with MMT. As shown in Table 1.7, all of the MMT-based nanocomposites reported here exhibit reduced flammability. The peak HRR is reduced by 50–75% for N6, PS, and PP-g-MA nanocomposites (Gilman et al., 2000). According to the authors, the MMT must be nanodispersed for it to affect the flammability of the nanocomposites. However, the clay need not be completely delaminated. In general, the nanocomposites' flame retardant mechanism involves a high-performance carbonaceous-silicate char, which builds up on the surface during burning. This insulates the underlying material and slows the mass loss rate of decomposition products. In a recent study, Zhu et al. (Zhu et al. 2001) reported the fire retardant properties of PS/MMT nanocomposites, which were prepared using three different types of new organically modified MMT. They initially used phosphonium salt for the modification of clay, and then examined the differences between organo ammonium and phosphonium salt treatments of clay fillers in nanocomposites towards thermal stability. The suggested mechanism by which clay nanocomposites function involves the formation of a *char*, i.e. the formation of a carbonaceus layer, that serves as a barrier to both mass and energy transport (Gilman et al., 2001). As the fraction of

Sample (structure)	% residue yield (+/- 0.5)	Peak HRR [kW/m^2] (Δ%)	Mean HRR [kW/m^2] (Δ%)	Mean H_c [MJ/kg]	Mean SEA [m^2/kg]	Mean CO yield [kg/kg]
N6	1	1010	603	27	197	0.01
N6 nanocomposite 2% (delaminated)	3	686 (32)	390 (35)	27	271	0.01
N6 nanocomposite 5% (delaminated)	6	378 (63)	304 (50)	27	296	0.02
PS	0	1120	703	29	1460	0.09
PS-silicate mix 3% (immiscible)	3	1080	715	29	1840	0.09
PS nanocomposite 3% (intercalated/delaminated)	4	567 (48)	444 (38)	27	1730	0.08
PS w/DBDPO/Sb_2O_3 30%	3	491 (56)	318 (54)	11	2580	0.14
PpgMA	5	1525	536	39	704	0.02
PpgMA-nanocomposites 2% (intercalated/delaminated)	6	450 (70)	322 (40)	44	1028	0.02
PpgMA-nanocomposites 4% (intercalated/delaminated)	12	381 (75)	275 (49)	44	968	0.02

Table 1.7. Heat flux, 35 kW/m^2. H_c: specific heat of combustion; SEA, specific extinction area. Peak HRR, mass loss rate, and SEA data, measured at 35 kW/m^2, are reproducible to within +/-10%. The carbon monoxide and heat of combustion data are reproducible to within +/-15% (Gilman et al., 2000).

clay increases, the amount of char that can be formed increases, and the rate at which heat is released decreases. The production of a char barrier must serve to retain some of the PS, and thus both the energy released and the mass loss rate decrease. The amount of smoke evolved and specific extinction area also decrease with the formation of the nanocomposites. There is some variability in the smoke production. Although it is observed that the formation of the nanocomposites reduces smoke production, the presence of additional clay does not continue this smoke reduction.

Gas barrier: The high aspect ratio characteristic of silicate layers in exfoliated nanocomposites has been found to highly reduce the permeability to small gases,

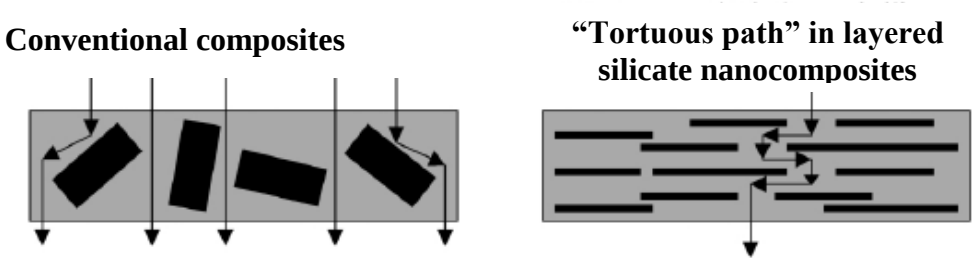

Figure 1.23. Schematic illustration of "tortuous path" in PLS nanocomposites (Ray and Okamoto, 2003).

like O_2, H_2O, He, CO_2. Clays are believed to increase the barrier properties by creating a maze or 'tortuous path' (Figure 1.23) that retards the progress of the gas molecules through the matrix resin.

Optical transparency: although layered silicates are microns in lateral size, they are just 1 nm thick. Thus, when single layers are dispersed in a polymer matrix, the resulting nanocomposite is optically clear in visible light. Figure 1.24 presents the UV/visible transmission spectra of pure PVA and PVA/Na^+-MMT nanocomposites with 4 and 10 wt% MMT. The spectra show that the visible region is not affected by the presence of the silicate layers, and retains the high transparency of PVA. For UV wavelengths, there is strong scattering and/or absorption, resulting in very low transmission of UV light. This behavior is not surprising, as the typical MMT lateral sizes are 50–1000 nm. Like PVA, various other polymers also show optical transparency after nanocomposite preparation with OMLS (Alexandre and Dubois, 2000; Nam et al., 2001).

Product	Characteristics	Applications	Producer
Nanomers	microfine powder	nylon, epoxy, unsaturated polyester, engineering resins	Nanocor
Closite	Organophilic	Additives, enhance flexural and tensile modulus, barrier properties and flame retardance of thermoplastics	Southern Clay Products
Bentone	With a broad range of polarity	Additives to enhance mechanical, flame retardant and barrier properties of thermoset and thermoplastics	Elementis Specialties
Masterbatches	pellet	thermoplastic olefin and urethane, styreneethylene butylene-styrene, Ethylene Vinyl Acetate	PolyOne Corporation, Clariant Corporation, RTP Company
Nanofil	Improve the mechanical, thermal and barrier properties	Thermoplastics and thermosets	Sud-Chemie
Planomers	additive, enhance mechanical barrier properties, thermal stability and flame resistance	electric and electronic, medical and healthcare, adhesive, building and construction materials	TNO
PlanoColors	nanopigments, e.g. blue, red, green, yellow, high UV-stability	decorative coloring, UV-stable coloring, heavy metal free coloring	TNO
PlanoCoatings	additive, excellent transparency and improved barrier properties	transparent packaging materials, protective coatings, transparent barrier coatings	TNO

Table 1.7. Main commercial nanoclays and applications (Source: www.nanocompositech.com).

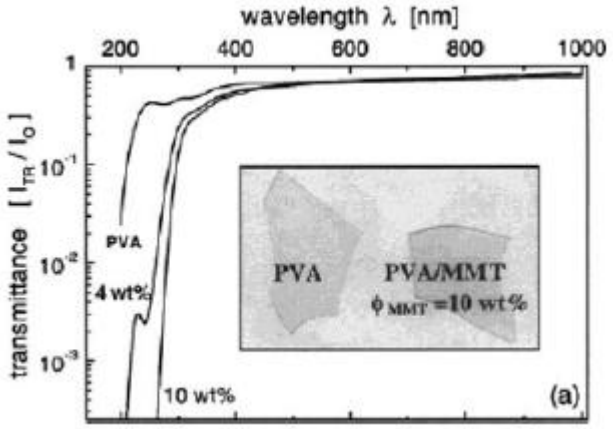

Figure 1.24. UV–vis transmittance spectra of PVA and PVA/MMT nanocomposites containing 4 and 10 wt% MMT (Strawhecker and Manias, 2000).

1.7.6 Applications

Table 1.7 shows some PLS nanocomposites applications. There are two main fields: the automotive and the packaging.

In the automotive, polypropylene and nylon composites are used for the covers of transmission belts in the engines and for components of the bodywork, like footboards or handles.

A promising future commercial development is in food packaging. The good barrier properties can grant a longer shelf life to food and drinks. Bayer is already selling some films for packaging containing nanolayered silicates dispersed in Nylon 6 (Carati et al. 2002).

1.8 Carbon nanotubes

The formation of carbon nanotubes can be traced back to the discovery of a third stable form of carbon after the well known diamond and graphite: the *fullerene*. The first fullerene structure C_{60}, the so called buckyball, was found in 1985 at Rice University by Smalley, Kroto and coworkers. Its structure consists of 60 atoms of carbon arranged by 20 hexagonal and 12 pentagonal faces to form a sphere. Six years later, in 1991, the Japanese electron microscopist Iijima first observed fullerene-related structures consisting of multi-graphene cylinders closed at either ends with semi-fullerene caps, which were formed by an arc

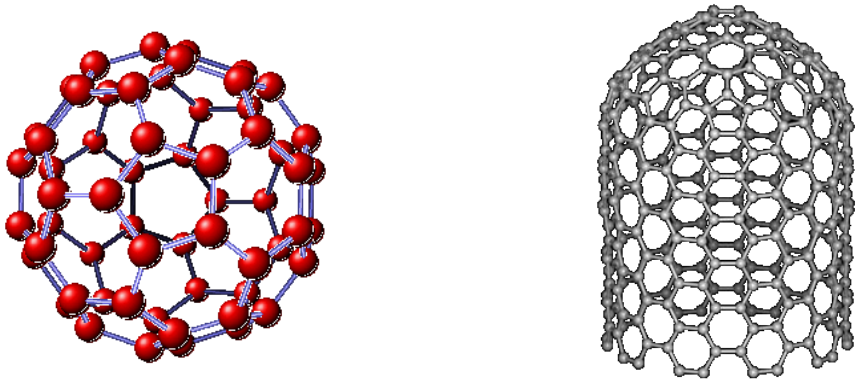

Figure 1.25. Schematic representation of a fullerene and a SWCNT.

discharge between carbon electrodes. He had just discovered *multi-walled carbon nanotubes* (MWCNTs) (Kau and Hiu, 2002). Two years after, Iijima and Bethune separately synthetized *single-walled carbon nanotubes* (SWCNTs) (Popov, 2004).

1.8.1 Structures and different CNT typologies

A SWCNT can be visualized as a sheet of sp^2-bonded graphite rolled up to form a seamless cylinder. Its atomic structure is described in terms of the tube *chirality*, or *helicity*, which is defined by the chiral vector, C_h , and the chiral angle, θ. In Figure.1.9, we can visualize cutting the graphite sheet along the dotted lines and

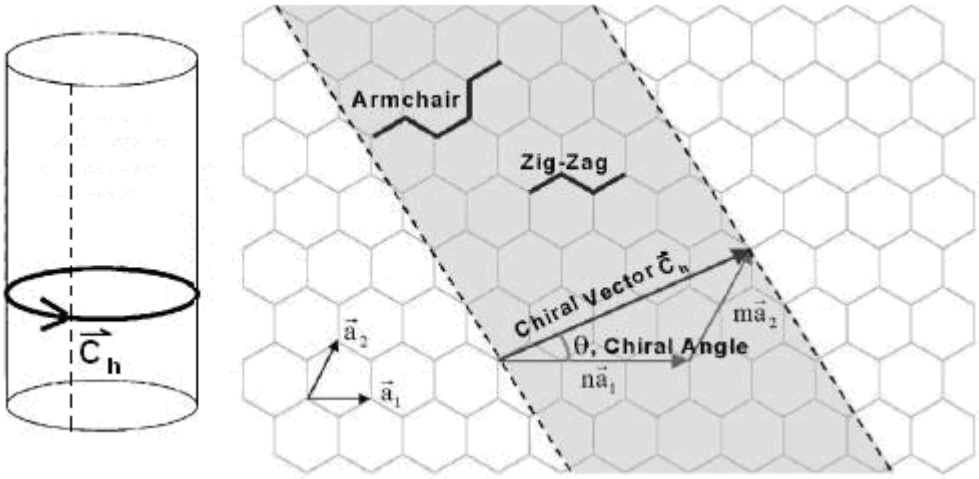

Figure 1.26. The chiral vector and the chiral angle in a carbon nanotube (Thostenson et al., 2001; Cohen, 2001; Thostenson et al., 2005).

rolling the tube so that the tip of the chiral vector touches its tail. The chiral vector

can be described by the following equation:

$$\overrightarrow{C_h} = n\ \overrightarrow{a_1} + m\ \overrightarrow{a_2} \tag{1.1}$$

where the integers (*n*, *m*) are the number of steps along the ziz-zag carbon bonds of the hexagonal lattice and a_1 and a_2 are unit vectors, shown in Figure 1.9. The chiral angle determines the amount of 'twist' in the tube. It can be related to *n* and *m* by means of the following formula (Bhushan et al., 2004):

$$\cos\theta = \frac{2n+m}{2\sqrt{n^2+m^2+nm}} \tag{1.2}$$

There is a strong correlation between nanotube diameter *D* and *n* and *m* which is expressed by means of the following equation (Bhushan et al., 2004):

$$D = \frac{\left|\overrightarrow{C_h}\right|}{\pi} = \frac{a_{CC}\sqrt{3\left(n^2+m^2+nm\right)}}{\pi} \tag{1.3}$$

The two limiting cases exist where the chiral angle is at 0° and 30° and they are referred to as *ziz-zag* (θ = 0°) and *armchair* (θ = 30°) based on the geometry of the carbon bonds around the circumference of the nanotube.

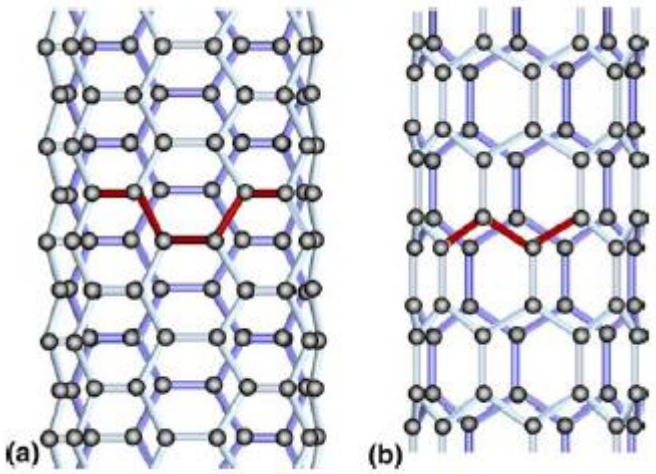

Figure 1.27. Atomic structures of a) armchair and b) zig-zag carbon nanotubes (Thostenson et al., 2001).

The difference in armchair and zig-zag nanotube structures is shown in Figures 1.27 and 1.28 a). In terms of the chiral vector, the ziz-zag nanotube is (n,0) and the armchair nanotube is (n,n). Double and multi walled nanotubes are essentially concentric single walled tubes, where each individual tube can have different chirality. The structure of a MWCNT is depicted in Figure 1.28 b). The concentric

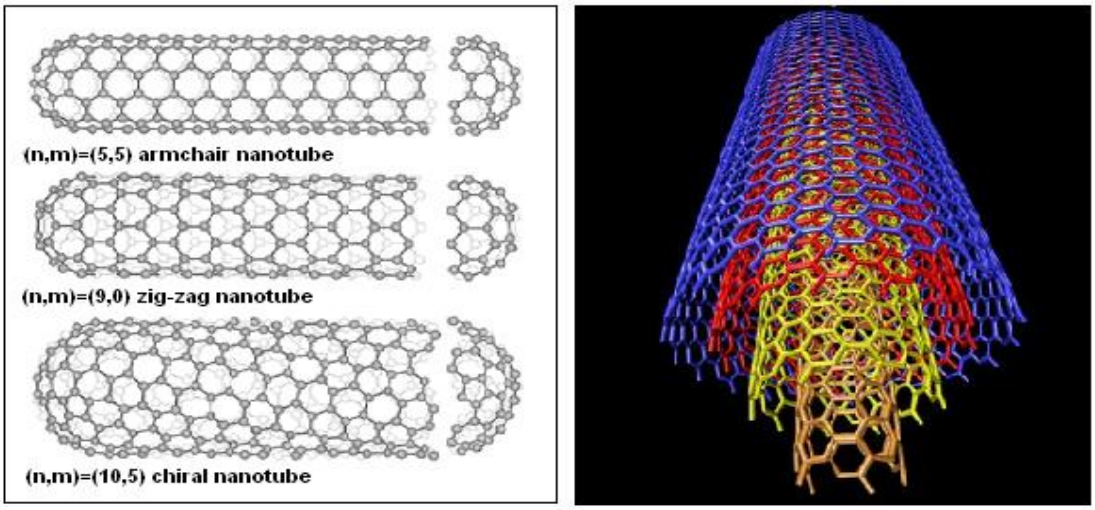

Figure 1.28. a) Types of CNTs depending on chirality. b) MWCNTs are concentric single walled carbon nanotubes (Lau and Hiu, 2002; Holister et al., 2003).

layers are held together by secondary, Van der Waals bonding. DWCNTs consist of two graphite sheets, MWCNTs typically have between 8 and 30 concentric layers.

1.8.2 Production processes of carbon nanotubes

The main methods that have been developed for producing carbon nanotubes are:

- *Direct-current arc discharge*: the carbon needles grow on the negative end of the carbon electrode used for the direct current arc discharge evaporation of carbon in an argon-filled vessel;
- *Laser ablation*: laser beam vaporizes target of a mixture of graphite and metal catalyst (Co,Ni) in a horizontal tube in a flow of inert gas at controlled pressure and in a tube furnace at 1200°C. The nanotube are deposited on a water-cooled collector outside the furnace;
- *Catalytic growth (CVD):* hydrocarbon gas is decomposed in a quarts tube in a furnace at 550-750°C over a transition metal catalyst (a CVD reactor);
- *Self-assembly of single crystals of SWNTs*: a mixture of C60 and Ni is evaporated through a nanostencil mask with an array of 300nm diameter holes, which is accurately positioned a few microns above a molybdenum substrate.

A detailed description of the abovementioned techniques can be found in Bushan et al. (Bushan et al. 2004).

1.8.3 Functionalization

In order to improve nanotubes dispersion and interfacial bonding with the polymeric matrix, CNTs are usually functionalized. S.J. Park et al. (Park et al., 2004) report that various surface treatments have been carried out to improve interfacial adhesion by achieving sites for strong hydrogen bonding on the surface of nanotubes, such as oxidation in acid solution, dry oxidation in oxygen, anodic oxidation and plasma treatments. They investigated a technique of oxyfluorination on MWCNTs, which consists in introducing a mixture of fluorine and oxygen gases in a previously evacuated batch reactor and heating at the reaction temperature. It was found that the oxygen/fluorine content was maximum at 100°C and it led to improved mechanical interfacial properties. The stronger interface was attributed to the formation of C-F and oxygen functional groups on the nanotubes which changed the polarity and the activity of the surface. Similar procedures of chemical modification are particularly useful also with SWCNTs, because they tend to assemble in ropes or bundles, which should be separated to maximize their interaction with the matrix. A process described by Ajatan et al. (Ajayan et al., 2004) involves breaking the bundles in an acidic solution, adding carboxylic groups to the ends of the tubes and placing the SWCNT in an octadecylammonium melt for several days, obtaining exfoliated nanotubes . Also the doping with boron atoms seems to result (in addition to changes in electronic states) in out-of-plane bonding configurations that increase the reactivity of the surface of the carbon nanotubes (Ajayan et al., 2004). A possible functionalisation process is schematically shown in Figure 1.29. An oxidative treatment of the nanotubes was used to develop carboxylic groups (step 1). The generation of these functional groups is combined with an opening of the CNT cap. This would enable a direct bonding of the tube ends via the carboxylic groups to the matrix, which would be favorable regarding a mechanical reinforcement. In the second step the carboxylic groups would react with multifunctional amines and form bonds (either ionic or under the given conditions covalent) to these amines (step 2) via an acid/base reaction. With the addition of the epoxy resin, the free amino

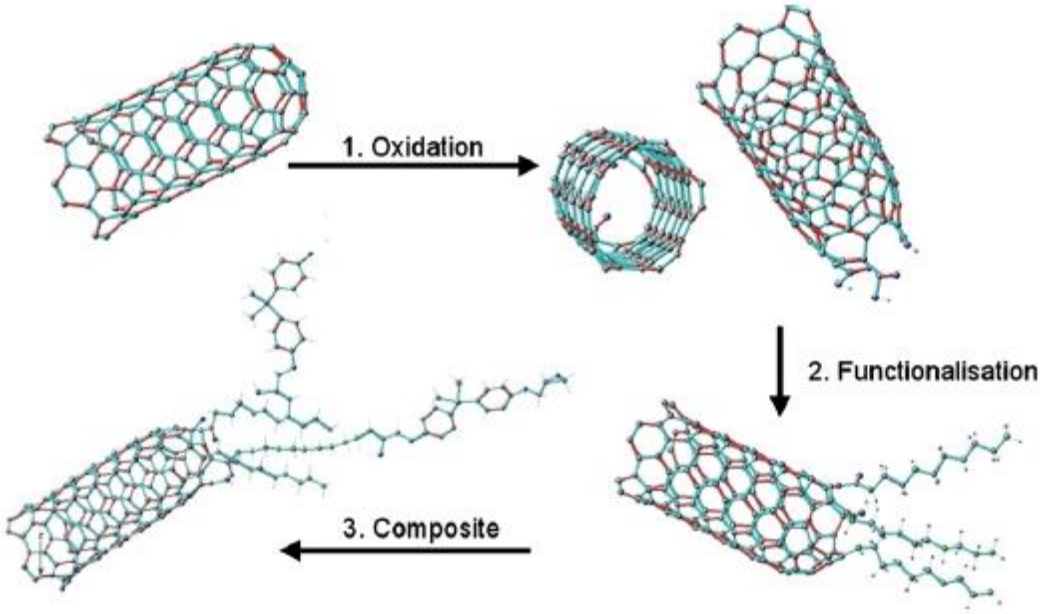

Figure 1.29. Scheme of the functionalisation process of CNTs showing the whole cycle from the oxidation to the composite manufacturing. An improved matrix/nanotube interaction can be achieved via an equivalent bonding between the functional groups on the nanotube surfaces and the epoxy. In a first step the nanotubes are oxidised (1) then functionalised (2) and finally processed to the nanocomposite (3) (Fiedler et al., 2006).

functions on the surface of the CNTs will react with the epoxy molecules forming equivalent bonds, which lead to an improved nanotube matrix bonding (step 3).

Besides the chemical functionalization, another common method to assimilate the polarity of CNTs and polymer is the functionalization with surfactants (Fiedler et al., 2006). Similar to this technique there is also the use of conjugated polymer, which can physically bond to CNTs. Some patented procedures are based on surfactants, an example is a suspension consisting of SWCNT coated with proprietary molecules sold by Zyvex. The advantage of surfactants is that the adhesion is physical and does not reduce the structural quality of the nanotubes, as chemical changes can do. However, the covalent bonding is stronger than physical interactions and simulations predict that a functionalization of less than 1 % would improve the interfacial adhesion with negligible influence on the mechanical properties.

1.8.4 Properties

Nanotubes have extraordinary mechanical, thermal and electrical properties with

providing strong, light and high toughness characteristics. Some typical properties of different kinds of nanotubes are given in Table 1.8.

The *tensile modulus and strength* of nanotubes has been reported (Lau and Hiu, 2002; Thostenson et al, 2005; Fiedler et al., 2006) to range about 270 GPa to 1 TPa and 11-200 GPa. This means that they are at least 100 times stronger than steel, even though they are only one-sixth as heavy. An idea of their extraordinary

Property	SWNT	DWNT	MWNT
Max Density [g/cm^3]	0.94	0.77	2.10
Diameter [nm]	1 - 5	2 - 6	13 - 50
Length [mm]	1 - 30	2 - 50	10 - 500
Length/Diameter Ratio	1,000 - 5,000	500 - 12,000	2,000 - 20,000
Elastic Modulus [GPa]	1,200 - 1,700	1,000 - 2,000	1,000 - 3,700
Tensile Strength [GPa]	300 - 1,500	300 - 1,000	300 - 600
Thermal Conductivity [W/mK]	3,000	1,500 - 3,000	1,500
Resistivity [mW cm]	0.03	0.03 - 0.1	0.1
Strain Failure [%]	20 - 40	20 - 40	20 - 40

Table 1.8. Typical properties for SWCNT, DWCNT and MWCNT.

tensile strength compared to graphite and Kevlar fibres and to stainless steel is given by Figure 1.30. However, many efforts have been put in the last years to investigate the elastic response of nanotubes, their inelastic behaviour and buckling, yield strength and fracture, from the experimental and theoretical point of view. In fact, large scatterings of the measurements have been found in different literatures, as reported by Lau and Hiu (Lau and Hiu, 2002), there are many experimental uncertainties and it is difficult to find accurate experimental methods dealing with such small dimensions.

Bending properties: Thostenson et al. (Thostenson et al., 2001) report that direct measurement of the stiffness and strength of individual, structurally isolated multi-wall carbon nanotubes has been made with an atomic-force microscope (AFM). The nanotube was pinned at one end to a molybdenum support and load was applied to the tube by means of the AFM tip. The bending force was measured as a function of displacement along the unpinned length, and it was obtained an elastic modulus of 1.26 TPa and an average bending strength of 14.2

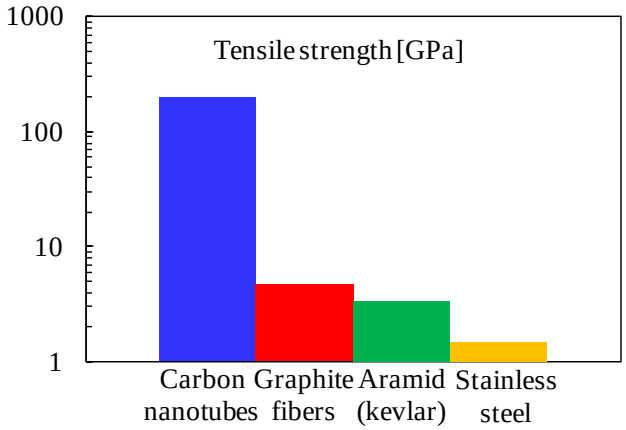

Figure 1.30. Tensile strength of carbon nanotubes compared to some engineering materials (from Lau and Hiu, 2002).

± 8 GPa. Also theoretical studies have been pursed and Iijima used molecular dynamics simulations to simulate the deformation properties of single- and multi-walled CNTs bent to large angles. Nanotubes showed a remarkably flexible behaviour with a completely reversible bending up to more than 110°.

It seems that chirality does not affect the mechanical properties of CNTs in tension and bending, while in torsion chiral tubes show an asymmetric behaviour different from that of armchair and zig-zag nanotubes.

Strain at failure: it has been reported (Popov, 2004) the computation of the strain energy of nanotubes with a continuum elastic model. It was concluded that nanotubes are ductile with small radius and small chiral angle, i.e. that for a given radius, a zig-zag and an armchair tubes are the lower and the upper limit in yield strain for a load applied along the tube's axis. Armchair nanotubes are believed to release their excess strain by the spontaneous formation of the Stone-Walls defect. This defect is shown in Figure 1.31 and it implies a dislocation in the hexagonal loop and the reallocation of the C-C bond forming two heptagons and two pentagons.

The *electric properties* of nanotubes depend on the diameter and the chirality. Stroscio and Feenstra (Stroncio and Feenstra, 1993) found a rule, which is displayed in Figure 1.32: armchair nanotubes (with n = m) are always metallic, while zig-zag (n,0) and chiral (n ≠ m) nanotubes can be either metallic or semiconductive. If n-m = 3p (with p integer), the nanotube is expected to behave as a metal, while if n-m ≠ 3p the tube should be semiconductors. Metallic

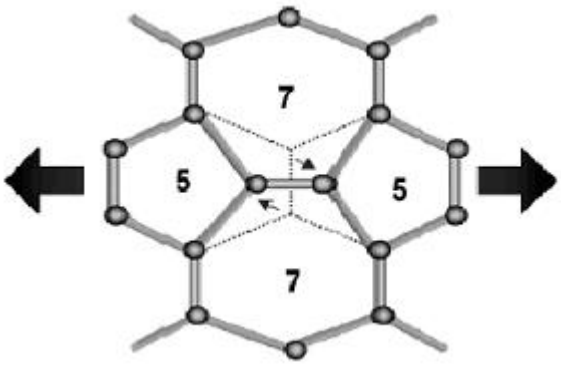

Figure 1.31. The Stone-Wales transformation in an armchair nanotube under axial tension (Thostenson et al., 2001).

nanotubes have an electrical conductivity similar to copper (10^4 $\Omega^{-1}cm^{-1}$ for CNTs in comparison with $0.6*10^6$ $\Omega^{-1}cm^{-1}$ for copper), but with the ability to carry much higher currents (10^9-10^{10}A/cm^2, over 1000 times higher than Cu). A material is classified semiconductor if the energy difference between the valence band and the conduction band, called energy gap, is between 0.2 and 1 eV. This energy gap (E_{gap}) in semiconductive nanotubes is in the order of 0.5 eV, but it is highly dependent on the diameter of the tube, with the following relationship:

$$E_{gap} = \frac{2\gamma_0 a_{C-C}}{d} \tag{1.4}$$

where γ_0 = 2.45 eV, $a_{c\text{-}c}$= 1.42 Å is the nearest neighbour C-C distance and *d* is the

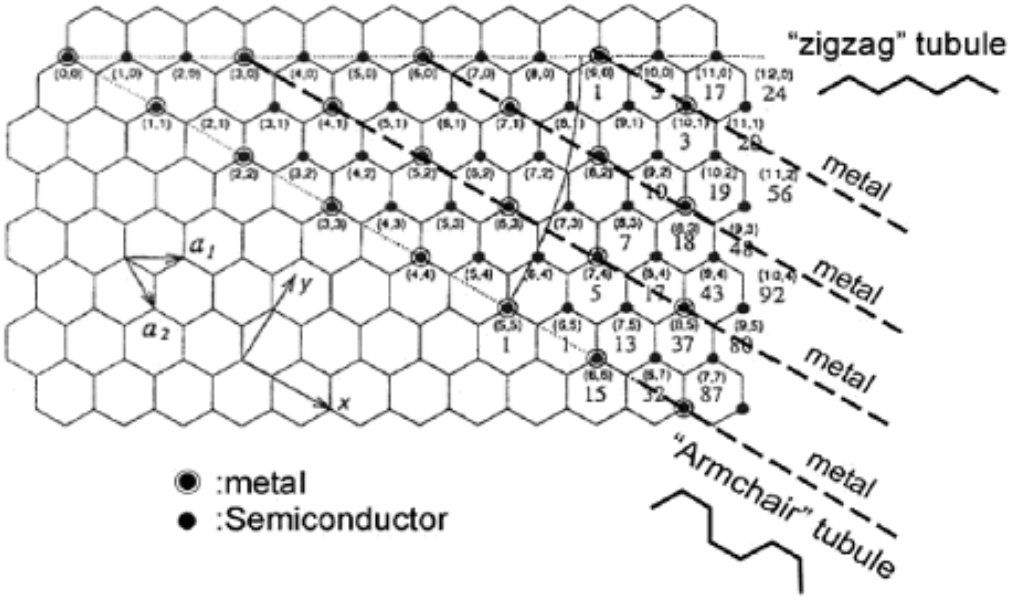

Figure 1.32. Nanotubes can behave like semiconductors or metals.

diameter of the tube. Furthermore, the electric resistance of the nanotubes has been found to increase with the bending angle, particularly over 45°, and with the twisting angle up to a critical limit. The dependency of electrical resistance of nanotubes from diameter and torsion angle is displayed in Figure 1.33.

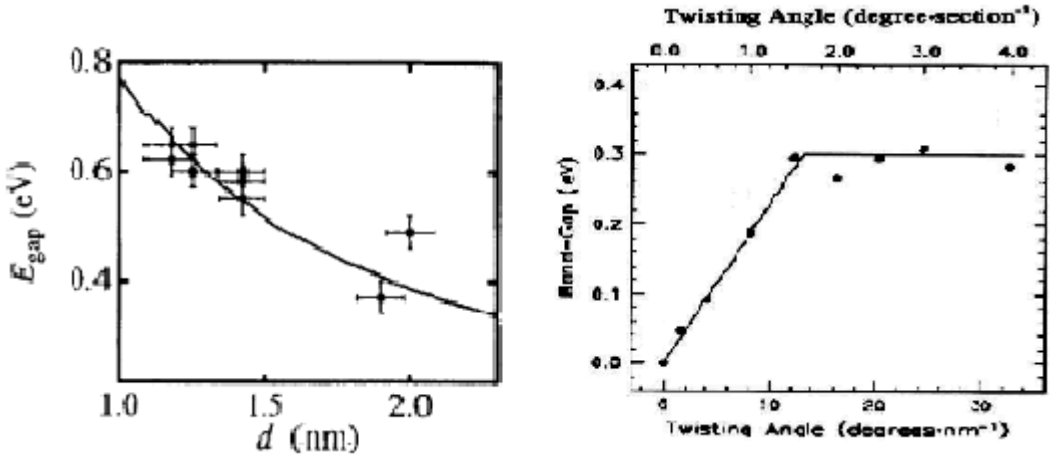

Figure 1.33. The electrical resistance of a semiconductive nanotube depends on the diameter and on the twisting angle.

1.8.4 Applications

The unique properties of CNTs lead to many possible applications (Gojny et al., 2005):

Conductive plastics: A mixture of conducting and insulating phases becomes conducting when the volume fraction of conducting phase exceeds a "percolation threshold", the minimum amount to give a continuous path across the whole sample. The higher the aspect ratio, the lower is this threshold. Nanotubes are ideal from this point of view since they have very high aspect ratios and percolation have been achieved in epoxy resins even at 0.01% or at 0.004% of MWCNTs. Examples of applications can be: eletrostatically painting on car components, antistatic shielding in airplane wings and fuselages, electromagnetic shielding and transparent electronic conductors for displays.

Structural composites: since nanotubes have extremely high mechanical properties, they have attracted much interest for low weight structural composites.

Filler type	Filler content (wt%)	Young's modulus (MPa)	Ultimate tensile strength (MPa)	Fracture toughness K_{IC} ($MPa*m^{1/2}$)
Epoxy	0.0	2599 (±81)	63.80 (±1.09)	0.65 (±0.062)
Epoxy/CB	0.1	2752 (±144)	63.28 (±0.85)	0.76 (±0.030)
	0.3	2796 (±34)	63.13 (±0.59)	0.86 (±0.063)
	0.5	2830 (±60)	65.34 (±0.82)	0.85 (±0.034)
Epoxy/SWCNT	0.05	2681 (±80)	65.84 (±0.64)	0.72 (±0.014)
	0.1	2691 (±31)	66.34 (±1.11)	0.80 (±0.041)
	0.3	2812 (±90)	67.28 (±0.63)	0.73 (±0.028)
Epoxy/DWCNT	0.1	2785 (±23)	62.43 (±1.08)	0.76 (±0.043)
	0.3	2885 (±88)	67.77 (±0.40)	0.85 (±0.031)
	0.5	2790 (±29)	67.66 (±0.50)	0.85 (±0.064)
Epoxy/DWCNT–NH2	0.1	2610 (±104)	63.62 (±0.68)	0.77 (±0.024)
	0.3	2944 (±50)	67.02 (±0.19)	0.92 (±0.017)
	0.5	2978 (±24)	69.13 (±0.61)	0.93 (±0.030)
Epoxy/MWCNT	0.1	2780 (±40)	62.97 (±0.25)	0.79 (±0.048)
	0.3	2765 (±53)	63.17 (±0.13)	0.80 (±0.028)
	0.5	2609 (±13)*	61.52 (±0.19)*	*
Epoxy/MWCNT –NH2	0.1	2884 (±32)	64.67 (±0.13)	0.81 (±0.029)
	0.3	2819 (±45)	63.64 (±0.21)	0.85 (±0.013)
	0.5	2820 (±15)	64.27 (±0.32)	0.84 (±0.028)

(*) High viscosity disabled degassing – composite contained numerous voids.

Table 1.9. Mechanical properties of nanoparticle reinforced nanocomposites (Gojny et al., 2005).

However, some challenges have to be overcome, like obtaining a good dispersion and a sufficient bonding across the nanotube/host interface to transfer forces. These conditions are necessary to have composites with satisfying properties, but they are not easy to be realized.

An example of the interesting mechanical properties that can be achieved reinforcing polymers with nanotubes is shown in Table 1.9 (Gojny et al., 2005), were the effects of SWCNT, DWCNT and MWCNT in an epoxy matrix are compared.

Not only the Young's modulus and the tensile strength are improved, but also the fracture toughness can be strikingly higher with the addition of only small amounts of nanotubes.

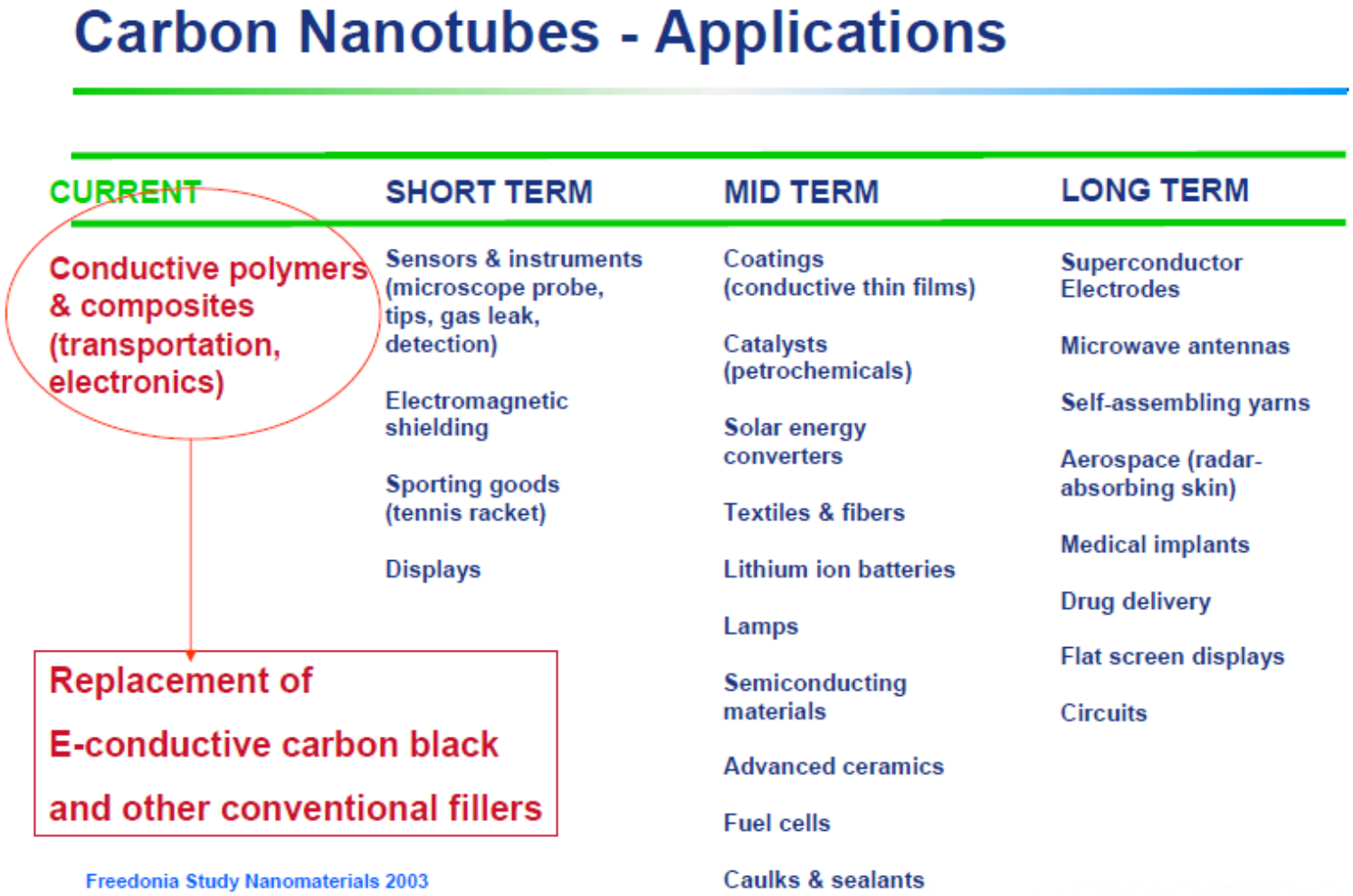

Table 1.10. Main potential applications of carbon nanotubes (Source: Bayer)

Fibers and fabrics: it has been attempted to spin carbon fibers from carbon nanotubes (Holister and Harper, 2003). Various methods have been tried and one of the newest consists in drawing and spinning a nanotube fibre directly from a CVD reaction chamber. Further developments in this area may potentially create a new form of carbon fibres characterized by exceptional flexibility as well as stiffness, strength and resilience.

Field emission: it is the emission of electrons from a solid under an intense electric field. Carbon nanotubes have excellent properties for field emission such as very high aspect ratio (>1000), atomically sharp tips, high temperature and chemical stability, high electrical and thermal conductivity. The most promising application is for electron guns for scanning and transmission electron microscopes (SEM and TEM). Other applications are as field emission cathodes in high power microwave amplifiers and as electron sources for miniature X-ray sources. A very attractive market for CNTs can also be field emission displays (FEDs), even though in this market they will have to compete with more consolidated technologies like liquid crystal displays and plasma display panels.

Energy storage: nanotubes could find application in batteries and in supercapacitors, which are devices for energy storage with high power density and high energy density. They can also be very useful in components for fuel cells.

Thermal materials: thermal conductivity of carbon nanotubes is enabling of applications where heat needs to move from one place to another, such as electronics, and particularly, advanced computing. Aligned structures and ribbons have been studied with the goal of producing highly efficient heat conduits.

Electronics: nanotubes can carry the highest current density of any metal and this property can be exploited to produce field emission transistors (FET) even though they still have to be improved because by now they are faster, but they need more space than the Si-based FETs. Without excessive processing CNTs can be good optical switches and they are giving a revival to the idea of building electronic circuits on the nanoscale. Table 1.10 summarizes the main potential applications.

Bibliography of chapter 1

Adebahr T, Roscher C., Adam J., "Reinforcing nanoparticles in reactive resin". *European Coatings Journal*, 4, 144-149, 2001.

Ajayan P.M., Schadler L.S., Braun P.V., "Nanocomposite Science and Technology", Wiley-VCH, 2004.

Alexandre M., Dubois P., "Polymer-layered silicate nanocomposites: preparation, properties and uses of a new class of materials", *Materials Science and Engineering* 28, 1-63, 2000.

Battistella M., Cascione M., Fiedler B., Wichmann M.H.G., Quaresimin M., Schulte K., "Fracture behaviour of fumed silica/epoxy nanocomposites", *Composites: Part A 39,*1851–1858, 2008.

Becker O., Varley R., Simon G., "Morphology, thermal relaxations and mechanical properties of layered silicate nanocomposites based upon high-functionality epoxy resins", *Polymer,* 43, 4365-4373, 2002.

Becker O., Cheng Y.B., Varley R., Simon G., "Layered Silicate Nanocomposites Based on Various High-Functionality Epoxy Resins: The Influence of Cure Temperature on Morphology, Mechanical Properties and Free Volume", *Macromolecules,* 36, 1616-1625, 2003.

Carati A., Gagliardi F., Rizzo C., " Nanocompositi: non è fantascienza", *Materiali innovativi,* pp. 8-12, TPoint 4/2002.

Term Thesis of Manuela Cascione, "Manufacturing and testing of nano-modified and conventional Glass-Fibre Reinforced Composites". Università di Padova-Technische Universitaet Hamburg-Harburg, 2005.

Chan C.M., Wu J., Li J-X, Chenung Y-K. "Polypropylene/calcium carbonate nanocomposites", *Polymer* 43, 2981-2992, 2002.

Cohen M.L. "Nanotubes, Nanoscience and Nanotechnology". *Materials Science and Engineering* C 15 , 1-11, 2001.

Feynmann R.P., "There's plenty of room at the bottom",Eng. Sci. **23** (1960) 22–36, and www.zyvex.com/nanotech/feynman.html (1959).

Fiedler B., Gojny F.H., Wichmann M.H.G., Nolte M.C.M., Schulte K., "Fundamental aspects of nano-reinforced composites", *Composites Science and Technology,* 66, 3115–31, 2006.

Fornes T.D., Paul D.R., "Modeling properties of nylon 6/claynanocomposites using composite theories", *Polymer*, 44, 4993–5013, 2003.

Gilman J.W., Kashiwagi T., Lichtenhan J.D. "Flammability studies of polymer-layered silicate nanocomposites". *SAMPE J*, 33:40–5, 1997.

Gilman J.W., "Flammability and thermal stability studies of polymer-layered silicate (clay) nanocomposites". *Appl Clay Sci*, 15:31–49, 1999.

Gilman JW, Jackson CL, Morgan AB, Harris Jr R, Manias E, Giannelis EP, Wuthenow M, Hilton D, Phillips SH., "Flammability properties of polymer-layered silicate nanocomposites. Propylene and polystyrene nanocomposites". *Chem Mater*, 12:1866–73, 2000.

Gojny F.H., Wichmann M.H.G., Koepke U., Fiedler B., Schulte K., "Carbon nanotube-reinforced epoxy composite: enhanced stiffness and fracture toughness at low nanotube content", *Composite Science and Technology 64*, 2363-2371, 2004.

Gojny F.H., Wichmann M.H.G., Fiedler B., Schulte K., "Influence of different carbon nanotubes on the mechanical properties of epoxy matrix composites – A comparative study" *Composites Science and Technology* 65, 2300-2313, 2005.

Holister P., Harper T.E., Roman Vas C., "Nanotubes", White Paper, CMP scientifica, 2003.

Iijima S., "Helical microtubules of graphitic carbon". *Nature*, 354:56–8, 1991.

Lau K.-T., Hiu D. "The revolutionary creation of new advance material- carbon nanotube composites". *Composites*: Part B 33, 263-277, 2002.

Liu W.K., Karpov E.G., Park H.S., "Nano Mechanics and Materials", Wiley, 2006

Lordi V., Yao N. "Molecular mechanics of binding in carbon-nanotube–polymer composites". *Journal of Material Research*, 15, 2770–9, 2000.

Luo J.J., Daniel I.M. "Characterization and modeling of mechanical behavior of polymer/clay nanocomposites", *Composite Science Technology*, 63, 1607–16, 2003.

Marzari N., Ferrari M., "Textural and micromorphological effects on the overall elastic response of macroscopically anisotropic composites". *Journal of Applied Mechanics*, 59:269–75, 1992.

Nam PH, Maiti P, Okamaoto M, Kotaka T., "Foam processing and cellular structure of polypropylene/clay nanocomposites". Proceeding Nanocomposites, June 25–27, Chicago, Illinois, USA: ECM Publication; 2001.

Park S.J., Yeong H.J., Nah C., "A study of oxyfluorination of multiwalled-carbon nanotubes on mechanical interfacial properties of epoxy matrix nanocomposites", *Materials Science and Engineering* A385, 13-16, 2004.

Popov V.N. "Carbon nanotube: properties and application". *Materials Science and Engineering* R 64, 61-102, 2004.

Quaresimin M. Varley R.J., "Understanding the effect of nanomodifier addition upon the properties of fibre reinforced laminates", *Composites Science and Technology* vol.68 No. 3-4,718-726, 2008.

Quaresimin M., Salviato M., Zappalorto M. "Fracture and interlaminar properties of clay-modified epoxies and their glass reinforced laminates. *Engineering Fracture Mechanics*, 81:80-93, 2012.

Ray S.S., Okamoto M., "Polymer layered silicate nanocomposites: a review from preparation to processing", *Progress in Polymer Science*, 28, 1539-1641, 2003.

Strawhecker K.E., Manias E., "Structure and properties of poly(vinyl alcohol)/Na^+-montmorillonite nanocomposites". *Chem Mater*,12:2943–9, 2000.

Stroscio J.A., Feenstra R.M., In: Stroscio J.A., Keiser W.J., editors, "Scanning tunnelling microscopy ". New York: Accademic Press., 95-141, 1993

Thostenson E.T., Ren Z., Chou T.-W. "Advances in the science and technology of carbon nanotubes and their composites: a review", *Composites Science and Technology* 61, 1899-1912, 2001.

Thostenson E.T., Li C., Chou T.W. "Nanocomposites in context" *Composites Science and Technology*, 65, 491–516, 2005.

Vaia R.A. "Polymer Nanocomposite open a new dimension for Plastic and Composites", *The AMPTIAC newsletter*, vol. 6, n. 1, 17-24, 2002.

Wagner H.D. and Vaia R.A. "Nanocomposites: issues at the interface". *Materials Today*, 38-42, 2004.

Wetzel B., Haupert F., Zhang M.Q., "Epoxy nanocomposites with high mechanical and tribological performance", *Composite Science and Technology* 63, 2055-2067, 2003.

Wichmann M.H.G., Sumfleth J., Gojny F. H., Quaresimin M., Fiedler B. and Schulte K., "Glass fibre-reinforced composites with enhanced mechanical and electrical properties – benefits and limitations of a nanoparticle-modified matrix", *Engineering Fracture Mechanics*, 73, 2346–2359, 2006a.

Wichmann M.H.G., Cascione M., Fiedler B., Quaresimin M., Schulte K., "Influence of surface treatment on mechanical behaviour of fumed silica/epoxy resin nano-composites", *Composite Interfaces*, vol. 13 No. 8-9, 699-715, 2006b.

Wichmann, M.H.G., Schulte, K., Wagner, H.D., "On nanocomposite toughness", *Composites Science and Technology*, 68, 329-331, 2008.

Wood J., "Facilitating nanoscale research", *Materials Today*, 56-61, 2004.

Yudasaka M., Komatsu T., Ichihashi T., Iijima S. "Single wall carbon nanotube formation by laser ablation using double targets of carbon and metal", *Chem. Phys. Lett.* 278**,** 102–106, 1997.

Zhang M., Singh R.P. "Mechanical reinforcement of unsatured polyester by Al_2O_3 nanoparticles". *Materials Letters* 58, 408-412, 2004.

Zhu J, Morgan AB, Lamelas FJ, Wilkie CA. "Fire properties of polystyrene–clay nanocomposites". *Chem Mater*,13: 3774–80, 2001.

2

Strategies for the assessment of nanocomposite mechanical properties

2.1 Introduction

In the first part of this chapter, some important issues to be taken into account in nanocomposite modelling are introduced and described. In the second part, the necessity for multi-scale modeling due to the intrinsic hierarchical structure of nanostructured materials is discussed. A classification of the modelling strategies available in the literature as a function of the scale used to address the problem is proposed.

2.2 Some important issues in nanocomposite modelling

The reduction of the filler size is the key issue of the extraordinary properties of nanocomposites. In this section the most important features related to the enormously increased specific surface area (SSA) to be accounted for modelling are briefly discussed (Quaresimin et al., 2012a).

2.2.1 The state of aggregation

One of the key limitations in nanocomposites performances, either structural or functional, is the state of aggregation of the nanofiller i.e its *distribution* and *dispersion* (Fiedler et al., 2006, Wichmann et al., 2006a, Wichmann et al., 2006b). *Distribution* of a nanofiller describes the homogeneity throughout the sample while the *dispersion* describes the level of agglomeration. For better understanding of these two key concepts Figure 2.1 schematically illustrates good distribution but poor dispersion (a), poor distribution and poor dispersion (b), poor

distribution but good dispersion (c), and good distribution and good dispersion (d) (Ajayan et al., 2004).

A proper distribution and dispersion is essential to get high *SSA*, which would be compromised by the emergence of clusters. A large particle density reduces the load transfer from the matrix to the nanofillers by strain shielding (Chen et al., 2008) and affects the overall elastic properties as well as the efficacy of some energy absorbing mechanisms. The ability to disperse SWCNTs and MWCNTs into a polymer, for instance, may be the most critical processing parameter for controlling properties. Nanotubes that are in clumps or are agglomerated with other carbonaceous materials create defect sites that will initiate failure. In

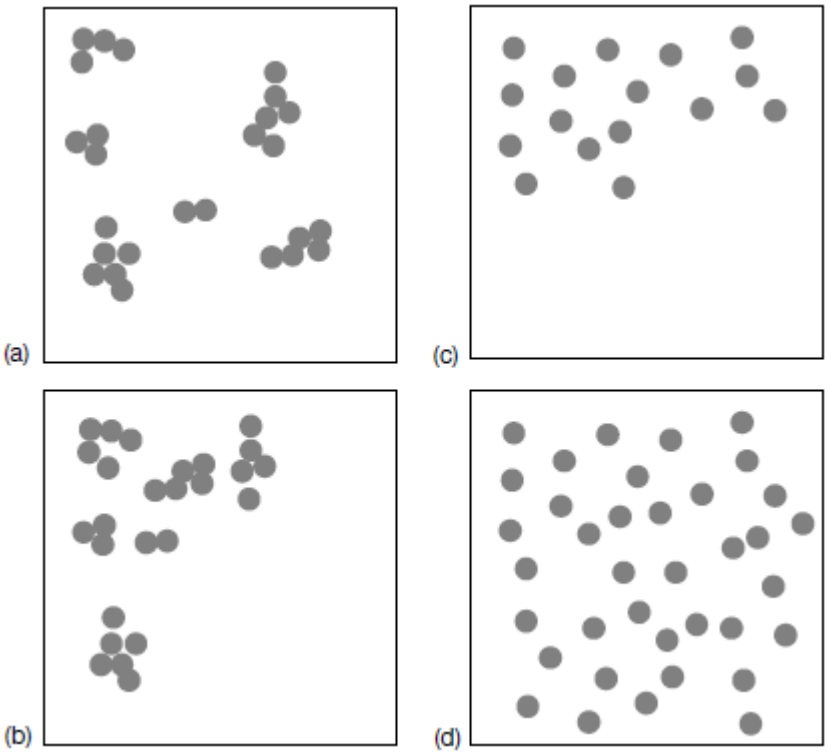

Figure 2.1. A schematic illustrating the difference between dispersion and distribution and giving examples of good and poor for each (Ajayan et al., 2004).

addition, they limit the efficiency with which the nanotubes carry load. This limitation has been illustrated explicitly in both polymer and ceramic matrix composites (Qian et al., 2002, Siegel et al., 2001, Qian et al, 2003). CVD-grown MWCNTs, which are easily dispersed and less agglomerated, increased the modulus and strength of polystyrene without compromising the strain-to-failure

factor significantly. Other works on arc-discharge-grown MWCNTs, which were not fully purified and not as well dispersed, did not show the increase in toughness observed for well-dispersed MWCNTs. Similarly, the toughness of MWCNT/alumina composites with excellent dispersion increased significantly compared to composites with somewhat worse dispersion because their small size does not create large stress concentrations that can be a problem with micro-sized fillers in traditional composites (Ajayan et al., 2004). Also regarding epoxy nanocomposites, a lot of experimental data available in the literature supports the importance of a good dispersion to obtain a toughness improvement (Adebahr et al., 2001, Becker et al., 2002, Ajayan et al., 2002, Becker et al., 2003, Ray and Okamoto, 2003, Wetzel et al., 2003, Zhang and Sing, 2004, Thostenson et al., 2005, Liu et al., 2006, Fiedler et al., 2006, Wichmann et al., 2006a, Wichmann et al., 2006b, Quaresimin and Varley, 2008, Battistella et al., 2008, Quaresimin et al., 2012b).

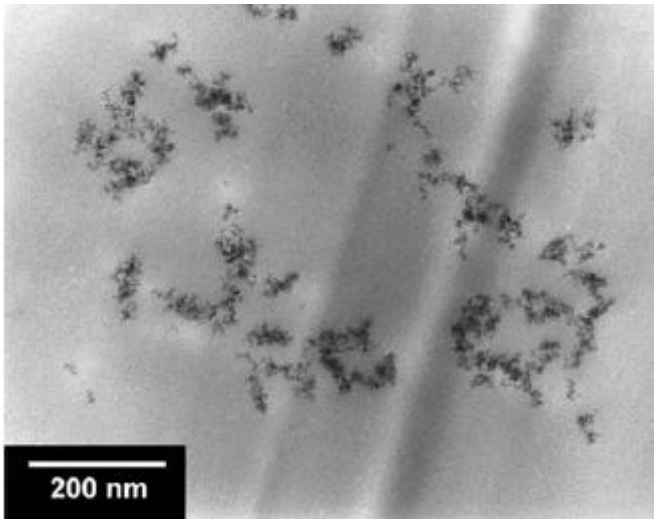

Figure 2.2. Example of good distribution but poor dispersion in a Al_2O_3 nanocomposite.

Whether by means of today processing a good distribution is a relatively easy achievement, the primary difficulty is proper dispersion of the fillers. Fiedler et al. (Fiedler et al. 2006) demonstrated that the maximum volume content of nanofiller that is theoretically possible to disperse in a polymer matrix without agglomerates is limited by geometric effects. They used the formula of the separation between

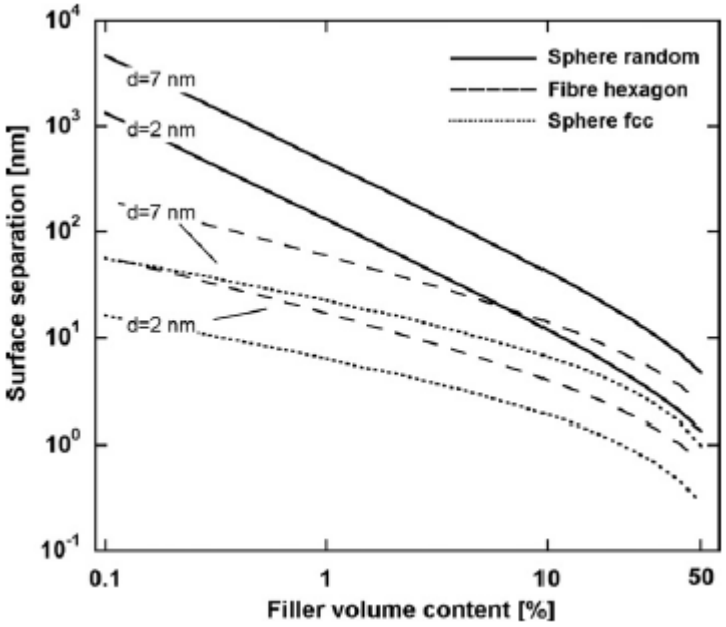

Figure 2.3. Influence of particle volume content on separation between spherical particles for different diameters and homogenous and random arrangements and for hexagon arrangement of fibers of the same diameter (Fiedler et al., 2006).

the particles surfaces as a function of volume content and of particle diameter in three homogeneous theoretical configurations (the face center cubic structure and the random arrangement for spherical particles and the hexagonal array of rod-like nanofillers) and they calculated the surface separation as a function of the filler volume content for some nanoparticles. The surface separation resulted from the following equations (Fiedler et al., 2006):

$$S_{fcc} = \sqrt[3]{\frac{32 \cdot \sqrt{2} \cdot \pi}{3 \cdot V_p}} \cdot \frac{d}{4} - d \tag{2.1}$$

where V_p is the nanoparticle volume fraction, d the nanoparticle diameter and a regular separation is supposed. For randomly arranged nanoparticles the equation is (Fiedler et al., 2006):

$$S'_{Ran} = \frac{2 \cdot d \cdot (1 - V_p)}{3 \cdot V_p} \tag{2.2}$$

In the case of fiber or rod-like nanostructures, as with SWCNTs or arc-grown multi-wall carbon nanotubes (MWCNTs), the dense packing is only possible if the

tubes arrange in periodic and aligned order. In case of the hexagon array and neglecting the CNT cross-section the separation S_{hex} between the tubes is given by the following equation (Fiedler et al., 2006):

$$S_{Hex} = d \cdot \left(\sqrt{\frac{\pi}{2 \cdot \sqrt{3} \cdot V_f}} - 1 \right) \tag{2.3}$$

being V_f is the nanotubes volume fraction.

The result is that depending on the particle size, over a volume content of 10% the separation between particles can be too small to curtain a polymer chain and agglomeration is unavoidable.

Anyhow, even at lower filler contents than this theoretical "threshold", often the nanoparticles tend to agglomerate due to attractive forces. The stability of the particles in the presence of polymer chains is led by two competitive forces: the short-range Van der Waals attraction and long-range Coulumb repulsion. The resulting potential V_{res} depending on the particles distance is depicted in Figure 2.4 and it shows two minima: a primary minimum at a short distance and a secondary minimum at a larger distance between the particles. In between these two minima there is a potential barrier V_{max}. In the processing of nanocomposites very high shear forces are needed to overcome the potential barrier and separate the particles, if they were agglomerated in the primary minimum. When this goal is achieved, then the particles tend spontaneously to agglomerate only in the less deep, secondary minimum and a lower shear rate is necessary to disperse the particles.

The production process seems to have some influence on the dispersion of carbon nanotubes, since CVD-grown MWCNTs are easier dispersed in PS matrix than arc-discharge produced MWCNTs (Ajayan et al., 2004). Also chemical modifications of nanotubes and the manufacturing process of the composites play an important role in separating the agglomerates.

After the considerations taken above, it is easy to understand that, given the importance of the state of aggregation of the nanofiller on the mechanical behaviour of the bulk nanocomposite, its modelling is a fundamental issue a good model, either concerned with elastic properties or toughening, can but take into consideration.

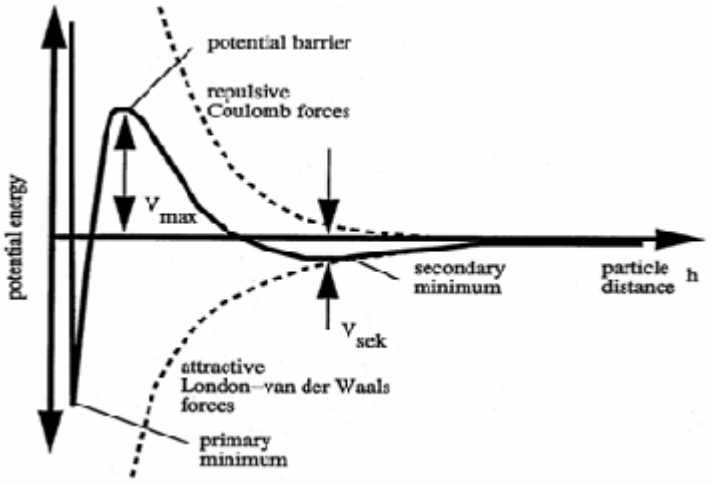

Figure 2.4. The behaviour of potential energy with particle distance.

2.2.2 The morphology

The properties of polymer nanocomposites are highly related to their overall morphology. Focusing on polymer layered silicate (*PLS*) nanocomposites, for instance, three different morphologies are thermodynamically achievable (Ray and Okamoto, 2003) depending on the interplay between the polymer matrix and layered silicates (organomodified or not) and also on the volume fraction of the nanofiller and the processing conditions. There are *separated*, *intercalated* and *exfoliated or delaminated nanocomposites*.

In the authors' opinion, being macroscopic properties largely influenced by the overall morphology, its modeling is basic and the research scope should be at least twofold. On the one hand, there is an evident need for understanding the effects of various factors such as the size and shape of the nanofiller, its clustering and the polymer architecture (e.g., homopolymer vs. copolymer) on morphology. On the other hand, once morphology is fully determined, capturing its effects on macroscopic properties by means of effective modelling is likewise important. Moreover, it is worth noting that also the nanofiller has its own nanostructure-related morphology. For example single wall carbon nanotubes (SWCNTs) are characterized by different nanotube lengths, diameter and chirality as well as the tube-end configuration (end-caps) and variability is even more pronounced for multiwall carbon nanotubes (MWCNTs) (since they can be considered as a number of nested SWCNTs). The major additional structural parameters include

nanotube outer and inner diameter, the number of nested SWCNTs (wall thickness), and the presence of growth-induced configurations, such as bamboo structures (Thostenson et al., 2005).

2.2.3 The matrix/nanofiller interface

The interfacial region surrounding the nanofiller is a zone of altered chemistry, chain mobility, degree of cure and cristallinity. Its properties are not just a synergistic combination of whose of each bulk constituent, rather, a set of new ones due to the inherent inter and supra- molecular interactions which can take place at the nano length scale (Zax et al., 2000, VanderHart et al., 2001, Ng et al., 2001, Odegard et al., 2005, Yu et al., 2009, Zammarano et al., 2011, Zappalorto et al., 2011a, Salviato et al., 2011a). As can be noted from Figure 2.5, since the small size of nanofillers leads to an exceptionally high interfacial area, already at low volume fractions the entire matrix is essentially part of the interfacial region

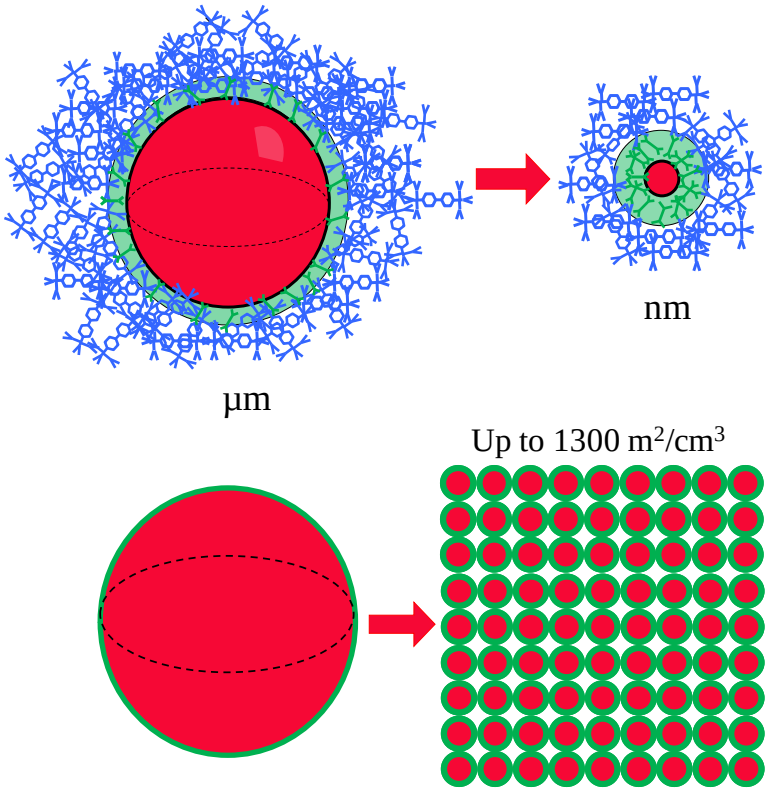

Figure 2.5. Schematic representation showing the increasing importance of the interphase with the filler size reduction and the consequent increase in SSA (Quaresimin et al., 2012a).

(Ajayan et al., 2004). Some methods have been tried to evaluate the interfacial

shear strength by the pull-out of single nanotubes (Wagner and Vaia, 2004), while no information about the direct measurement of the interfacial shear strength of single nanoparticles or nanoclays has been found in literature. Wagner and Vaia (Wagner and Vaia, 2004) measured for nanotubes a pull-out strength of 50 MPa, which is ten times larger than that of carbon fibres in the same polymer. However, it is still not completely clear which are the molecular mechanisms that lead to an optimized adhesion at the interface. A high interfacial strength in nanotube-polyvinyl-alcohol composites has been ascribed to the formation of a crystalline layer of material around the nanotube surface, but the existence of this crystalline coating has not been experimentally demonstrated. Recently, it seems that a considerable potential for improving the interfacial strength between nanotubes and polymers can come by promoting strong chemical bonds. While Van der Waals interactions give interfacial strength values of less than 3 MPa, covalent bonding for only 1% of the nanotube's carbon atoms to the polymer can raise the interfacial shear strength up to more than 100 MPa (Wagner and Vaia, 2004).

Given the importance of the nanofiller/matrix interface in determining either the elastic properties or toughness of the nanocomposite, the necessity of its modeling is evident. Since in nanocomposites at least one dimension of the filler is comparable to the gyration radius of the polymeric chains, the actual effect of molecular bonds between polymer and nanofiller can be fully appreciated only on the basis of discrete models. Many works available in the literature showed the effectiveness of *Molecular Dynamics* (*MD*) in predicting the interfacial characteristics (Lordi and Yao, 2000; Liao and Li, 2001; Wong et al, 2003; Gou et al, 2004; Gou et al., 2005).

2.2.4 Defects

The production process, the functionalization and other treatments to improve dispersion, can damage the nanofiller compromising its functional and structural properties (Figure 2.6 shows an example of possible defects). In facts, one of the main drawbacks of CVD growth of nanotubes is that, being it a rather "low temperature" process, it does not allow any structural rearrangement. Accordingly, any lattice discontinuity or vacancy cannot be relaxed unless further expansive heat treatment in vacuum or in inert atmosphere are done. Moreover,

also the treatment in vacuum or in inert atmosphere are done. Moreover, also the functionalization process by the introduction of functional groups produces defects in the graphite walls of the CNTs, reducing their strength and stiffness as reported, among others, by Mielke et al. (Mielke et al., 2004) by means of Quantum Mechanics and Molecular Dynamics simulations. As an example, Figure 2.7 compares the stress-strain curves of differently damaged nanotubes predicted by means of diverse modeling approaches. As can be observed, a drop in CNT Young's modulus, elongation at break and yield stress are reported (Mielke et al, 2004).

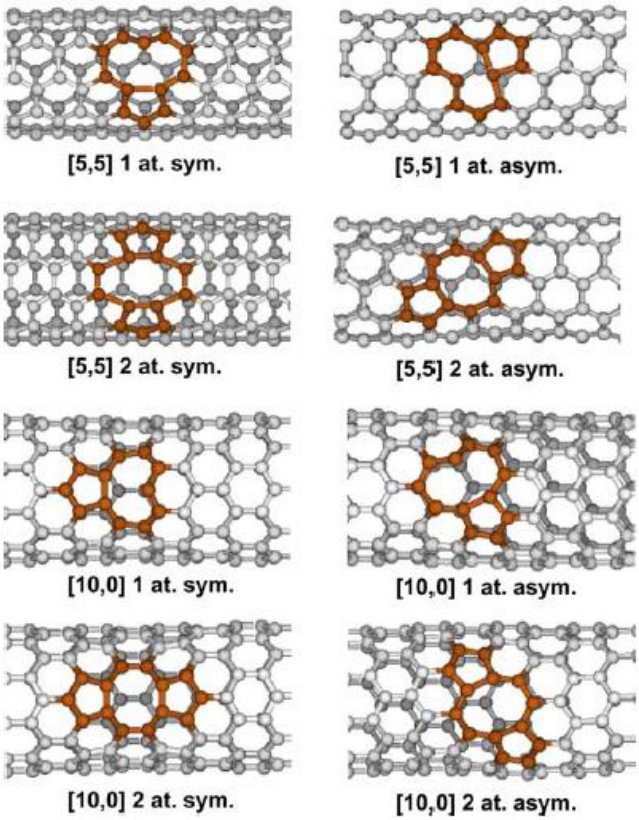

Figure 2.6. Reconstructions of the one- and two-atom vacancy defects for different nanotube typologies (Mielke et al., 2004).

Besides, armchair nanotubes are believed to release their excess strain by the formation of irregular pentagons and heptagons alongside the tubes. This phenomena is called the Stone-Wales defect (Thostenson et al., 2001) and it has been discussed in paragraph 1.8.1. Of course these phenomena are intimately concerned with the nanotube lattice and so, in the author opinion, they must be modeled trough atomistic approaches.

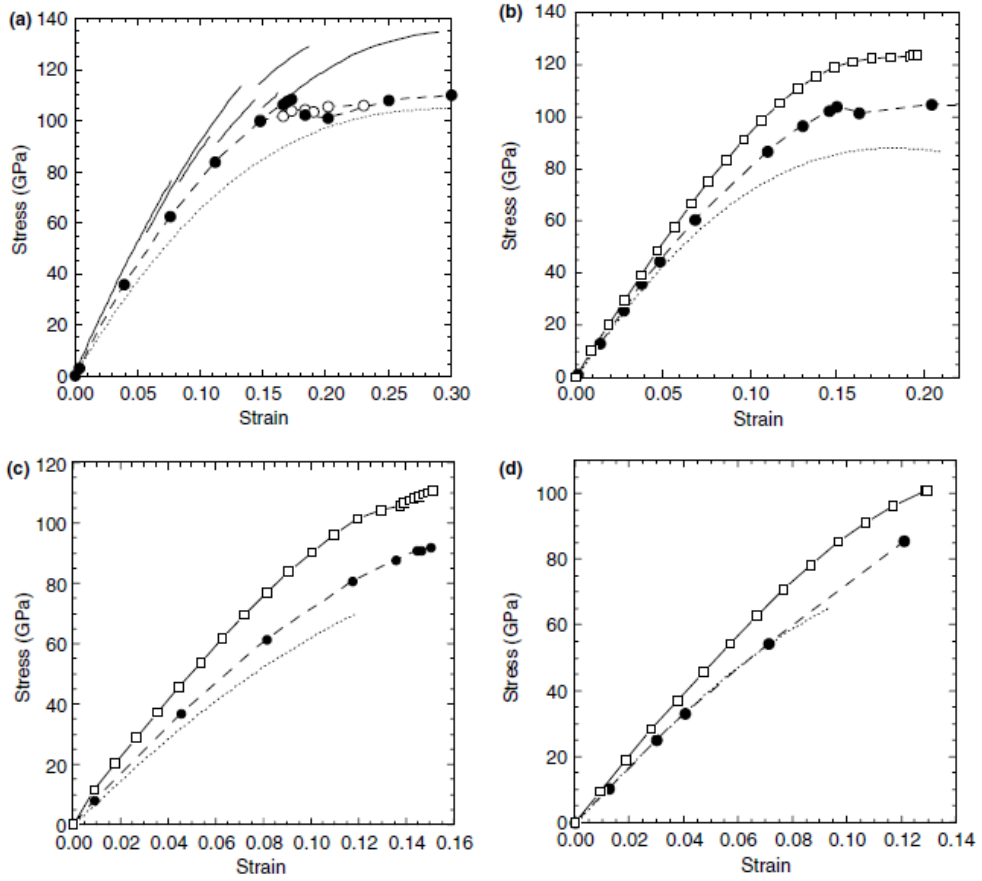

Figure 2.7. Stress–strain curves for a selection of tubes calculated via DFT (long dashes), PM3 (solid line), and MTB-G2 (short dashes). (a) Pristine [5,5] CNT; (b) pristine [10,0] CNT; (c) two-atom vacancy (asymmetric configuration) in a [5,5] CNT; and (d) one-atom vacancy in a [10,0] CNT (Mielke et al., 2004).

2.3 The importance of a multiscale approach

To effectively exploit the huge potential of nanocomposites it is of primary concern that with the experimental analysis, abundantly developed in the literature among the rest, comes an adequate modeling activity. Of course, the creation of models, either analytical or numerical, is a milestone for the comprehension and prediction of the mechanical behavior of this kind of materials and their successive application in engineering design.

One of the most critical issue in modeling macro-mechanical properties of nanostructured materials is their *hierarachical structure* which spans from nano to macro length-scales. A good model should take into account the characteristic phenomena of each length-scale and bridge their effects from the "smaller" scale to the macroscale. As a consequence, a different way of thinking from traditional

approaches is needed. In micromechanics, as a matter of facts, one is used to face problems concerning two different characteristic lengths at most (microscale and macroscale) so that continuum mechanics is reasonable. In the case of nanocomposites, the presence of three length-scales (nano-, micro- and macroscales) all of which characterized by peculiar mechanisms, requires a more flexible way to address the problem. Indeed, while modelling molecular interactions between the nanofiller and the matrix would require a discrete approach, the introduction of such an atomistic model up to macro length-scales is limited by the impracticability of accounting for more than some hundred millions of atoms. To give an idea of the size of the problem (Figure 2.8), it is useful to remind here that a nanoclay cluster with a diameter of 0.5 μm and 100 layers has about 85 million atoms (Zeng et al., 2008).

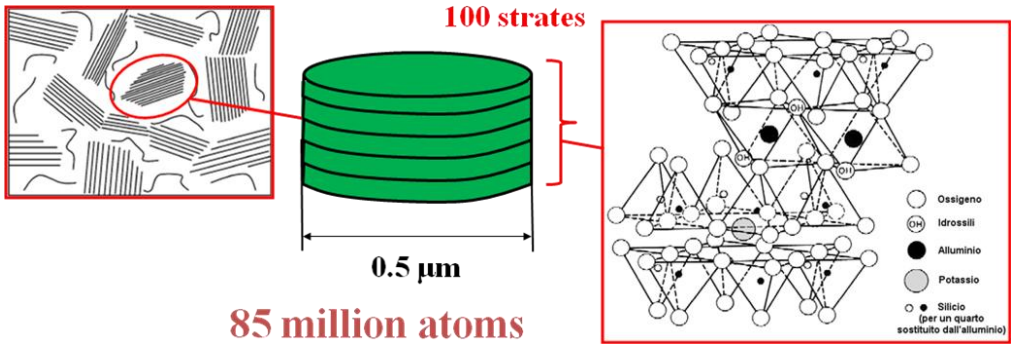

Figure 2.8. Difficulties in atomistic modeling spanning more than one length-scale.

This fact gives rise to the need of a multiscale modelling, each dominant mechanism being studied by means of the best suited model with reference to the given length and time scales. The more a model is able to account for these features, the more it moves from a microscale towards a nanoscale perspective.

2.4 A classification of the different modelling strategies available in the literature

2.4.1 Preliminary remarks

Great efforts have been devoted in the recent literature to develop appropriate models for the assessment of the mechanical properties of nanocomposites, with

special focus on elastic properties. The same cannot be said regarding the modelling of toughness and dissipative damage mechanisms, despite of their importance in the view of developing ternary namomodified laminates. A reason is that toughness is inherently more complicated to assess. While for what concerns elastic property prediction, a model can be directly validated by means of macroscopic experimental data, when dealing with toughening mechanisms the processes at the nanoscale not only are difficult to be identified but they also require the observation and the validation at the same length-scale. Moreover, the dominant mechanisms may change at different nanofiller contents and are influenced by several parameters such as the type of nanoparticle, the dispersion level, the matrix/nanoreinforcement interface, the nanofiller morphology and the loading conditions (quasi-static or cyclic), just to mention a few (Quaresimin et al., 2012a).

The aim of this section is to carry out a comprehensive analysis of the currently available modelling strategies, which is still missing in the literature. The same basic ideas can then be translated in the assessment of toughness and, consequently, of dissipated energy.

Within this aim, it is first basic to acknowledge that in the most general case three main stages should be addressed in nanocomposite modelling. Each stage might be tackled with the aid of a dedicated model, with the aim to range from the nanoscale to the macroscale:

- **Molecular Models**. Starting from the bottom, the chemical-physical interactions arising at the nanoscale can be accounted for by means of discrete methodologies (Lau et al., 2004, Odegard et al., 2005, Yu et al., 2009), that allow to predict the time evolution of a system of interacting particles (e.g., atoms, molecules, granules, etc.) and to estimate its physical properties. The most common of these methodologies is Molecular Dynamics (MD) (see, among the others Odegard et al., 2003, Odegard et al., 2005, Fermeglia and Pricl, 2007, Yu et al., 2009).
- **Nanostructural Models**. Proceeding from the bottom to the top, there is the need to assess mechanical interactions, which depend on the morphology. This can be achieved by specific nanostructural models for each kind of nanofiller,

usually developed within a continuum mechanics-based frame, in order to effectively describe the stress transfer with the matrix.

- **Micromechanical Models**. Going further to the top, it is necessary to scale up the nanoscale-related properties to the macroscale or the mesoscale. This can be tackled by means of classical micromechanical relationships, satisfactorily used for conventional composites with micro-sized reinforcements. This last scale-up often needs to exploit the concept of RVE by a finite element model, with the number of degree of freedom (DOF) much smaller than those required by MD.

Once having identified the main stages and the related models, the large number of published works aimed at assessing nanocomposite properties can be gathered according to how many and which of the mentioned models are used within the strategy. This inherently define the scale from which the problem is addressed (micro, nano and molecular) and, consequently, the effectiveness in the description of the nanoscale.

Then, a classification of the possible multiscale modelling strategies into three main groups is proposed here: "*Micromechanical modelling strategies"*, "*NanoStructural modelling strategies"* and "*Molecular modelling strategies"*. In brief:

- *Micromechanical modelling strategies* represent the simplest way to address the property prediction although often it is not the most effective. They make use of micromechanical models only. Consequently, the matrix and the nanofiller are described by means of Cauchy's continuum mechanics without accounting for interfacial interactions and nanostructure.
- A more insightful investigation is possible through *Nanostructural modelling strategies.* They make use of both micromechanical models and nanostructural models, thus accounting for the effects of the inherent nanostructure on the overall macroscopic properties but not of the chemical-physical interactions.
- Finally, *Molecular modelling strategies*, make a combined use of all the above mentioned models. The scope of the analysis is taken to the actual nanoscale level to account for intermolecular and supramolecular interactions by means of discrete methodologies. Accordingly, the scale-up from nano to macro

length scales is not straightforward and requires an effective multiscale approach combining nanostructural and micromechanical models.

The concept of assembling basic models to build a multiscale modelling strategy is defined as "Three Stage Strategy" (TSS) (Quaresimin et al., 2012a).

A schematic representation of this concept is shown in Figure 2.9, while the main characteristics of each strategy are listed in Table 1, together with the relevant advantages and disadvantages. Each strategy is then briefly discussed and representative examples available in the literature are provided as well in next sections. I apologize in advance to all authors who have presented contributions in this field which have not been accounted for in the present work for reasons of space.

	Micromechanical Strategy	**Nanostructural Strategy**	**Molecular Strategy**
Features	Nanostructure is neglected	– Continuum nanofiller; – Matrix-nanofiller mechanical interactions are accounted for;	Scaling up from atoms and/or molecules to macro length scale; Physical and chemical interactions are considered;
Advantages	– Availability of a large bulk of experimental data (at the micrometric level); – Simple analytical expressions; – The overall morphology is accounted for	– Nano scale morphology is accounted for; – Scaling-up from micro to macro with the aid of micromechanical models; – Reasonably reliable predictions;	– The effects of chemical interactions can be fully seized (surfactants etc.); – Mechanical properties of the interphase can be reliably assessed;
Disadvantages	– The model cannot seize size dependent effects; – Often the predictions are not reliable;	The chemical interactions between filler particles and polymer chains cannot be considered	– Complex molecular models; – High computational power required; – Complex scaling-up;

Table 1 Summary of the main advantages and disadvantages related to the different modelling strategies (Quaresimin et al., 2012a).

To conclude this section, it is also important to remind that multiscale strategies can be hierarchical or concurrent. In the former case each model is addressed

separately, inputs being provided by the solution of the previous model (at the smaller scale). Differently, in the latter case, all the models are solved simultaneously by using inputs from all scales.

However, being easier to be implemented and more efficient from the computational point of view, almost all the available modelling strategies in the literature are hierarchical. For the same reason there are only few examples of concurrent approaches (Brougthon et al., 1999, Lee et al., 2009)

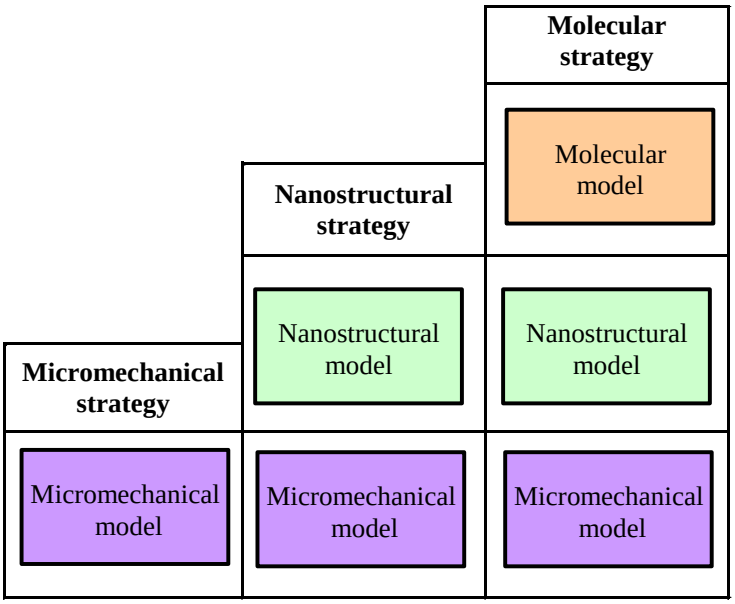

Figure 2.9. The concept of the "Three Stage Strategy" (TSS): building of modelling strategies from basic models (Quaresimin et al., 2012a).

2.4.2 The Micromechanical modelling strategy

The micromechanical modelling strategy extends Cauchy's continuum concept to the polymeric chain length-scale. It neglects the nanoscale structure as well as the nanofiller-matrix molecular interactions, and thus fails in capturing the "nano-effect" since it cannot account for the inherent hierarchical structure of the material.

In general, this kind of modelling strategy does not produce reliable predictions of elastic properties, disregarding also the enhanced tendency of the nanofiller to agglomerate (Fornes and Paul, 2003). Regarding toughness assessments, micromechanical strategies proved to be incapable of predicting the reported high

increments in dissipated energy at low nanofiller volume fractions as documented in (Wetzel et al., 2006, Zhao et al., 2008).

In spite of these limitations micromechanical models, according to the formulation used for conventional composites (Lange, 1970, Evans, 1972, Green et al., 1979), have been applied in the description of some mechanisms like *crack pinning* or *crack deflection* in nanocomposites (Wetzel et al., 2006, Zhao et al., 2008).

For example, while investigating the mechanical properties of alumina nanoparticles reinforced epoxies, Wetzel *et al.* (Wetzel et al., 2006) reported TEM images of the fracture surfaces revealing the emergence of "tail-like" features. Based on this experimental evidence, they suggested to use the micromechanical model formulated for the crack pinning mechanism (Lange, 1970, Evans, 1972, Green et al., 1979) to predict the strain energy release rate of the studied nanomodified system, and compared theoretical predictions with experimental results.

An example of application of this modelling strategy is shown in Figure 2.10; data are taken from (Wetzel et al., 2006) and refer to TiO_2 (diameter: 200-500 nm) and Al_2O_3 (primary particles size: 13 nm) nanoparticle reinforced epoxies. Note that in (Wetzel et al., 2006) fracture toughness improvements were plotted as a function of nanoparticles diameter to interparticles distance ratio; in Figure 2.10, differently, data are plotted as a function of the nanofiller content, as estimated through the following expression:

$$V_f = \frac{\pi}{6} \times \frac{1}{(1 + c/r_0)^3} \tag{2.4}$$

where V_f is the nanofiller volume content, r_0 is the nanoparticle radius and 2c is the interparticle distance. Eq. (2.4) has been obtained assuming a cubic array of nanoparticles.

Figure 2.10 clearly shows the limits of this strategy, the predicted values exhibiting a far more pronounced energy absorption with respects to those detected experimentally. Indeed, the applied micromechanical model (Lange, 1970, Evans, 1972, Green et al., 1979) does account neither for the size dependency nor for the effects of the region with the altered-chemistry interphase.

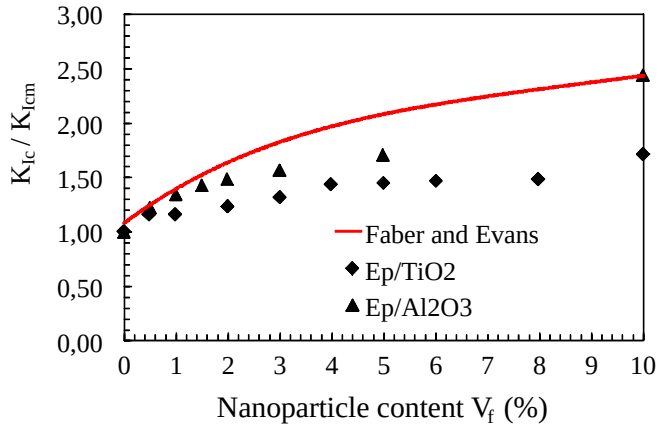

Figure 2.10. Fracture toughness improvements of Al_2O_3 and TiO_2 nanoparticles reinforced epoxy. Comparison between experimental results and predictions based on the modelling strategy proposed by Wetzel *et al*. Data taken from (Wetzel et al., 2006). V_f according to Eq. (2.4).

2.4.3 The Nanostructural modelling strategy

The nanostructural modelling strategy represent an attempt of considering the morphology of the nanofiller at the nanoscale while maintaining the hypothesis of continuity.

They start from a specific model of the nanofiller defined "nanostructural", which allows one to account for its structure at the nanoscale level and the way it mechanically interacts with the matrix. The results of the previous model are implemented in a micromechanical model (e.g. the Mori-Tanaka's scheme, the Halpin-Tsai equation etc.) often by taking advantage of the concept of an "effective filler" (which allows to account for the actual nanostructure) (Thostenson and Chou, 2003, Luo and Daniel, 2003). Alternatively, the scale up can be done by means of full numerical models (e.g. FEA) of a representative volume element (*RVE)* (Spencer and Sweeney, 2006).

An inherent advantage of nanostructural modelling strategies, when compared to micromechanical ones, is that they offer a more insightful analysis of the nanofiller-matrix mechanical interactions without compromising simplicity. As far as elastic properties are concerned, this usually results in more reliable predictions. Of course, since they do not include a molecular model, they cannot account, by nature, for chemical-physical interactions. It is further worth noting that most of the modelling strategies available in the literature can be classified as

Nanostructural. For the sake of brevity, in the following we will then discuss only two representative examples (Thostenson and Chou, 2003, Luo and Daniel, 2003) (for further examples see Guzmàn de Villoria and Miravete, 2007, Chia et al., 2007).

Thostenson and Chou's modelling strategy for the elastic property prediction of MWCNT nanocomposites

A significant example of a Nanostructural modelling strategy is that due to Thostenson and Chou (Thostenson and Chou, 2003) for epoxy matrix reinforced by aligned MWCNTs.

The main hypotheses of the analysis are a perfect nanotube/matrix adhesion and that only the outer wall of the MWCNT can carry load by neglecting the contribution of the inner layers. In addition, a double Lorentzian distribution of outer diameters is assumed.

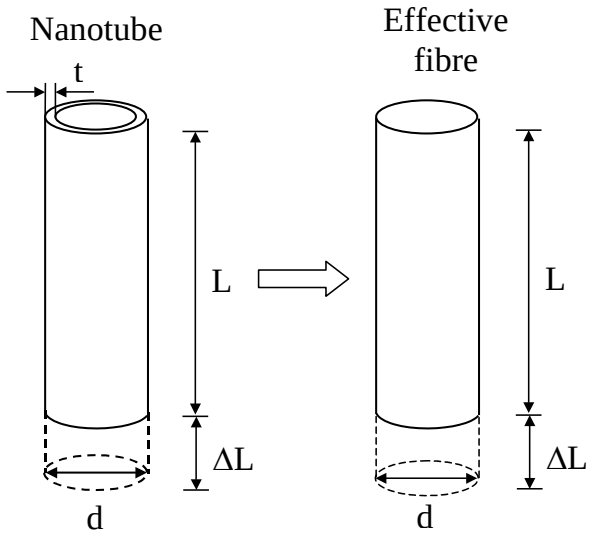

Figure 2.11. Schematic of (*a*) nanotube and (*b*) effective fibre used to model the elastic properties of a nanotube embedded in a composite. (Figure arranged from Thostenson and Chou, 2003).

The actual filler nanostructure is accounted for by introducing a solid *effective fiber* (see Figure 2.11). Through an isostrain condition, the Young modulus of the effective fiber is linked to the outer layer thickness, the outer diameter and the nanotube Young's modulus.

Then, assuming all nanotubes to be perfectly aligned, the Halpin-Tsai micromechanical model is used to determine the longitudinal Young modulus, E_{11} (Thostenson and Chou, 2003).
In this way, E_{11} depends not only on the reinforcement aspect ratio but also on the outer nanotube wall thickness, being then size dependent.

Luo and Daniel's modelling strategy for the elastic property prediction of clay nanocomposites

The nanostructural modelling strategy proposed by Luo and Daniel for PLS nanocomposites (Luo and Daniel, 2003) aims at accounting for the effect of the nanofiller morphology (i.e. its state of intercalation) by means of a three phase Mori-Tanaka model (matrix, exfoliated clays and cluster of intercalated clays).
The properties of intercalated clay clusters are computed by treating them as a system of parallel nanolayers (Figure 2.12) assuming an ellipsoidal geometry and the isotropy of each constituent. It is further assumed that the interlayer (intragallery) material has the same Poisson ratio of the bulk matrix, but a Young's modulus a_m times greater, a_m being an intragallery stiffness enhancement factor.

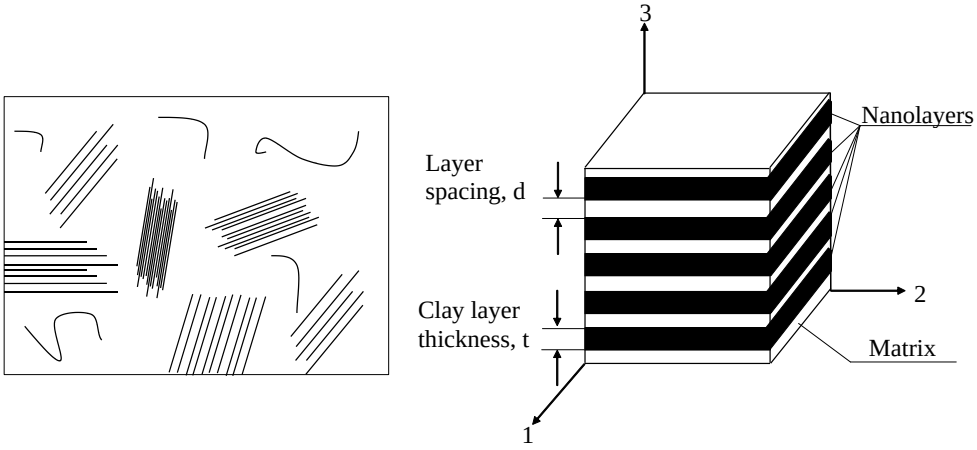

Figure 2.12. A representative element of an intercalated cluster of clay nanolayers (Figure arranged from Luo and Daniel, 2003).

Assuming the in-plane strains (1, 2 directions) and out-of-plane stresses (3 direction) to be the same in both the clay phase and the interlayer matrix, equilibrium and compatibility conditions are used to determine the stiffness tensor of the stack.

The stiffness tensor is found to depend, besides on the clay and the matrix elastic properties, on nanostructural parameters such as the layer thickness to layer spacing ratio and the intragallery stiffness enhancement factor a_m (Luo and Daniel, 2003).

Finally a three phase Mori-Tanaka's model is used. In more details:

- the exfoliated region is considered as a two-phase system composed of matrix and exfoliated layers, and the stiffener tensor of this simplified system is first determined;
- the exfoliated region is then considered as the effective matrix phase and the intercalated region as the inclusion phase;

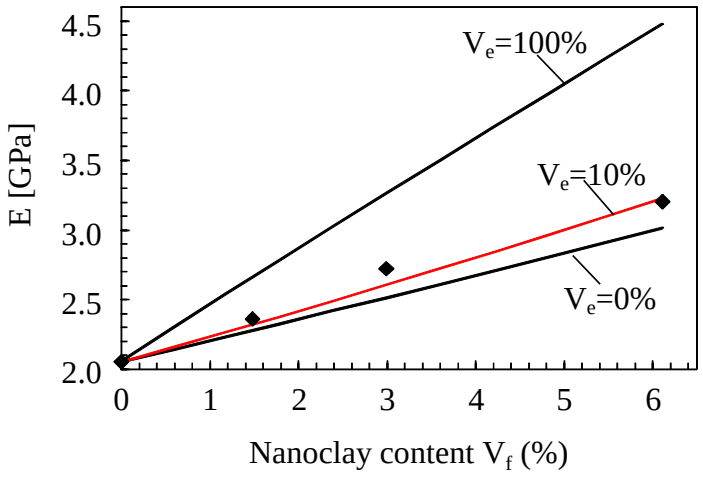

Figure 2.13. Elastic modulus of nanoclay reinforced epoxy resin. Comparison between experimental results and predictions based on the modelling strategy proposed by Luo and Daniel. Experimentally detected exfoliation ratio V_e =10%. (Figure arranged from Luo and Daniel, 2003).

In this way, not only the effects of the nanostructure of the clusters but also those of the overall morphology are considered.

An example of application is shown in Figure 2.13, where the overall elastic modulus is plotted versus the nanofiller volume content for different exfoliation ratio,V_e. It is evident that the use of V_e=10%, which is consistent with measured values (Luo and Daniel, 2003), provides a reasonably good agreement with experimental results for clay epoxy resin.

2.4.4 The Molecular modelling strategy

The molecular modelling strategy makes a combined use of the molecular, nanostructural and micromechanical models described in section 2.4.1. At the bottom level it abandons the continuity hypothesis in favour of discrete theories; Molecular Dynamics (*MD*) is an example of these theories.

Molecular modelling strategies are penalised by the elevated computational power required to encompass the different characteristic length-scales, and differ one from the others by the way in which they deal with the property bridging (Pipes and Hubert, 2002, Li and Chou, 2003, Odegard et al., 2003, Frankland et al., 2003, Odegard et al., 2005, Fermeglia and Pricl, 2007, Scocchi et al., 2009, Giannopoulos et al., 2010, Tsai et al, 2010, Zappalorto et al., 2011a, Salviato et al., 2011a, Zappalorto et al., 2011b, Salviato et al., 2011b). The more elevated computational cost is justified by the need of seizing chemical-physical interactions at the nanoscale, which have a basic influence on functional as well as mechanical properties.

Odegard et al. equivalent continuum model for elastic property prediction of MWCNT nanocomposites

An example of Molecular modelling strategy is the *equivalent continuum model* proposed by Odegard *et al.* (Odegard et al, 2003) for elastic property assessment of MWCNT nanocomposites.

The approach is based on the construction of a unit cell and an equivalent continuum cell, the former one being constituted by a nanotube only and being thought of as a *RVE*. The initial equilibrium conditions are determined by means of MD analyses.

The continuum cell elastic properties are determined by an Energy Equivalence Rule, which bridges the molecular model to the equivalent continuum. To do so, an *equivalent truss model* is introduced, in which every intermolecular bond is modelled by a truss pinned in the centres of mass of each particle between the two cells under the same boundary conditions.

Finally, the scale-up to the macroscale is pursued by means of the Mori-Tanaka method, modeling nanotubes as ellipsoidal inhomogeneities with different orientation distributions.

A similar approach has been presented independently by Li and Chou (Li and Chou, 2003) for nanotube elastic property assessment. In this case, each bond is simulated as a beam instead of a truss in order to account also for its flexural rigidity.

Scocchi et al. hierarchical modelling for nanocomposites elastic properties

Other significant examples of Molecular modelling strategy for the prediction of the overall properties of nanocomposites are due to Scocchi *et al.* (Scocchi et al., 2009) and Fermeglia and Pricl (Fermeglia and Pricl, 2007, Fermeglia and Pricl, 2009).

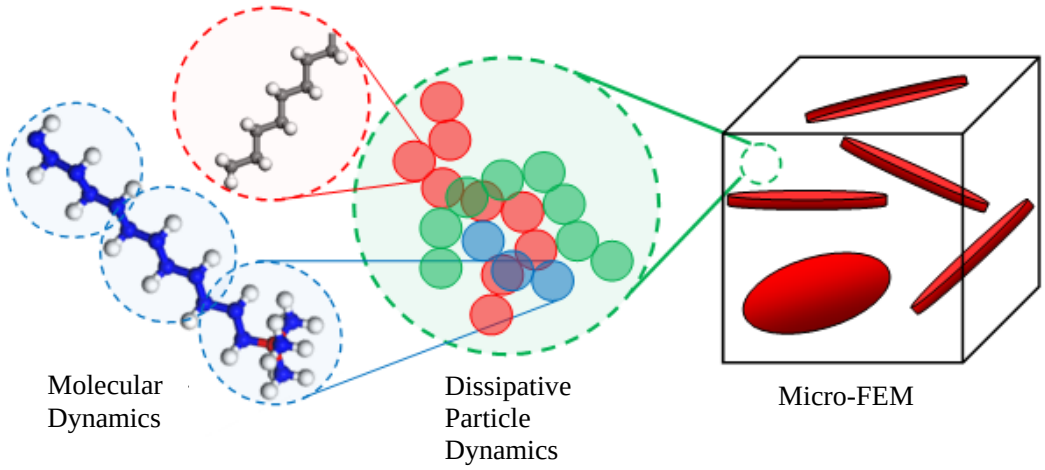

Figure 2.13. Schematic of the coarse-graining of a surfactant molecules into beads and the following scale up of the density fields computed by means of DPD to the micro-FEM simulation, according to the modelling strategy proposed by Fermeglia and Pricl (Fermeglia and Pricl, 2009).

The authors propose to bridge the gap between mesoscale and atomistic scale by means of a *Dissipative Particle Dynamics* (DPD) analysis. In the DPD, differently from classical MD, atoms or molecules are not represented directly by a particle but they are coarse-grained into beads (Figure 2.13) moving according to Newton's equation of motion and interacting dissipatively through simplified force laws.

The forces acting on each bead are made of three distinct contributions: a conservative, a dissipative and a random force. Each of them is strictly dependent on the interaction energy values to be calculated by means of MD. The required computational power to this end is reduced, as the dimensions of the cell are much lower than those of the mesoscale cell. Accordingly, being the DOF of the system also highly reduced, the simulation can be performed within a mesoscale cell whose dimensions are longer than those commonly set in MD.

The morphology and density fields computed by means of the DPD simulations are then implemented in the FE model of the mesoscale cell. In this way the mechanical properties of mesoscale structures (nanoclay clusters) are determined applying six infinitesimally small deformations and minimizing the resulting total strain energy.

System	V_f [%]	Property	Predicted [GPa]	Experimental [GPa]	Δ [%]
Polyamide/SWNT acid treated	0.1	E	1.32	1.19	11
Nylon 6/MMT with M_3C_{18}	1.9	E	4.19	4.32	3
Nylon 6/MMT with $M_2(C_{18})_2$	1.9	E	4.41	4.60	4
ABS-MMT	2	G	3.15	2.75	15

Table 2. Elastic properties of nanocomposites. Comparison between experimental results and predictions based on different Molecular Strategies (Quaresimin et al., 2012a).

Once the stack properties are calculated, the overall mechanical properties of nanocomposites are calculated by a micro-FE simulation within a RVE. The mechanical properties of the mesostructures of the RVE come from the lower length scale simulations while the overall morphology can be estimated from TEM (Fermeglia and Pricl, 2007, Scocchi et al., 2009, Fermeglia and Pricl, 2009). In this way, the computation of the elastic constants can be performed by the energy minimization described above thus completing the scaling up from the nano to the macroscale.

An example of application of these modelling strategies together with a comparison between experimental and predicted results is shown in Table 2. Data are taken from different references (Odegard et al., 2003, Fermeglia and Pricl, 2007, Scocchi et al., 2009, Fermeglia and Pricl, 2009). It is evident that the adoption of a Molecular Modelling Strategy results in a satisfactory agreement between experimental results and predictions. It is also evident that such strategies are capable to account for the effects of different functionalisation on the overall elastic properties of the nanocomposite.

2.5 Discussion

In this chapter the main issues concerning the assessment of nanocomposite mechanical properties have been discussed.

One of the reasons of the extraordinary properties of nanocomposites is acknowledged to be the enormous increase in the specific surface area (*SSA*), together with the emergence of molecular interactions at the nanoscale.

However, the resulting multiscale structure makes the problem of predicting nanocomposite properties complicated being it governed by several assorted variables (such as morphology, surface functionalisation, nanofiller content etc.) which do affect different length scales.

The improvement of matrix toughness and all the other weak matrix-controlled properties of composite laminates is the ultimate task of nanomodification. The full exploitation of these benefits requires, however, the development of reliable predictive models. Despite this, while a large bulk of modelling strategies has been proposed in the previous literature to assess elastic properties of nanocomposites, relatively little attention has been paid to strength or toughness assessment.

The analysis carried out in this work highlights the main features of the modelling strategies available up to now as well as their main advantages and disadvantages and can be useful also for the formulation of toughness assessment strategies.

A classification is proposed which gathers the state-of-art strategies into three main groups according to the scale from which the problem is addressed: Micromechanical, Nanostructural and Molecular.

In the author's opinion the Molecular modelling strategy is the most effective way to tackle the issue of nanocomposite property assessments. Despite of its high computational costs, it represents the only way to account for intermolecular and supramolecular interactions at the nanoscale. By doing so it allows assessing many properties related to chemical-physical interactions, such as the interphase elastic properties, the interfacial energy or the density fields surrounding a nanoparticle, which might have important effects on the overall properties.

The properties coming from the "bottom", which have been computed by a numerical simulation at the nanoscale, can be employed in user-friendly nanostructural and micromechanical models developed within a robust analytical frame.

This is a considerable advantage in the prospect of the engineering of nanostructured materials as relatively simple descriptive models can be obtained.

An example of this concept can be found in (Odegard et al., 2005, Yu et al., 2009) where the elastic properties of the interphase surrounding the nanoparticles are first computed by a MD simulation and then employed within a multiphase Mori-Tanaka scheme. A full numerical approach is also possible as well, as documented in (Fermeglia and Pricl, 2007, Scocchi et al., 2009, Fermeglia and Pricl, 2009).

In principle, there are substantial differences and difficulties in modelling the elastic constants (small deformations and undamaged material) with respect to the fracture toughness. However a similar strategy can be used to assess toughness improvements and the dissipated energy by dealing with the several parameters affecting the fracture process. In the authors' opinion, this can be achieved by means of a "multi-mechanism" modelling strategy, in which each contribution is weighted according to the specific case (accounting for the nanofiller typology, the morphology and the functionalisation).

As a first step in this direction the present author has developed some models to assess nanoparticle debonding stress which accounts for surface stresses and the emergence of an interphase surrounding the nanoparticle with a relevant change in the local elastic properties (Zappalorto et al., 2011a, Salviato et al., 2011a). Indeed, nanoparticle debonding might take an important role not only as

mechanism itself, but also as trigger for phenomena like plastic void growth or matrix shear yielding (Zappalorto et al., 2011b, Salviato et al., 2011b).

2.6 Conclusions

In the present chapter the main issues of nanocomposite modelling have been discussed and a description of some modelling strategies available in the literature has been provided. Most of these are micromechanical-based, and should then be updated to include the typical features of the nanoscale.

It has been acknowledged that in the most general case three main stages should be addressed in nanocomposite modelling, and each stage might be tackled with the aid of a dedicated model. Accordingly, the different strategies available in the literature, aimed at predicting the mechanical properties of nanocomposites, have been classified into three groups: Micromechanical, Nanostructural and Molecular, depending on how many and which of the basic models have been used within the strategy. The concept of assembling basic models to build a multiscale modelling strategy has been defined here as “Three Stage Strategy” (TSS).

The most important features of each strategy have been discussed, together with benefits and drawbacks. Significant examples, taken from the literature, have been provided as well.

Bibliography of chapter 2

Adebahr T, Roscher C., Adam J., "Reinforcing nanoparticles in reactive resin". *European Coatings Journal*, 4, 144-149, 2001.

Ajayan P.M., Schadler L.S., Braun P.V., "Nanocomposite Science and Technology", Wiley-VCH, 2004.

Alexandre M., Dubois P., "Polymer-layered silicate nanocomposites: preparation, properties and uses of a new class of materials", *Materials Science and Engineering* 28, 1-63, 2000.

Arai M., Noro Y., Sugimoto K., Endo M. "Mode I and mode II interlaminar fracture toughness of CFRP laminates toughened by carbon nanofiber interlayer". *Compos Sci Technol*, 68:516–525, 2008.

Battistella M., Cascione M., Fiedler B., Wichmann M.H.G., Quaresimin M., Schulte K., "Fracture behaviour of fumed silica/epoxy nanocomposites", *Composites: Part A 39,*1851–1858, 2008.

Becker O., Varley R., Simon G., "Morphology, thermal relaxations and mechanical properties of layered silicate nanocomposites based upon high-functionality epoxy resins", *Polymer*, 43, 4365-4373, 2002.

Becker O., Cheng Y.B., Varley R., Simon G., "Layered Silicate Nanocomposites Based on Various High-Functionality Epoxy Resins: The Influence of Cure Temperature on Morphology, Mechanical Properties and Free Volume", *Macromolecules*, 36, 1616-1625, 2003.

Brougthon JQ, Abraham FF, Bernstein N, Kaxiras E. "Concurrent coupling of length scales: Methodology and application". *Physical Review B* volume 60, number 4 15 July 1999-II.

Term Thesis of Manuela Cascione, "Manufacturing and testing of nano-modified and conventional Glass-Fibre Reinforced Composites". Università di Padova-Technische Universitaet Hamburg-Harburg, 2005.

Chan Mo-lin, Lau Kin-tak, Wonga Tsun-tat, Ho Mei-po, Hui D. "Mechanism of reinforcement in a nanoclay/polymer composite". *Comp Part B*, 42:1708–12, 2011.

Chan C.M., Wu J., Li J-X, Chenung Y-K. "Polypropylene/calcium carbonate nanocomposites", *Polymer* 43, 2981-2992, 2002.

Chen Q, Chasiotis I, Chen C, Roy A. "Nanoscale and effective mechanical behavior and fracture of silica nanocomposites". *Compos Sci Technol*, 68:3137–44, 2008.

Chia J, Hbaieb K, Wang QX. "Finite element modelling epoxy/clay nanocomposites". *Key Eng Mat*, 334:785-88, 2007.

Cohen M.L. "Nanotubes, Nanoscience and Nanotechnology". *Materials Science and Engineering* C 15 , 1-11, 2001.

Evans AG. "The strength of brittle materials containing second phase dispersions". *Philos Mag*, 26:1327–44, 1972.

Fermeglia M, Pricl S. "Multiscale modeling for polymer systems of industrial interest". *Progress Org Coat*, 58:187-99, 2007.

Fermeglia M, Pricl S. Multiscale molecular modeling in nanostructured material design and process. *Comput Chem Eng*, 33:1701–10, 2009.

Fiedler B., Gojny F.H., Wichmann M.H.G., Nolte M.C.M., Schulte K., "Fundamental aspects of nano-reinforced composites", *Composites Science and Technology*, 66, 3115–31, 2006.

Fischer H. "Polymer nanocomposites: from fundamental research to specific applications", *Mater Sci Eng C* 23:763-72, 2003.

Fornes T.D., Paul D.R., "Modeling properties of nylon 6/claynanocomposites using composite theories", *Polymer*, 44, 4993–5013, 2003.

Frankland SJV, Harik VM, Odegard GM, Brenner DW, Gates TS. The stress–strain behavior of polymer–nanotube composites from molecular dynamics simulation. *Compos Sci Technol*, 63:1655–61, 2003.

Giannopoulos G.I, Georgantzinos S.K., Anifantis N.K., "A semi-continuum finite element approach to evaluate the Young's modulus of single-walled carbon nanotube reinforced composites". *Comp Part B*, 41:594–601, 2010.

Gou JH, Minaie B, Wang B, Liang ZY, Zhang C. "Computational and experimental study of interfacial bonding of single-walled nanotube reinforced composites". *Comp Mater Sci*, 31:225–36, 2004.

Gou JH, Liang ZY, Zhang C, Wang B. Computational analysis of effect of single-walled carbon nanotube rope on molecular interaction and load transfer of nanocomposites. *Comp Part B*, 36:524–33, 2005.

Green DJ, Nicholson PS, Embury JD. "Fracture of a brittle particulate composite – part 2. Theoretical aspects". *J Mater Sci*, 14:1657–61, 1979.

Guzmàn de Villoria R, Miravete A. "Mechanical model to evaluate the effect of the dispersion in nanocomposites". *Acta Mater*, 55:3025-31, 2007.

Ha Sung-Rok, Rhee Kyong-Yop, Park Soo-Jin, Lee Joong Hee. "Temperature effects on the fracture behavior and tensile properties of silane-treated clay/epoxy nanocomposites". *Comp Part B*, 41:602–607, 2010.

Lange FF. "The interaction of a crack front with a second-phase dispersion". *Philos Mag*, 22:983–92, 1970.

Lau Kin-Tak, Chipara Mircea, Ling Hang-Yin, Hui D. "On the effective elastic moduli of carbon nanotubes for nanocomposite structures". *Comp Part B*, 35:95-101, 2004.

Lee J.D., Wang X.Q., Chen Y.P. "Multiscale material modeling and its application to a dynamic crack propagation problem". *Theor Appl Fract Mec*, 51:33-40, 2009.

Li C, Chou T-W. "A structural mechanics approach for the analysis of carbon nanotubes". *Int J Solids Struct*, 40:2487–99, 2003.

Liao K, Li S. Interfacial characteristics of a carbon nanotube-polystyrene composite system. *Appl Phys Lett*, 79:4225–7, 2001.

Lordi V, Yao N. "Molecular mechanics of binding in carbon-nanotube–polymer composites". *J Mater Res*, 15:2770–9, 2000.

Luo J.J., Daniel I.M. "Characterization and modeling of mechanical behavior of polymer/clay nanocomposites", *Composite Science Technology*, 63, 1607–16, 2003.

Ng CB, Ash BJ, Schadler LS, RW Siegel. "A Study of the Mechanical and Permeability Properties of Nano- and Micron-TiO2 Filled Epoxy Composites". *Adv Compos Lett*, 10:101-11, 2001.

Odegard GM, Gates TS, Nicholson LM, Wised KE. "Equivalent-continuum modeling of nano-structured materials". *Compos Sci Technol*, 62:1869–80, 2002.

Odegard GM, Gates TS, Wise KE, Park C, Siochi EJ. "Constitutive modeling of nanotube-reinforced polymer composites". *Compos Sci Technol*, 63:1671–87, 2003.

Odegard GM, Clancy TC, Gates TS. "Modeling of mechanical properties of nanoparticle/polymer composites". *Polymer*, 46:553-62, 2005.

Pipes RB, Hubert P, "Helical carbon nanotube arrays: mechanical properties". *Compos Sci Technol*, 62:419–28, 2002.

Qian D, Liu WK, Ruoff RS. Load transfer mechanism in carbon nanotube ropes. *Compos Sci Technol*, 63 :1561–9, 2003.

Quaresimin M. Varley R.J., "Understanding the effect of nanomodifier addition upon the properties of fibre reinforced laminates", *Composites Science and Technology* vol.68 No. 3-4,718-726, 2008.

Quaresimin M., Salviato M., Zappalorto M. Strategies for the assessment of nanocomposite mechanical properties. *Composites part B: Engineering*, 43, 2290-2297, 2012a.

Quaresimin M., Salviato M., Zappalorto M. "Fracture and interlaminar properties of clay-modified epoxies and their glass reinforced laminates. *Engineering Fracture Mechanics*, 81:80-93, 2012b.

Ray S.S., Okamoto M., "Polymer layered silicate nanocomposites: a review from preparation to processing", *Progress in Polymer Science,* 28, 1539-1641, 2003.

Salviato M., Zappalorto M., Quaresimin M. "The effect of surface stresses on the critical debonding stress around nanoparticles". *International Journal of Fracture*, 172:97-103, 2011a.

Salviato M., Zappalorto M., Quaresimin M. "Plastic Yielding Around Nanovoids". *Procedia Engineering*, 10:3325–3330, 2011b.

Scocchi G., Posocco P., Handgraaf J-H, Fraaije J., Fermeglia M., Pricl S., "A Complete Multiscale Modelling Approach for Polymer–Clay Nanocomposites". *Chem-Eur J*, 15: 7586-7592, 2009.

Spencer PE, Sweeney J. "Modelling of polymer Clay Nanocomposites for a Multiscale appoach". arXiv:0809.0888v1 [cond-mat.mtrl-sci], 2006.

Thostenson E.T., Ren Z., Chou T.-W. "Advances in the science and technology of carbon nanotubes and their composites: a review", *Composites Science and Technology* 61, 1899-1912, 2001.

Thostenson ET, Chou TW. "On the elastic properties of carbon nanotube-based composites: modeling and characterization". *J Phys D*, 36;573–82, 2003.

Thostenson E.T., Li C., Chou T.W. "Nanocomposites in context" *Composites Science and Technology*, 65, 491–516, 2005.

Tsai Jia-Lin, Tzeng Shi-Hua, Chiu Yu-Tsung. "Characterizing elastic properties of carbon nanotubes/polyimide nanocomposites using multi-scale simulation". *Comp Part B*, 41:106–115, 2010.
VanderHart DL, Asano A, Gilman JW, Solid State NMR. "Investigation of Paramagnetic Nylon-6 Clay Nanocomposites. 1. Crystallinity, Morphology, and

the Direct Influence of Fe3+ on Nuclear Spins". *Chem Mater*, 131:3796–809, 2001.

Wagner H.D. and Vaia R.A. “Nanocomposites: issues at the interface”. *Materials Today*, 38-42, 2004.

Wetzel B., Haupert F., Zhang M.Q., “Epoxy nanocomposites with high mechanical and tribological performance”, *Composite Science and Technology* 63, 2055-2067, 2003.

Wetzel B, Rosso P, Haupert F, Friedrich K. Epoxy nanocomposites – fracture and toughening mechanisms. *Eng Fract Mech*, 73:2375–98, 2006.

Wichmann M.H.G., Sumfleth J., Gojny F. H., Quaresimin M., Fiedler B. and Schulte K., “Glass fibre-reinforced composites with enhanced mechanical and electrical properties – benefits and limitations of a nanoparticle-modified matrix”, *Engineering Fracture Mechanics*, 73, 2346–2359, 2006a.

Wichmann M.H.G., Cascione M., Fiedler B., Quaresimin M., Schulte K., “Influence of surface treatment on mechanical behaviour of fumed silica/epoxy resin nano-composites”, *Composite Interfaces*, vol. 13 No. 8-9, 699-715, 2006b.

Wong M, Paramsothy M, Xu XJ, Ren Y, Li S, Liao K. Physical interactions at carbon nanotube–polymer interface. *Polymer*, 44:7757–64, 2003.

Yokozeki T., Iwahori Y., Ishibashi M., Yanagisawa T., Imai K., Arai M., Takahashi T., Enomoto K. "Fracture toughness improvement of CFRP laminates by dispersion of cup-stacked carbon nanotubes". *Compos Sci Technol*, 69: 2268-2273, 2009.

Yu S, Yang S, Cho M. "Multi-scale modeling of cross-linked epoxy nanocomposites". *Polymer*, 50:945-52, 2009.

Zax DB, Yang DK, Santos RA, Hegemann H, Giannelis EP, Manias E. "Dynamical heterogeneity in nanoconfined polystyrene chains". *J Chem Phys*, 112:2945–51, 2000.

Zammarano M., Maupin PH, Sung LP, Gilman JW, McCarthy ED, Kim YS, Fox DM. "Revealing the Interface in Polymer Nanocomposites". *ACS NANO*, 5: 3391-3399, 2011.

Zappalorto M, Salviato M, Quaresimin M. "Influence of the interphase zone on the nanoparticle debonding stress". *Compos Sci Technol*, 72:48-55, 2011a.

Zappalorto M., Salviato M., Quaresimin M. "Assessment of Debonding-Induced Toughening in Nanocomposites". *Procedia Engineering*, 10:2973–2978, 2011b.
Zeng QH, Yu AB, Lu GQ. "Multiscale modeling and simulation of polymer nanocomposites". *Progr Polym Sci*, 33:191–269, 2008.

Zhang M., Singh R.P. “Mechanical reinforcement of unsatured polyester by Al_2O_3 nanoparticles”. *Materials Letters* 58, 408-412, 2004.

Zhao S, Schadler LS, Duncan R, Hillborg H, Auletta T. "Mechanisms leading to improved mechanical performance in nanoscale alumina filled epoxy". *Compos Sci Technol*, 68:2965–75, 2008.

3

Nanoparticle debonding strength: a comprehensive study on interfacial effects

3.1 Introduction

The recent advance in nanofabrication techniques has made it possible to manufacture composite materials containing nanoscale fillers and giving rise to a new class of materials termed "Nanocomposites". Polymer nanocomposites have been proven to be outstanding materials, characterised by a unique mix of physical and mechanical properties coming from the synergistic combination of the constituent properties (Ajayan *et al.*, 2004, Thostenson *et al.*, 2005, Quaresimin *et al*., 2012a).

Such performances are acknowledged to be related to the energy dissipated through the damage mechanisms taking place at the nanoscale. Among these, nanoparticle debonding could take an important role either as a mechanism itself or as a trigger for phenomena like plastic void growth or the matrix shear yielding (Salviato *et al*. 2011a, Zappalorto *et al*. 2011b, Zappalorto *et al*. 2012b, Salviato et al., under review).

The debonding process in particulate composites has been widely studied in the literature.

A micromechanics-based analysis of the debonding strength of rigid spherical inclusion embedded in and completely adhered to a larger sphere of matrix under uniform radial stress was carried out by Nicholson (1979). The case of a rigid spherical inclusion under a tensile stress applied to the elastomeric matrix was analysed, instead, by Gent (1980) who supposed the inclusion to have an initially-debonded patch on its surface.

Nicholson's work has been extended to the interfacial debonding of nanoparticles by Chen *et al.* (2007), who derived a simple size-dependent formulation for the debonding stress and used it to compute the energy dissipation due to this mechanism.

The significant improved mechanical properties exhibited by nanocomposites, when compared to that obtainable with microcomposites with similar micro-structure, can be attributed to the large ratio of surface area to volume which makes surface and interphase phenomena the prominent contributions to mechanical property enhancements. Accordingly, when dealing with polymer nanocomposites it is extremely important to describe the interphase and surface effects and to be able to correctly estimate properties accounting for those contributions (Ajayan *et al.*, 2004*).*

It is acknowledged that, around a nanoparticle, the molecular structure of the polymer matrix might be significantly altered at the particle/matrix interface and this perturbed region is comparable in size with that of the nanoparticle and characterised by chemical and physical properties different from those of the constituents (Odegard *et al*., 2005, Yu *et al*., 2009, Zammarano et al., 2010). Being its size at the nanometer scale, this zone of altered chemistry is commonly ignored in the analysis of microfilled polymers but, as the filler size is decreased to the nanoscale, it might substantially influence the overall mechanical properties. Several authors studied the effect of an interphase layer different from the matrix on the stiffness and strength of particle and nanoparticle filled polymers.

Lauke widely analysed the stress state around a coated particle in a polymer matrix to determine the adhesion strength at the interface (Lauke *et al*. 2000, Lauke and Schüller 2002, Lauke 2006).

Boutaleb *et al*. (2009) developed a micromechanical analytical model to predict the stiffness and yield stress of nanocomposites accounting for an interphase around the nanoparticles and found out that this zone plays a key role on both the overall stiffness and yield stress of the nanocomposite. Similar conclusions have been drawn by Sevostianov and Kachanov (2007) for elastic and conductive properties and by Li *et al*. (2011) who also highlighted an analogy between the

strain gradient effect and the role of an interphase in accounting for the synergistic elastic stiffening in nanocomposites.

Zappalorto *et al*. (2011a and 2012a) determined a closed form solution for the stress fields around a rigid nanoparticle under uniaxial tensile load accounting for the presence, around the nanoparticle, of an interphase of thickness comparable to the particle size and different elastic properties from those of the matrix. Then, they developed a closed form expression for the critical debonding stress and showed that the interphase properties, linked to surface functionalizers, significantly affects the debonding stress, especially for nanoparticle radii below 50 nm. The effects of the interphase size and properties on the nanocomposite fracture toughness have been also analysed by the same authors (Zappalorto *et al*. , 2011b, Zappalorto *et al.*, 2012b, Salviato *et al.*, 2011a, b).

Another important aspect to be carefully considered when analyzing the deformation behaviour of nanofilled polymers is the mechanical behaviour of the filler-polymer interfacial surface, where surface-stresses might be present. The consequences of such stresses are commonly ignored as they are generally considered to be unimportant for macroscopic features. At the nanoscale, however, these stresses, which quantify the ability of a solid to change its surface energy under elastic deformation, might be comparable with stresses of mechanical nature.

In the recent years the effects of surface stresses have been investigated by several authors with reference to the stress concentration at a nanoscale hole (He and Li, 2006), an elastic nanoinhomogeneity (Sharma and Ganti, 2002; Sharma *et al*., 2003, Tian and Rajapakse, 2007), a surface flaw (Gill 2007), and for multiple interacting spherical inhomogeneities (Kushch *et al*, 2011) as well as to the elastic behaviour of a screw dislocation in an eccentric core–shell nanowire (Ahmadzadeh-Bakhshayesh *et al*., 2012).

Size-dependent effective elastic constants of solids containing nano-inhomogeneities with interface stresses was derived by Duan *et al*. (2005) while the surface effect and size dependence on the energy release due to a nano InAs inclusion expansion in a plane GaAs matrix under uni-axial or bi-axial loadings was analysed by Hui and Chen (2010).

On parallel tracks, the effects of surface elastic constants on the debonding stress of nanoparticles have been investigated by Salviato *et al*. (2011a) who showed that the range of the nanoparticle radii where those effects are significant is limited to the nanoscale.

In the present chapter, a comprehensive study on the interphase and surface effects on the nanoparticle debonding strength is carried out. The analysis is developed within the frame of Finite Fracture Mechanics (Leguillon, 2002) and Surface Elasticity (Gurtin and Murdoch, 1975, 1978). It accounts, contemporaneously, for the emergence of an interphase zone around the nanoparticle and for surface stresses on the nanoparticle periphery. The relevant features of the solution and the role played by all parameters are discussed in detail through examples.

3.2 Description of the system under analysis

The high surface/volume ratio of nanoscale materials and structures makes the surface effects significant in the analysis of nanocomposites (Ajayan *et al.*, 2004, Quaresimin *et al*., 2012*).* As the reinforcement dimensions are of the same length scale as the radius of gyration of polymeric chains, molecular interactions between nanoparticle surface and the matrix cause the formation of an interphase "layer" of which the properties can be very different from those of the constituents (Zax *et al*, 2000, VanderHart *et al*., 2001, Odegard *et al*, 2005, Yu *et al*, 2009).

Unfortunately, the data available so far in the literature about the interphase zone are not enough to precisely formulate the law of variation of its properties across the thickness, as well as its size. Those parameters varies from case to case (Sevostianov and Kachanov, 2007, Odegard *et al*, 2005, Yu *et al*, 2009). Accordingly, for the sake of simplicity, in this work it has been assumed that, even if there might be a gradual transition of the interphase properties across its thickness to the bulk ones, a through-the-thickness average is representative of the overall property distribution. This is in agreement with some recent numerical and analytical investigations (Odegard *et al*, 2005, Yu *et al*, 2009, Zappalorto *et al.*, 2011a,b, 2012a,b). Consequently, the interphase is supposed to be homogeneous and isotropic.

Thus the system under investigation, shown in Figure 3.1a, is constituted by:

- a spherical nanoparticle of radius $\boldsymbol{r_0}$;
- a shell-shaped interphase of external radius **a**, thickness **t** and uniform properties;
- a matrix of radius ***b*** loaded by a hydrostatic stress *S*.

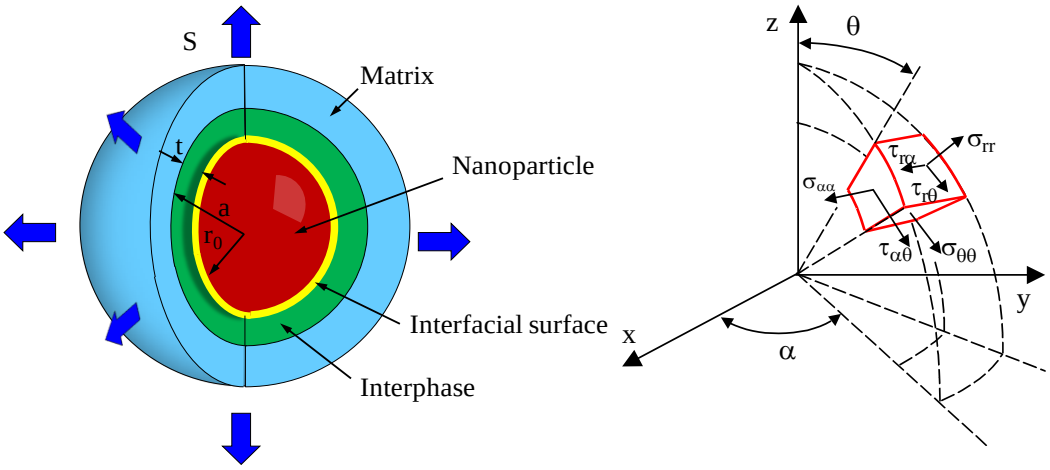

a) b)

Figure 3.1. a) description of the system under analysis: nanoparticle of radius r_0 embedded in an interphase region or radius a. Bulk material of radius b subjected to an hydrostatic stress S and b) the spherical coordinates system and stress components used to address the problem.

The properties required by the analysis can be computed by means of numerical simulations carried out within the frame of MD as done by Odegard *et al.* (2005) and Yu *et al.* (2009); such method provides, as outputs, the radial extension of the interphase as well as the elastic properties averaged through the interphase thickness. Moreover surface stresses are supposed to act on the nanoparticle periphery. These stresses quantify the ability of a solid to change its surface energy under elastic deformation and, for nanoscale systems they might be comparable with stresses of mechanical nature (Gill, 2007).

3.3 An approach based on energy

In the ambit of a Finite Fracture Mechanics approach (Leguillon, 2002), the critical detachment strength of a nanoparticle can be assessed by imposing the following energy condition (Zappalorto *et al*, 2011a, Salviato et al., 2011a):

$$-\frac{\delta U}{\delta A} \geq \Gamma \tag{3.1}$$

where δU is the change in potential energy, δA is the newly created debonded surface and Γ is the interfacial fracture energy.

Applying an energy balance to the system shown in Figure 3.1a, Eq. (3.1) can be more conveniently re-written in the following form:

$$\delta W \leq \delta U^{m+a} + \delta U^{p} + 4\pi r_0{}^2 \Gamma \tag{3.2}$$

where δW is the work done by external forces, δU is the variation in the elastic energy stored in the matrix and interphase (δU^{m+a}) and in the nanoparticle (δU^{p}) and $\boldsymbol{r_0}$ is the nanoparticle radius.

Moreover, the term Γ accounts for the energy spent to deform the already created surfaces (Müller and Saul, 2004).

The term δW in equation (3.2) can be simply re-written as:

$$\delta W = S \times \delta u^{m}(b) \times 4\pi b^2 \tag{3.3}$$

while Clapeyron's theorem gives:

$$\begin{aligned} \delta U^{p} &= -\frac{1}{2}\sigma_{cr} \times \delta u^{p}(r_0) \times 4\pi r_0{}^2 \\ \delta U^{m+a} &= -\frac{1}{2}\sigma_{cr} \times \delta u^{a}(r_0) \times 4\pi r_0{}^2 + S \times \delta u^{m}(b) \times 4\pi b^2 \end{aligned} \tag{3.4a,b}$$

In Eq. (3.3) and Eqs. (3.4) terms δu^{p}, δu^{i} and δu^{m} represent the variation of the displacement fields from the initial condition (incipient debonding) to the final condition (post debonding) in the particle, the interphase and the matrix, respectively. *S* is, instead, the remotely applied hydrostatic stress, which is not supposed to change during the debonding process and σ_{cr} is the critical detachment strength. Substitution of Eq. (3.3) and Eqs. (3.4) into Eq. (3.2) gives:

$$\sigma_{cr} \times \left\{ \delta u^{p}(r_0) + \delta u^{a}(r_0) \right\} \leq 2\Gamma \tag{3.5}$$

It is then evident that the solution of Eq. (3.5) requires a stress and displacement analysis of the system at two different states: incipient debonding and post debonding.

3.4 Stress analysis

3.4.1 General equations in the bulk material

A linear elastic analysis is carried out on the system shown in Figure 3.1a, where all constituents are regarded as isotropic materials, according to Chen *et al*. (2007), Sevostianov and Kachanov (2007) and Zappalorto *et al*. (2011a,b).

Consider the spherical coordinate system shown in Figure 3.1b, of which the origin is located in the centre of the nanoparticle. Thanks to the spherical symmetry of the problem only the radial displacement *u* is nonzero and it is independent of the spherical coordinates θ and α.

The governing equation of the problem is a second order Euler equation for *u* whose general solutions are in the following form:

$$u^m = A_m r + \frac{B_m}{r^2} \qquad r \in (a,b] \qquad \text{in the matrix} \tag{3.6}$$

$$u^a = A_a r + \frac{B_a}{r^2} \qquad r \in (r_0,a] \qquad \text{in the interphase} \tag{3.7}$$

$$u^p = A_p r + \frac{B_p}{r^2} \qquad r \in [0,r_0] \qquad \text{in the nanoparticle} \tag{3.8}$$

then, radial stress components can be written as:

$$\sigma_{rr}^k = 3K_k A_k - 4\frac{B_k G_k}{r^3} \qquad \text{with } k=m,\ a,\ p \tag{3.9}$$

where $K_k = E_k/[3(1-2\nu_k)]$ and $G_k = E_k/[2(1+\nu_k)]$ are the bulk and the shear moduli of the *k*-th sub-dominion respectively.

3.4.2 Equilibrium equations on the nanoparticle outer surface

According to Surface Elasticity theory (Gurtin and Murdoch, 1975, 1978) the following equilibrium equations hold valid on the nanoparticle surface ($r=r_0$):

$$\begin{aligned}
&\sigma_{rr}{}^a - \sigma_{rr}{}^p = \frac{\sigma_{\alpha\alpha}{}^s + \sigma_{\theta\theta}{}^s}{r} \\
&\tau_{r\alpha}{}^a - \tau_{r\alpha}{}^p = -\left(\frac{1}{r}\frac{\partial \sigma_{\alpha\alpha}{}^s}{\partial \alpha} + \frac{1}{r\sin\alpha}\frac{\partial \tau_{\alpha\theta}{}^s}{\partial \theta} + \frac{\sigma_{\alpha\alpha}{}^s - \sigma_{\theta\theta}{}^s}{r}\cot\alpha\right) \\
&\tau_{r\theta}{}^a - \tau_{r\theta}{}^p = -\left(\frac{1}{r}\frac{\partial \tau_{\theta\alpha}{}^s}{\partial \alpha} + \frac{1}{r\sin\alpha}\frac{\partial \sigma_{\theta\theta}{}^s}{\partial \theta} + \frac{2\tau_{\theta\alpha}{}^s}{r}\cot\alpha\right)
\end{aligned} \tag{3.10a-c}$$

where $\tau_{\theta\alpha}{}^{s}$, $\sigma_{\theta\theta}{}^{s}$ and $\sigma_{\alpha\alpha}{}^{s}$ are the surface stress components while $\sigma_{rr}{}^{a}$, $\tau_{r\alpha}{}^{a}$, $\tau_{r\theta}{}^{a}$ and $\sigma_{rr}{}^{p}$, $\tau_{r\alpha}{}^{p}$, $\tau_{r\theta}{}^{p}$, are the stress components in the interphase and the nanoparticle respectively.

Under non-sliding conditions between the surface and the bulk, the surface strain field is continuous and no shear strains are present. Accordingly, surface stresses can be linked to strain components through the following equation (Sharma *et al.*, 2003):

$$\sigma_{ji}{}^{s} = \sigma^{0}\delta_{ji} + 2\left(\mu^{s} - \sigma^{0}\right)\delta_{jk}\varepsilon_{ki} + \left(\lambda^{s} + \sigma^{0}\right)\varepsilon_{kk}\delta_{ji} \tag{3.11}$$

where the residual stress σ^{0} can be neglected since surface defects are not assumed to be present (Sharma *et al.*, 2003). Accordingly, Eqs. (3.10) simplify as follows:

$$\sigma_{rr}{}^{(a)} - \sigma_{rr}{}^{(p)} = \frac{2K_s\varepsilon}{r} \qquad \tau_{r\alpha}{}^{(a)} - \tau_{r\alpha}{}^{(p)} = 0 \qquad \tau_{r\theta}{}^{(a)} - \tau_{r\theta}{}^{(p)} = 0 \tag{3.12a-c}$$

where $K_s = 2(\lambda_s+\mu_s)$ is the surface elastic modulus and ε is the hoop strain on the surface.

3.5 Stress and displacement fields at incipient debonding

At incipient debonding (id state) the following conditions must be contemporaneously satisfied:

$$\sigma_r^{p}\Big|_{r=r_0} = \sigma_{cr} \qquad \sigma_r^{a}\Big|_{r=r_0} = \sigma_{cr} + \frac{2K_s^{(id)}}{r_0}\varepsilon \qquad \sigma_r^{a}\Big|_{r=a} = \sigma_r^{m}\Big|_{r=a}$$
$$u^{p}\Big|_{r=r_0} = u^{a}\Big|_{r=r_0} \qquad u^{a}\Big|_{r=a} = u^{m}\Big|_{r=a} \tag{3.13a-e}$$

which can be rewritten in the following form:

$$\begin{cases} \sigma_{cr} + \dfrac{2K_s^{(id)}}{r_0}\left(A_a^{(id)} + \dfrac{B_a^{(id)}}{r_0{}^{3}}\right) = 3K_aA_a^{(id)} - 4\dfrac{B_a^{(id)}G_a}{r^{3}} \\ \dfrac{\sigma_{cr}}{3K_p}r_0 = A_a^{(id)}r_0 + \dfrac{B_a^{(id)}}{r_0{}^{2}} \\ A_a^{(id)}a + \dfrac{B_a^{(id)}}{a^{2}} = A_m^{(id)}a + \dfrac{B_m^{(id)}}{a^{2}} \\ 3K_aA_a^{(id)} - 4\dfrac{B_a^{(id)}}{a^{3}}G_a = 3K_mA_m^{(id)} - 4\dfrac{B_m^{(id)}}{a^{3}}G_m \end{cases} \tag{3.14 a-d}$$

noting that, to avoid displacement singularities within the particle, B_p must vanish, so that Eq. (3.13a) gives $A_p^{(id)} = \sigma_{cr} / 3K_p$ and substituting Eqs. (3.6-9) into Eqs. (3.13).

The solutions of Eqs 3.14 are:

$$
\begin{aligned}
A_a^{(id)} &= \sigma_{cr} \frac{3K_m + 4G_m}{3K_p\left(3K_a + 4G_a\right)}\alpha \\
B_a^{(id)} &= -\sigma_{cr} \frac{3K_m + 4G_m}{3K_p\left(3K_a + 4G_a\right)}\beta r_0^3 \\
A_m^{(id)} &= \frac{\sigma_{cr}}{3K_p}\zeta \\
B_m^{(id)} &= -\frac{\sigma_{cr}}{3K_p}\left[\alpha\frac{3\left(K_a - K_m\right)}{3K_a + 4G_a}a^3 + \beta\frac{3K_m + 4G_a}{3K_a + 4G_a}r_0^{\,3}\right]
\end{aligned}
\qquad \text{(3.15a-d)}
$$

where:

$$
\begin{aligned}
\alpha &= \left(3K_p + 4G_a + \frac{2K_s^{(id)}}{r_0}\right)\left(3K_m + 4G_m\right)^{-1} \\
\beta &= \left(3\left(K_p - K_a\right) + \frac{2K_s^{(id)}}{r_0}\right)\left(3K_m + 4G_m\right)^{-1} \\
\zeta &= \frac{\left(\xi + 4\right)}{\left(\xi + 4\chi\right)}\alpha + 4\beta\frac{\left(\chi - 1\right)}{\left(\xi + 4\chi\right)}\left(\frac{r_0}{a}\right)^3
\end{aligned}
\qquad \text{(3.16a-c)}
$$

and $\chi = G_a / G_m$ and $\xi = 3K_a / G_m$ (Zappalorto *et al*. 2011a).

Finally, stress and displacement fields within the nanoparticle and the interphase can be written as a function of the critical debonding strength, σ_{cr}:

$$
\begin{aligned}
u^{p,(id)} &= \frac{\sigma_{cr}}{3K_p}r \\
u^{a,(id)} &= \frac{\sigma_{cr}}{3K_p}\frac{3K_m + 4G_m}{3K_a + 4G_a}r\left[\alpha - \beta\left(\frac{r}{r_0}\right)^3\right] \\
\sigma_r^{p,(id)} &= \sigma_{cr} \\
\sigma_r^{a,(id)} &= \sigma_{cr}\frac{3K_m + 4G_m}{3K_a + 4G_a}\frac{3K_a\alpha + 4G_a\beta\left(\frac{r_0}{r}\right)^3}{3K_p}
\end{aligned}
\qquad \text{(3.17a-d)}
$$

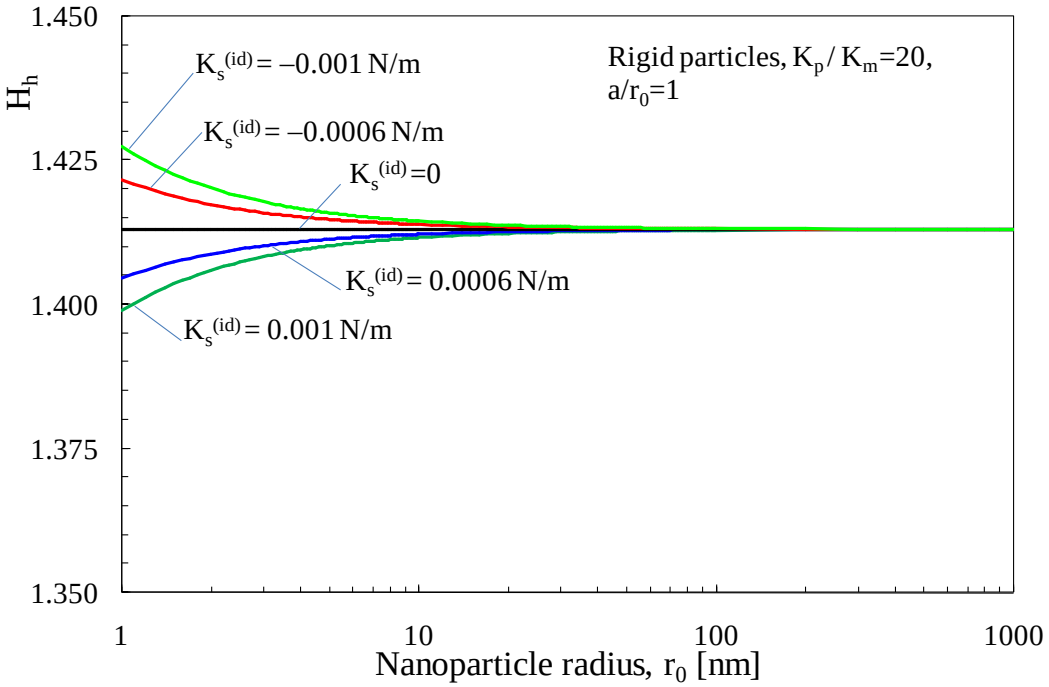

Figure 3.2 Effects of surface elastic constants on H_h factor in the absence of interphase effects. Rigid particles (K_p/K_m=20).

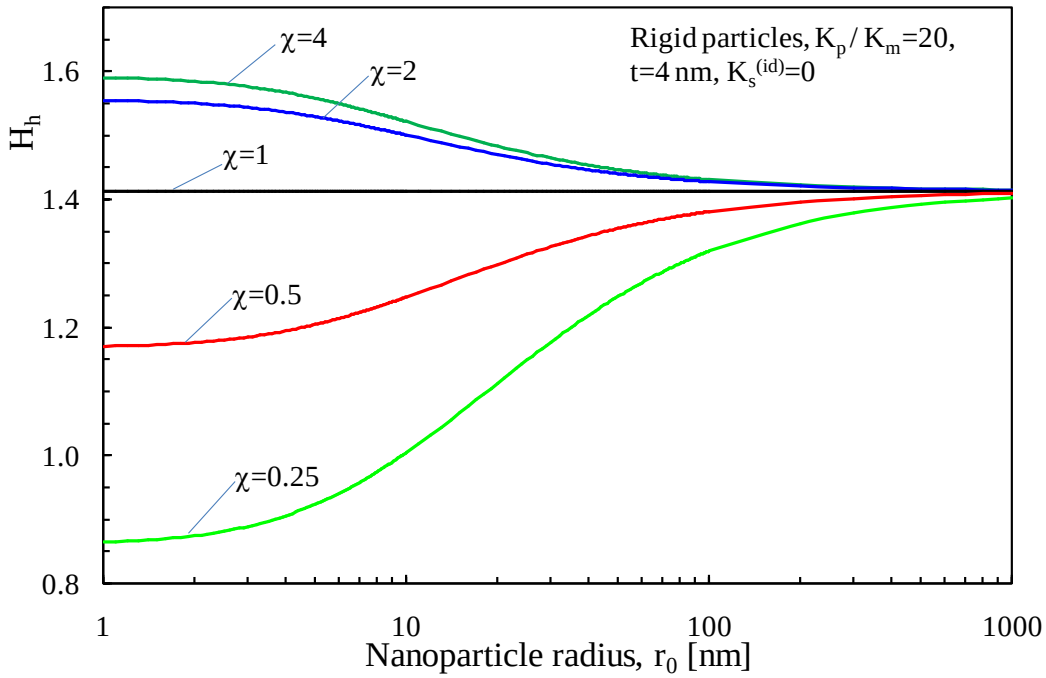

Figure 3.3. Effects of the elastic properties of the interphase on H_h factor in the absence of surface stresses. Rigid particles (K_p/K_m=20), t= 4nm.

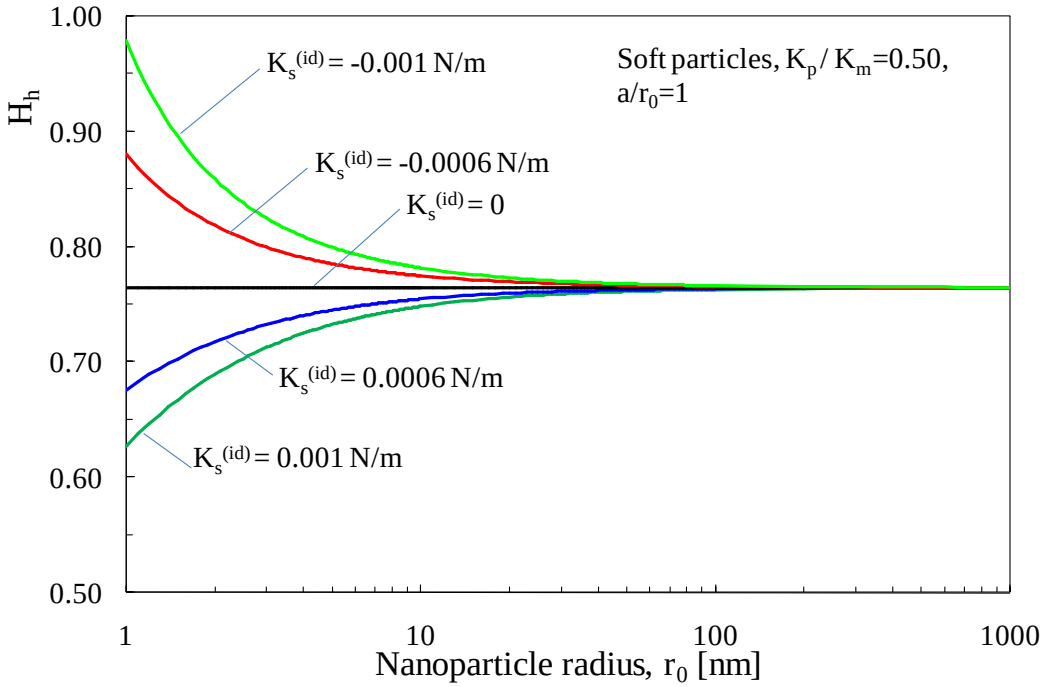

Figure 3.4. Effects of surface elastic constants on H_h factor in the absence of interphase effects. Soft particles (K_p/K_m=0.5).

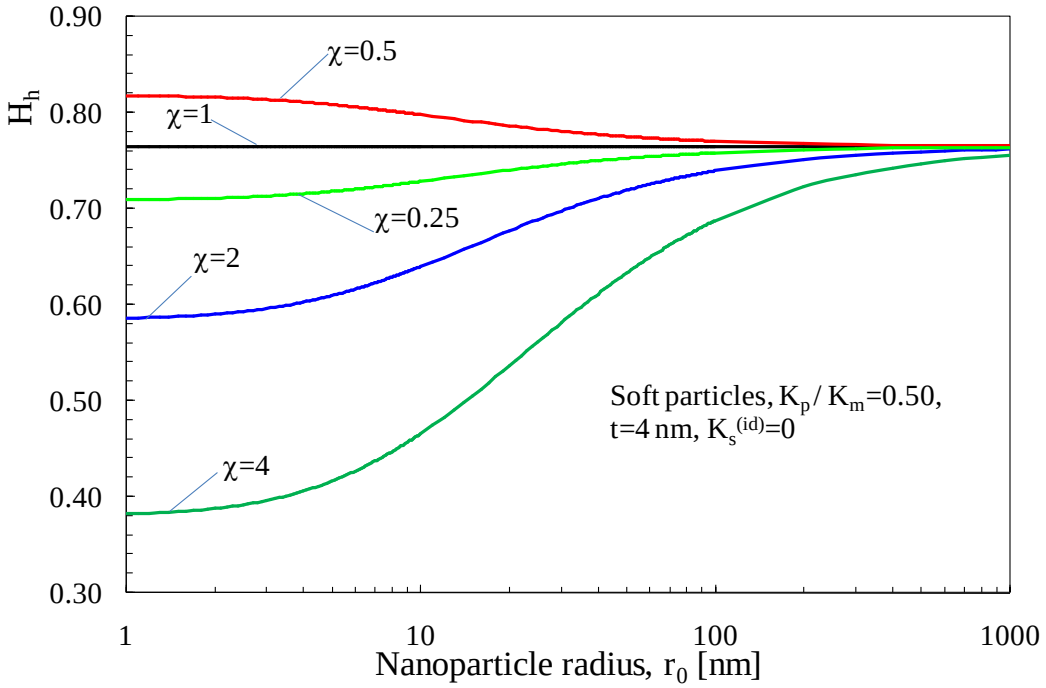

Figure 3.5. Effects of the elastic properties of the interphase on H_h factor in the absence of surface stresses. Soft particles (K_p/K_m=0.5), t= 4nm.

It is worth noting that when $\beta > 0$ (rigid nanoparticles) the interphase radial stress is increasing while r decreases whereas for $\beta < 0$ (soft nanoparticles) the radial stress increases with increasing r values.

Noting that $b >> a, r_0$, the boundary stress S can be equivalently written as:

$$S = 3K_m A_m^{(id)} \qquad S = \frac{\sigma_{cr}}{H_h} \tag{3.18a-b}$$

where H_h is the the hydrostatic component of the *Global Stress Concentration Tensor* of the problem. Equating Eqs. (3.18a) and (3.18b) gives:

$$H_h = \frac{K_p}{K_m}\zeta^{-1} \tag{3.19}$$

A plot of H_h for different cases is shown in Figures 3.2-7.

3.6 Stress and displacement fields after debonding

In the post debonding state ("pd" state), the nanoparticle becomes unloaded and its displacement field is trivially zero. Then, only the following four boundary conditions need to be satisfied:

$$\sigma_r^a\Big|_{r=r_0} = \frac{2K_s^{(pd)}}{r_0}\varepsilon \qquad \sigma_r^a\Big|_{r=a} = \sigma_r^m\Big|_{r=a} \qquad \sigma_r^m\Big|_{r=b} = S \qquad u^a\Big|_{r=a} = u^m\Big|_{r=a} \tag{3.20a-d}$$

leading to the following linear system:

$$\begin{cases} 3K_a A_a^{(pd)} - 4\dfrac{B_a^{(pd)}G_a}{r_0^{\,3}} = \dfrac{2K_s^{(pd)}}{r_0}\left(A_a^{(pd)} + \dfrac{B_a^{(pd)}}{r_0^{\,3}}\right) \\ 3K_a A_a^{(pd)} - 4\dfrac{B_a^{(pd)}G_a}{a^3} = 3K_m A_m^{(pd)} - 4\dfrac{B_m^{(pd)}G_m}{a^3} \\ A_m^{(pd)}a + \dfrac{B_m^{(pd)}}{a^2} = A_a^{(pd)}a + \dfrac{B_a^{(pd)}}{a^2} \\ 3K_m A_m^{(pd)} = S \end{cases} \tag{3.21a-d}$$

The solutions of Eq. (3.21) are:

$$A_a^{(pd)} = \frac{\sigma_{cr}\zeta}{3K_p}\varsigma\frac{(4G_m + 3K_m)}{(4G_m + 3K_a)\varsigma + 4(r_0/a)^3(G_a - G_m)(\varsigma - 3K_a - 4G_a)}$$
$$B_a^{(pd)} = -\frac{\sigma_{cr}\zeta}{3K_p}\frac{(4G_m + 3K_m)(\varsigma - 3K_a - 4G_a)}{(4G_m + 3K_a)\varsigma + 4(r_0/a)^3(G_a - G_m)(\varsigma - 3K_a - 4G_a)}r_0^{\,3} \tag{3.22a-b}$$

$$A_m^{(pd)} = \frac{\sigma_{cr}}{3K_p}\zeta$$
$$B_m^{(pd)} = -\frac{\sigma_{cr}\zeta}{3K_p}\frac{3(K_a - K_m)\varsigma + (3K_m + 4G_a)(\varsigma - 3K_a - 4G_a)(r_0/a)^3}{(4G_m + 3K_a)\varsigma + 4(r_0/a)^3(G_a - G_m)(\varsigma - 3K_a - 4G_a)}a^3 \quad (3.22c\text{-}d)$$

where $\varsigma = 2\left(K_s^{pd}/r_0 + 2G_a\right)$.

The corresponding radial displacement field is:

$$u^{a,(pd)} = \frac{\sigma_{cr}\zeta}{3K_p}\frac{(4G_m + 3K_m)\left[\varsigma - (\varsigma - 3K_a - 4G_a)\left(\frac{r_0}{r}\right)^3\right]}{(4G_m + 3K_a)\varsigma + 4(r_0/a)^3(G_a - G_m)(\varsigma - 3K_a - 4G_a)}r \quad (3.23a,b)$$
$$u^{m,(pd)} = \frac{\sigma_{cr}\zeta}{3K_p}r\left[1 - \frac{3(K_a - K_m)\varsigma + (3K_m + 4G_a)(\varsigma - 3K_a - 4G_a)(r_0/a)^3}{(4G_m + 3K_a)\varsigma + 4(r_0/a)^3(G_a - G_m)(\varsigma - 3K_a - 4G_a)}\left(\frac{a}{r}\right)^3\right]$$

3.7 Analytical solution for the critical debonding stress

The stress analysis carried out in the previous sections allows one to determine the displacement variations from the incipient debonding state to the post debonding state to be inserted in Eq. (3.5):

$$\delta u^p(r_0) = u^{p,(pd)}(r_0) - u^{p,(id)}(r_0) = -F\sigma_{cr}$$
$$\delta u^a(r_0) = u^{a,(pd)}(r_0) - u^{a,(id)}(r_0) = C\sigma_{cr} \quad (3.24\ a,b)$$

where:

$$F = \frac{r_0}{3K_p} \qquad \eta = \frac{3K_a + 4G_m + 4(G_a - G_m)\left(\frac{r_0}{a}\right)^3}{3K_a + 4G_a}$$
$$M = \frac{(3K_a + 4G_a)r_0\eta}{\varsigma(3K_a + 4G_m) + 4(G_a - G_m)(\varsigma - 3K_a - 4G_a)\left(\frac{r_0}{a}\right)^3} \quad (3.25a\text{-}c)$$

Substituting Eqs. (3.24) into Eq. (3.5) and re-arranging:

$$\frac{1}{2}\sigma_{cr}{}^2C - \frac{1}{2}\sigma_{cr}{}^2F = \gamma + \frac{K_s^{(pd)}}{r_0{}^2}D^2\sigma_{cr}{}^2 - \frac{K_s^{(id)}}{r_0{}^2}F^2\sigma_{cr}{}^2 \quad (3.26)$$

where γ is the interfacial fracture energy and:

$$C = M\left(1 - \frac{2}{3}\frac{K_s^{(pd)} - K_s^{(id)}}{r_0K_p}\right) \quad (3.27a,b)$$

$$D=\frac{\left(3K_a+4G_m\right)\left(\frac{2}{3}\frac{K_s^{(id)}}{r_0K_p}+1+\frac{4G_a}{3K_p}\right)+4\left(G_a-G_m\right)\left(\frac{r_0}{a}\right)^3\left(\frac{2}{3}\frac{K_s^{(id)}}{r_0K_p}+\frac{K_p-K_a}{K_p}\right)}{\varsigma\left(3K_a+4G_m\right)+4\left(G_a-G_m\right)\left(\varsigma-3K_a-4G_a\right)\left(\frac{r_0}{a}\right)^3}r_0$$

Solving Eq. (3.26) by σ_{cr}:

$$\sigma_{cr}=r_0\sqrt{\frac{2\gamma}{\left(C-F\right)r_0^2-2\left(K_s^{(pd)}D^2-K_s^{(id)}F^2\right)}} \tag{3.28}$$

3.8 Limit solutions

Based on the general solution given by Eq. (3.28) it is also possible to determine the limit values which might be representative of special conditions.

3.8.1 Negligible surface stresses

Whenever surface stresses can be regarded to negligibly contribute to the debonding process, the surface elastic constants $K_s^{(pd)}$ and $K_s^{(id)}$ can be set equal to zero. Accordingly:

$$C\cong M\cong\frac{\left(3K_a+4G_a\right)r_0\eta}{4G_a\left(3K_a+4G_m\right)-12K_a\left(G_a-G_m\right)\left(\frac{r_0}{a}\right)^3} \tag{3.29}$$

and Eq. (3.28) simplifies as:

$$\sigma_{cr}=r_0\sqrt{\frac{2\gamma}{\left(M-F\right)r_0^2}} \tag{3.30}$$

Under the further assumption that the nanoparticle is much more rigid than the interphase, F tends to zero and Eq. (3.30) turns out to be:

$$\sigma_{cr}\cong\sqrt{\frac{2\gamma}{M}}=\sqrt{\frac{4\Gamma}{r_0}\frac{E_m}{1+\nu_m}}\sqrt{\frac{\chi\left(\xi+4\right)-\xi\left(\chi-1\right)\left(r_0/a\right)^3}{\xi+4+4\left(\chi-1\right)\left(r_0/a\right)^3}} \tag{3.31}$$

in agreement with Zappalorto *et al*. (2011a).

3.8.2 Negligible interphase effects

Whenever the elastic properties of the interphase zone are not significantly different from those of the matrix ($K_a=K_m$, $G_m=G_a$) or, equivalently, the

interphase zone extension is negligible with respect to the nanoparticle size ($a/r_0 \to 1$) one obtains:

$$\eta = 1 \qquad M = \frac{r_0}{\varsigma} \qquad D = \frac{\left(\frac{2}{3}\frac{K_s^{(id)}}{r_0 K_p} + 1 + \frac{4G_a}{3K_p} \right)}{\varsigma} r_0 \tag{3.32a-c}$$

Under the further assumption that the nanoparticle is much more rigid than the interphase F tends to

zero and $D \cong C \cong M \cong \frac{r_0}{\varsigma}$. Accordingly, Eq. (3.29) simplifies as:

$$\sigma_{cr} = \varsigma \sqrt{\frac{\gamma}{2 r_0 G_m}} \tag{3.33}$$

in agreement with Salviato *et al.* (2012).

3.8.3 Negligible surface stresses, negligible interphase effects and infinitely rigid nanoparticle

If surface stresses are neglected and K_p is supposed to be much higher than K_a and K_m Eq. (3.33) simplifies as:

$$\sigma_{cr} = \sigma_{cr,0} = \sqrt{\frac{4\gamma}{r_0}\frac{E_m}{1+\nu_m}} \tag{3.34}$$

in agreement with Chen *et al*. (2007).

3.9 Discussion

In this section the range of applicability and the most relevant features of the solution proposed in the previous section will be clarified through examples, with particular attention to the range of nanoparticle size where interphase and surface effects are important. Indeed, since no size limitations have been formulated in the model, Eq. (3.19) and Eq. (3.28) are valid both for nanosized and microsized particles.

Initially the attention will be focused on the hydrostatic component of the *Global Stress Concentration Tensor*, H_h, which has been plotted versus the nanoparticle radius for several surface and interphase elastic properties in Figures 3.2-5.

In the following, the effects of the interphase properties and surface elastic

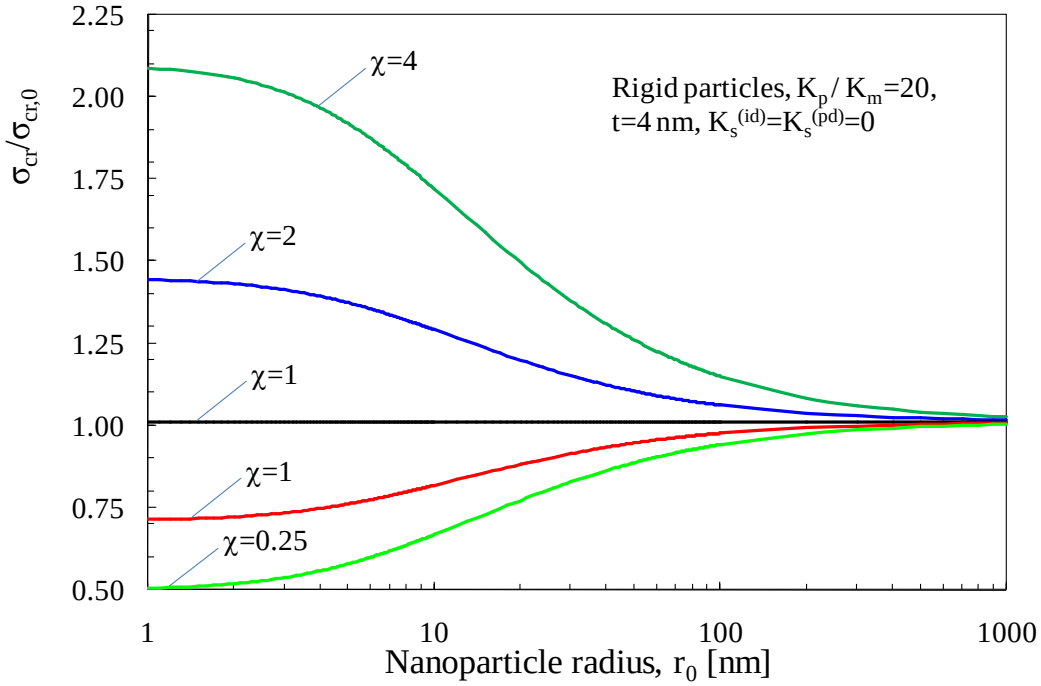

Figure 3.6. Effects of the elastic properties of the interphase on the normalized critical debonding stress in the absence of surface stresses. Rigid particles (K_p/K_m=20), t= 4nm.

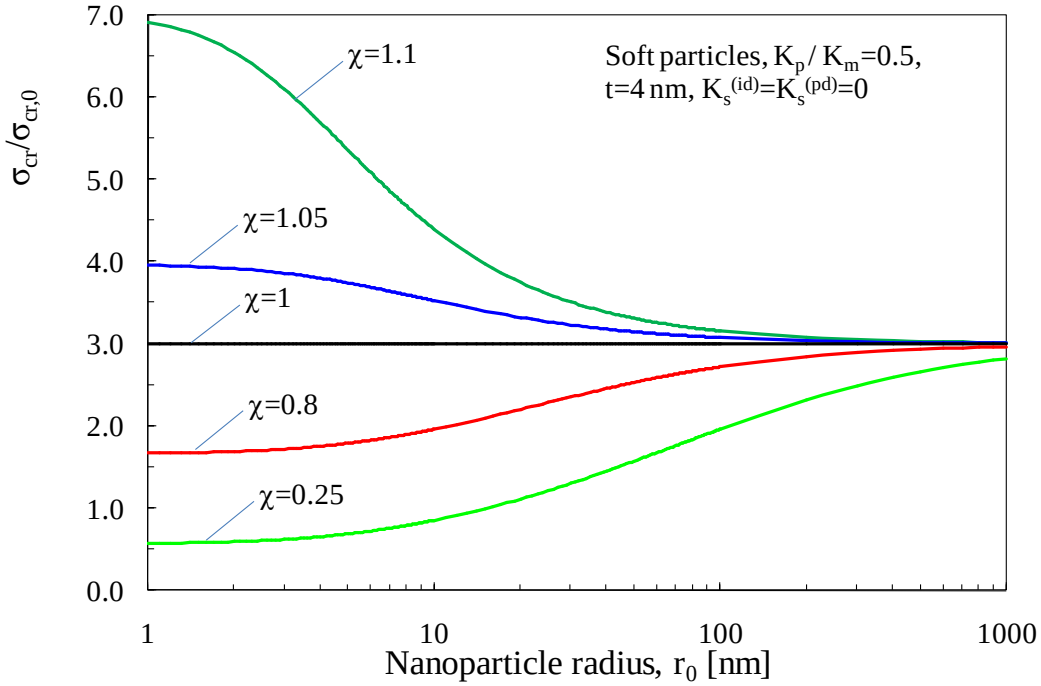

Figure 3.7 Effects of the elastic properties of the interphase on the normalized critical debonding stress in the absence of surface stresses. Soft particles (K_p/K_m=0.5), t= 4nm.

constants is analysed separately. However, as a general trend, it can be stated that both interface and interphase effects become important in the nanometer scale,

namely for nanoparticle radii smaller than about 70nm. Figure 3.2 and 3.3 refer to the case of rigid particles (K_p/K_m=20). In particular figure 3.2 shows that, under such a condition, surface effects are almost negligible. This is intuitive essentially because, under the hypothesis that the interface is coherent with the matrix, a stiff nanoparticle does not let the surface to deform significantly and to produce surface stresses.

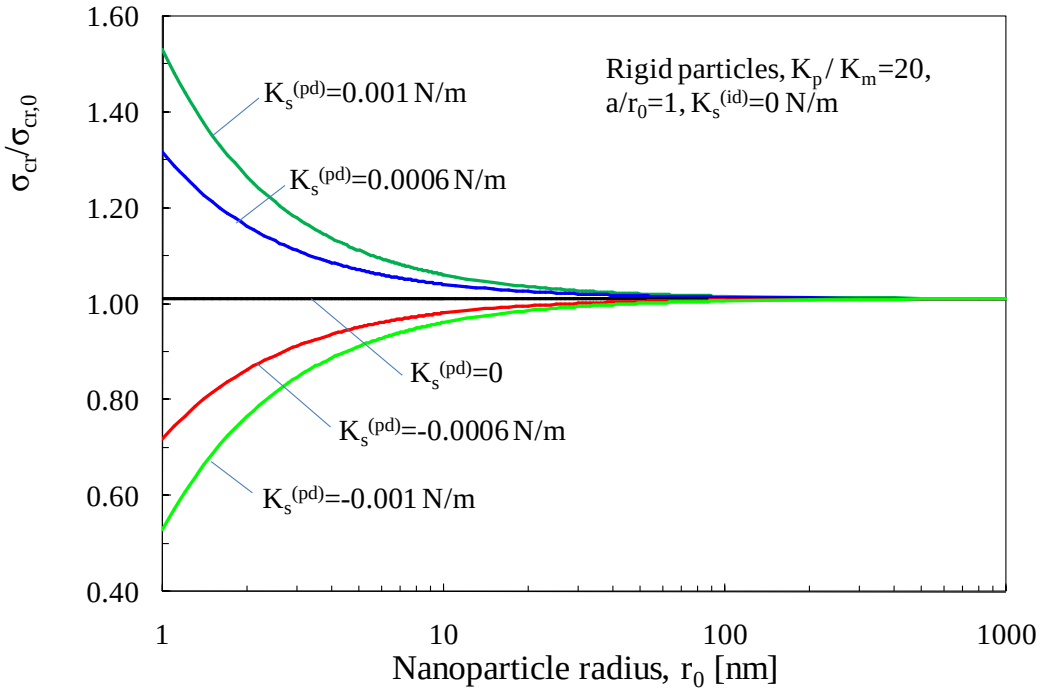

Figure 3.8. Effects of the surface elastic constant $K_S^{(pd)}$ on the normalized critical debonding stress in the absence of interphase effects. Rigid particles (K_p/K_m=20), $K_S^{(id)}$=0.

Differently, Figure 3.3 shows that interphase effects are significant for rigid particles, leading to an increase or a decrease of H_h depending on whether the interphase is softer (χ<1) or stiffer (χ>1) than the matrix. Thus, when dealing with rigid nanoparticles (as silica or alumina nanoparticles), surface stresses give a negligible contribution to H_h and the key role is played by the interphase. Under these circumstances H_h can be estimated according to the expression provided by Zappalorto *et al*. (2011a).

The case of a soft particle is presented in Figures 3.4 and 3.5, where it is evident that, as expected, both interface and interphase effects significantly affect the

solution in the nanometer range. Moreover it is evident that the effects of the interphase are inverted with respect to the previous case: stiff interphases lead to lower H_h while soft interphases lead to higher stress concentrations. On the other side, positive surface bulk moduli lead to lower H_h while negative ones lead to higher values of H_h.

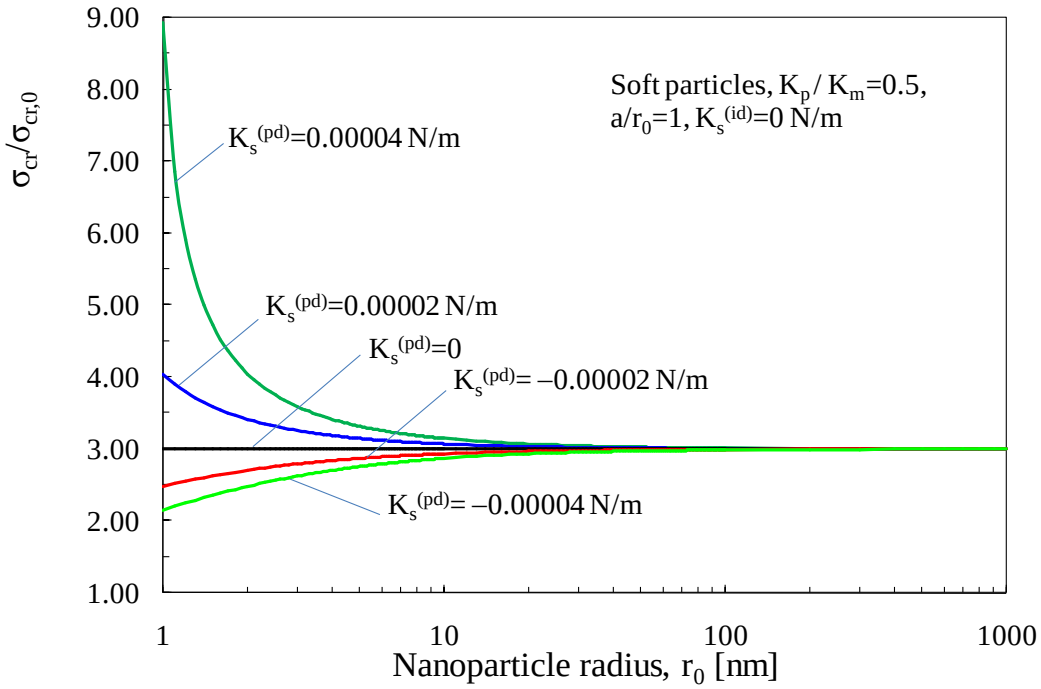

Figure 3.9. Effects of the surface elastic constant $K_S^{(pd)}$ on the normalized critical debonding stress in the absence of interphase effects. Soft particles (K_p/K_m=0.5), $K_S^{(id)}$=0.

Concerning the critical debonding stress, the analysis has revealed that interfacial effects are significant within the nanometer range (see Figures 3.6-11).

The effects of the interphase elastic properties, in the absence of surface stresses, is shown in Figure 3.6 (for rigid particles, K_p/K_m=20) and in Figure 3.7 (for soft particles, K_p/K_m=0.5). In these figures the debonding stress provided by Eq. (3.28) normalised to the limit value $\sigma_{cr,0}$, which neglects interfacial effects and assumes an infinitely rigid particle (see Eq. (3.34)), is plotted versus the particle radius. A 4 nm thick interphase is considered with different elastic properties. Figure 3.6 makes it evident that the interphase significantly affects the debonding stress, leading to higher or lower values for σ_{cr} depending whether the interphase is

stiffer (χ>1) or softer (χ<1) than the matrix. It is noteworthy, however, that these effects are non-negligible only at the nanometer size (for particle radii smaller than 70 nm). Similar conclusions can be drawn from Figure 3.7 where the behaviour of soft particles is analysed. In this case, the effect of the interphase is even more pronounced, leading to high variations of the critical debonding stress for interphase elastic properties only slightly different from those of the matrix. It is also important to note that, even neglecting the interphase effects (χ=1), Eq. (3.28) gives a debonding stress which is three times the one predicted by Chen's solution (2007, Eq. (3.34)). This suggests that debonding is more prone to occur for rigid particles than for soft ones, which are more likely to be interested by other damage mechanisms (e.g cavitation of rubber particles, for example).

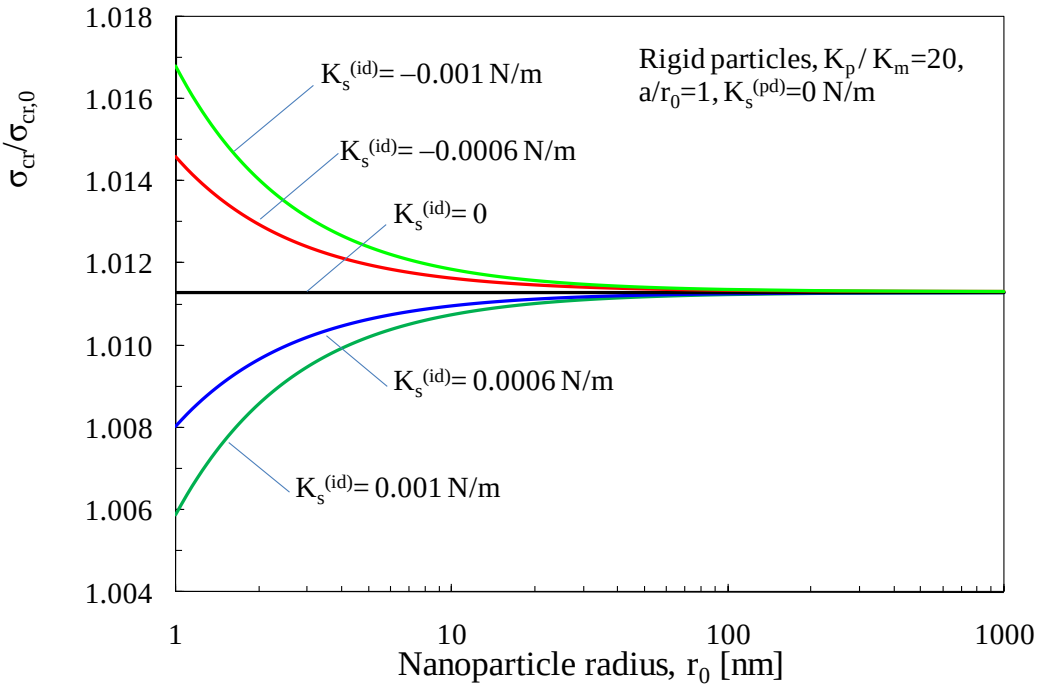

Figure 3.10. Effects of the surface elastic constant $K_S^{(id)}$ on the normalized critical debonding stress in the absence of interphase effects. Rigid particles (K_p/K_m=20), $K_S^{(pd)}$=0.

Figures 3.8-11 show the normalised debonding stress as a function of the particle radius for different surface elastic properties in the absence of an interphase layer. With reference to rigid particles, the effects of the post debonding surface bulk modulus, $K_s^{(pd)}$, on the normalised σ_{cr} is shown in Figure 3.8. It is evident that

surface stresses play a significant role (with a difference greater than 10%) only at the very nanoscale (r_0< 5 nm) leading to higher value of σ_{cr} with higher values of $K_s^{(pd)}$. Similar conclusions can be drawn from Figure 3.9 where the case of a soft nanoparticle is considered.

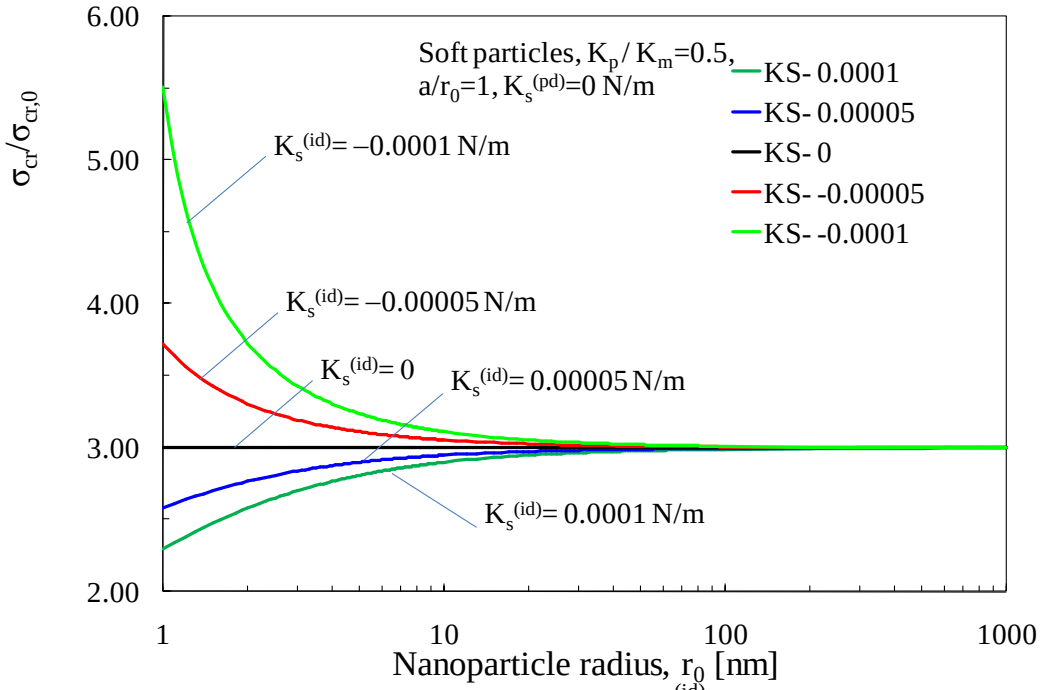

Figure 3.11. Effects of the surface elastic constant $K_S^{(id)}$ on the normalized critical debonding stress in the absence of interphase effects. Soft particles (K_p/K_m=0.5), $K_S^{(pd)}$=0.

Finally, the effects of the incipient surface bulk modulus, $K_s^{(id)}$, are shown in Figures 3.10 and 3.11, both for stiff and soft particles. As expected, for stiff particles, Figure 3.10, the role played by $K_s^{(id)}$ is almost negligible, the surface deformation being hindered by the rigidity of the particle. Conversely, for soft particles, $K_s^{(id)}$ does significantly affect the solution only within the very nanoscale (r_0<5 nm). As it can be noted in Figure 3.11, this time, higher $K_s^{(id)}$ values lead to lower debonding stresses.

3.10 Conclusions

A closed form expression for the nanoparticle detachment strength has been derived, using, contemporaneously, the Finite Fracture Mechanics approach and

the Surface Elasticity theory and considering all constituents as isotropic materials. The solution accounts either for the emergence of an interphase zone around the nanoparticle or for surface stresses on the nanoparticle periphery.

The analytical solution suggests that the range of nanoparticle radii where interfacial effects do affect the solution is limited to the nanometer scale. In more details, considering the interphase and surface elastic properties used in the analysis, it has been found that for rigid particles with radius between 5 nm and 70 nm (silica, alumina and other metal oxide nanoparticles) the prominent role is played by the interphase elastic properties. Surface elastic constants was found to have, instead, only a negligible effect (for the considered range of $K_s^{(id)}$ and $K_s^{(pd)}$ values).

Bibliography of chapter 3

Ahmadzadeh-Bakhshayesh, H., Gutkin, M.Yu. , Shodja, H.M. "Surface/interface effects on elastic behavior of a screw dislocation in an eccentric core–shell nanowire". *Int. J. Solids Struct*. 49, 1665–75, 2012.

Ajayan, P.M., Schadler, L.S., Braun, P.V. "Nanocomposite science and technology". Wiley-VCH, Weinheim, 2004.

Boutaleb, S., Zaıri, F., Mesbah, A.N., Abdelaziz, M., Gloaguen, J.M., Boukharouba. T. "Micromechanics-based modelling of stiffness and yield stress for silica/ polymer nanocomposites". *Int. J. Solids Struct*. 46, 1716–26, 2009.

Chen, J.K., Huang, Z.P., Zhu, J. "Size effect of particles on the damage dissipation in nanocomposites". *Compos. Sci. Technol*. 14, 2990–96, 2007.

Duan, H.L., Wang, J., Huang, Z.P., Karihaloo, B.L. "Size-dependent effective elastic constants of solids containing nano-inhomogeneities with interface stress". *J. Mech. Phys. Solids* 53, 1574–96, 2005.

Gent, A.N. "Detachment of an elastic matrix from a rigid spherical inclusion". *J. Mater. Sci.* 15, 2884-88, 1980.

Gill, S.P.A. "The effect of surface-stress on the concentration of stress at nanoscale surface flaws". *Int. J. Solids Struct*. 44, 7500–09, 2007.

Gurtin, M.E., Murdoch, A.I. "A continuum theory of elastic material surfaces". *Arch. Ration. Mech. An*. 57, 291-323, 1975.

Gurtin, M.E., Murdoch, A.I. "Surface stress in solids". *Int. J. Solids Struct*. 14, 431–40, 1978.

He, L.H., Li, Z.R. "Impact of surface stress on stress concentration". *Int. J. Solids Struct*. 43, 6208–6219, 2006.

Hui, T., Chen, Y.-H. "Surface Effect and Size Dependence on the Energy Release due to a Nano InAs Inclusion Expansion in a GaAs Matrix Material". *Adv. Studies Theor. Phys*. 4, 369 – 81, 2010.

Kushch, V.I., Mogilevskaya, S. G., Stolarski, H.K., Crouch, S. "Elastic interaction of spherical nanoinhomogeneities with Gurtin–Murdoch type interfaces". *J. Mech. Phys. Solids* 59, 1702–16, 2011.

Lauke, B., Schüller, T., Beckert, W. "Calculation of adhesion strength at the interface of a coated particle embedded within matrix under multiaxial load". *Comput. Mater. Sci.* 18, 362–380, 2000.

Lauke, B., Schüller, T. "Calculation of stress concentration caused by a coated particle in polymer matrix to determine adhesion strength at the interface". *Compos. Sci. Technol.* 62, 1965–78, 2002.

Lauke, B. "Determination of adhesion strength between a coated particle and polymer matrix". *Compos. Sci. Technol*. 66, 3153-60, 2006.

Leguillon, D. "Strength or toughness? A criterion for crack onset at a notch". *Eur. J. Mech. A-Solid*. 21, 61-72, 2002.

Li, Y., Waas, A. M., Arruda, E.M. "The effects of the interphase and strain gradients on the elasticity of layer by layer (LBL) polymer/clay nanocomposites". *Int. J. Solids Struct*. 48, 1044–53, 2011.

Müller, P., Saúl, A. "Elastic effects on surface physics". *Surf. Sci. Rep.* 54, 157-258, 2004.

Nicholson, D.W "On the detachment of a rigid inclusion from an elastic matrix". *J. Adhesion* 10, 255-60, 1979.

Odegard, G.M., Clancy, T.C., Gates, T.S. "Modeling of mechanical properties of nanoparticle/polymer composites". *Polymer* 46, 553-62, 2005.

Quaresimin, M., Salviato, M., Zappalorto, M. "Strategies for the assessment of nanocomposite mechanical properties". *Compos. part B-Eng*. 43, 2290–97, 2012.

Salviato, M., Zappalorto, M., Quaresimin, M. "Plastic Yielding Around Nanovoids". *Procedia Engineering* 10, 3325-30, 2011a.

Salviato, M., Zappalorto, M., Quaresimin, M. "The effect of surface stresses on the critical debonding stress around nanoparticles". *Int. J. Fract.* 172, 97-103, 2011b.

Salviato, M., Zappalorto, M., Quaresimin, M. "A multiscale analytical model to assess fracture toughness improvements due to plastic shear bands". Proceedings of the 15th European Conference on Composite Materials, ECCM 15, Venice, Italy, 24-28 June 2012.

Sevostianov, I., Kachanov, M. "Effect of interphase layers on the overall elastic and conductive properties of matrix composites. Applications to nanosize inclusion". *Int. J. Solids Struct*. 44, 1304–15, 2007.

Sharma, P., Ganti, S. "Interfacial elasticity corrections to size-dependent strain-state of embedded quantum dots". *Phys. Status Solidi* 234, R10–R12, 2002.

Sharma, P., Ganti, S., Bhate, N. "Effect of surfaces on the size-dependent elastic state of nano-inhomogeneities". *Appl. Phys. Lett*. 82, 535–537, 2003.

Thostenson, E.T., Li, C., Chou, T.W. "Nanocomposites in context". *Compos. Sci. Technol.* 65, 491–516, 2005.

Tian, L., Rajapakse, R.K.N.D. "Analytical solution for size-dependent elastic field of a nanoscale circular inhomogeneity". *J. Appl. Mech*. 74, 568-574, 2008.

VanderHart, D.L., Asano, A., Gilman, J.W. "Solid State NMR. Investigation of Paramagnetic Nylon-6 Clay Nanocomposites. 1. Crystallinity, Morphology, and the Direct Influence of Fe3+ on Nuclear Spins". *Chem. Mater*. 131, 3796–809, 2001.

Yu, S., Yang, S., Cho, M. "Multi-scale modeling of cross-linked epoxy nanocomposites". *Polymer* 50, 945-52, 2009.

Zappalorto, M., Salviato, M., Quaresimin, M. "Influence of the interphase zone on the nanoparticle debonding stress". *Compos. Sci. Technol.* 72, 49-55, 2011a.

Zappalorto, M., Salviato, M., Quaresimin, M. "Assessment of Debonding-Induced Toughening in Nanocomposites". *Procedia Engineering* 10, 2982–87, 2011b.

Zappalorto, M., Salviato, M., Quaresimin, M. "Stress distributions around rigid nanoparticles". *Int. J. Fract.* 176, 105–112, 2012a.

Zappalorto, M., Salviato, M., Quaresimin, M. "A multiscale model to describe nanocomposite fracture toughness enhancement by the plastic yielding of nanovoids". *Compos. Sci. Technol*. 72, 1683-1691, 2012b.

Zax, D.B., Yang, D.K., Santos, R.A., Hegemann, H., Giannelis, E.P., Manias, E. "Dynamical heterogeneity in nanoconfined polystyrene chains". *J. Chem. Phys*. 112, 2945–51, 2000.

4

A multiscale and multimechanism model for the fracture toughness of nanoparticle filled thermosetting polymers

4.1 Introduction

Nanotechnology has recently emerged as a suitable tool to optimise material properties by designing the internal structure of materials at the very nanoscale level and assisting in the achievement of desirable combinations of physical and mechanical properties (Ajayan et al., 2004, Thostenson et al., 2005). However to fully exploit the potential benefits of nanomodification, appropriate models able to soundly predict the macroscale mechanical properties from material structure need to be developed.

With the aim to explain the significant ameliorations of polymer toughness obtainable with low nanofiller contents and considering the importance of the several damaging mechanisms that might take place at the nanoscale, some authors have recently suggested to use a "multi-mechanism" modelling strategy (Lauke, 2008, Williams, 2010, Hsieh et al, 2010, Hsieh et al. 2011, Quaresimin et al. ,2012).

However, modelling the effects of nanoscale damaging mechanisms on macroscale properties is far from easy, essentially because at that length scale classical micromechanics is no longer valid as is. Instead, the adoption of a multiscale strategy is necessary in order to decompose, physically and mathematically, the nanocomposite material in each individual scale of interest.

In the recent literature several authors dealt with the analysis of toughening mechanisms in nanocomposites.

Chen et al. (Chen et al, 2007) carried out a theoretical study on the amount of energy dissipated by interfacial debonding of nanoparticles and provided a close form solution for the critical detachment stress. The size distribution of particles and the debonding probability was included into the analytical formulation using a logarithmic normal distribution and the Weibull distribution function.

Some year later, the present author and coworkers refined the analysis carried out in studying the effects of a small interphase zone embedding the nanoparticle (Zappalorto et al., 2011a) and of surface elastic constants (Salviato et al., 2011a) on the critical debonding stress. In both cases, the range of the nanoparticle radii where those effects are significant was proved to be limited to the nanoscale (Zappalorto et al., 2011a, Salviato et al., 2011a).

The energy dissipation phenomena due to particle debonding, voiding and subsequent yielding of the polymer has been analysed by Lauke (Lauke 2008) who assumed particles to have a mean diameter and used a simple geometrical model of particle–particle interaction in a regular particle arrangement. By further applying a critical stress criterion Lauke found a dissipation zone which was independent of the particle diameter and justified the increase of crack resistance with decreasing particle size by the increase in the volume specific debonding energy (Lauke 2008).

Williams (Williams, 2010) re-analysed in detail the toughening of particle filled polymers assuming that plastic void growth around debonded or cavitated particles is the dominant mechanism for energy dissipation. He assumed a tri-axial state of stress around the spherical particle and supposed the debonding and cavitation conditions to be controlled by either surface energy or the cohesive energy of the particle. Williams (Williams, 2010) further noted that, even if the debonding process is generally considered to absorb little energy, it is essential to reduce the constraint at the crack tip and, in turn, to allow the epoxy polymer to deform plastically via a void-growth mechanism. A similar result was found also by the present authors (Zappalorto et al., 2011b, Zappalorto et al., 2012).

Hsieh et al. (Hsieh et al., 2010, Hsieh et al., 2011) studied the fracture toughness improvements resulting from nanomodification of epoxy resins with silica nanoparticles. Based on experimental observations, they identified two dominant mechanisms responsible of toughening improvements, namely localised shear banding of the polymer and particle debonding followed by subsequent plastic void growth. They finally adapted a previous model due to Huang and Kinloch (Huang and Kinloch, 1992) for rubber modified epoxy polymers to predict the fracture toughness improvements resulting from nanomodification.

The investigations in (Lauke, 2008, Hsieh et al., 2010, Hsieh et al., 2011, Quaresimin et al., 2012) support the idea, recently formulated also by the present authors (Quaresimin et al., 2012), that the most effective approach to predict the nanocomposite toughness is a "multi-mechanism" modelling strategy, in which the contribution of each mechanism is appropriately determined and weighted according to the specific case (accounting for the type, the morphology and the functionalisation of the nanofiller). Accordingly the nanocomposite fracture toughness can be written as $G_{Ic} = G_{Im} + \sum_i \Delta G_i$, where G_{Im} is the fracture toughness of the unloaded matrix and ΔG_i is the fracture toughness improvement due to the i-th damaging mechanism.

Great efforts have been recently devoted by the present authors to develop analytical formulations for ΔG_i contributions due to the most relevant toughening mechanisms occurring in nanoparticle filled polymer resins. Among these, debonding of nanoparticles followed by plastic yielding of nanovoids (Salviato et al., 2011b, Zappalorto et al., 2012) and plastic shear banding of the polymer (Salviato et al., in press) have been analysed . The major novelty of these recent works, with respect to those in the previous literature dealing with the same subject (Lauke, 2008, Williams, 2010, Hsieh et al., 2010, Hsieh et al., 2011), lays on the fact that the effect of an interphase zone surrounding the nanoparticle, characterised by mechanical properties different from those of the constituents, is explicitly considered.

The aim of the present paper is to integrate the models developed in (Zappalorto et al., 2012, Salviato et al., in press) in order to provide a unique multiscale

analytical procedure useful to evaluate the overall fracture toughness of a polymer/nanoparticle nanocomposite. After a brief introduction on the basic concepts and the relevant length scales adopted in the analysis, the models developed for each damaging mechanism are introduced, highlighting the most important parameters. All models are finally integrated and comparison is carried out between the predicted nanocomposite fracture toughness and some experimental data taken from the literature.

4.2 Description of the hierarchical multiscale structure adopted for the analysis

4.2.1 General concepts

A successful engineering application of nanocomposites requires models capable of accounting for their inherent hierarchical structure which encompasses the nano and the macro length-scales. An effective modelling should take into account the characteristic phenomena of each length-scale and bridge their effects from the smaller scale to the macroscale (Quaresimin et al., 2012). For this reason the present analysis deals with three different length scales, macro-, micro- and nano-, each of them being characterised by mechanical quantities which are, by a conceptual point of view, different. Accordingly, we will use terms like “macroscale stress” and “microscale stress”. Thus, in order to avoid misunderstandings it is worth giving the correct definitions for the quantities used at each scale, as well as to briefly discuss the link between them.

The macro-scale system and the macro-scale quantities: the macroscale system is thought of as an amount of material over which all the mechanical quantities (such as stresses and strains) are regarded as averaged values (Bishop and Hill, 1951) and are supposed to be representative of the overall material behaviour. Within this scale, it is assumed that the material is homogeneously and continuously distributed over its volume "*so that the smallest element cut from the body possesses the same specific physical properties as the body*" (Timoshenko and Goodier, 1970). So long as the geometrical dimensions defining the form of the body are very large in comparison with the dimensions relevant at the smaller

scales (such as the size of a single nanofiller), the assumption of homogeneity can be used with great accuracy. In addition, if the nanofiller is randomly oriented and uniformly distributed, the material can also be treated as isotropic.

The macroscale system accounts for the loading conditions and the presence of material defects (like macroscopic cracks) and all the governing equations are dependent only on macroscopic averaged quantities.

The micro-scale system and the micro-scale quantities: the micro-scale system is thought of as being sufficiently small to be regarded, mathematically, as an infinitesimal volume of the macro-scale one. At the same time it has to be, by definition, large enough to be statistically representative of the properties of the material system. The latter hypothesis is supposed to hold valid as far as the nanofiller is uniformly distributed and dispersed over the volume. Within this scale, all the mechanical properties are supposed to be pointwise values (Bishop and Hill, 1951). The micro-scale system is often regarded as a RVE (*Representative Volume Element*).

The nano-scale system: the nanoscale system represents a single unit cell of those compounding the micro-scale system; it accounts for the material morphology (such as nanofiller type and size).

4.2.2 Relationship between stresses and strains in the different systems

Let consider a general boundary value problem in statics; the macro-scale stress or strain, σ or ε, can be regarded as a general function of material coordinates:

$$\{\sigma, \varepsilon\} = \{f_1(X_1, X_2, X_3),\ \ f_2(X_1, X_2, X_3)\} \tag{4.1}$$

According to (Bishop and Hill, 1951, Hutchinson, 1964, Gurson, 1977), functions f_i, which are supposed to satisfy the governing equations of statics at the macroscale, can be regarded as an average value over a RVE:

$$\{\sigma, \varepsilon\} = \{\overline{\sigma}, \overline{\varepsilon}\} = \left\{ \frac{1}{V}\int_V \hat{\sigma}\, dV,\ \frac{1}{V}\int_V \hat{\varepsilon}\, dV \right\} \tag{4.2}$$

where $\hat{\sigma}$ and $\hat{\varepsilon}$ are the micro-scale stress and strain distributions and V is the volume of the RVE. In principle, there might exist an infinite number of $\{\hat{\sigma}, \hat{\varepsilon}\}$ distributions over the V volume resulting in the same average value, but only one corresponds to the particular boundary value one addresses to. The solution comes

from the governing equation and the boundary conditions for this scale which, according to conventional micromechanics, can be expressed, without any loss of generality, within the frame of continuum mechanics.

However, within a multiscale approach to the problem, the knowledge of the correct microscale distributions within the RVE, $\{\hat{\sigma}, \hat{\varepsilon}\}$, is not strictly necessary. Indeed, the Mori-Tanaka theorem allows to disregard of the actual microscale fields and to approximate the stress or the strain acting on the boundary of a single nano-inhomogeneity (nanoscale). This can be carried out taking advantage of the Global Concentration Tensors of Eshelby diluite solution and of the mean value for the stress/strain fields over the RVE which, in turn, equates the macroscale one (Figure 4.1).

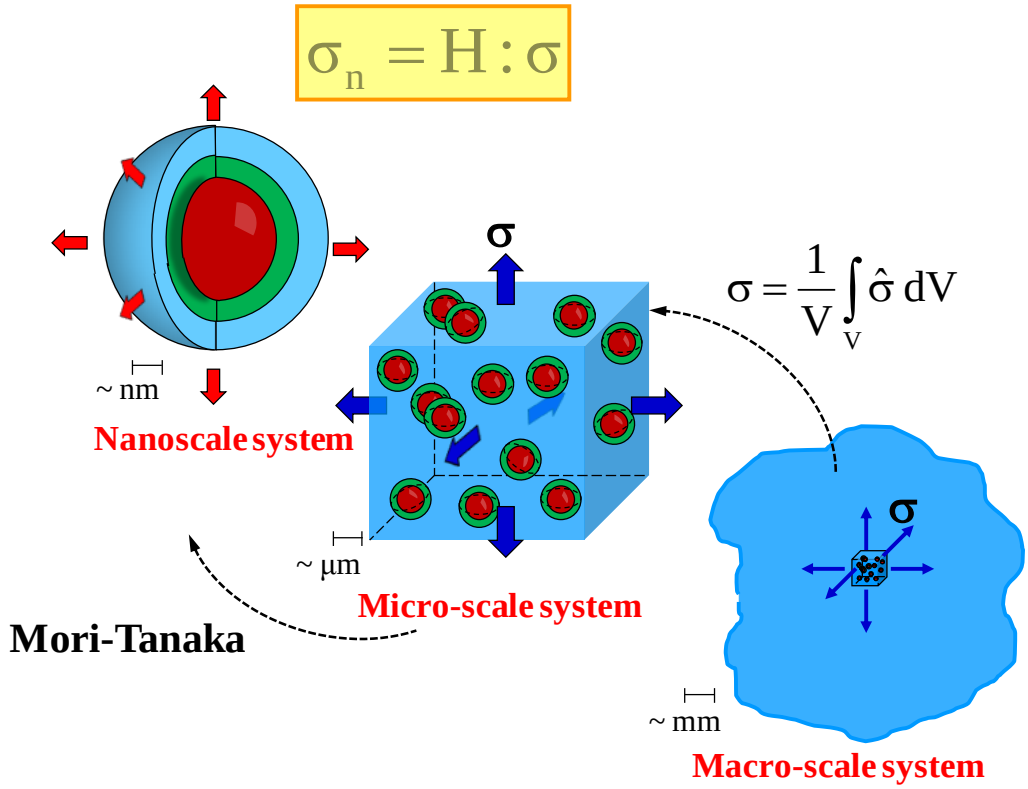

Figure 4.1. Multiscale strategy and systems of interest.

4.3 Modelling of the fracture toughness enhancements due to the different damaging mechanisms

It is acknowledged in the literature that the two dominant mechanisms responsible of toughening improvements for polymers reinforced by rigid nanoparticles (such as silica or alumina nanoparticles) are the localised shear banding of the polymer

and particle debonding followed by subsequent plastic void growth (Hsieh et al., 2010, Hsieh et al., 2011, Zappalorto et al., 2012a, Salviato et al., in press).

In the following sessions close form expressions useful to evaluate the fracture toughness improvements, ΔG_i, due to the above mentioned mechanisms are given. Finally, in section 3.4 a unified expression for the overall nanocomposite fracture toughness is derived.

4.3.1 Multiscale strategy to analyse debonding of nanoparticles and subsequent plastic yielding

In this work particular attention is paid to the interphase zone surrounding the nanoparticle, which might be characterised by chemical and physical properties different from those of the constituents.

Indeed, different from traditional microsized composites, in nanoscale materials and structures, the surface effects become significant (Ajayan et al., 2004, Wichmann et al., 2006, Tian and Rajapakse, 2007), due to the high surface/volume ratio and for this reason the amount of interphase volume may represent a large part of the matrix.

Recently, Zappalorto *et al.* (Zappalorto et al., 2011a) developed a closed form expression for the critical debonding stress accounting for the existence of an interphase zone of properties different from those of the matrix. Since different functionalizers lead to different elastic properties of the interphase, this solution shows that the debonding stress is affected by the surface treatment depending also on the interphase radius to the nanoparticle radius ratio, $\mathbf{a/r_0}$.

Unfortunately, the data available so far in the literature about the interphase zone are not enough to precisely formulate the law of variation of its properties across the thickness, as well as its size (Sevostianov and Kachanov, 2007). Thus, according to (Odegard et al., 2005, Yu et al., 2009, Zappalorto et al., 2011a), in this work we assume that a through-the-thickness average is representative of the overall property distribution within the interphase Consequently, the interphase is supposed to be homogeneous and isotropic.

In the light of this, the system under investigation at the nanoscale, shown in Figure 4.2a and b, is constituted by:

- a spherical nanoparticle of radius $\boldsymbol{r_0}$, which creates a nanovoid of the same diameter;
- a shell-shaped interphase of external radius **a** and uniform properties;
- a matrix of radius ***b*** loaded by a hydrostatic stress σ_h, b being much greater than a and r_0;

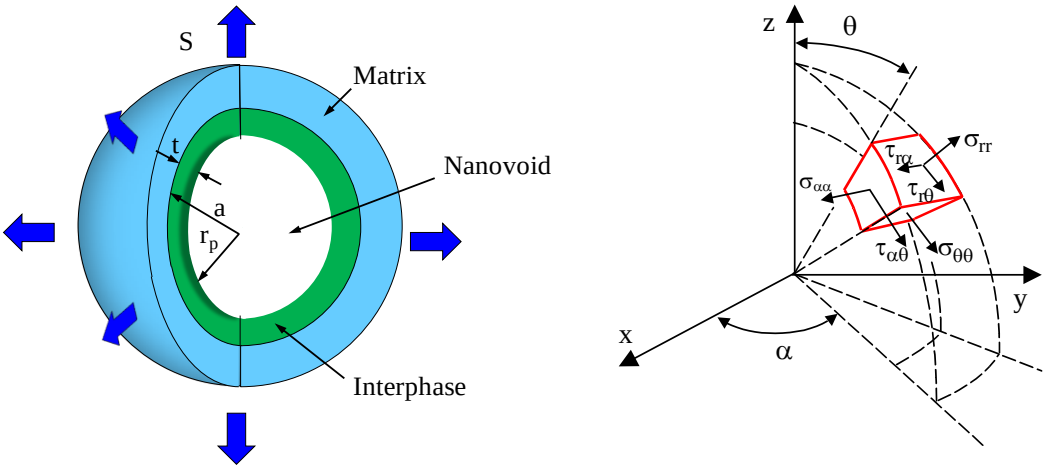

Figure 4.2. Description of the system under analysis at the nanoscale (a). Spherical coordinate system and stress components used to describe the stress field around nanovoids (b).

The properties required by the analysis can be computed by means of numerical simulations carried out within the frame of MD as done for example by Odergard *et al.* (Odegard et al., 2005) and Yu *et al.* (Yu et al., 2009), which provide, as outputs, the radial extension of the interphase as well as the elastic properties averaged through the thickness. Alternatively, for a specific system, they could be fitted *a posteriori* on the basis of some experimental results.

4.3.2 Application of the multiscale strategy

Let consider a macrosized crack in a nano-modified matrix (see figure 4.3). In agreement with (Rice and Tracey, 1969, McMeeking and Evans, 1982, Williams, 2010), it can be assumed that only the hydrostatic stress component of the crack tip stress field is of major importance for the present analysis. This choice is justified by the spherical symmetry of the problem at the nanoscale and the high constraint effects arising close the crack tip. Indeed, Rice and Tracey (Rice and

Tracey, 1969) showed that, when the mean normal stress is large enough, the volume changing contribution to void growth is much larger than the shape changing part, so that growth is basically spherical.

Under the hypothesis of plane strain conditions such a component turns to be:

$$\sigma_h = \frac{\sigma_x + \sigma_y + \sigma_z}{3} = \frac{2(1+\nu_o)K_I}{3\sqrt{2\pi\rho}}\cos\frac{\phi}{2} \tag{4.3}$$

where K_I and ν_o are the Stress Intensity Factor of the macroscopic stress fields and the Poisson's ratio of the nanocomposite, respectively.

Within a multiscale approach to the problem, according to the concepts discussed in sections 4.2.1 and 4.2.2, the macroscale stress, σ_h, can be regarded as the average of the microscale stresses over a RVE (see again figure 4.2). The bridge with the nanoscale can be established by means of the Mori-Tanaka approach, so that the hydrostatic stress component around the nanoparticle can be approximated by:

$$\sigma_n(\rho,\phi) = \frac{\sigma_h}{C_h} = \frac{1}{C_h}\frac{2(1+\nu_o)K_I}{3\sqrt{2\pi\rho}}\cos\frac{\phi}{2} \tag{4.4}$$

where C_h is the reciprocal of the hydrostatic part of the global stress concentration tensor (Johnsen et al., 2007):

$$C_h = \frac{K_m}{K_p}\zeta \tag{4.5}$$

with

$$\begin{aligned}\zeta = {} & \frac{(3K_a+4G_m)(3K_p+4G_a)}{(3K_a+4G_a)(3K_m+4G_m)} + 12\frac{(K_a-K_p)(G_m-G_a)}{(3K_a+4G_a)(3K_m+4G_m)}\left(\frac{r_0}{a}\right)^3 + \\ & + 4\frac{G_m}{K_m}\frac{3K_m+4G_a}{3K_m+4G_m}\frac{K_p-K_a}{3K_a+4G_a}\left(\frac{r_0}{b}\right)^3 + \\ & + 4\frac{G_m}{K_m}\frac{3K_p+4G_a}{3K_m+4G_m}\frac{K_a-K_m}{3K_m+4G_m}\left(\frac{a}{b}\right)^3\end{aligned} \tag{4.6}$$

Here K_m, K_a, K_p are the bulk moduli of the matrix, the interphase and the nanoparticle, and G_m, G_a, G_p are the shear elastic moduli of the matrix, the interphase and the nanoparticle. Further accounting for the conditions b>>a, r_0 and K_p>>K_m, K_a, C_h simplifies:

$$C_h = \frac{\xi + 4 - 4\cdot(1-\chi)(r_0/a)^3}{(\xi+4\chi)\left(\frac{3(1-\nu_m)}{1+\nu_m}\right)} = C_{h,0}\frac{\xi + 4 - 4\cdot(1-\chi)(r_0/a)^3}{(\xi+4\chi)} \tag{4.7}$$

where $\chi = G_a/G_m$, $\xi = 3K_a/G_m$ and $C_{h,0}$ is the reciprocal of the hydrostatic part of the global stress concentration tensor evaluated by neglecting the interphase (χ=1).

Debonding at a nanoparticle takes place whenever the hydrostatic stress component around the nanoparticle reaches a critical value, σ_{cr}. Then, the extension of the debonding region (DBR), meant as the region around the crack tip confining all the debonded particles, can be assessed by simply equating σ_n, Eq. (4.2), with the critical debonding stress σ_{cr}:

$$\sigma_{cr} = \sigma_n(\rho,\phi) = \frac{1}{C_h}\times\frac{2(1+\nu_o)K_I}{3\sqrt{2\pi\rho}}\cos\frac{\phi}{2} \tag{4.8}$$

In Eq. (4.8) σ_{cr} can be estimated by (Zappalorto et al., 2011a):

$$\sigma_{cr} \cong \sqrt{\frac{4\gamma}{r_0}\frac{E_m}{1+\nu_m}}\sqrt{\frac{\chi(4+\xi)-\xi(\chi-1)(r_0/a)^3}{4+\xi+4(\chi-1)(r_0/a)^3}} \tag{4.9a,b}$$

$$\sigma_{cr} = \sigma_{cr,0}\sqrt{\frac{\chi(4+\xi)-\xi(\chi-1)(r_0/a)^3}{4+\xi+4(\chi-1)(r_0/a)^3}}$$

where $\sigma_{cr,0}$ is the debonding stress evaluated by neglecting the interphase zone (Chen et al., 2007).

Solving Eq. (4.8) by ρ results in:

$$\rho^*(\phi) = \frac{1}{(C_h)^2}\times\frac{2(1+\nu_o)^2K_I^2}{9\pi\sigma_{cr}^2}\cos^2\left(\frac{\phi}{2}\right) \tag{4.10a}$$

The amount of nanoparticles subjected to debonding, N_p, as well as the total surface subjected to debonding, S_p can then be calculated as:

$$N_p = \int_V \frac{f_{p0}}{4/3\pi r_0^3}dV = \frac{9}{32}\frac{f_{p0}}{r_0^3}\left[\frac{1}{(C_h)^2}\cdot\frac{2(1+\nu)^2K_I^2}{9\pi\sigma_{cr}^2}\right]^2 \tag{4.11a-b}$$

$$S_p = N_p\times 4\pi r_0^2 = \frac{9}{8}\pi\times f_{p0}\times\frac{A^2}{r_0}$$

Eq. (4.11a) can be also re-written in the following normalised form:

$$\frac{N_p}{N_{p,0}} = \left(\frac{C_{h,0}\sigma_{cr,0}}{C_h\sigma_{cr}} \right)^4 \tag{4.11c}$$

where $N_{p,0}$ is the the amount of nanoparticles subjected to debonding when neglecting the interphase.

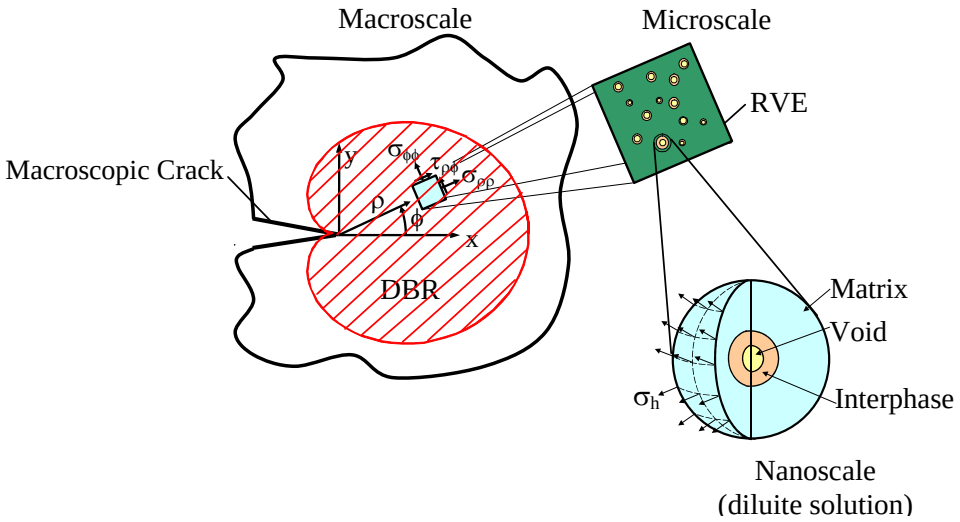

Figure 4.3. Description of the multiscale system under analysis.

In this work, the DBR is thought of as the active process zone. Indeed, it is assumed that the crack-induced stress field causes debonding of nanoparticles, resulting in a distribution of nanovoids which later undergo plastic yielding; both debonding of nanoparticles and the subsequent plastic yielding of nanovoids represent mechanisms acting for energy dissipation at the nanoscale.

Denoting with U_i the energy produced at the nanoscale for the single mechanism considered, according to the adopted multiscale system, the strain energy density in a RVE (microscale) can be calculated as:

$$u_i = U_i \times \frac{3f_{p0}}{4\pi r_0^3} \tag{4.12}$$

where f_{p0} is the volume fraction of the nanovoids (which coincides, by hypothesis, with the initial volume fraction of nanoparticles). Finally, the fracture toughness enhancement due to the considered mechanism can be determined, according to (Huang and Kinloch, 1992, Freund and Hutchinson, 1985, Evans et al.1985, Lauke, 2008), as:

$$\Delta G_i = 2\times\int_0^{\rho^*(\phi=\pi/2)} u_i \; d\rho \tag{4.13}$$

The problem of determining the overall fracture toughness enhancement is, in this way, reconverted into finding the energy produced at the nanoscale by debonding and plastic yielding of a nanovoid, and thus requires a stress and strain analysis at such scale level.

4.3.3 Modelling of fracture enhancement due particle debonding

The energy produced at the nanoscale by debonding of a single nanoparticle is:

$$U_{db} = \gamma_{db}\times 4\pi r_0^2 \tag{4.14}$$

where γ_{db} is the interfacial fracture energy. Accordingly, the strain energy density in a RVE (microscale) can be calculated as:

$$u_{db} = U_{db}\times\frac{3f_{p0}}{4\pi r_0^3} = \gamma_{db}\times 4\pi r_0^2\times\frac{3f_{p0}}{4\pi r_0^3} = 3\frac{\gamma_{db}}{r_0}f_{p0} \tag{4.15}$$

Finally, the macroscale increment in terms of Strain Energy Release Rate can be estimated by Eq. (4.13) and turns out to be:

$$\begin{aligned}\Delta G_{db} &= 2\times\int_0^{\rho^*(\phi=\pi/2)} u_{db}d\rho = 3\frac{\gamma_{db}}{r_0}f_{p0}A = \\ &= 3\times\frac{\gamma_{db}}{r_0}\times\frac{1}{(C_h)^2}\times\frac{2(1+\nu_o)^2K_I^2}{9\pi\sigma_{cr}^2}\times f_{p0}\end{aligned} \tag{4.16}$$

where σ_{cr} is given by Eq. (4.9).

By further noting that $G = K_I^2/E_o\times\left(1-\nu_o^{\,2}\right)$, the toughness improvement due to debonding becomes:

$$\Delta G_{db} = \left\{\frac{2}{3\pi}\times\frac{\gamma_{db}}{r_0}\times\frac{1+\nu_o}{1-\nu_o}\times\frac{E_o}{\sigma_{cr}^2(C_h)^2}\right\}\times f_{p0}\times G_{Ic} = f_{p0}\times\psi_{db}\times G_{Ic} \tag{4.17}$$

where now G_{Ic} is the fracture toughness of the nanocomposite and ψ_{db} is the term in curly brackets.

Since, according to (Huang and Kinloch, 1992, Lauke, 2008), the overall fracture toughness can be written as:

$$G_{Ic} = G_{Im} + \Delta G_{db} \tag{4.18}$$

being G_m the matrix fracture toughness, Eq. (4.17) can also be re-written as:

$$\frac{\Delta G_{db}}{G_{Im}} = \frac{f_{p0} \times \psi_{db}}{1 - f_{p0} \times \psi_{db}} \tag{4.19}$$

4.3.4 Plastic yielding of nanovoids

Elastic plastic analysis

Displacement and stress fields are determined here within the frame of the Cauchy Continuum Theory, regarding constituents as isotropic materials, in agreement with some recent works about nanocomposites (Chen et al., 2007, Sevostianov and Kachanov, 2007, Boutaleb et al., 2009).

It is assumed that debonding of nanoparticles takes place and creates a number of nanovoids of the same diameter of the nanoparticles. Whenever the stress field around a nanovoid is high enough to cause local yielding, denoting by R_P the extension of the plastic zone, two different conditions are possible:

- the entire interphase and a part of the matrix are yielded (R_P>a);
- only a part of the interphase is yielded (R_P<a).

To simplify the mathematical treatise to the problem, the first condition is considered. Moreover, it is assumed that the crack induced macro-scale stress, σ_h, does not vary within the DBR but assumes a constant value equal to its mean value:

$$\sigma_h = \overline{\sigma_h} = \frac{1}{\rho^*(\phi = \pi/2)} \times \int_0^{\rho^*(\phi=\pi/2)} \sigma_h \, d\rho = 2 \times C_h \sigma_{cr} \tag{4.20}$$

where the averaging path ($\phi=\pi/2$) matches that suggested in Eq. (4.13).

A strain hardening behaviour for the interphase and the matrix

When detailed information about the elastic-plastic response of the matrix and the interphase, the materials can be thought of as obeying to an elastic-power hardening plastic law.

Thanks to the spherical symmetry of the problem, equilibrium and compatibility equations can be written as:

$$\frac{\partial \sigma_{rr}}{\partial r} + 2 \times \frac{\sigma_{rr} - \sigma_{\theta\theta}}{r} = 0 \tag{4.21}$$

$$\frac{\partial \varepsilon_{\theta\theta}}{\partial r} = \frac{\varepsilon_{rr} - \varepsilon_{\theta\theta}}{r} \tag{4.22}$$

The hardening behaviour of materials can be treated in a simplified way by considering an elastic response up to the yield limit σ_Y and thereafter a power law for stresses and strains in the plastic region (Chakrabarty, 2006, Lazzarin and Zappalorto, 2008):

$$\begin{cases} \bar{\varepsilon}_P = E \cdot \bar{\sigma}_P & \text{if} \quad \bar{\sigma}_P \le \sigma_Y \\ \dfrac{\bar{\varepsilon}_P}{\varepsilon_Y} = \left(\dfrac{\bar{\sigma}_P}{\sigma_Y} \right)^n & \text{if} \quad \bar{\sigma}_P \ge \sigma_Y \end{cases} \tag{4.23}$$

where $\bar{\sigma}_p$ and $\bar{\varepsilon}_p$ are the equivalent stress and the equivalent strain, respectively, while $\varepsilon_Y = \sigma_Y / E$.

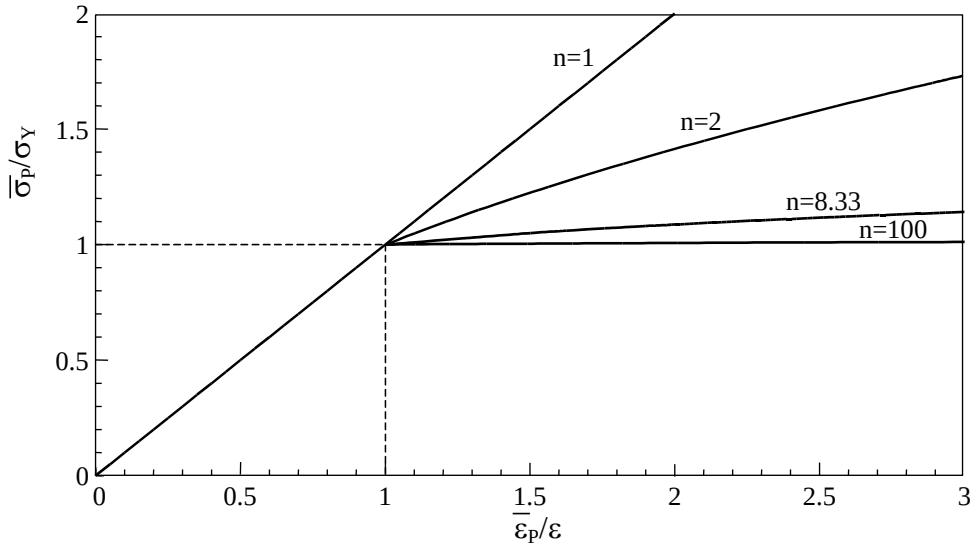

Figure 4.4. Simplified stress-strain law for power-hardening material; with hardening exponent *n*.

Eq. (4.23) is represented in Figure 4.4 for different hardening exponents, n.

Consider the coordinate system shown in figure 4.1b. Hencky's equation links the plastic components of the strains to the plastic components of the stresses (Chakrabarty, 2006) and for the law given by Eq. (4.23) turns out to be:

$$\varepsilon_{ij}^{(pl)} = \lambda s_{ij}^{(pl)} = \frac{3}{2} \frac{\bar{\varepsilon}_P}{\bar{\sigma}_P} s_{ij}^{(pl)} = \frac{3}{2} \frac{\varepsilon_Y}{\sigma_Y} \left(\frac{\bar{\sigma}_P}{\sigma_Y} \right)^{n-1} s_{ij}^{(pl)} \tag{4.24}$$

where:

$$s_{ij}^{(pl)} = \sigma_{ij} - \sigma_h = \sigma_{ij} - \frac{\sigma_{rr} - 2\sigma_{\theta\theta}}{3} \tag{4.25}$$

is the deviatoric component of stresses. Thanks to the Tresca yielding condition the equivalent plastic stress can be evaluated as:

$$\overline{\sigma}_P = \sigma_{\theta\theta} - \sigma_{rr} \tag{4.26}$$

Accordingly, the hydrostatic stress component of the plastic stress tensor turns out to be:

$$\sigma_h = \frac{\sigma_{rr} - 2\sigma_{\theta\theta}}{3} = \sigma_{rr}^{(pl)} + \frac{2}{3}\overline{\sigma}_P = \sigma_{\theta\theta}^{(pl)} - \frac{1}{3}\overline{\sigma}_P \tag{4.27}$$

Then

$$s_{rr}^{(pl)} = \sigma_{rr}^{(pl)} - \sigma_h = -\frac{2}{3}\overline{\sigma}_P \qquad s_{\theta\theta}^{(pl)} = \sigma_{\theta\theta}^{(pl)} - \sigma_h = \frac{1}{3}\overline{\sigma}_P \tag{4.28a-b}$$

Finally, the plastic strain components are:

$$\varepsilon_{rr}^{(pl)} = \lambda s_{rr}^{(pl)} = -\varepsilon_Y\left(\frac{\overline{\sigma}_P}{\sigma_Y}\right)^n \qquad \varepsilon_{\theta\theta}^{(pl)} = \lambda s_{\theta\theta}^{(pl)} = \frac{1}{2}\varepsilon_Y\left(\frac{\overline{\sigma}_P}{\sigma_Y}\right)^n \tag{4.29a-b}$$

Substituting Eqs. (4.29) into the compatibility equation, Eq. (4.22), results in:

$$n\frac{\partial\overline{\sigma}_P}{\partial r} + 3\frac{\overline{\sigma}_P}{r} = 0 \tag{4.30}$$

The general solution of Eq. (4.30) can be sought in the form:

$$\overline{\sigma}_P = Cr^{-3/n} \tag{4.31}$$

At the same time, substituting Eq. (4.31) and Eq. (4.32) into the equilibrium equation results in:

$$\sigma_{rr}^{(pl)} = \tilde{C} - \frac{2}{3}C\,n\,r^{-3/n} \tag{4.32}$$

Then the solutions for stress and displacement fields in the plastic zone are:

$$\sigma_{rr}^{(pl),a} = C_2 - \frac{2}{3}C_1\,n_a\,r^{-3/n_a} \qquad \overline{\sigma}_P^a = C_1 r^{-3/n_a} \qquad u^{(pl),a} = \frac{1}{2}\frac{\varepsilon_{Ya}}{r^2}\left(\frac{C_1}{\sigma_{Ya}}\right)^{n_a} \tag{4.33}$$

when r<a and

$$\sigma_{rr}^{(pl),m} = C_4 - \frac{2}{3}C_3\,n_m\,r^{-3/n_m} \quad \overline{\sigma}_P^m = C_3 r^{-3/n_m} \qquad u^{(pl),m} = \frac{1}{2}\frac{\varepsilon_{Ym}}{r^2}\left(\frac{C_3}{\sigma_{Ym}}\right)^{n_m} \tag{4.35}$$

when $a<r<R_P$.

Outside the plastic core the behaviour is linear elastic and stress and displacement fields can be described as (Zappalorto et al., 2011a):

$$\sigma_{rr}^{(el)} = E_m\left[\frac{A}{1-2\nu_m} - 2\frac{B}{r^3(1+\nu_m)}\right]$$
$$\sigma_{\theta\theta}^{(el)} = E_m\left[\frac{A}{1-2\nu_m} + \frac{B}{r^3(1+\nu_m)}\right] \quad (4.35)$$
$$u^{(el)} = A\ r + \frac{B}{r^2}$$

where E_m and ν_m are the matrix Young modulus and Poisson's ratio.

Boundary conditions to the problem can be written as follows:

$$\sigma_{rr}^{(pl),a}(r = r_0) = 0$$
$$\sigma_{rr}^{(pl),a}(r = a) = \sigma_{rr}^{(pl),m}(r = a)$$
$$u^{(pl),a}(r = a) = u^{(pl),m}(r = a)$$
$$\overline{\sigma}_P(r = R_P) = \sigma_{Ym} \quad (4.36a\text{-}g)$$
$$\sigma_{rr}^{(el),m}(r = b) = \sigma_h$$
$$\sigma_{\theta\theta}^{(el),m}(r = R_P) - \sigma_{rr}^{(el),m}(r = R_P) = \sigma_{Ym}$$
$$\sigma_{rr}^{(pl),m}(r = R_P) = \sigma_{rr}^{(el),m}(r = R_P)$$

The solutions of the first six equations of the previous system are:

$$C_1 = R_P^{3/n_a}\sigma_{Ya}\left(\frac{\varepsilon_{Ym}}{\varepsilon_{Ya}}\right)^{\frac{1}{n_a}}$$
$$C_2 = \frac{2}{3}n_a\sigma_{Ya}\left(\frac{R_p}{r_0}\right)^{3/n_a}\left(\frac{\varepsilon_{Ym}}{\varepsilon_{Ya}}\right)^{\frac{1}{n_a}}$$
$$C_3 = R_P^{3/n_m}\sigma_{Ym}$$
$$C_4 = \frac{2}{3}\left\{n_a\sigma_{Ya}\left(\frac{R_p}{a}\right)^{3/n_a}\left(\frac{\varepsilon_{Ym}}{\varepsilon_{Ya}}\right)^{\frac{1}{n_a}}\left[\left(\frac{a}{r_0}\right)^{3/n_a} - 1\right] + n_m\sigma_{Ym}\left(\frac{R_p}{a}\right)^{3/n_m}\right\} \quad (4.37a\text{-}f)$$
$$A \cong \frac{\sigma_h}{E_m}(1-2\nu_m) = \frac{\sigma_h}{3K_m}$$
$$B = \frac{\sigma_{Ym}R_p{}^3(1+\nu_m)}{3E_m}$$

Instead, the last equation can be re-written as:

$$\sigma_h - \frac{2}{3}\sigma_{Ym}(1-n_m) = \frac{2}{3}\left\{n_a\sigma_{Ya}\left(\frac{R_p}{a}\right)^{3/n_a}\left(\frac{\varepsilon_{Ym}}{\varepsilon_{Ya}}\right)^{\frac{1}{n_a}}\left[\left(\frac{a}{r_0}\right)^{3/n_a} - 1\right] + n_m\sigma_{Ym}\left(\frac{R_p}{a}\right)^{3/n_m}\right\} \quad (4.38)$$

Eq. (4.38) can be easily solved numerically. Alternatively the assumption $n_m \approx n_a$ results in the following approximation for R_P:

$$R_P = a \cdot \left\{ \frac{\frac{3}{2}\frac{\sigma_h}{\sigma_{Ym}} - (1-n_m)}{n_a \frac{\sigma_{Ya}}{\sigma_{Ym}} \left(\frac{\varepsilon_{Ym}}{\varepsilon_{Ya}} \right)^{\frac{1}{n_a}} \left[\left(\frac{a}{r_0} \right)^{3/n_a} - 1 \right] + n_m} \right\}^{\frac{n_m}{3}} \tag{4.39}$$

Substituting Eq. (4.39) into Eq. (4.37f) allows one to re-write coefficient B as follows:

$$B = \frac{\sigma_{Ym} R_p{}^3 (1+\nu_m)}{3E_m} = \frac{6\sigma_{Ym}}{G_m} \cdot a^3 \cdot \left\{ \frac{\frac{3}{2}\frac{\sigma_h}{\sigma_{Ym}} - (1-n_m)}{n_a \frac{\sigma_{Ya}}{\sigma_{Ym}} \left(\frac{\varepsilon_{Ym}}{\varepsilon_{Ya}} \right)^{\frac{1}{n_a}} \left[\left(\frac{a}{r_0} \right)^{3/n_a} - 1 \right] + n_m} \right\}^{n_m} \tag{4.40}$$

In principle, the displacement increase at r=b, between the yielded and the un-yielded states, should be equal to:

$$\Delta u \cong \frac{(B - \overline{B})}{b^2} \tag{4.41}$$

where B is given by Equation (4.40) and $\overline{B}$ is, instead (Zappalorto et al., 2011a):

$$\overline{B} = \sigma_h a^3 \frac{4G_a(K_m - K_a) + K_a(4G_a + 3K_m)(r_0/a)^3}{4K_m \left[G_a(4G_m + 3K_a) + 3K_a(G_m - G_a)(r_0/a)^3 \right]} \tag{4.42}$$

However, since B>> $\overline{B}$, Δu can be reasonably approximated by:

$$\Delta u \cong \frac{B}{b^2} = \frac{6\sigma_{Ym}}{G_m} \cdot \frac{a^3}{b^2} \cdot \left\{ \frac{\frac{3}{2}\frac{\sigma_h}{\sigma_{Ym}} - (1-n_m)}{n_a \frac{\sigma_{Ya}}{\sigma_{Ym}} \left(\frac{\varepsilon_{Ym}}{\varepsilon_{Ya}} \right)^{\frac{1}{n_a}} \left[\left(\frac{a}{r_0} \right)^{3/n_a} - 1 \right] + n_m} \right\}^{n_m} \tag{4.43}$$

and the energy produced at the nanoscale by plastic yielding of a single nanovoid results:

$$U_P = F \times \Delta u = 4\pi\sigma_h \frac{6\sigma_{Ym}}{G_m} \cdot a^3 \cdot \left\{ \frac{\frac{3}{2}\frac{\sigma_h}{\sigma_{Ym}} - (1-n_m)}{n_a \frac{\sigma_{Ya}}{\sigma_{Ym}} \left(\frac{\varepsilon_{Ym}}{\varepsilon_{Ya}} \right)^{\frac{1}{n_a}} \left[\left(\frac{a}{r_0} \right)^{3/n_a} - 1 \right] + n_m} \right\}^{n_m} \tag{4.44}$$

Finally, recalling $u_P = U_P \frac{3f_{p0}}{4\pi r_0^3}$, the strain energy density in a RVE (microscale) can be calculated as:

$$u_P = \sigma_h f_{p0} \frac{18\sigma_{Ym}}{G_m} \left(\frac{a}{r_0} \right)^3 \left\{ \frac{\frac{3}{2}\frac{\sigma_h}{\sigma_{Ym}} - (1-n_m)}{n_a \frac{\sigma_{Ya}}{\sigma_{Ym}} \left(\frac{\varepsilon_{Ym}}{\varepsilon_{Ya}} \right)^{\frac{1}{n_a}} \left[\left(\frac{a}{r_0} \right)^{3/n_a} - 1 \right] + n_m} \right\}^{n_m} \tag{4.45}$$

Elastic-perfectly plastic behaviour for the interphase and the matrix

In the absence of detailed information about the hardening behaviour of the matrix and the interphase, as a simplified assumption, the materials can be thought of as obeying to an elastic-perfectly plastic law.

To this end, it is easier to reformulate the problem from the beginning, instead than consider this case as the limit condition of the hardening solution for n tending to infinity.

With reference to the coordinate system shown in Fig. 1b, invoking the Tresca yielding criterion, the yielding condition and the equilibrium equation result in (Kachanov, 1971):

$$\overline{\sigma}_P = \sigma_{\theta\theta} - \sigma_{rr} = \sigma_Y \tag{4.46}$$

$$\frac{\partial \sigma_{rr}}{\partial r} + 2 \times \frac{\sigma_{rr} - \sigma_{\theta\theta}}{r} = 0 \tag{4.47}$$

where σ_Y is the material yield stress and $r<R_P$.

Substituting Eq. (4.46) into Eq. (4.47) one obtains:

$$\frac{\partial \sigma_{rr}}{\partial r} - 2 \times \frac{\sigma_Y}{r} = 0 \tag{4.48}$$

The solution for σ_{rr} in the plastic zone is then:

$$\sigma_{rr}^{(pl),a} = C_1 + 2\sigma_{Ya} \cdot Ln(r) \qquad \text{when } r<a \qquad (4.49a)$$

$$\sigma_{rr}^{(pl),m} = C_2 + 2\sigma_{Ym} \cdot Ln(r) \qquad \text{when } a<r<R_P \qquad (4.49b)$$

where σ_{Ya} and σ_{Ym} are the yield stress of the interphase and of the matrix, respectively. Applying the appropriate boundary conditions, one finally obtains:

$$R_P = a \cdot \left(\frac{r_0}{a}\right)^{\frac{\sigma_{Ya}}{\sigma_{Ym}}} \cdot e^{\left(\frac{\sigma_h}{2\sigma_{Ym}} - \frac{1}{3}\right)} \qquad B = \frac{6\sigma_{Ym}}{G_m} a^3 \cdot \left(\frac{r_0}{a}\right)^{\frac{3\sigma_{Ya}}{\sigma_{Ym}}} \cdot e^{\left(\frac{3\sigma_h}{2\sigma_{Ym}} - 1\right)} \qquad (4.50a\text{-}b)$$

So that:

$$\Delta u \cong \frac{(1+\nu_m)\,\sigma_{Ym}}{3E_m} \times \frac{a^3}{b^2}\left(\frac{r_0}{a}\right)^{3\times\frac{\sigma_{Ya}}{\sigma_{Ym}}} e^{\left(\frac{3\sigma_h}{2\sigma_{Ym}} - 1\right)} \qquad (4.51)$$

The energy produced at the nanoscale by plastic yielding of a single nanovoid is then:

$$U_P = F \times \Delta u = 4\pi\sigma_h \times \frac{(1+\nu_m)\,\sigma_{Ym}}{3E_m} \times a^3 \times \left(\frac{r_0}{a}\right)^{3\times\frac{\sigma_{Ya}}{\sigma_{Ym}}} e^{\left(\frac{3\sigma_h}{2\sigma_{Ym}} - 1\right)} \qquad (4.52)$$

Accordingly, the strain energy density in a RVE (microscale) can be calculated as:

$$u_P = U_P \times \frac{3f_{p0}}{4\pi r_0^3} = f_{p0} \times \frac{(1+\nu_m)\,\sigma_{Ym}\sigma_h}{E_m} \times \left(\frac{a}{r_0}\right)^{3\times\left(1-\frac{\sigma_{Ya}}{\sigma_{Ym}}\right)} \times e^{\left(\frac{3\sigma_h}{2\sigma_{Ym}} - 1\right)} \qquad (4.53)$$

Fracture toughness enhancement due to plastic yielding of nanovoids

Once the microscale strain energy density has been determined, the macroscale fracture toughness enhancement can be computed by Eq. (11).

The hypothesis formulated at the beginning of section 4.1 by which $\sigma_h = \overline{\sigma}_h$, with the further substitution $G = K_I^2\left(1-\nu_o^{\,2}\right)/E_o$, allows one to rewrite Eq. (4.13) as follows:

$$\Delta G_{py} = 2\rho^*(\phi = \frac{\pi}{2}) \cdot u_P = \frac{u_P}{(C_h)^2} \cdot \frac{2G_c}{9\pi\sigma_{cr}^2} \cdot E_o \frac{1+\nu_o}{1-\nu_o} \qquad (4.54)$$

Substituting Eq. (4.53) and Eq. (4.45) into Eq. (4.54) one obtains:

$$\Delta G_{py} = G_{Ic} f_{p0} \left\{ \frac{4}{9\pi C_h} \cdot \frac{E_o}{E_m} \frac{(1+\nu_o)(1+\nu_m)}{1-\nu_o} \frac{\sigma_{Ym}}{\sigma_{cr}} \left(\frac{a}{r_0}\right)^{3\times\left(1-\frac{\sigma_{Ya}}{\sigma_{Ym}}\right)} e^{\left(3C_h\frac{\sigma_{cr}}{\sigma_{Ym}} - 1\right)} \right\} = \qquad (4.55)$$

$$= f_{p0} \times \psi_p \times G_{Ic}$$

for the elastic perfectly plastic case, and:

$$\Delta G_{py} = G_{Ic} f_{p0} \left\{ \frac{2}{9\pi C_h} \cdot \frac{1+\nu_o}{1-\nu_o} \frac{E_o}{G_m} \frac{\sigma_{Ym}}{\sigma_{cr}} \cdot \left(\frac{a}{r_0} \right)^3 \cdot \left[\frac{3C_h \frac{\sigma_{cr}}{\sigma_{Ym}} - (1-n_m)}{n_a \frac{\sigma_{Ya}}{\sigma_{Ym}} \left(\frac{\varepsilon_{Ym}}{\varepsilon_{Ya}} \right)^{\frac{1}{n_a}} \left[\left(\frac{a}{r_0} \right)^{3/n_a} - 1 \right] + n_m} \right]^{n_m} \right\} =$$

$$= f_{p0} \times \psi_p \times G_{Ic} \tag{4.56}$$

for the power hardening case, respectively. In both cases, ψ_p is the term in curly brackets and quantifies the energy dissipation at the nanoscale by plastic yielding. Since, according to [28], the overall fracture toughness can be written as:

$$G_{Ic} = G_{Im} + \Delta G_{py} \tag{4.57}$$

being G_{Im} the fracture toughness of the pure (unloaded) matrix, the fracture toughness improvement due to plastic yielding of nanovoids can be written in the following normalised form:

$$\frac{\Delta G_{py}}{G_{Im}} = \frac{f_{p0} \times \psi_p}{1 - f_{p0} \times \psi_p} \tag{4.58}$$

4.3.5 Results and discussion on the analysis of debonding and plastic yielding

In the previous sections, a general multi-scale approach has been proposed for the damage analysis at the nanoscale induced by the plastic yielding of nanovoids. It has been assumed that the nanofiller is uniformly dispersed and distributed within the volume, agglomeration being neglected at present.

By equating the hydrostatic component of the stress field within the nanoscale to the critical debonding stress, estimated through an expression recently proposed, Eq.(4.9), (Zappalorto et al., 2011a) the region containing all the damage due to debonding has been determined in closed form and is given by Eq. (4.10). This zone, named Debonding Region (DBR) is thought of as the active process zone.

Finally, by means of an energy balance, according to (Freund and Hutchinson, 1985, Evans et al., 1985) the fracture toughness improvement related to nanoparticle debonding has been determined.

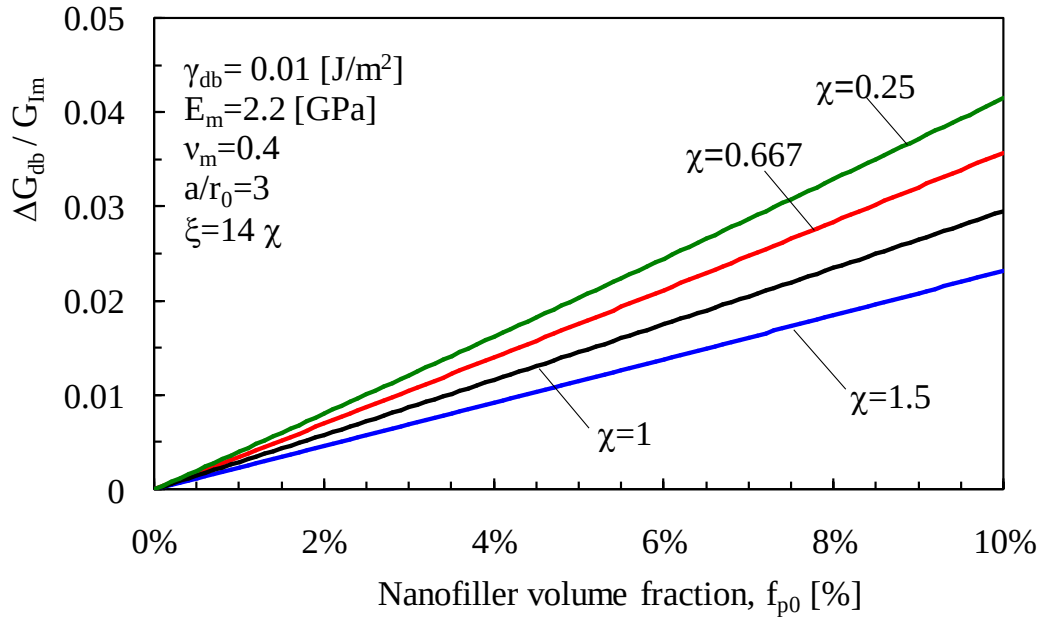

Figure 4.5. Plots of $\Delta G_{db} / G_{Im}$ according to Eq. (4.19) versus the nanofiller volume fraction. The bulk material properties match those of the epoxy resin used by Chen *et al*., 2007.

An example of application of Eq. (4.19) is reported in Fig. 4.5, which shows the normalized fracture toughness improvement due to debonding, $\Delta G_{db} / G_{Im}$, versus the nanofiller volume fraction; three different interphase size and properties have been considered. It is evident that, in all cases, the improvement is rather limited (less than 5%). This means that the energy absorbed through nanoparticle debonding is almost negligible.

However, it is quite easy to prove that debonding is a necessary condition for the subsequent plastic yielding around nanovoids created by debonded nanoparticles, such a toughening mechanism being of primary concern. With the aim to prove that, as a first approximation, we can substitute the linear elastic solution for the undebonded particle (Zappalorto et al., 2011a) within the Tresca yielding condition. By so doing, the yielding condition can be written as:

$$\sigma_{rr} - \sigma_{\theta\theta} = \sigma_n \times \frac{1-2\nu_a}{1-\nu_a} > \sigma_{Ya} \tag{4.59}$$

where σ_{Ya} is the yield strength of the interphase. As soon as the interphase behaves plastically, ν_a tends to 0.5 and the yielding condition can never be satisfied. This suggests that nanoparticle debonding can be thought of as a

"secondary toughening mechanism" being more important as a trigger for plastic yielding (Williams, 2010).

This result is supported by the experimental observation by Hsieh *et al.* (Hsieh et al., 2010, Hsieh et al., 2011) and has urged the authors to develop a more insightful analysis, focusing the attention also on the number of nanovoids nucleated from debonding. In Fig. 4.6 the normalized number of nanovoids predicted by the model, Eq. (4.11c), is shown as a function of $\mathbf{a/r_0}$. It is evident that the number of possible void grow sites is highly dependent on the interphase properties and that, in particular, softer interphases lead to an higher number of nanovoids.

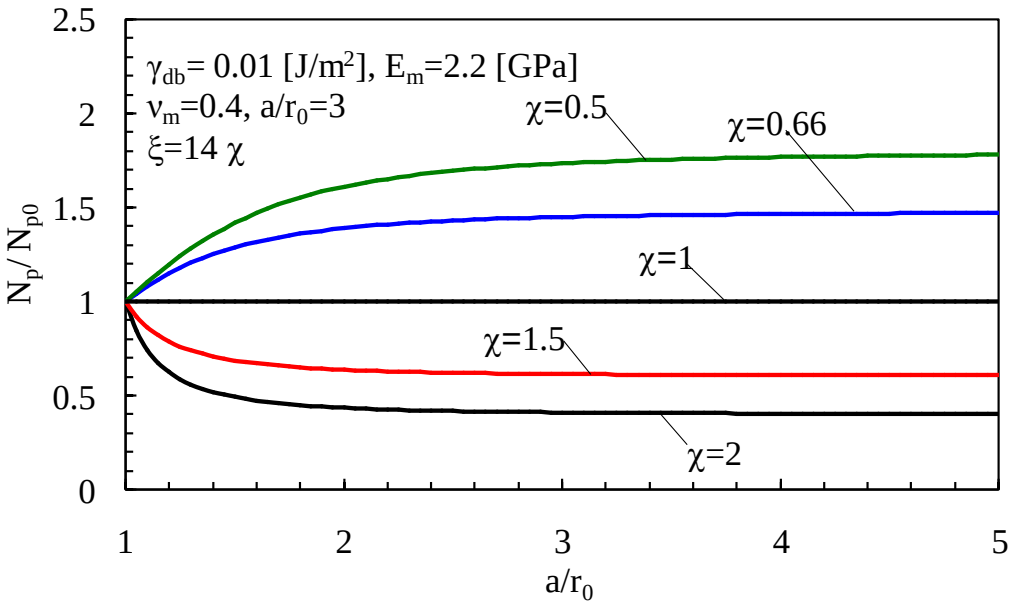

Figure 4.6. Influence of the interphase size and properties on the normalised amount of debonded nanoparticles, N_p / $N_{p,0}$. The bulk material properties match those of the epoxy resin used by Chen *et al.* 2007.

In the second part of the paper an analysis of the energy spent by the plastic yielding of nanovoids has been carried out. Two different material behaviours have been investigated, the power hardening and the elastic perfectly plastic behaviour. The analysis has highlighted that the elastic and plastic properties of the interphase as well as the nanovoid size play a lead role in the fracture toughness improvements due to this mechanism. In particular the toughness increment to the matrix toughness ratio has been plotted in Fig. 4.7 as a function

of the nanoparticle volume fraction for different values of the nanovoid diameter. The great influence exerted by the nanovoid diameter, d_0, is evident, the ratio $\Delta G_{py}/G_{Im}$ rapidly decreasing as d_0 increases. This strong size effect is in agreement with a large number of experimental results.

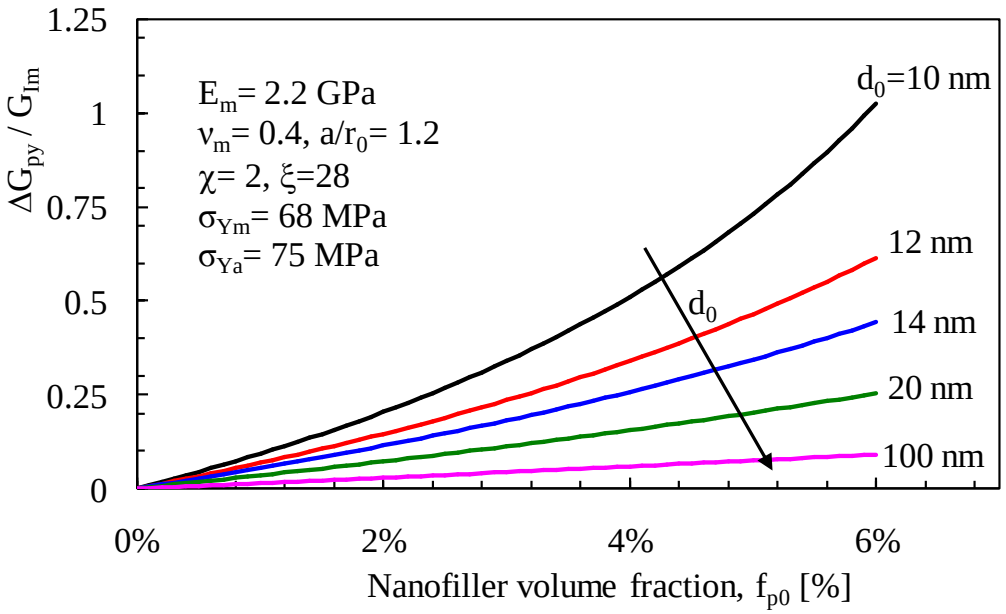

Figure 4.7. Plots of ΔG_{py} / G_{Im} according to Eq. (4.55) versus the nanofiller volume fraction; nanovoid of different diameter, d_0. The bulk material properties match those of the epoxy resin used by Chen *et al.* 2007.

Differently, Fig. 4.8 shows the substantial effect of the interphase properties on the fracture toughness improvement. Once again the model agrees with the experimental evidence: as different functionalizers lead to different properties of the interphase, nanocomposite toughening may be strongly affected by surface treatments.

It is further important to note that, different from debonding, the plastic yielding of nanovoids is a dominant mechanism for energy dissipation, resulting in high fracture toughness improvements. This is clearly shown in figures 4.7 and 4.8.

An example of the effect of the hardening exponent is finally shown in figure 8. The results indicate that the effect of the hardening exponent is, in general, not negligible, higher n values resulting in higher fracture toughness improvements. However, it has to mentioned that this result strongly depends on the particle and interphase sizes.

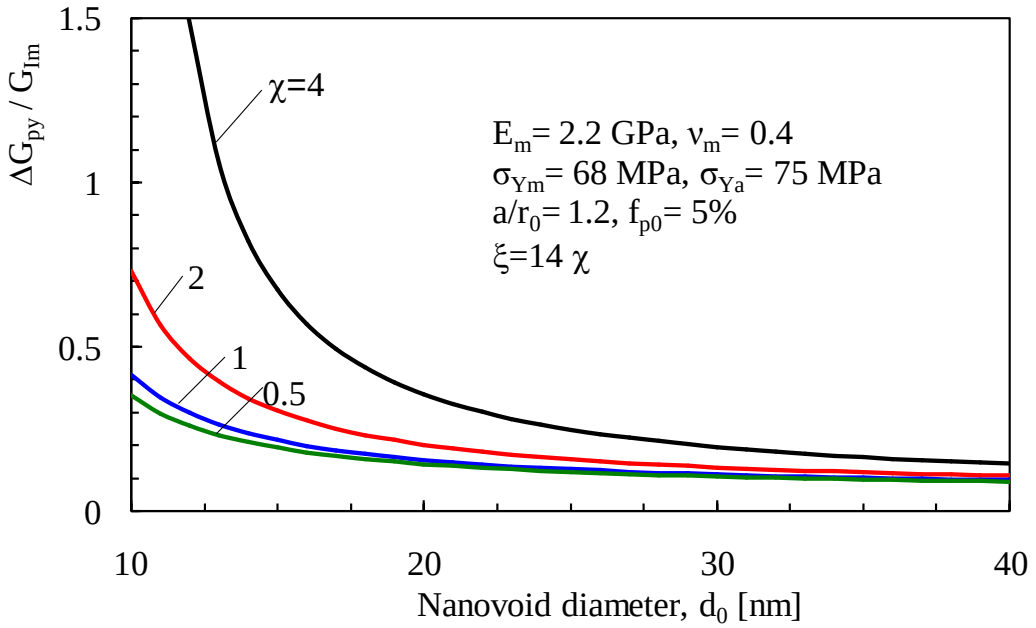

Figure 4.8. Plots of $\Delta G_{py} / G_{Im}$ according to Eq. (4.55) versus the nanovoid diameter: different interphase properties. The bulk material properties match those of the epoxy resin used by Chen *et al.* 2007.

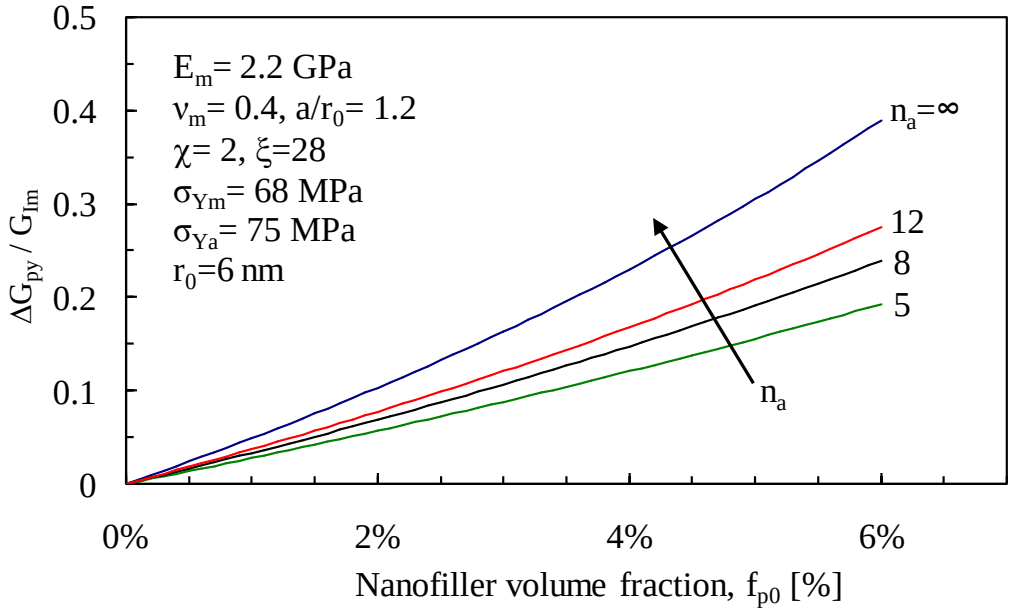

Figure 4.9. Influence of the hardening exponent on the $\Delta G_{py} / G_m$ ratio, according to Eq. (4.55) and Eq. (4.56).

It is important to note that, as a basic assumption of the present work, the nanofiller is supposed to be uniformly dispersed and distributed, neglecting the high tendency to agglomerate exhibited by nanoparticles beyond a certain value of

the volume fraction. It is clear that this approximation limits the application of the model to low nanofiller volume fractions.

4.3.6 Shear banding analysis

Consider the system at the macro-scale constituted of a cracked nano-modified matrix (see Fig. 4.3). Under the hypothesis of plane strain conditions, with reference to the coordinate system shown in Figure 4.3, the stress components at the crack tip can be divided into an hydrostatic part:

$$\sigma_h = \frac{\sigma_x + \sigma_y + \sigma_z}{3} = \frac{2(1+\nu_0)K_I}{3\sqrt{2\pi\rho}}\cos\frac{\phi}{2} \tag{4.60}$$

and a deviatoric one:

$$\begin{Bmatrix} s_{xx} \\ s_{yy} \\ s_{zz} \\ \tau_{xy} \end{Bmatrix} = \begin{Bmatrix} \sigma_{xx}-\sigma_h \\ \sigma_{yy}-\sigma_h \\ \sigma_{zz}-\sigma_h \\ \tau_{xy} \end{Bmatrix} = \frac{K_I}{\sqrt{2\pi\rho}} \begin{Bmatrix} \frac{1}{6}\cos\frac{\phi}{2}\left[2(1-2\nu_0)-3\mathrm{Cos}\phi+3\mathrm{Cos}2\phi\right] \\ \frac{1}{6}\cos\frac{\phi}{2}\left[2(1-2\nu_0)+3\mathrm{Cos}\phi-3\mathrm{Cos}2\phi\right] \\ \frac{2}{3}(2\nu_0-1)\cos\frac{\phi}{2} \\ \cos\frac{\phi}{2}\sin\frac{\phi}{2}\cos\frac{3\phi}{2} \end{Bmatrix} \tag{4.61}$$

where K_I and ν are the Stress Intensity Factor of local stress fields and the Poisson's ratio of the nanocomposite, respectively. The deviatoric stress field given by Eq. (4.61) can also be represented in terms of principal stresses; by doing so one obtains:

$$\bar{s} = \begin{Bmatrix} s_{11} \\ s_{22} \\ s_{33} \end{Bmatrix} = \frac{K_I}{\sqrt{2\pi\rho}} \begin{Bmatrix} \frac{(1-2\nu_0)}{3}\cos\frac{\phi}{2} - \frac{1}{2}\sin\phi \\ \frac{(1-2\nu_0)}{3}\cos\frac{\phi}{2} + \frac{1}{2}\sin\phi \\ -\frac{2}{3}(1-2\nu_0)\cos\frac{\phi}{2} \end{Bmatrix} \tag{4.62}$$

The associated equivalent macroscopic von Mises stress is:

$$\sigma_{vM} = \frac{K_I}{\sqrt{4\pi\rho}}\cos\frac{\phi}{2}\sqrt{2\,(1-2\nu_0)^2 + 3(1-\cos\phi)} \tag{4.63}$$

Within the multiscale approach to the problem, the deviatoric crack macroscale stress field $\bar{\mathbf{s}}$ can be regarded as the average value of the microscale stresses over a Representative Volume Element (RVE). The bridge with the nanoscale can finally be established by means of the Mori-Tanaka approach (see figure 4.1).

Then, the maximum von Mises stress and the hydrostatic stress arising around the nanoparticle can be approximated by:

$$\sigma_{vM,n} = H_{vM}\sigma_{vM} = H_{vM}\frac{K_I}{\sqrt{4\pi\rho}}\cos\frac{\phi}{2}\sqrt{2\,(1-2\nu_0)^2+3(1-\cos\phi)} \tag{4.64}$$

$$\sigma_{h,n} = H_h\sigma_h = H_h\frac{2(1+\nu_0)K_I}{3\sqrt{2\pi\rho}}\cos\frac{\phi}{2} \tag{4.65}$$

where H_h is the hydrostatic part the of the global stress concentration tensor and, under the hypothesis of a rigid nanoparticle, can be determined by (Zappalorto et al., 2011a):

$$H_h = \frac{\left(\frac{3K_a}{G_m}+4\frac{G_a}{G_m}\right)\left(\frac{3(1-\nu_m)}{1+\nu_m}\right)}{\frac{3K_a}{G_m}+4-4\cdot(1-\frac{G_a}{G_m})(r_0/a)^3} \tag{4.66}$$

Differently, H_{vM} is the deviatoric component of the global stress concentration tensor, and it is determined in closed form in the (Zappalorto et al., 2012b).

Whenever the stress field around a nanoparticle is high enough, it causes local shear yielding, with the formation of plastic shear bands. The region of material containing all the nanoparticles subjected to shear yielding is denoted as Shear Banding Region (SBR). According to (Huang and Kinloch, 1992, Johnsen et al., 2007, Hsieh et al., 2010 and 2011), the shear bands are modelled as four plastic strips departing from the nanoparticle periphery (Fig. 4.10a). As we will argue better later, the size of these strips depends on the distance from the crack tip.

The extension of the SBR can be determined by applying the modified von Mises yielding criterion, which explicitly takes into account the level of the hydrostatic stress (Crist, 1997):

$$\sigma_{vM,n}+\sqrt{3}\mu\sigma_{h,n} = \sigma_{Ya,c}\left(1-\frac{\mu}{\sqrt{3}}\right)^2 \tag{4.67}$$

where $\sigma_{Ya,c}$ is the interphase yield stress under compression and μ is a dimensionless pressure coefficient. Substituting Eqs. (4.64, 4,65) and solving by ρ:

$$\rho_{SB}(\phi)=\frac{H_{vM}^2}{4\pi}\left[\frac{K_I\cos\frac{\phi}{2}}{\sigma_{Ya,c}\left(1-\mu/\sqrt{3}\right)}\right]^2\left[\sqrt{2\,(1-2\nu_0)^2+3(1-\cos\phi)}+\sqrt{\frac{8}{3}}\mu\frac{H_h}{H_{vM}}(1+\nu_0)\right]^2 \quad (4.68)$$

Eq. (4.68) gives the region of the material subjected to shear banding (SBR). From Eq. (4.68) it is also evident that the actual value of ρ_{SB} strongly depends on ϕ.

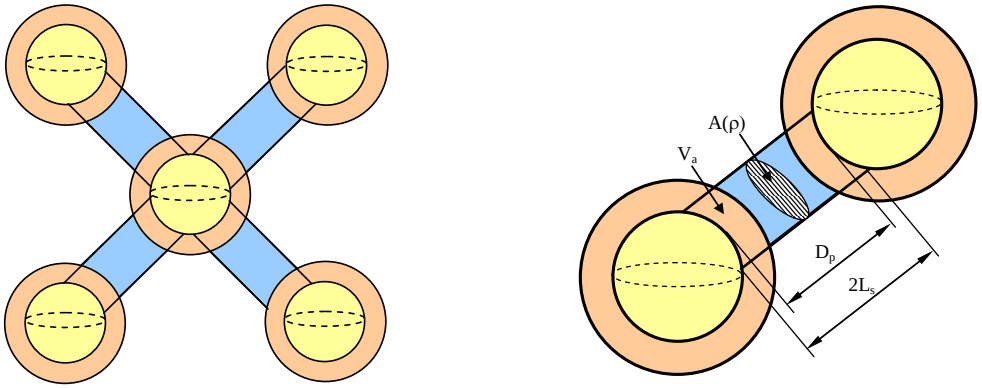

(a) (b)

Figure 4.10. Schematic representation of the four plastic shear bands departing from a nanoparticle (a). Relevant geometrical quantities used to describe the localised shear banding around nanoparticles (b).

However, the use of an average value for the extension of the damage zone makes it representative of the overall damage behaviour over ϕ. Such an average value can be defined as:

$$\bar{\rho}_{SB}=\frac{1}{2\pi}\int_{-\pi}^{+\pi}\rho_{SB}(\phi)\,d\phi=\frac{1}{4\pi}\left[\frac{K_I}{\sigma_{Ya,c}\left(1-\mu/\sqrt{3}\right)}\right]^2 I_{SB} \quad (4.69)$$

where:

$$I_{SB}=\frac{1}{2\pi}\int_{-\pi}^{+\pi}\left[H_{vM}\sqrt{2\,(1-2\nu_0)^2+3(1-\cos\phi)}+\sqrt{8/3}\mu H_h(1+\nu_0)\right]^2\cos^2\frac{\phi}{2}\,d\phi \quad (4.70)$$

The analytical solution for I_{SB} is given in (Salviato et al., in press).

Then, in the following we approximate the actual SBR with a circle, centred at the crack tip and having a radius equal to $\bar{\rho}_{SB}$. This is in agreement with (Hsieh et al., 2010 and 2011, Zappalorto et al., 2012).

Denoting with U_{SB} the energy produced at the nanoscale, according to the adopted multiscale system, the strain energy density in a RVE (microscale) can be calculated as:

$$u_{SB} = U_{SB} \times \frac{3f_{p0}}{4\pi r_0^3} \tag{4.71}$$

where f_{p0} is the volume fraction of nanoparticles. Finally, the fracture toughness enhancement due to shear band formation can be determined, according to (Freund and Hutchinson, 1985, Evans et al., 1985, Lauke et al., 2008, Hsieh et al., 2010 and 2011, Zappalorto et al., 2012) as:

$$\Delta G_{SB} = 2 \times \int_0^{\bar{\rho}_{SB}} u_{SB}\ d\rho \tag{4.72}$$

The problem of determining the overall fracture toughness enhancement is, in this way, reconverted into finding the energy produced at the nanoscale by shear banding.

4.3.7 Modelling of toughness improvement due to shear banding

In a recent work, analyzing the transmission optical micrographs from the (non-propagating) crack-tip region of DN4PB test specimens, Hsieh *et al.* (Hsieh et al., 2010 and 2011) demonstrated the tendency of the epoxy polymers to form localised plastic shear bands. In agreement with previous works (Hsieh et al., 2010 and 2011, Zappalorto et al., 2012), this phenomenon of localized damage can be modeled using a very simple network according to which the local stress concentration around each nanoparticle gives rise to four shear bands, departing from the nanoparticle surface. According to this schematic, the cross sectional area of the single shear band soundly scales with the diametrical cross sectional of the nanoparticle as:

$$A(\rho) = f(\rho)\,\pi r_0^2 \tag{4.73}$$

In this expression, $f(\rho)$, of which the values must fall within the range (0,1), is an appropriate function of the distance from the crack tip. For the sake of simplicity, in this work we assume the following expression for $f(\rho)$:

$$f(\rho) = 1 - \sqrt{\frac{\rho}{\bar{\rho}_{SB}}} \tag{4.74}$$

where the square root law has been chosen to agree with the square root

singularity.

The length of the shear bands can then be estimated as:

$$L_s = r_0 + \frac{D_p}{2} - r_0\sqrt{1 - f(\rho)} \tag{4.75}$$

where D_p is the interparticle distance. Under the hypothesis of a cubic array, which is likely to occur for low nanofiller volume fraction, D_p can be estimated as:

$$D_p = \left[\left(\frac{4\pi}{3f_{p0}}\right)^{\frac{1}{3}} - 2\right] r_0 \tag{4.76}$$

It is worth noting (see figure 4.10b) that it has been considered the presence of an interphase zone between the nanoparticle and the matrix, thought of a zone of matrix of altered chemistry. Then the shear band departing from the nanoparticle boundary develops partly in the interpahse zone and partly in the un-altered matrix. It is then basic to estimate the volume fraction of the interphase and of the matrix which has encountered shear yielding.

With the aid of simple geometrical considerations, the total volume of the shear yielded material can be estimated by:

$$V_{tot} = \frac{3f_{p0}}{\pi r_0^3}\left[\pi f(\rho) r_0^2 L_s - \frac{\pi}{3}\left(L_s - \frac{D_p}{2}\right)^2\left(3r_0 - L_s + \frac{D_p}{2}\right)\right] \tag{4.77}$$

The interphase volume fraction per unit volume within the bands can be expressed, instead, by means of the following equation for $D_p \geq 2t$:

$$\begin{aligned} V_a = \frac{3f_{p0}}{\pi r_0^3}\Bigg[& \pi f(\rho) r_0^2\left(r_0\sqrt{\left(\frac{a}{r_0}\right)^2 - f(\rho)} - r_0 + L_s - \frac{D_p}{2}\right) + \\ & - \frac{\pi}{3}\left(L_s - \frac{D_p}{2}\right)^2\left(3r_0 - L_s + \frac{D_p}{2}\right) \\ & + \frac{\pi}{3} r_0^3\left(\frac{a}{r_0} - \sqrt{\left(\frac{a}{r_0}\right)^2 - f(\rho)}\right)^2\left(2\frac{a}{r_0} + \sqrt{\left(\frac{a}{r_0}\right)^2 - f(\rho)}\right)\Bigg] \end{aligned} \tag{4.78}$$

Finally, the matrix fraction can be evaluated as:

$$V_m = \frac{3f_{p0}}{\pi r_0^3}\left[\pi f(r) r_0^2 L_s - \frac{\pi}{3}\left(L_s - \frac{D_p}{2}\right)^2\left(3r_0 - L_s + \frac{D_p}{2}\right)\right] - V_a \tag{4.79}$$

If we assume, for the sake of simplicity, that the matrix and the interphase yield according to a perfectly plastic law, we can disregard the elastic part of the stress-strain curve, and determine the strain energy density related to shear banding as:

$$u_{SB} = f(\rho)\tau_{ym} V_m \gamma_{fm} + f(\rho)\tau_{ya} V_a \gamma_{fa} = u_m + u_a \tag{4.80}$$

where τ_{ym} and τ_{ya} are the shear yielding stress of the matrix and of the interphase, while γ_{fm} and γ_{fa} are the shear fracture strain of the matrix and of the interphase, respectively.

Substituting Eq. (4.80) into Eq. (4.72) results in:

$$\Delta G_{SB} = 2\int_0^{\bar{\rho}_{SB}} u_{SB} d\rho = \bar{\rho}_{SB}\, f_{p0}\, \Gamma \tag{4.81}$$

where:

$$\Gamma = \tau_{ym}\gamma_{fm}\left\{\left(\frac{\pi}{6f_{p0}}\right)^{\frac{1}{3}} - \frac{52}{63}\frac{\tau_{ya}\gamma_{fa}}{\tau_{ym}\gamma_{fm}} - \left(1 - \frac{\tau_{ya}\gamma_{fa}}{\tau_{ym}\gamma_{fm}}\right)\left[\frac{32}{21}Q\left(\frac{1}{3} + \frac{\bar{a}^4}{5}\right) + \frac{\bar{a}^2}{315}\left(4S - 32\bar{a}^4 Z + 128\bar{a}^6 M\right)\right]\right\} \tag{4.82a}$$

$$\bar{a} = \frac{a}{r_0} \qquad Q = \sqrt{\bar{a}^2 - 1} \qquad M = \bar{a} - Q \qquad S = 105\,\bar{a} - 88Q \qquad Z = 9\,\bar{a} - 7Q \tag{4.82b}$$

and $\bar{\rho}_{SB}$ is given by Eq. (4.69).

Further taking into consideration that:

$$G_I = K_I^2\left(1 - \nu_0^{\,2}\right)/E_0 \tag{4.83}$$

the fracture toughness improvement turns finally out to be:

$$\Delta G_{SB} = G_{Ic} f_{p0} \times \left(\frac{I_{SB}}{4\pi\sigma_{ya}^2(1-\mu\sqrt{3})^2}\frac{E_0}{1-\nu_0^2} \times \Gamma\right) = f_{p0} \times \psi_{SB} \times G_{Ic} \tag{4.84}$$

where ψ_{SB} quantifies the energy dissipation at the nanoscale by localised shear banding:

$$\psi_{SB} = \left(\frac{I_{SB}}{4\pi\sigma_{ya}^2(1-\mu/\sqrt{3})^2}\frac{E_0}{1-\nu_0^2} \times \Gamma\right) \tag{4.85}$$

Since, according to (Lauke, 2008, Zappalorto et al., 2012) the overall fracture toughness can be written as:

$$G_{Ic} = G_{Im} + \Delta G_{SB} \tag{4.86}$$

being G_{Im} the fracture toughness of the pure (unloaded) matrix, the fracture toughness improvement can also be written in the following normalised form:

$$\frac{\Delta G_{SB}}{G_{Im}} = \frac{f_{p0} \times \psi_{SB}}{1 - f_{p0} \times \psi_{SB}} \tag{4.87}$$

4.3.8 Results and discussion on the analysis of shear yielding

In the previous section, a general multi-scale approach has been proposed for the damage analysis at the nanoscale induced by shear banding around nanoparticles. It has been assumed that the nanofiller is uniformly dispersed and distributed within the volume, agglomeration being neglected at present. The effect of an interphase zone surrounding the nanoparticle, characterised by mechanical properties different from those of the matrix, is explicitly considered.

Plastic shear bands are thought of as created by the stress concentration around nanoparticles. The shear bands are modelled as four plastic strips departing from the nanoparticle periphery (see figure 4.10a, b) of which the size depend on the distance from the crack tip. The extension of the SBR, the region of material containing all the nanoparticles subjected to shear yielding, has been determined in closed form by applying the modified von Mises yielding criterion. This zone, is thought of as the active process zone.

The aim of this section is to clarify the range of applicability and to highlight, through examples, the most relevant features of the solution proposed in the previous sections.

The following properties have been adopted for the matrix, according to the suggestions in (Hsieh et al., 2010 and 2011): τ_{ym}=61.3 MPa, τ_{fm}=0.75, E_m=2.96 GPa, ν_m=0.35. Conversely, the properties of the interphase have been changed in order to analyze their contribution on the final solution.

The effect of the interphase zone on the total strain energy, u_{tot}, dissipated within the RVE, Eq. (4.80), is shown in Figure 4.11. In the figure, the strain energy absorbed within the matrix, u_m, the interphase, u_a, and the total energy absorbed, u_{tot}, normalised to the maximum total strain energy, $u_{tot,max}$, are plotted as a function of the nanoparticle radius for given interphase thickness and ultimate properties. It is worth noting that, moving from micro to nanoparticles, the

fraction of energy dissipated within the interphase, u_a, increases. Figure 4.11 also shows, with reference to the case investigated, the strong size dependency of the phenomenon, the contribution of the interphase becoming lower than 10% for nanoparticle diameters larger than 60 nm.

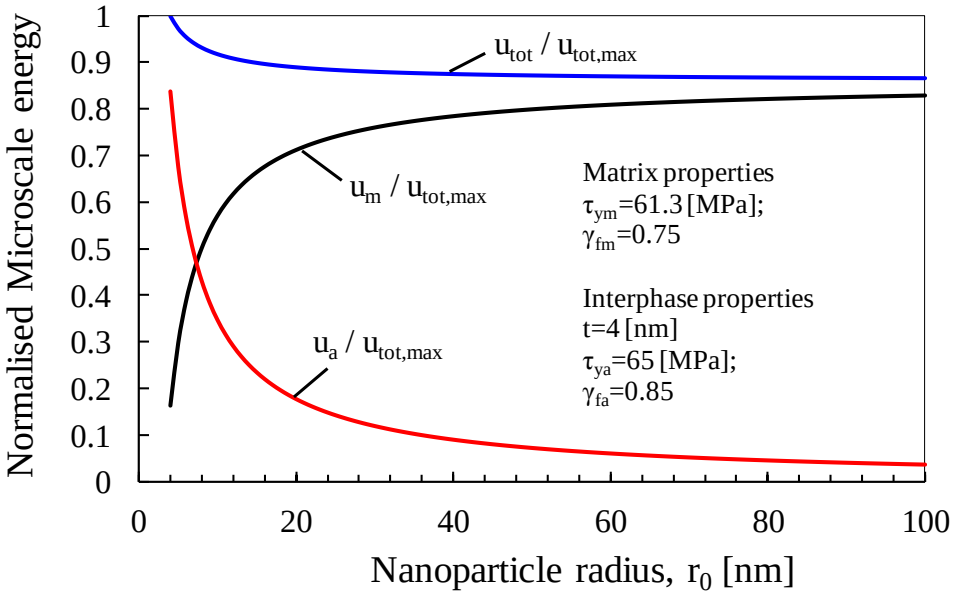

Figure 5. Normalised microscale energy dissipated by shear banding within the matrix, u_m, and the interphase, u_a, as a function of the nanoparticle radius ($f(\rho)$ equal to 0.5).

It is also worth noting, in addition, that the interphase elastic properties highly affects the stress concentration at the nanoparticle periphery. In Figure 4.12, the normalised Von Mises stress concentration factor, determined by accounting for the presence of the interphase, is plotted as a function of a/r_0, considering different interphase elastic properties. It can be seen that the stiffer the interphase, the higher H_{vM}, which reaches an almost asymptotic value for a/r_0 higher than 2. This leads to, ceteris paribus, a higher extension of the shear banding process zone, see Eq. (4.69, 4.70), and, in turn, in a much higher fracture toughness improvement, according to Eq. (4.84).

The analytical model developed in this work indicates that the fracture toughness improvements of nanoparticle reinforced polymers is mainly affected by two important parameters: elastic properties of the interphase (related to the surface

functionalization of nanoparticles) and the nanofiller size. This is shown in Figures 4.13-16.

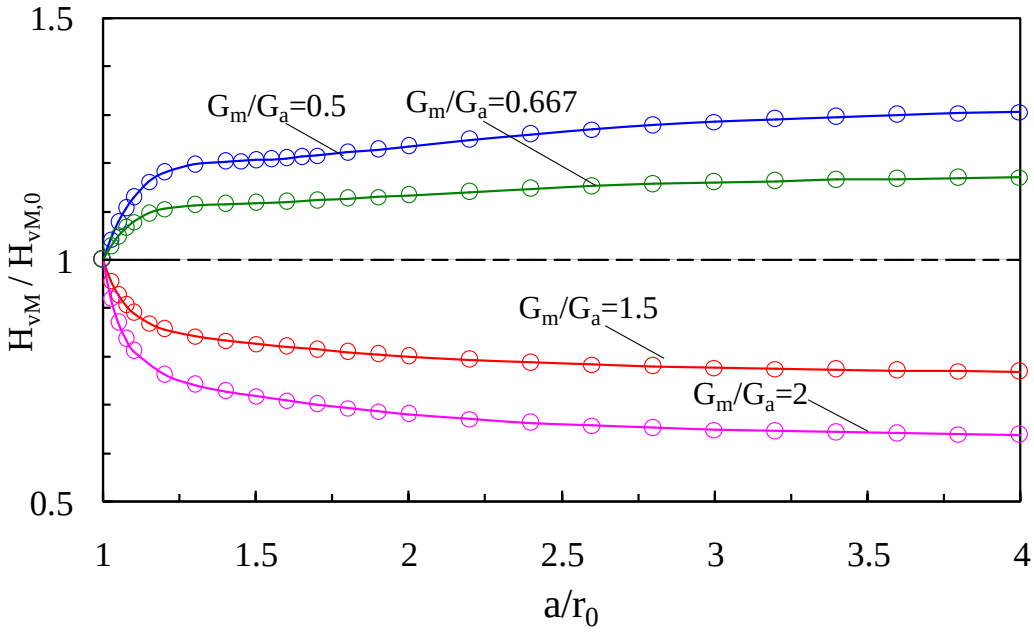

Figure 4.12. Influence of the interphase properties on the von Mises stress concentration around nanoparticles, according to Eq. (A.24). $H_{vM,0}$ is the stress concentration disregarding the interphase.

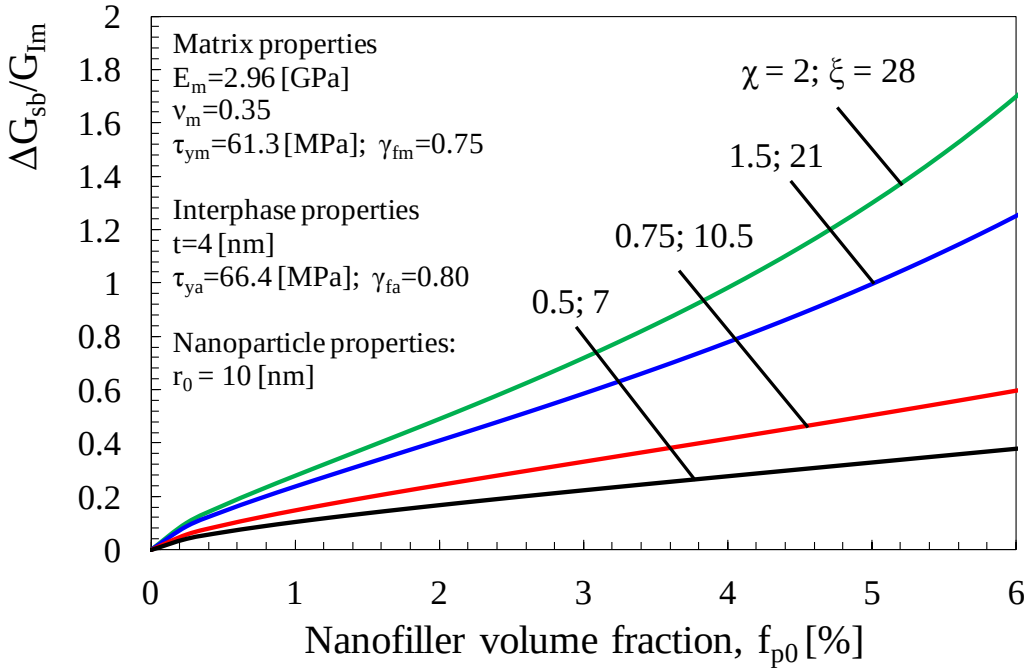

Figure 4.13. Normalised fracture toughness increment due to shear banding as a function of the nanofiller volume fraction. Different interphase elastic properties ($\chi = G_a/G_m$; $\xi = 3K_a/G_m$).

In particular, Figure 4.13 shows the fracture toughness increase due to shear banding as a function of the nanofiller volume content, for different elastic properties of the interphase. The model shows that the formation of local shear bands is a highly dissipative mechanism (causing a high fracture toughness improvement at low nanofiller content) and it is affected by the characteristics of the interphase. In this sense, the model agrees with the experimental evidence: as different functionalizers lead to different properties of the interphase, nanocomposite toughening may be strongly affected by surface treatments.

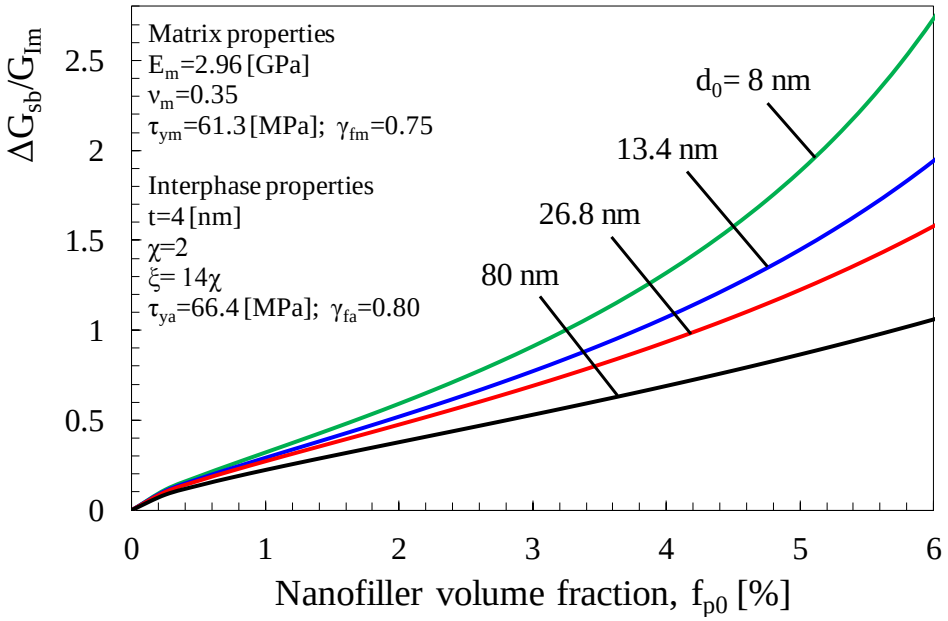

Figure 4.14. Normalised fracture toughness increment as a function of the nanofiller volume fraction. Stiff interphase ($\chi = G_a/G_m = 2$; $\xi = 3K_a/G_m = 28$). Different nanoparticle diameters ($d_0=2r_0$).

Differently, figures 4.14 and 4.15 show the influence of the particle size on the fracture toughness improvements, such an effect being different depending whether the interface is stiffer or softer than the matrix. In Figure 4.14, the case of an interphase stiffer than the matrix is presented. The toughness increase becomes more than 200% and it is higher for smaller nanoparticles.

With reference to the case of a softer interphase, figure 4.15 shows that the increase is smaller with respect to the previous case and greater nanoparticle radii lead to higher fracture toughness.

To better clarify the size effect on the model, the toughness improvement is shown in Figure 10 versus the nanoparticle radius for two different interphase properties and a volume fraction of 5%. For radii higher than 60 nm, the results for both the case of a soft interphase and of a stiff interphase lead to the same asymptotic value. Differently, for smaller particles, a stiff interphase gives far higher improvements than a soft one.

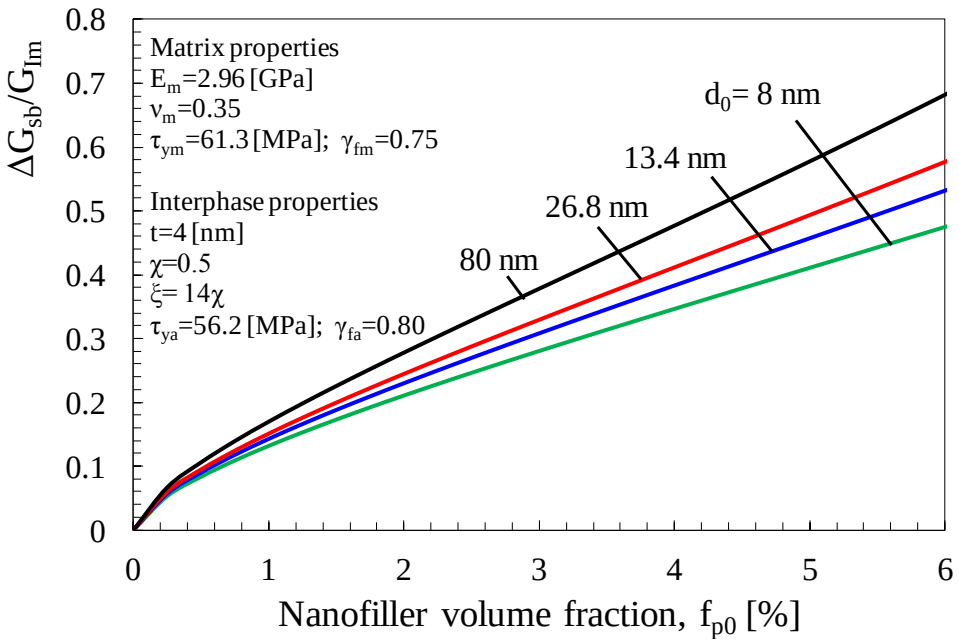

Figure 4.15. Normalised fracture toughness increment as a function of the nanofiller volume fraction. Soft interphase ($\chi = G_a/G_m = 0.5$; $\xi = 3K_a/G_m = 7$). Different nanoparticle diameters ($d_0=2r_0$).

It is worth noting that as a basic assumption of the present work the nanofiller is supposed to be uniformly dispersed and distributed, neglecting the high tendency to agglomerate exhibited by nanoparticles beyond a certain value of the volume fraction. It is clear that this approximation hampers the application of the model to low nanofiller volume fractions.

Eventually, it is important to remember that a correct prediction of the fracture toughness of the nanoparticle filled polymers should include, besides the effect of the shear bands formation, the amount of energy dissipated by other mechanisms taking place at the nanoscale (like for example the plastic yielding of nanovoids [15]) which are not dealt with in the present work. Indeed, the assessments based solely on the multiscale model developed in this work inevitably lead to an

underestimation of the fracture toughness for nanoparticle filled polymers. This is the reason why a direct comparison with experimental results is not reported here.

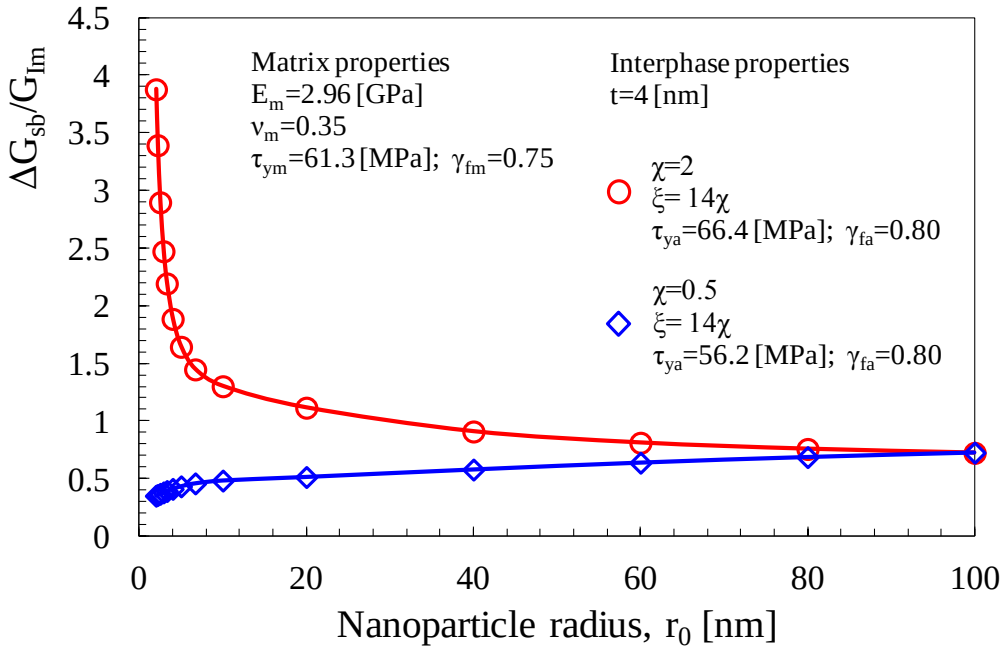

Figure 4.16. Normalised fracture toughness increment as a function of the nanoparticle radius for a volume fraction, f_{p0}, of 5%.

4.4 Application of the model

4.4.1 Overall fracture toughness of the nanocomposites

As far as the fracture toughness improvements due to each relevant damaging mechanism, ΔG_i, are known, the overall nanocomposite fracture toughness can be estimated according to Eq. (4.2).

Thus, substituting Eq. (4.17), Eq. (4.55) and Eq. (4.84) into Eq. (4.2) one obtains the overall fracture toughness of the nanocomposite as a function of G_{Im} and f_{p0}

$$G_{Ic} = \frac{G_{Im}}{1 - f_{p0}\left(\psi_{db} + \psi_p + \psi_{SB}\right)} \cong \frac{G_{Im}}{1 - f_{p0}\left(\psi_p + \psi_{SB}\right)} \tag{4.88}$$

the latter substitution being motivated by the negligible contribution due to debonding.

4.4.2 Estimation of the interphase size and elastic properties

In order to apply Eq. (4.88) the properties and size of the interphase need to be determined. The elastic properties and the thickness of the interphase can be

computed by means of numerical simulations carried out within the frame of MD as done for example by Odergard *et al.* (Odegard et al., 2005) and Yu *et al*. (Yu et al., 2009), which provide, as outputs, the radial extension of the interphase as well as the elastic properties averaged through the thickness.

Alternatively, for a specific system, they could be determined *a posteriori* by fitting the experimental values for the elastic properties of the nanocomposite by a multi-phase, micromechanical model.

The model provided by Dunn and Ledbetter (Dunn and Ledbetter, 1995) is used:

$$K_c = K_m + \frac{1}{3}\frac{f_p (a/r_0)^3 (K_a - K_m) T_{pa}^H + f_p (K_p - K_a) T_p^H}{1 - f_p + f_p (a/r_0)^3 T_{pa}^H} \tag{4.89}$$

where:

$$T_{pa}^H = 1 - 3\gamma_0 \left\{ \left(\frac{r_0}{a}\right)^3 \frac{K_p - K_m}{3\gamma_0 (K_p - K_m) + K_m} + \left[1 - \left(\frac{r_0}{a}\right)^3\right] \frac{K_a - K_m}{3\gamma_0 (K_a - K_m) + K_m} \right\}$$
$$T_p^H = 1 - \frac{3\gamma_0 (K_p - K_m)}{3\gamma_0 (K_p - K_m) + K_m} \qquad 3\gamma_0 = (1+\nu)/[3(1-\nu)] \tag{4.90}$$

The best fitting of elastic properties of nanocomposite materials using equations (4.89) allows to estimate, through a reverse engineering approach, the "*optimum*" value for the interphase elastic properties and size to be used in the proposed modelling strategy.

As highlighted by Eq. (4.55) and Eqs. (4.82), in principle, the estimated value of the overall fracture toughness of the nanocomposite depends also on the strength and yield properties of the interphase. However, for the sake of simplicity, in this work we propose to equate all the yield and strength properties of the interphase to those of the matrix. Indeed, as argued in (Zappalorto et al., 2012, Salviato et al., in press) the fracture toughness improvements as calculated through Eqs. (4.55, 4.82) are mostly due to the elastic mismatch between the matrix and the interphase.

4.5 Comparison with some experimental data

In this section, the theoretical predictions of the nanocomposite fracture toughness obtained by Eq. (4.88) are compared to some experimental data taken from the literature.

4.5.1 Data from Hsieh et al., 2011

In Figure 4.18 the fracture toughness values predicted by Eq. (4.88) are compared to the fracture data from specimens made of a DGEBA epoxy nanomodified by silica nanoparticle of 10 nm of radius (Hsieh et al., 2011). The proprieties of the matrix necessary for the theoretical prediction were reported in the original work (Hsieh et al., 2011). The interphase elastic properties and thickness have been determined, instead, by fitting the experimental data on the nanocomposite Young modulus for low weight contents. Other data, such as the compressive strength of the interphase has been supposed to be sufficiently close to those of the matrix polymer. Figures 4.18 makes it evident that predicted values well agree with the experimental results.

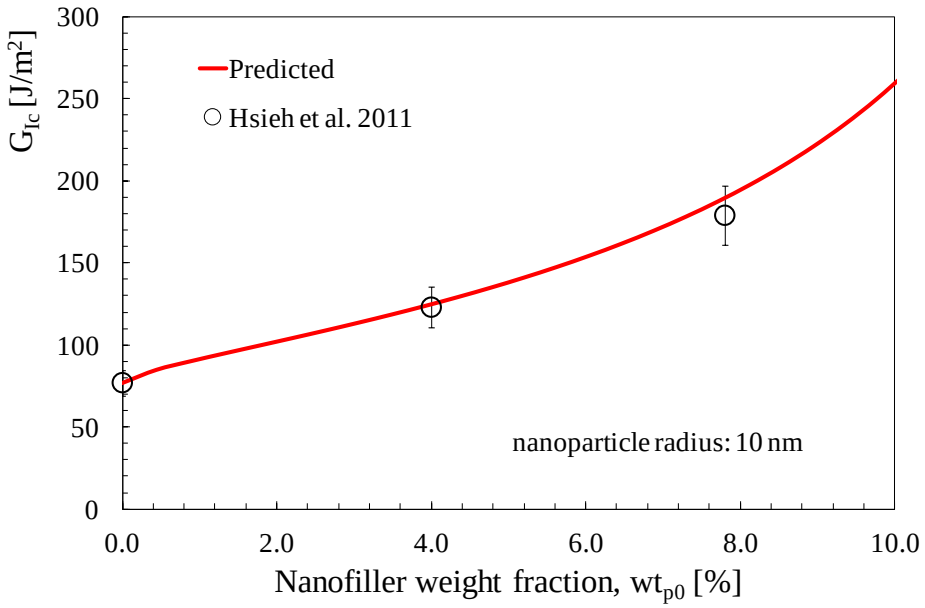

Figure 4.18. Comparison of the model (solid line) to experimental data taken from (Hsieh et al., 2011). Matrix properties are given by the authors. Interphase properties have been obtained by fitting, *a posteriori*, with the overla elastic properties of the nanocomposite.

4.5.2 Data from Zamanian et al., 2012

Figures 4.19-20 shows a comparison between the fracture toughness values predicted by Eq. (4.88) the fracture data from specimens made of a DGEBA epoxy resin nanomodified by silica nanoparticles with a radius of 6 and 10 nm (Zamanian et al., 2012). As done before, the material properties necessary to the analytical predictions which were not provided in the original work have been

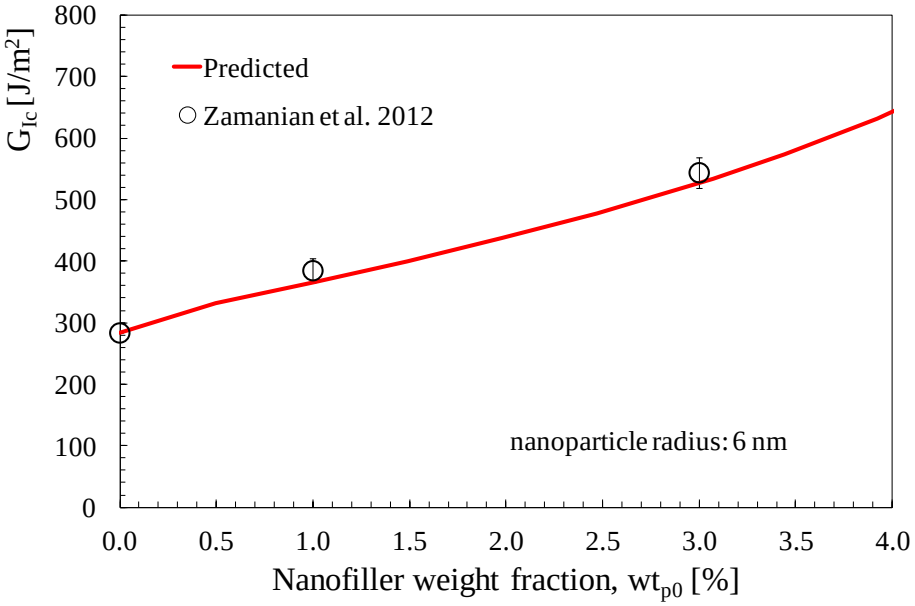

Figure 4.19. Comparison of the model (solid line) to experimental data taken from (Zamanian et al., 2012). Matrix properties are given by the authors. Interphase properties have been obtained by fitting, *a posteriori*, with the overall elastic properties of the nanocomposite.

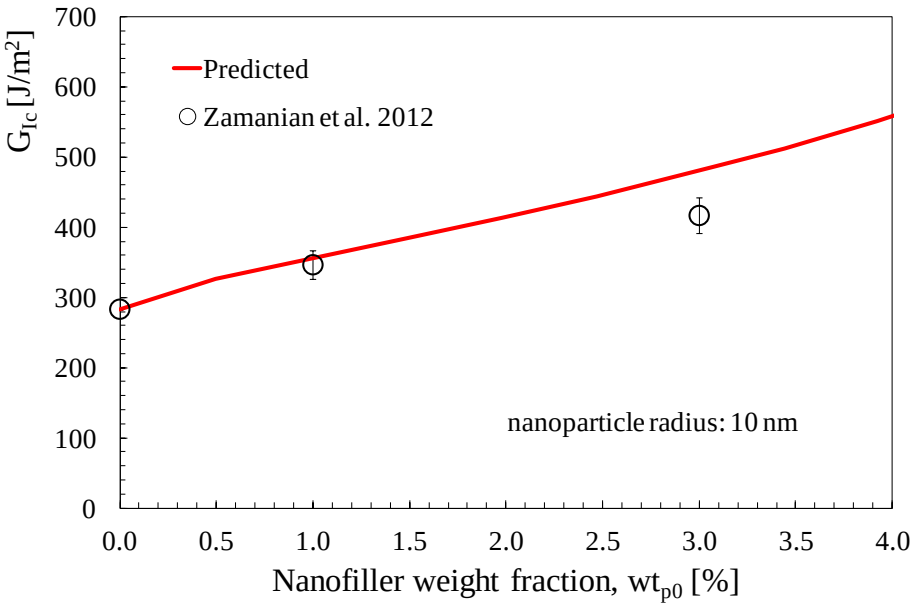

Figure 4.20. Comparison of the model (solid line) to experimental data taken from (Zamanian et al., 2012). Matrix properties are given by the authors. Interphase properties have been obtained by fitting, *a posteriori*, with the overall elastic properties of the nanocomposite.

partially determined by fitting the elastic properties of the nanocomposite and partially inferred. Figure 4.19 documents that also for the second studied system the agreement between theoretical predictions and experimental results is very

satisfactory.

4.5.3 Data from Liang et al., 2009

In Figure 4.21 the fracture toughness values predicted by Eq. (4.88) are compared to the fracture data from specimens made of a DGEBA epoxy nanomodified by silica nanoparticle of 40 nm of radius (Liang et al., 2009). The proprieties of the matrix necessary for the theoretical prediction were reported in the original work (Liang et al., 2009). The interphase elastic properties and thickness have been determined, instead, by fitting the experimental data on the nanocomposite Young modulus for low weight contents. Other data, such as the compressive strength of the interphase has been supposed to be sufficiently close to those of the matrix polymer. Figures 4.18 shows a good agreement with the experimental results.

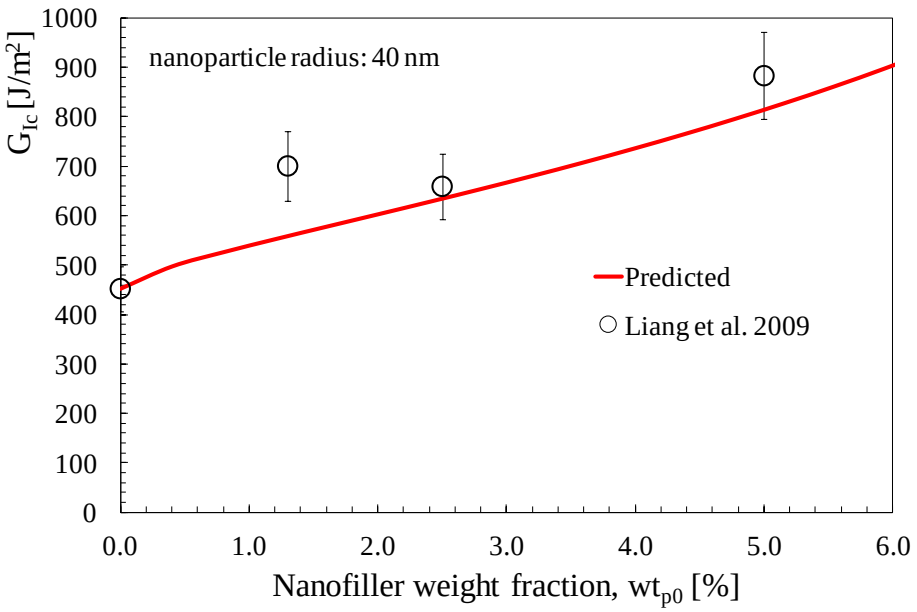

Figure 4.21. Comparison of the model (solid line) to experimental data taken from (Liang et al., 2009). Matrix properties are given by the authors. Interphase properties have been obtained by fitting, *a posteriori*, with the overall elastic properties of the nanocomposite.

It is finally worth mentioning that, as a basic assumption of the present work, the nanofiller is supposed to be uniformly dispersed and distributed, neglecting the high tendency to agglomerate exhibited by nanoparticles beyond a certain value of the volume fraction. This assumption hampers the application of the model to high nanofiller volume fractions.

4.5 Conclusions

In the present work a multi-scale multi-mechanism modelling strategy has been provided for the prediction of toughness increments caused by the emergence of plastic yielding and localised plastic shear bands in nanoparticle filled resins. The model stems from the quantification of the energy absorbed at the lower scale and accounts for the emergence of an interphase, created by the inter- and supra-molecular interactions arising at the nanoscale, with mechanical properties different from those of the matrix. The model has been compared to some experimental data collected from the literature, showing good agreements.

Bibliography of chapter 4

Chen JK, Huang ZP, Zhu J. "Size effect of particles on the damage dissipation in nanocomposites". *Compos Sci Technol*, 14:2990–96, 2007.

Dunn, M. and Ledbetter, H., "Elastic constants of composites reinforced by multiphase particles". *J. Appl. Mech.*, 62, 1023–1028, 1995.

Freund LB, Hutchinson JW. "High-strain-rate crack growth in rate dependent plastic solids". *J Mech Phys Solids*, 33:169-91, 1985.

Hsieh TH, Kinloch A.J, Masania K, Sohn Lee J, Taylor AC, Sprenger S. "The toughness of epoxy polymers and fibre composites modified with rubber microparticles and silica nanoparticles". *J Mater Sci*, 45:1193–1210, 2011.

Hsieh TH, Kinloch AJ, Masania K, Taylor AC, Sprenger S. "The mechanisms and mechanics of the toughening of epoxy polymers modified with silica nanoparticles". *Polymer*, 51:6284-6294, 2010.

Huang Y, Kinloch AJ. "Modelling of the toughening mechanisms in rubber-modified epoxy polymers. Part II A quantitative description of the microstructure-fracture property relationships". *J Mater Sci*, 27:2763-69, 1992.

Lauke B. "On the effect of particle size on fracture toughness of polymer composites". *Compos Sci Technol*, 68, pp. 3365–72, 2008.

Y.L. Liang, R.A. Pearson. "Toughening mechanisms in epoxy–silica nanocomposites (ESNs)", *Polymer* 50, 4895–4905, 2009.

Odegard GM, Clancy TC, Gates TS. "Modeling of mechanical properties of nanoparticle/polymer composites". *Polymer*, 46, 553-62, 2005.

Quaresimin M, Salviato M, Zappalorto M. "Strategies for the assessment of nanocomposite mechanical properties". *Compos part B-Eng.*, 43, pp. 2290–2297 2012.

Salviato M, Zappalorto M, Quaresimin M. "Plastic shear bands and fracture toughness improvements of nanoparticle filled polymers: a multiscale analytical model". In press.

Salviato M, Zappalorto M, Quaresimin M. "The effect of surface stresses on the critical debonding stress around nanoparticles". *Int J Fract*, 172:97-103, 2011.

Sevostianov I, Kachanov M. "Effect of interphase layers on the overall elastic and conductive properties of matrix composites. Applications to nanosize inclusion". *Int J Solids Struct*, 44:1304–15, 2007.

Thostenson ET, Li C, Chou TW. "Nanocomposites in context". *Compos Sci Technol*, 65:491–516, 2005.

Timoshenko SP, Goodier JN.. "Theory of Elasticity", third ed., McGraw-Hill, New York, 1970.

Williams JG. "Particle toughening of polymers by plastic void growth". *Compos Sci Technol*, 70:885–91, 2010.

Yu S, Yang S, Cho M. "Multi-scale modeling of cross-linked epoxy nanocomposites". *Polymer*, 50, 945-952, 2009.

Zamanian M., Mortezaei M, Salehnia B., Jam J.E., "Fracture toughness of epoxy polymer modified with nanosilica particles: particle size effect". *Engineering Fracture Mechanics*, doi: http://dx.doi.org/10.1016/j.engfracmech.2012.10.027, 2012

Zappalorto M, Salviato M, Quaresimin M. "A multiscale model to describe nanocomposite fracture toughness enhancement by the plastic yielding of nanovoids". *Compos Sci Technol*, 72; 1683-1691, 2012a.

Zappalorto M, Salviato M, Quaresimin M. "Assessment of Debonding-Induced Toughening in Nanocomposites". *Procedia Engineering*, 10, pp. 2982–87, 2011b.

Zappalorto M, Salviato M, Quaresimin M. "Influence of the interphase zone on the nanoparticle debonding stress". *Compos Sci Technol*, 72:49-55, 2011a.

Zappalorto M, Salviato M, Quaresimin M. "Stress distributions around rigid nanoparticles". *Int J Fract*, 176:105–112, 2012b.

5

Mixed mode (I+II) fracture toughness of polymer nanoclay nanocomposites

5.1 Introduction

Nanotechnology is a rapidly emerging technology with great potential to create new multifunctional materials, characterized by enhanced physical and mechanical properties and new improved products for numerous fields of application (Fischer H., 2003, Ajayan et al., 2004, Thostenson et al., 2005).

The most interesting aspect related to nanomodified polymers is that, different from traditional fiber reinforced composites, they are endowed with exceptionally improved properties at very low filler concentrations. The explanation of this peculiar phenomenon, often regarded as "nano-effect", can be sought in the atomic structure of the material. Indeed as the filler size is decreased to the nanoscale, the specific surface area rapidly increases, making surface properties the dominant factor and providing unique properties with widespread applications in many industrial sectors. Moreover, as the reinforcement size is comparable with that of polymeric chains, molecular interactions with the matrix produce an interphase "layer", whose properties can differ substantially from those of the constituents. The properties of this interphase zone play a very important role in the amount of energy dissipated by the different damaging mechanisms taking place at the nano scale and, in turn, on the overall mechanical properties of the nanocomposite, depending also on the filler size and geometry (Zappalorto et al., 2011a and b, Salviato et al., 2011a and b).

Dealing with the filler morphology, main differences are essentially due to the nanofiller typology, which might be distinguished in nanoclays, nanoparticles and

nanotubes. In particular nanoclay based nanocomposites have revealed to be a very promising technology in the perspective of achieving high performances at a relative low cost, especially if compared to carbon nanotubes.

Nanoclays are layered silicates of which the platelets are micro-sized in area, about 1 nm thick and disposed in stacks called tactoids. Once dispersed in the polymeric matrix three typical nanoclay morphologies are possible, namely, exfoliated, partially intercalated and phase separated. With the aim to maximize the "nano-effect", complete exfoliation is high desirable but it is far from easy to be obtained since it requires the separation of the tactoids from the primary particle, followed by the destruction of the order of the clay platelets within the tactoids. However a balance between an exfoliated and intercalated structure is often sufficient to obtained the desired property enhancements. Polymer-nanoclay nanocomposites offer exceptional performances, when compared to those of the neat polymer, in terms of flammability, barrier and mechanical properties. In particular, due to their very high aspect ratio, nanoclay platelets are suitable to improve the tensile elastic modulus of polymeric systems (see, amongst the others, (Cho and Paul, 2001, Wang et al., 2006). On the contrary, conflicting results have been reported with reference to the strength of nanoclay reinforced resins, which has been proven either to increase (Lee and Jang, 1997, Luo and Daniel, 2003) and to decrease (Bharadwaj et al., 2002, Luo and Daniel, 2003, Wang et al., 2005, Quaresimin et al., 2012b), depending on the studied system. The fracture toughness of nanomodified polymers is acknowledged to be the most important mechanical property to be studied, mainly in the perspective they are used as toughed matrixes in ternary, fiber reinforced, nanocomposites (Quaresimin et al., 2012a and 2012b). This does explain the large attention recently paid by several researchers to the study of the fracture toughness of binary nanocomposites (polymer matrix plus nanofillers) (Zerda and Lesser, 2001, Becker et al., 2002, Kornman et al., 2002, Weon and Sue, 2005, Liu et al., 2005, Subramaniyan and Sun, 2007, Quaresimin et al., 2012a).

Although in practice the stress state ahead of a crack is often of the mixed type, in the best of authors' knowledge all the previous studies dealing with the toughness of nanoclay nanocomposites are limited to pure mode I fracture, whilst extending

the analysis to other nanofillers, the only exception seems to be a recent contribution by Ayatollahi *et al.* for carbon nanotubes nanocomposites (Ayatollahi et al., 2011).

With the aim to fill this gap, in this study the mixed mode fracture behavior of an epoxy resin filled with montmorillonite nanoclays is analysed. After a preliminary investigation on tensile properties, the fracture behaviour of the nanocomposite system is studied and discussed in detail by taking advantage of the results from Single Edge Notch Bending (SENB) tests, considering four loading conditions, ranging from pure mode I to pure mode II. The effect of the mode mixity on the crack paths, fracture toughness improvements and fracture surface morphology are discussed in details as well.

Finally experimental results are compared to the predictions based on some classical mixed mode fracture criteria, discussing their degree of accuracy.

5.2 Materials and specimens used in the experimental analysis

In this study, a DGEBA-based epoxy resin (EC157 with W152LR hardener) from ELANTAS-Camattini was chosen as polymer matrix. The main mechanical properties of the adopted epoxy system, as specified by the supplier, are summarized in Table 5.1.

E	3.2 – 3.5 GPa
σ_R	68 – 76 MPa
ε_R	6 – 8 %

Table 5.1. Properties of EC157/W131 epoxy system as provided by Elantas-Camattini.

In addition, a montmorillonite clay, Cloisite 30B® from Southern Clay Products, was used as nanosized reinforcement, considering different weight fractions. 30B nanoclays are characterised by 1 nm thick lamellae, lateral dimensions from 70 to 150 nm and average d-spacing of about 18,5 Å.

Dog bones (DB) specimens as well as Single Edge Notch Bending (SENB) specimens (Figure 5.1) have been produced.

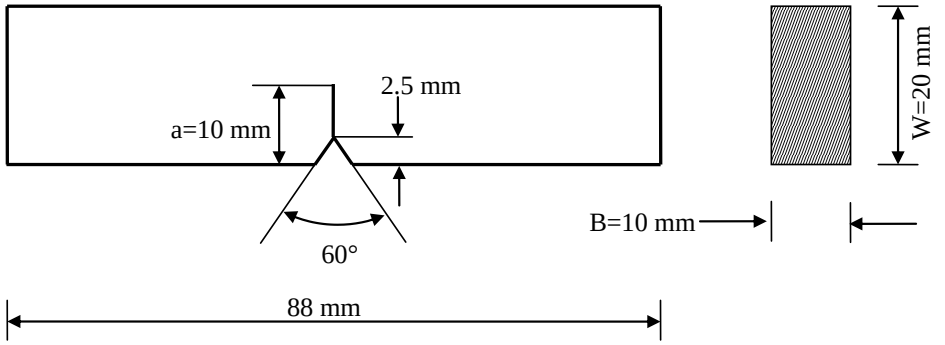

Figure 5.1. Single Edge Notch Bending (SENB) specimens used in the tests.

The specimens were manufactured according to the following steps:

1. *Dispersion of the filler within the resin*. Initially, in order to get an as good as possible dispersion and distribution of the filler, nanoclays were dispersed within the polymer resin through shear mixing followed by sonication. The shear mixing process was carried out with a DISPERMAT TU shear blender from VMA-Getzmann, at an average rate of 2000 rpm for about 1 hour. The sonication process, instead, was performed using a HIELSCHER UP 200s Sonicator, set on 140W (70% of the maximum power) and a duty cycle of 50%, for 10 minutes. After sonication, the hardener was added and the obtained blend was mixed at low rate (1000 rpm) for further 5 minutes.
2. *Degassing and moulding of the obtained blend*. As a major drawback of the shear mixing process, a large amount of air is trapped in the matrix. Thus, in order to prevent void traps and bubbles in the specimens, a degassing process was carried out. To this end, a low-vacuum pump was used to induce a very low pressure in the resin pot, promoting bubbles explosion. 1 hour of degassing process was enough to obtain a clear and translucent nanomodified resin which was later slowly poured into silicone rubber moulds. The different stages of the degassing process are shown in Figure 5.2.

As far as the SENB specimens are concerned, two further manufacturing steps were carried out:

3. *Milling and surface polishing*. In order to match the geometric recommendations by ASTM D 5045, once de-moulded, the specimens were milled to cut out the higher surface, where some inclusions and voids due to the pouring process could have been present, and polished up to the final thickness.
4. *Manual tapping and fatigue propagation up to a 10 mm long crack*. Using a razor blade, the samples were pre-cracked by manual tapping. Finally, 10 mm long cracks (half the specimen width, according to ASTM D 5045 were obtained from the artificial short cracks after some zero-to-tension-stressing fatigue cycles.

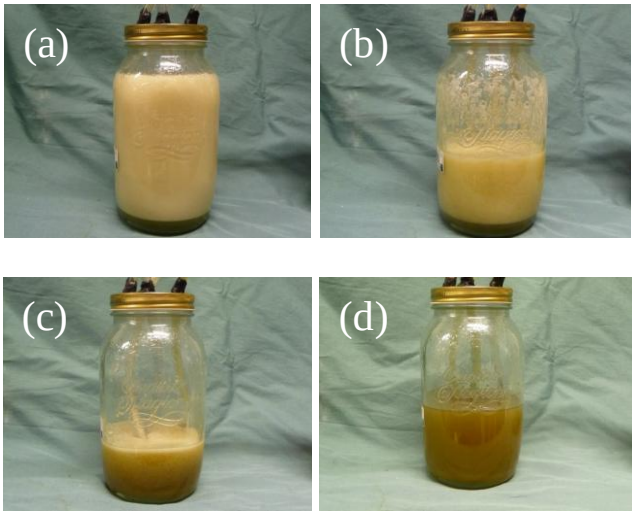

Figure 5.2. Degassing process of the nanomodified resin (5wt% of nanoclay). (a) Nanomodified resin at low pressure as just poured into the pot; (b) after 10 minutes; (c) after 25 minutes and (d) after 35 minutes. At the end of the process, the mixture is devoid of any bubble.

5.3 Experimental equipment and tests

All tests described in the following have been carried out by using a MTS 858 servo-hydraulic machine, equipped with a 2.5/25 kN load cell.

5.3.1 Tensile tests

Tensile tests on dog-bone specimens (dimensions: 2x15x110 mm) were carried out with the aim to determine the failure stress, σ_R, the elastic modulus, E, the Poisson ratio, ν, and the strain to failure, ε_f of the neat epoxy and nanomodified resins, by using a crosshead speed equal to 2 mm/min. A MTS 632.29F-30

extensometer was used for accurate strain measurements. For each material configuration, at least three specimens were tested. In all the performed tests failure took place in the centre of the specimen.

5.3.2 Single Edge Notch Bending tests

As far as SENB tests are concerned, different loading conditions have been applied, resulting in different mixed mode loadings, which ranged from pure mode I to pure mode II.

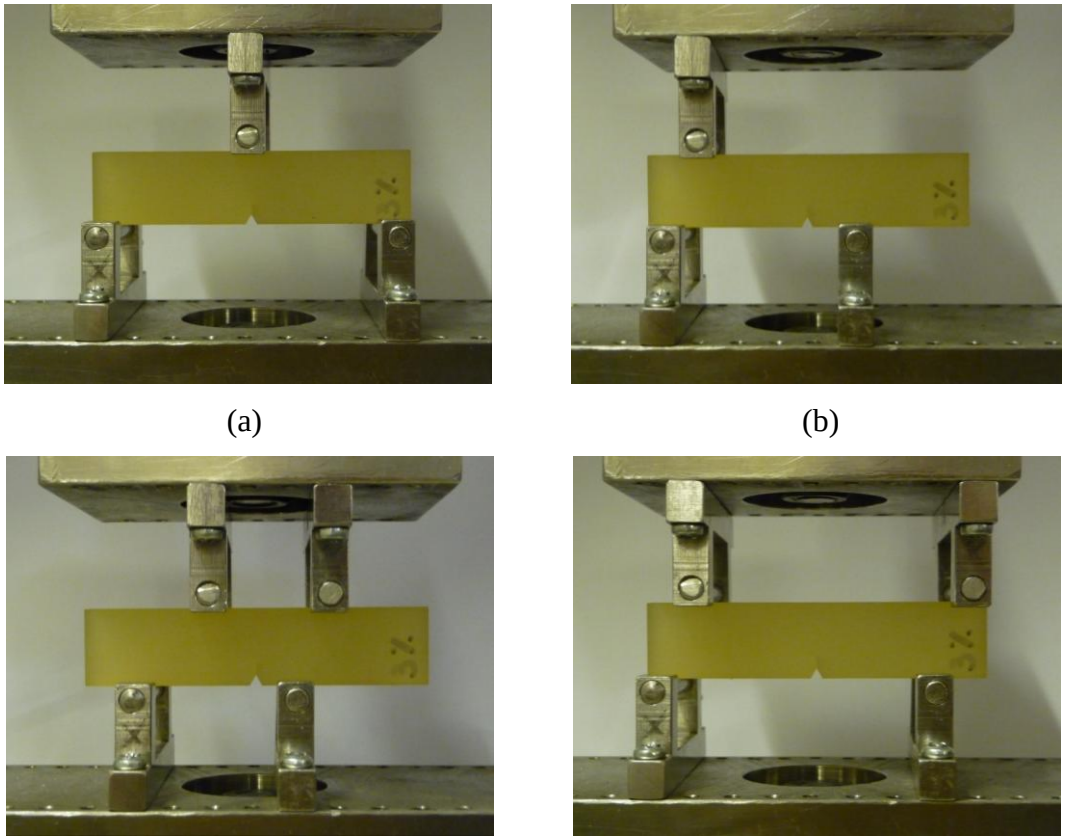

(a) (b)

(c) (d)

Figure 5.3. Pictures of the loading configurations for pure mode I tests (a), non-Symmetric three Point Bending (NS3PB) tests with ϕ=0.3 (b), non-Symmetric four Point Bending (NS4PB) tests with ϕ=1.35 (c), non-Symmetric four Point Bending (NS4PB) for pure mode II tests (d).

The fracture tests have been carried out using a crosshead speed equal to 10 mm/min, as suggested in ASTM D 5045. At least three specimens for every loading condition and every filler weight fraction were tested.

The testing device consisted of two steel plates, 18 mm thick, one fixed on the load cell, the other attached to a vertical moving ram. One or two pin supports could be mounted on each plate. Some pictures of the loading system are shown in Figures 5.3.

Mode Mixity K_{II}/ K_I	Loading condition	L_1 [mm]	L_2 [mm]	L_3 [mm]	L_4 [mm]
0.3	NS3PB	30	/	40	10
1.35	NS4PB	10	20	30	10
∞	NS4PB	30	40	40	30

Table 5.2. Details of loading conditions for mixed mode tests.

Mode I loading tests

The mode I fracture toughness was evaluated using three-point bending tests according to the ASTM-D5045-99 standard (see figure 3a). Mode I fracture toughness can be computed from the following expression (ASTM-D5045-99):

$$K_{Ic} = \frac{P_{cr}}{B W^{0.5}} f\left(\frac{a}{W}\right) \tag{5.1}$$

where P_{cr} is the critical load and, with reference to Figure 5.1, B is the specimen thickness, W the ligament, a the crack length. The suggested expression for f(a/W) is (ASTM-D5045-99):

$$f\left(\frac{a}{W}\right) = 6\left(\frac{a}{W}\right)^{0.5} \frac{\left[1.99 - \frac{a}{W}\left(1-\frac{a}{W}\right)\left(2.15 - 3.93\frac{a}{W} + 2.7\left(\frac{a}{W}\right)^2\right)\right]}{\left(1+2\frac{a}{W}\right)\left(1-\frac{a}{W}\right)^{1.5}}$$

$$0 < \frac{a}{W} < 1 \tag{5.2}$$

Mixed mode and pure mode II loadings tests

In the best of authors' knowledge there are no standardized procedure to carry out mixed mode or pure mode II fracture tests. Accordingly the same specimen size and geometry suggested for mode I loading tests (ASTM-D5045-99) have been used, while variations of mode mixity have been obtained changing the loading conditions, using non-symmetric three- and four-point bending configurations. This allowed to broaden out the range of possible loading conditions.

Besides mode I, the following fracture tests have been carried out:

1. Fracture tests under prevalent mode I loading conditions, $\phi=K_{II}/K_I \cong 0.3$. These tests have been carried out using the Non-Symmetric three Point Bending (NS3PB) configuration sketched in Fig. 5.4a and depicted in figure 5.3b;
2. Fracture tests under prevalent mode II loading conditions, $\phi=K_{II}/K_I \cong 1.35$ and under pure mode II loading conditions. These tests have been carried out using the non-symmetric four point bending (NS4PB) configuration sketched in Fig. 5.4b and depicted in figure 5.3c and 3d.

Details of loading conditions for mixed mode tests are given in Table 5.2.

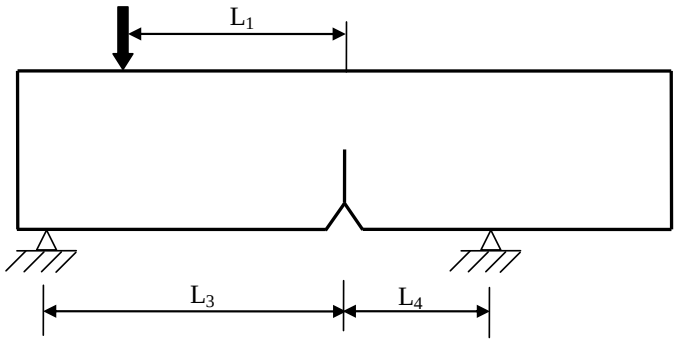

(a)

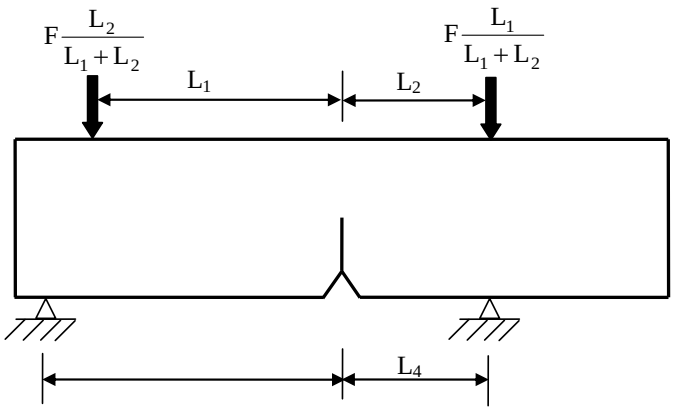

(b)

Figure 5.4. Schematic of the non-Symmetric three Point Bending (NS3PB) (a) and of the non-Symmetric four Point Bending (NS4PB) (b) loading configurations.

In all cases the crack tip stress intensity factors have been evaluated as:

$$K_I = \sigma_{ng}\ \alpha_1(a/W)\sqrt{\pi a} \qquad K_{II} = \tau_{ng}\ \alpha_2(a/W)\sqrt{\pi a} \qquad (5.3)$$

where σ_{ng} and τ_{ng} are the maximum nominal stresses on the gross section, evaluated according to the beam theory (see figure 5.1):

$$\sigma_{ng} = \frac{6M}{BW^2} \qquad \tau_{ng} = \frac{3}{2}\frac{Q}{BW} \tag{5.4a-b}$$

In Eqs. (5.4a) and (5.4b) M and Q are the bending moment and the shear force evaluated on the crack plane resulting from static equilibrium equations. Accordigly:

$$M = F\frac{L_3 - L_1}{L_3 + L_4}L_4 \qquad Q = F\frac{L_3 - L_1}{L_3 + L_4} \tag{5.5}$$

for non-symmetric three point bending (Figure 5.4a) and:

$$M = F\left(\frac{L_1 L_2}{L_1 + L_2} - \frac{L_3 L_4}{L_3 + L_4}\right) \qquad Q = F\left(\frac{L_1}{L_1 + L_2} - \frac{L_3}{L_3 + L_4}\right) \tag{5.6}$$

for non-symmetric four point bending (figure 5.4b).

Shape functions α_1 and α_2 to be used have been evaluated by means of some finite element analyses and were found, for a/W=0.5 (which was used for all specimens in the fracture tests):

$$\alpha_1 = \frac{443}{295} \qquad \alpha_2 = \frac{97}{106} \tag{5.7}$$

for NS3PB (Figure 5.4a) and:

$$\alpha_1 = -\frac{543}{322} \qquad \alpha_2 = -\frac{188}{205} \tag{5.8}$$

for NS4PB (figure 5.4b).

5.4 Experimental results

5.4.1 Tensile tests

The effects of the weight content of Cloisite 30B® nano-additives upon the nanocomposite elastic modulus, strength and strain to failure are reported in Table 3 and summarised in Figure 5.5.

The elastic modulus is only slightly affected by nano-additives with improvement up to 8.5% for a 5% wt of nanoclay content.

Conversely, nanomodification has a detrimental effect in terms of strength and

strain to failure.

Nanoclay Content	E [GPa]	σ_R [MPa]	ε_f [%]	ν
Neat epoxy	3.392 ± 0.016	68.8 ± 4.5	2.72 ± 0.32	0.347 ± 0.003
1 wt%	3.382 ± 0.079	68.0 ± 0.9	2.96 ± 0.13	0.377 ± 0.002
3 wt%	3.599 ± 0.038	57.5 ± 7.6	2.19 ± 0.32	0.373 ± 0.005
5 wt%	3.679 ± 0.116	51.5 ± 4.2	1.66 ± 0.14	0.370 ± 0.006

Table 3. Tensile properties of neat epoxy and nanomodified polymers.

Indeed the nanocomposite strength is decreased from 68.8 MPa (neat resin) to 51.5 MPa (5% wt nanoclay) with a reduction of about 25.1 %, while the addition of nanoclays leads to an initial improvement of the strain to failure (+10% for 1% wt) followed by a monotonic reduction (-39% for 5% wt). These results agree with previous findings in the literature (Bharadwaj et al., 2002, Luo and Daniel, 2003, Wang et al., 2005, Quaresimin et al., 2012b).

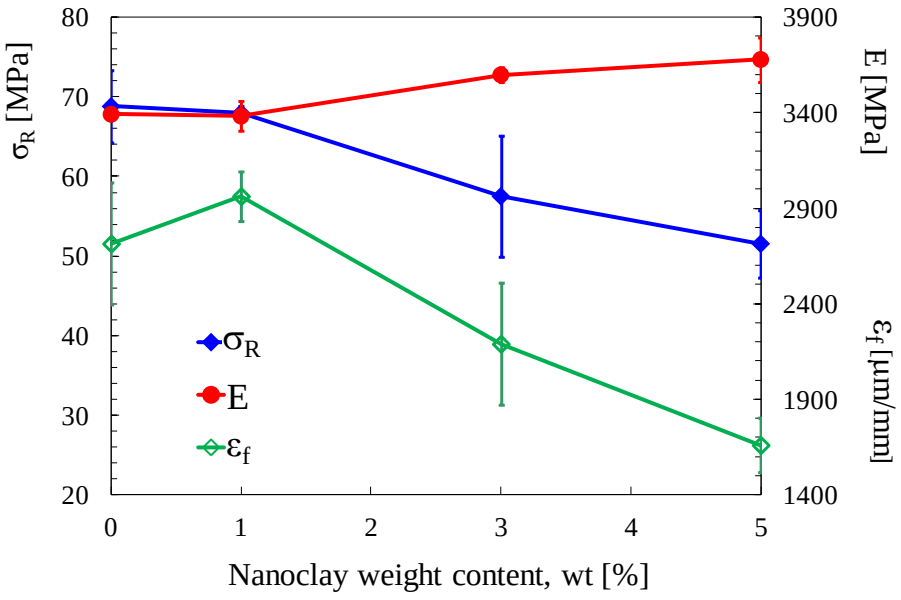

Figure 5.5. Results of tensile tests on neat and nanomodified epoxy resins.

It is finally worth mentioning that the limited reduction of the tensile strength due to nanomodification is commonly regarded as non-significant, the improvement of the polymer fracture toughness, shown later, being much more important.

5.4.2 Fracture tests

The force displacement curves of the tests, of which an example is shown in Figure 5.6 for mode I loadings, allow to conclude that during the tests the material exhibited a pure linear elastic behaviour, the force - displacement plots being linear up to the fracture load.

A synthesis of all experimental data, reconverted in terms of SIFs, is shown in Figure 5.7.

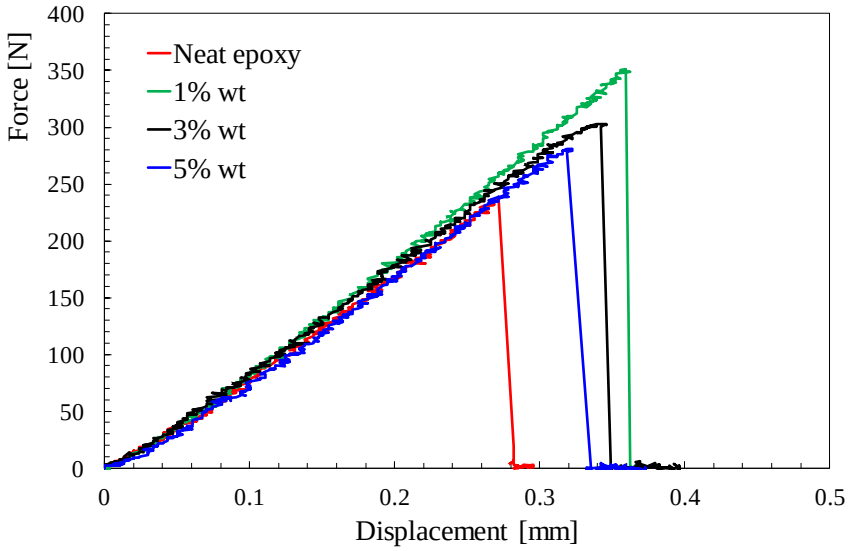

Figure 5.6. Force-displacement diagrams for neat epoxy and nanomodified specimens under mode I loading.

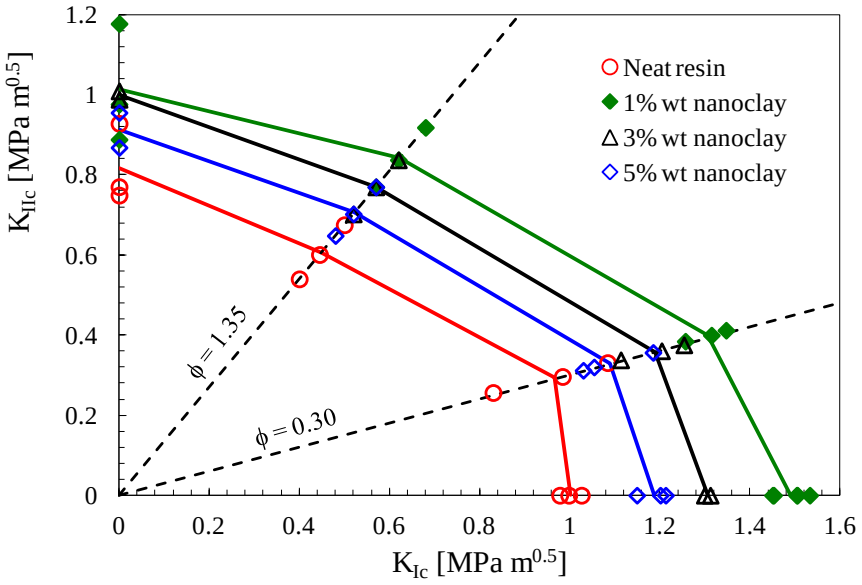

Figure 5.7. Fracture toughness of neat and nanomodified specimens under various loading conditions.

It is evident that nanomodified specimens exhibit a higher fracture toughness, independently of the loading mode.

The highest improvement was obtained under pure Mode I loading conditions, with a maximum increment of 48.7% in terms of K_{IC} for 1% wt content of nanofiller.

Ranging from pure mode I to pure mode II less pronounced improvements can be noted. Under pure Mode II loading conditions the higher fracture toughness is exhibited by specimens loaded with 1% wt content of nanofiller (+24.1%).

5.4.3 Crack paths

Some pictures of fractured specimens are shown in Figure 5.8. Mode I loaded specimens fractured along the initial crack plane (θ=0). Differently, the presence of mode II loadings gives rise to a crack tilting. For specimens under mixed mode loadings with ϕ=0.3 (figure 5.8b), the fracture took place at a measured angle θ= 36-38° with respect to the crack line. For ϕ=1.35 (figure 5.8c), θ= 44-45° while for Mode II loaded specimens (figure 5.8d) the crack tilted at about 63-65°. No clear effect of nanomodification was noted on the crack initiation angle.

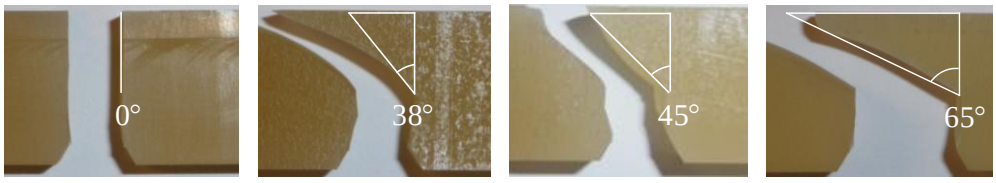

(a) (b) (c) (d)

Figure 5.8. Fracture angles for (a) Mode I, (b) mixed mode K_{II}/K_I=0.30, (c) mixed mode K_{II}/K_I=1.35 and (d) Mode II loading conditions.

5.4.4 Morphological analysis of the fracture surfaces

In order to better understand the mechanical behaviour of the nanocomposite systems at different loading conditions, a morphological analysis of the fracture surfaces was carried out by means of a Quanta400 scanning electron microscope produced by FEI.

The fracture surfaces of the neat epoxy, taken from a region close to the initial crack front, are shown in Figure 5.9, where the arrows indicate the direction of

crack propagation. It is evident that, except for some river line markings near the crack initiation site, the fracture surfaces appeared to be very smooth, independently of the investigated loading condition. Such a morphology is typical of brittle polymers.

Different, for all the analysed loading conditions, the fracture surfaces of nanomodified specimens were found very rough. An example from 5% wt nanomodified specimens is shown in Figures 5.10. All pictures have been taken from a region close to the initial crack front and the arrows indicate the direction of crack propagation. Under pure mode I loading (Figure 5.10a), the emergence of many steps throughout the whole surface can be noted. This morphology is commonly acknowledged to be due to secondary crack fronts divided by aggregates and it denotes that microcracking and subsequent microcrack coalescence in different planes have taken place.

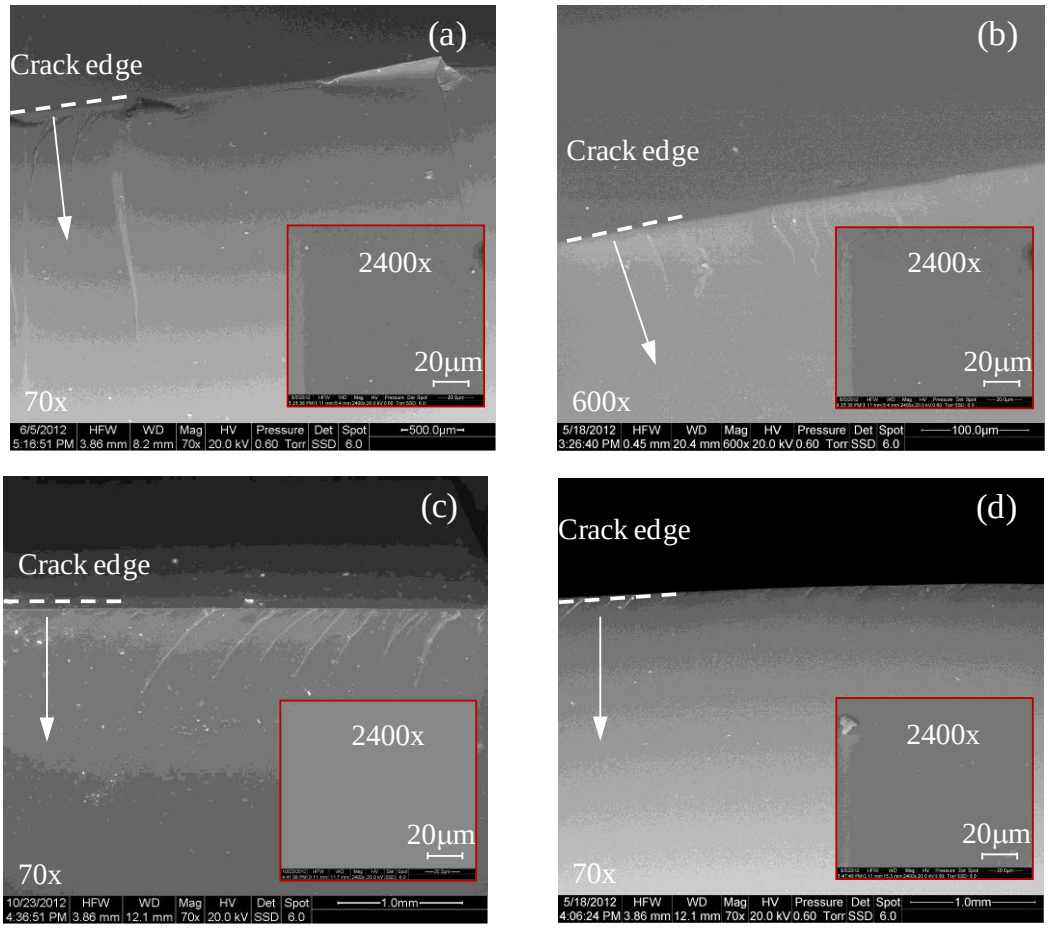

Figure 5.9. SEM micrographs of fracture surfaces for neat epoxy. Pure Mode I (a), ϕ=0.30 (b), ϕ=1.35 (c), pure Mode II (d)**.**

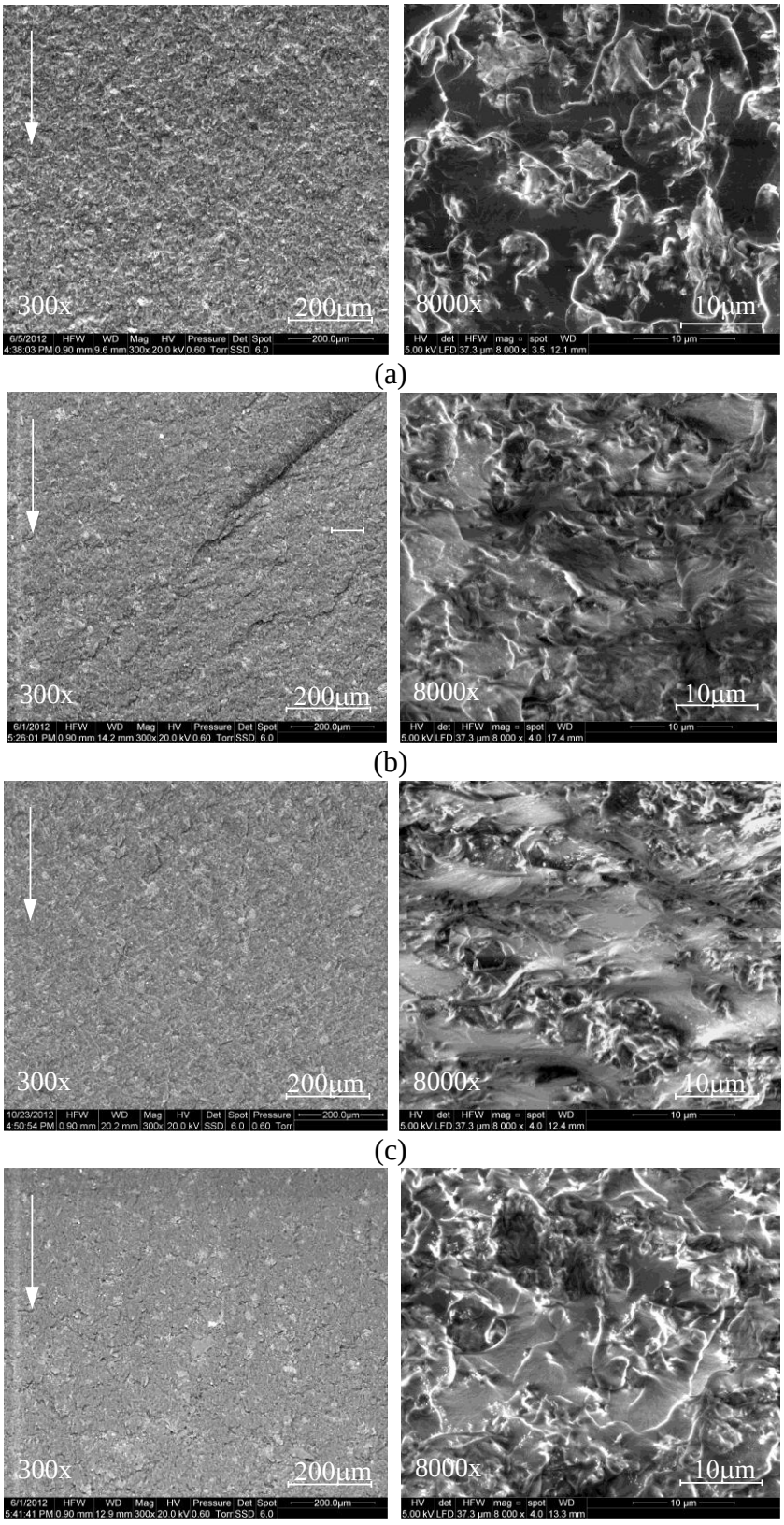

Figure 5.10. SEM micrographs of fracture surfaces for 5% wt nanocomposite. Pure Mode I (a), ϕ=0.30 (b), ϕ=1.35, Pure Mode II (d).

These phenomena, which are reasonably due to the presence of nanoclays in the epoxy resin, are the main detected toughening mechanism, which can be regarded as responsible of fracture toughness improvements exhibited by nanoclay loaded specimens. It is worth mentioning that a similar morphology was observed also by Wang *et al*. (Wang et al., 2006) for a Epoxy/Cloisite 93A system.

Figures 5.10b,c,d document that the step area density is strictly dependent on the loading mode. Indeed, higher magnification images show that, even if the toughening mechanism is the same, its extent within the process zone reduces while moving from pure mode I to pure mode II. This is compliant with experimental results discussed in previous sections, according to which the fracture toughness improvement due to nanomodification is strictly dependent on the loading mode, being higher under pure mode I loadings.

5.5 Prediction of mixed mode fracture behaviour of nanocomposites

In the past and recent literature several theoretical or empirical criteria for mixed mode fracture for brittle homogeneous materials have been proposed and validated (see, amongst the others, Erdogan and Sih, 1963, Sih, 1974, Hussain et al., 1974, Lazzarin and Zambardi, 2001, Richard et al., 2005, Araki et al., 2005, Yosibash et al., 2006). Depending on the nature of the criterion, in addition to the critical conditions required for the fracture onset, predictions for the angle of fracture initiation can be also estimated.

However it is recognised that nanocomposite fracture toughness strictly depends on the amount of energy dissipated by the damaging mechanisms taking place at the nanoscale, which are responsible for material toughening (Johnsen et al., 2007, Lauke et al., 2008, Hsieh et al., 2010, Williams 2010, Zappalorto et al., 2012a). Moreover the toughness improvements associated with nanomodification are strongly influenced by many factors, such as the filler morphology (size, geometry and distribution) and, in particular, the applied loading conditions (Zappalorto et al., 2012a and 2012b). Accordingly additional inherent difficulties are expected while modelling the mixed mode fracture behaviour of this kind of new materials.

In the following sections a brief overview of three mixed mode fracture criteria widely used in the literature, i.e. the MTS criterion (Erdogan and Sih, 1963), the S-criterion (Sih, 1974) and Richard's criterion (Araki et al., 2005) is provided. Then, with the main aim to identify a mixed mode criterion providing reliable predictions for nanomodified polymers, a comparison is carried out with the experimental results obtained in the present work.

5.5.1 Maximum tangential stress criterion (MTS criterion)

The Maximum Tangential Stress criterion (MTS) (Erdogan and Sih, 1963) assumes that the crack propagation is controlled by the maximum value of the hoop stress at the crack tip, $\sigma_{\theta\theta,max}$. In particular, the fracture initiation angle equates the direction of $\sigma_{\theta\theta,max}$ (Erdogan and Sih, 1963):

$$\theta_0 = -\arccos\left(\frac{3\phi^2+\sqrt{1+8\,\phi^2}}{1+9\,\phi^2}\right) \tag{5.9}$$

The general condition for the crack onset can instead be written as (Erdogan and Sih, 1963):

$$K_I\left[\cos\frac{\theta_0}{2}\left(\cos^2\frac{\theta_0}{2}-\frac{3}{2}\phi\sin\theta_0\right)\right]=K_{Ic} \tag{5.10}$$

5.5.2 Minimum strain energy density criterion (S criterion)

The S criterion (Sih, 1974) states that brittle fracture is controlled by the strain energy density factor S, which, under mixed mode (I+II) assumes the following quadratic form:

$$S = a_{11}K_I^2 + 2\,a_{12}K_IK_{II} + a_{22}K_{II}^2 \tag{5.11}$$

where:

$$\begin{aligned} a_{11} &= \frac{1}{16\pi\mu}\left[(1+\cos\theta)(\kappa-\cos\theta)\right] \\ a_{12} &= \frac{1}{16\pi\mu}\sin\theta\left[2\cos\theta-(\kappa-1)\right] \\ a_{22} &= \frac{1}{16\pi\mu}\left[(\kappa+1)(1-\cos\theta)+(1+\cos\theta)(3\cos\theta-1)\right] \end{aligned} \tag{5.12 a,b,c}$$

being μ the shear modulus and, for plane strain conditions, $\kappa = 3-4\nu$

The initial crack growth is assumed to take place in the direction along which the

S factor possesses a stationary (minimum) value (Sih 1974):

$$\left.\frac{\partial S}{\partial \theta}\right|_{\theta=\theta_0} = 0 \tag{5.13}$$

or, in more explicit form:

$$4\phi\cos 2\theta_0 + \left[(\kappa+1)+(\kappa-1)\phi^2\right]\sin\theta_0 - 2\cos\theta_0\left[(\kappa-1)\phi+\left(1+3\phi^2\right)\sin\theta_0\right] = 0 \tag{5.14}$$

Moreover, it is supposed that crack initiation occurs when the S factor reaches a critical value, i.e. $S=S_{cr}$. This last condition gives the following fracture locus:

$$K_I = K_{Ic}\left\{\frac{8}{\kappa-1}\left[\frac{1}{16}(1+\cos\theta_0)(\kappa-\cos\theta_0)+\frac{1}{8}\sin\theta_0(2\cos\theta_0-(\kappa-1))\phi+\right.\right.$$
$$\left.\left.+\frac{1}{16}\left((\kappa+1)(1-\cos\theta_0)+(1+\cos\theta_0)(3\cos\theta_0-1)\right)\phi^2\right]\right\}^{-0.5} \tag{5.15}$$

5.5.3 Richard's criterion

According to Richard's criterion (Richard et al., 2005, Araki et al., 2005), the mixed mode fracture locus is described by the following equation:

$$\frac{K_I}{K_{Ic}}+\frac{K_{II}^2}{K_{IIc}^2}=1 \tag{5.16}$$

where K_{Ic} and K_{IIc} are the pure mode I and pure mode II fracture toughness, respectively.

Eq. (5.16) can be equivalently rewritten as follows:

$$K_I = K_{Ic}\left[1-\left(\frac{K_{II}}{K_{IIc}}\right)^2\right] \tag{5.17}$$

As a major drawback with respect to the previous ones, Richard's criterion requires fracture toughness under pure mode I, K_{Ic}, and pure mode II, K_{IIc}, to be known.

5.6 Discussion

The predictions based on the mixed mode fracture toughness criteria discussed in the previous sections have been compared with the experimental data obtained in the present work. The comparison is shown in Figures 5.11-14 for different nanoclay contents.

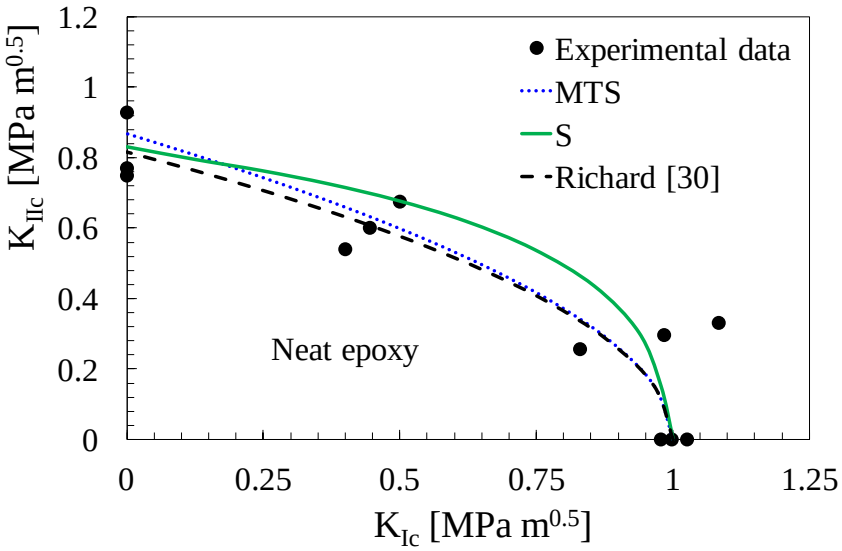

Figure 5.11. Comparison between predicted fracture toughness values and experimental results. Cracked specimens made of neat epoxy.

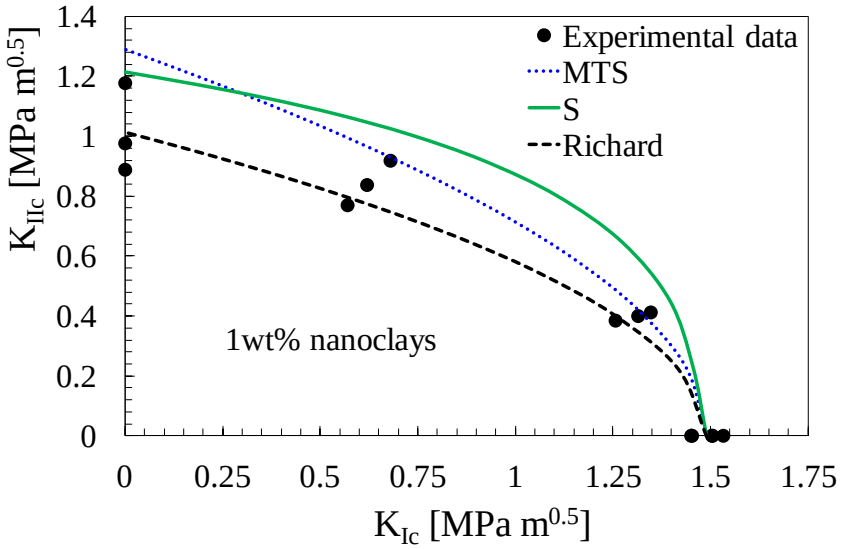

Figure 5.12. Comparison between predicted fracture toughness values and experimental results. Cracked specimens made of epoxy resin filled with 1% wt of nanoclays.

Figure 5.11 shows that the results from specimens made of pure epoxy are well predicted by almost all the fracture criteria before mentioned.

Differently, in the case of nanomodified specimens, the accuracy of the fracture criteria based only on K_{Ic} is poorer and the best prediction of mixed mode fracture toughness is provided by Richard's criterion (see figures 5.12-14).

In order to give a quantitative analysis of the accuracy of the different approaches, the sum of the squared residuals:

$$\Delta_r = \sum_n \left(K_{I,i} - K_{I,predicted}\right)^2 \quad (5.18)$$

were computed and reported Figure 5.15. It is evident that the best, among the approaches requiring only K_{IC}, is the S criterion which provides the lowest value

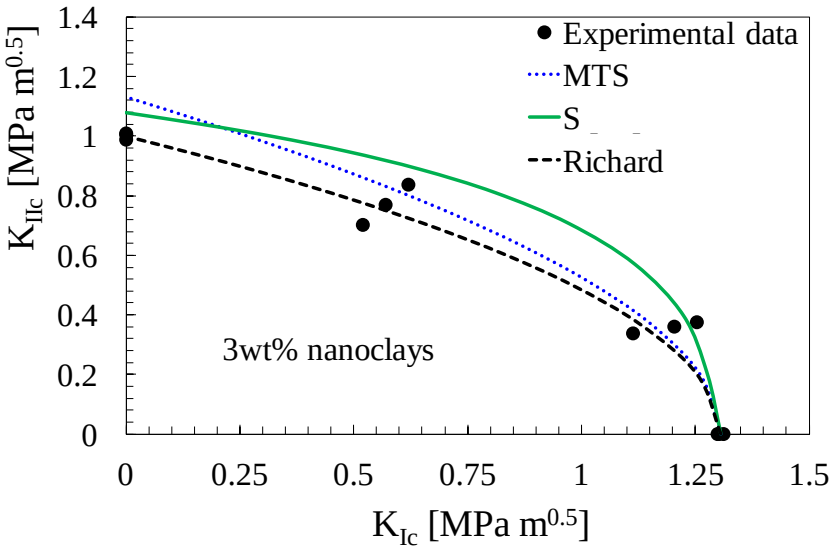

Figure 5.13. Comparison between predicted fracture toughness values and experimental results. Cracked specimens made of epoxy resin filled with 3% wt of nanoclays.

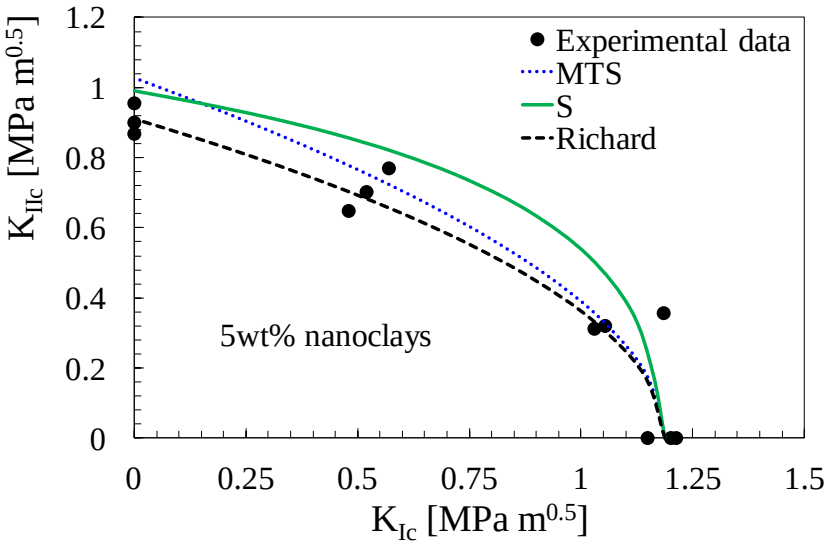

Figure 5.14. Comparison between predicted fracture toughness values and experimental results. Cracked specimens made of epoxy resin filled with 5% wt of nanoclays.

of Δ_r for almost all the nanoclay contents. However, in general, the best

predictions are set by Richard's criterion which always gives the lowest values of Δ_r. It is also noteworthy that, in general, the worst prediction are given for the case of 1%wt which is related to the higher toughness increment.

The inaccuracy of classical mixed mode fracture criteria, MTS and S, for results from nanomodified polymers can be due to the emergence of different damaging mechanisms taking place at the microscale and nanoscale which can be influenced by the loading mode, as discussed in section 5.4.4.

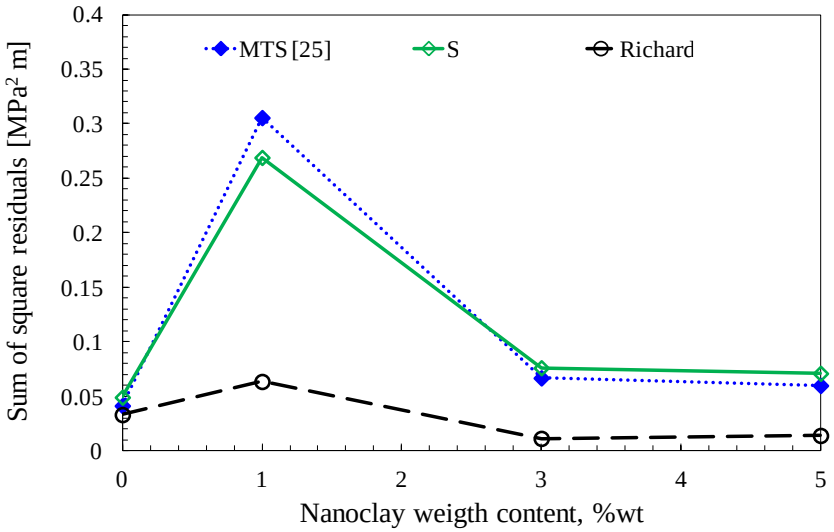

Figure 5.15. Comparison of the different fracture criteria in terms of Δ_r.

Richard's criterion, instead, is capable of better predictions since it is based either on K_{IC} or on K_{IIC}, thus accounting, in some way, for the change of material damaging moving from pure mode I to pure mode II.

5.7 Conclusions

In the present work the effects of nanoclay addition on the fracture behaviour of an epoxy resin under mixed mode (I plus II) loadings have been studied by analysing the results from Single Edge Notch Bending (SENB) tests. The results allow to conclude that, for weight contents up to 5wt%, nanomodification significantly enhances the fracture toughness of the epoxy resin upon the entire

range of mixed mode loadings, the improvements being dependent on the mode mixity ratio.

Experimental results have been compared to the theoretical predictions based three mixed mode fracture criteria for brittle homogeneous solids. The results from specimens made of pure epoxy are well predicted, almost independently of the approach used for the synthesis. Conversely, as far as the results from specimens made of nanomodified polymer are concerned, the agreement with theoretical predictions by one-parametrical approaches is worse. This can be thought of as linked to the emergence, due to nanomodification, of different damaging mechanisms depending on the mode mixity.

Better predictions were obtained using Richard's criterion.

Bibliography of chapter 5

Ajayan, P.M., Schadler, L.S., Braun, P.V. "Nanocomposite science and technology". Wiley-VCH, Weinheim, 2004.

ASTM D 5045. Standard Test Methods for Plane-Strain Fracture Toughness and Strain Energy Release Rate of Plastic Materials (1999).

Ayatollahi MR, Shadlou S, Shokrieh MM. "Mixed mode brittle fracture in epoxy/multi-walled carbon nanotube nanocomposites". *Eng Fract Mech*, 78: 2620–2632, 2011.

Becker O, Varley R, Simon G. "Morphology, thermal relaxations and mechanical properties of layered silicate nanocomposites based upon high-functionality epoxy resins". *Polymer*, 43: 4365–4373, 2002.

Bharadwaj RK, Mehrabi AR, C Hamilton, Trujillo C, Murgaa M, Fan R, Chavira A, Thompson AK. "Structure-property relationships in cross-linked polyester–clay nanocomposites". *Polymer*, 43 :3699–705, 2002.

Cho JW, Paul DR. "Nylon 6 nanocomposites by melt compounding". *Polymer*, 42: 1083–94, 2001.

Erdogan F, Sih GC. "On the crack extension in plates under plane loading and transverse shear". *Trans ASME, J Basic Eng*, 85: 519–27, 1963.

Fischer H. "Polymer nanocomposites: from fundamental research to specific applications". *Mater Sci Eng C, 23*: 763–72, 2003.

Hsieh TH, Kinloch AJ, Masania K, Taylor AC, Sprenger S. "The mechanisms and mechanics of the toughening of epoxy polymers modified with silica nanoparticles". *Polymer*, 51:6284-6294, 2010.

Hussain MA, Pu SL, Underwood J. "Strain energy release rate for a crack under combined mode I and Mode II". Fracture Analysis, ASTM STP 560 American Society for Testing and Materials, Philadelphia 2-28 (1974).

Johnsen BB, Kinloch AJ, Mohammaed RD, Taylor AC, Sprenger S. "Toughening mechanisms of nanoparticle-modified epoxy polymers". *Polymer*, 48:530-41, 2007.

Kornman X, Thomann R, Mulhaupt R, Finter J, Berglund LA. "High Performance Epoxy-Layered Silicate Nanocomposites". *Polym Eng Sci*, 42: 1815-1826, 2002.

Lauke B. "On the effect of particle size on fracture toughness of polymer composites". *Compos Sci Technol*, 68:3365–72, 2008.

Lazzarin P, Zambardi R. "A finite-volume-energy based approach to predict the static and fatigue behaviour of components with sharp V-shaped notches". *Int J Fract*, 112: 275-298, 2001.

Lee DC, Jang LW. "Preparation and characterization of PMMA-clay hybrid composite by emulsion polymerization". *J Appl Polym Sci*, 61: 1117–22, 1996.

Liu TX, Liu ZH, Ma KX, Shen L, Zeng KY, He CB. "Morphology, thermal and mechanical behavior of polyamide 6/layered-silicate nanocomposites". *Compos Sci Technol*, 63: 331–337, 2003.

Liu W, Hoa SV, Pugh M. "Fracture toughness and water uptake of high-performance epoxy/nanoclay nanocomposites". *Compos Sci Technol*, 65: 2364–2373, 2005.

Luo J, Daniel IM. "Characterization and modeling of mechanical behavior of polymer/clay nanocomposites". *Compos Sci Technol*, 63: 1607–16, 2003.

Odegard, G.M., Clancy, T.C., Gates, T.S. "Modeling of mechanical properties of nanoparticle/polymer composites". *Polymer* 46, 553-62, 2005.

Quaresimin M, Salviato M, Zappalorto M. "Fracture and interlaminar properties of clay-modified epoxies and their glass reinforced laminates". *Eng Fract Mech*, 81: 80-93, 2012a.

Quaresimin, M., Salviato, M., Zappalorto, M. "Strategies for the assessment of nanocomposite mechanical properties". *Compos. part B-Eng*. 43, 2290–97, 2012b.

Richard HA, Fulland M, Sander M. "Theoretical crack path prediction". *Fatigue Fract Eng Mater Struct*, 28: 3–12, 2005.

Salviato, M., Zappalorto, M., Quaresimin, M. "Plastic Yielding Around Nanovoids". *Procedia Engineering* 10, 3325-30, 2011a.

Salviato, M., Zappalorto, M., Quaresimin, M. "The effect of surface stresses on the critical debonding stress around nanoparticles". *Int. J. Fract.* 172, 97-103, 2011b.

Salviato M, Zappalorto M, Quaresimin M., "Plastic shear bands and fracture toughness improvements of nanoparticle filled polymers: a multiscale analytical model". In press.

Sih GC. "Strain-energy-density factor applied to mixed mode crack problems". *Int J Fract*, 10: 305-21, 1974.

Subramaniyan AK, Sun CT. "Toughening polymeric composites using nanoclay: Crack tip scale effects on fracture toughness". *Compos Part A-Appl S*, 38: 34–43,

2007.

Thostenson, E.T., Li, C., Chou, T.W. "Nanocomposites in context". *Compos. Sci. Technol.* 65, 491–516, 2005.

W. Araki , K. Nemoto, T. Adachi, A. Yamaji. Fracture toughness for mixed mode I/II of epoxy resin. *Acta Materialia* 53, 869–875, 2005.

Wang K, Chen L, Wu J, Toh ML, He C, Yee AF. "Epoxy Nanocomposites with Highly Exfoliated Clay: Mechanical Properties and Fracture Mechanisms". *Macromolecules*, 38: 788-800, 2005.

Wang L, Wang K, Chen L, Zhang Y, He C. "Preparation, morphology and thermal/mechanical properties of epoxy/nanoclay composite". *Compos Part A-Appl S*, 37: 1890–1896, 2006.

Weon JI, Sue HJ. "Effects of clay orientation and aspect ratio on mechanical behaviour of nylon-6 nanocomposite". *Polymer*, 46: 6325–6334, 2005.

Williams JG. "Particle toughening of polymers by plastic void growth". *Compos Sci Technol*, 70:885–91, 2010.

Yosibash Z, Priel E, Leguillon D. "A failure criterion for brittle elastic materials under mixed-mode loading". *Int J Fract*, 141: 291–312, 2006.

Yu, S., Yang, S., Cho, M. "Multi-scale modeling of cross-linked epoxy nanocomposites". *Polymer* 50, 945-52, 2009.

Zappalorto, M., Salviato, M., Quaresimin, M. "A multiscale model to describe nanocomposite fracture toughness enhancement by the plastic yielding of nanovoids". *Compos. Sci. Technol*. 72, 1683-1691, 2012a.

Zappalorto, M., Salviato, M., Quaresimin, M. "Assessment of Debonding-Induced Toughening in Nanocomposites". *Procedia Engineering* 10, 2982–87, 2011b.

Zappalorto, M., Salviato, M., Quaresimin, M. "Influence of the interphase zone on the nanoparticle debonding stress". *Compos. Sci. Technol.* 72, 49-55, 2011a.

Zappalorto, M., Salviato, M., Quaresimin, M. "Stress distributions around rigid nanoparticles". *Int. J. Fract.* 176, 105–112, 2012b.

Zerda AS, Lesser AJ. "Intercalated Clay Nanocomposites: Morphology, Mechanics, and Fracture Behavior". *J Polym Sci Pol Phys*, 39: 1137–1146, 2001.

6

Fracture and interlaminar properties of clay-modified epoxies and their glass reinforced laminates

6.1 Introduction

The chance to get substantial improvements of mechanical properties at low nanofiller volume fraction has aroused significant interest in the use of nano-modified epoxy resins.

It is well acknowledged that to achieve these results, the nano-filler must be sufficiently dispersed and compatible with the epoxy resin. This requirement leads to a number of processing challenges, which depend on the adopted nano-filler.

As far as layered silicates are concerned, the dimensions of the clay platelets are of the order of microns in area, around 1 nm thick and arranged in stacks (tactoids). Complete exfoliation requires the separation of the tactoids from the primary particle, followed by the destruction of the order of the clay platelets within the tactoids.

In principle, a full exfoliation of the clay platelets will maximise the strength, modulus and toughness improvement (Vaia and Giannelis, 1997, Alexandre and Dubois, 200). However a balance between an exfoliated and intercalated structure might be preferable to maximise enhancements in the mentioned properties (Zilg et al., 1999), intercalated tactoids promoting some toughening mechanisms such as crack deflection or crack pinning (Boo et al., 2006).

The weak out-of-plane inter-laminar properties of laminates are definitely those with the greatest potential and need to be improved. Indeed, for ternary laminates, matrix toughness improvement itself is the most interesting and promising result,

the interlaminar fracture behaviour of traditional composites being a weak matrix dominated property (Quaresimin et al., 2012b).

Unluckily, the research performed to date, aimed at translating resin properties to the fibre reinforced composite, has met with changing fortunes. Rice *et al.* (Rice et al., 2001) reported a 12% improvement in modulus for aerospace composite materials at 2 wt% of organosilicate, without improvements in other mechanical properties. Timmerman *et al.* (Timmerman et al., 2001), reported negligible improvements in mechanical properties of nanoclay composites compared to traditional composites. However, they reported a significant reduction in transversal microcracking during cryogenic cycling thus indicating the need for careful selection of nanoclay concentration and surface modification. Becker *et al.* (Becker et al., 2003) have shown that improvements in crack opening fracture toughness can be achieved at low levels of clay addition. Quaresimin and Varley (Quaresimin and Varley, 2008) reported "selective" improvements in toughness properties of carbon/clay-modified epoxy laminates due to the clay distributions: mode I toughness was slightly decreased while mode II slightly increased with respect to the values for neat epoxy laminates. The same behaviour was seen also for vapour grown carbon fibers (VGCF) modified laminates.

This chapter presents the results of the ongoing studies carried out by the author on the effect of nano-modification and its industrial potential by discussing the experimental results obtained on neat and nano-modified epoxy, as well as on neat and nano-modified epoxy laminates (ternary laminates).

After a brief description of the adopted materials and the manufacturing process, chosen for their industrial potential, the experimental results obtained on nanomodified resins and laminates as well as investigations on the material morphology will presented and discussed.

6.2 Materials

A DGEBA-based epoxy resin (EC157) from Elantas-Camattini was used as matrix polymer in this study. Due to a very low viscosity and long average pot life at 25 °C, it is especially suited for resin infusion techniques. In addition, an amminic hardener (W131) has been used. The fraction of this component has been

the one suggested by the manufacturer for the neat epoxy (3:1) for each investigated nanofiller content.

The main mechanical properties of the adopted epoxy system, as specified by the supplier, are summarized in Table 6.1.

E	3.2 – 3.5 GPa
σ_R	68 – 76 MPa
ε_R	6 – 8 %

Table 6.1. Properties of EC157/W131 epoxy system by Elantas-Camattini.

Nano-modification was achieved by using two different kind of commercial nanoclay, namely RXG7000® and Cloisite 30B® from Southern Clay Products (USA). They are surface modified lamellae of montmorillonite, 1 nm thick and with lateral dimensions from 70 to 150 nm according to the product data sheet supplied. The specific surfactants allow to improve the hydrophobicity of the clay. The surface of 30B lamellas is treated by a methyl, tallow, bis-2-hydroxyethyl, quaternary ammonium salt while RXG7000 one by a dimethyl, hydrogenated tallow, 2-ethylhexyl quaternary ammonium salt.

Finally a twill glass fibre fabric VV-350T with generic sizing supplied by G. Angeloni S.r.l. has been used as reinforcement for neat and nano-modified epoxy laminates.

6.3 Nanocomposite and laminate manufacturing

The nanoclays were dispersed in the resin through a shear mixing (SM) process carried out with a DISPERMAT TU shear blender from VMA-Getzmann (see figure 6.1a).

The nanoclays were added into the resin while mixing at an average rate of about 3500 rpm; this was kept on for about 1 hour, in order to get an as good as possible distribution and dispersion of the nanofiller within the resin, promoting nanoclays intercalation/exfoliation and breaking of nanoclay clusters.

To reach finer results, the obtained system was then sonicated by means of a HIELSCHER UP 200s SONICATOR (figure 6.1b). The sonication process was

always operated at the maximum power amplitude of 200 W; conversely, various duty cycles (25%, 50%, 75%) were chosen, in order to investigate the effect of this parameter on the fracture toughness.

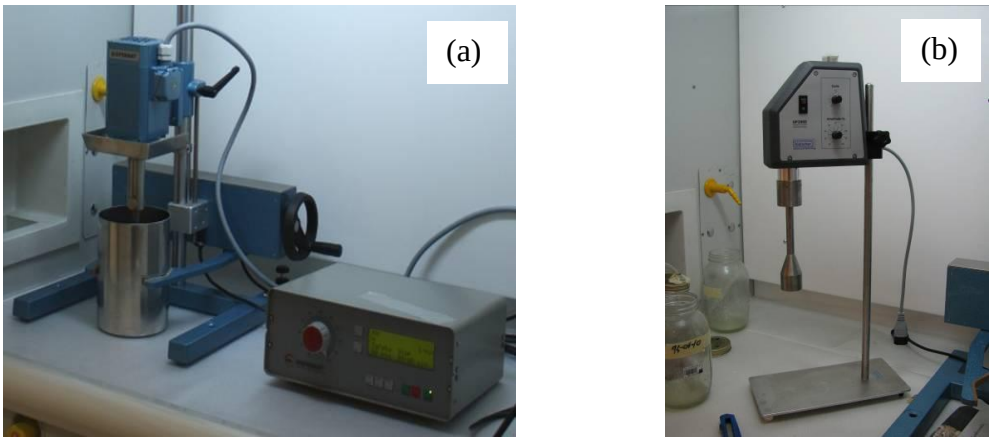

Figure 6.1. Shear blender (a) and sonicator (b) used for material preparation.

The process was continued for about 40 minutes, until the hardener was added. Finally, SM of the overall system followed for further 10 minutes, just to improve the resin-hardener mixing. During the entire process the resin has been cooled by an external bath suitable to avoid temperature rise and possible resin overheating.

As a major drawback of the shear mixing process, an amount of air was trapped making the obtained system foamy (figure 6.2a). Then, before moulding, an extensive degassing process was carried out in order to reduce the amount of trapped air and, consequently, to avoid the presence of voids in the matrix.

A low-vacuum pump has been used to induce a very low pressure in the resin's pot and to promote bubbles explosion. After 30 minutes most of air was released providing a brownish mixture (figure 6.2b). At the end of the degassing process, the modified resin was devoid of any bubble and translucent (figure 6.2c).

CT specimens were manufactured by simply pouring the resin into a silicone mould. The dimensions of the specimens were in agreement with the geometric specifications suggested by ASTMD 5045-99.

Laminates, instead, were fabricated by vacuum infusion of the degassed neat or nanomodified resin into a vacuum bag, where 16 layers of twill glass fabric were laid up. The resulting laminate thickness was about 4 mm and the volumetric

fraction of fibres after infusion was about 53% as estimated by means of thermogravimetric analyses. The infusion system is shown in Figure 5.3.

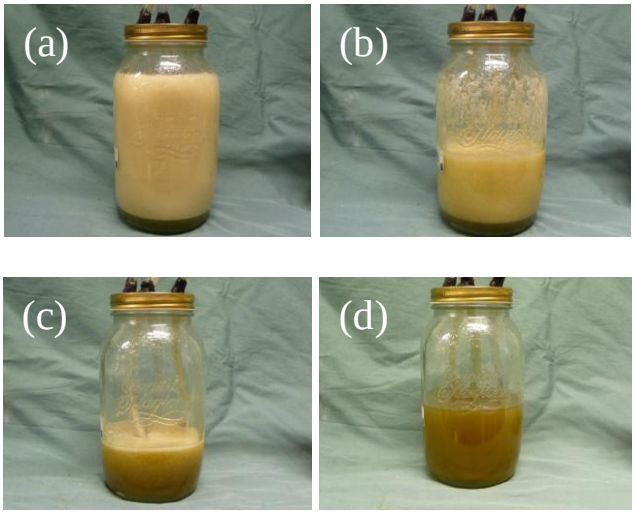

Figure 5.2. Degassing process of the nanomodified resin (5wt% of nanoclay). (a) Nanomodified resin at low pressure as just poured into the pot; (b) after 10 minutes; (c) after 25 minutes and (d) after 35 minutes. At the end of the process, the mixture is devoid of any bubble (Quaresimin et al., 2012a).

All the fabric layers were placed with their warp direction parallel to the longitudinal direction of the mould. A teflon® film 50 μm thick has been used to create a pre-crack on the DCB specimens. Geometry and size of specimens were those suggested by ASTMD 5528-01.

Demoulding has been performed after complete curing at room temperature, followed by a post curing in a oven at a 60 °C temperature for 12 hours.

6.4 Morphological analysis

The morphology of the cured systems has been investigated using Scanning Electron Microscopy, in order to identify the presence of nanofiller agglomerates.

As an example, figures 6.4,5 and 6.6 report some SEM images for 1,3 and 5wt% loaded resins showing a different morphology for 30B and RXG7000 nanocomposites. At 1%wt some traces of clay agglomeration are present for both the nanofillers even if it must be noticed that RXG7000 agglomerates are smaller (size about 15 μm) than 30B ones (size about 20 μm). Figures 6.4a,b,c and d show some example of the reported clay cluster. For higher contents, in the case of 30B

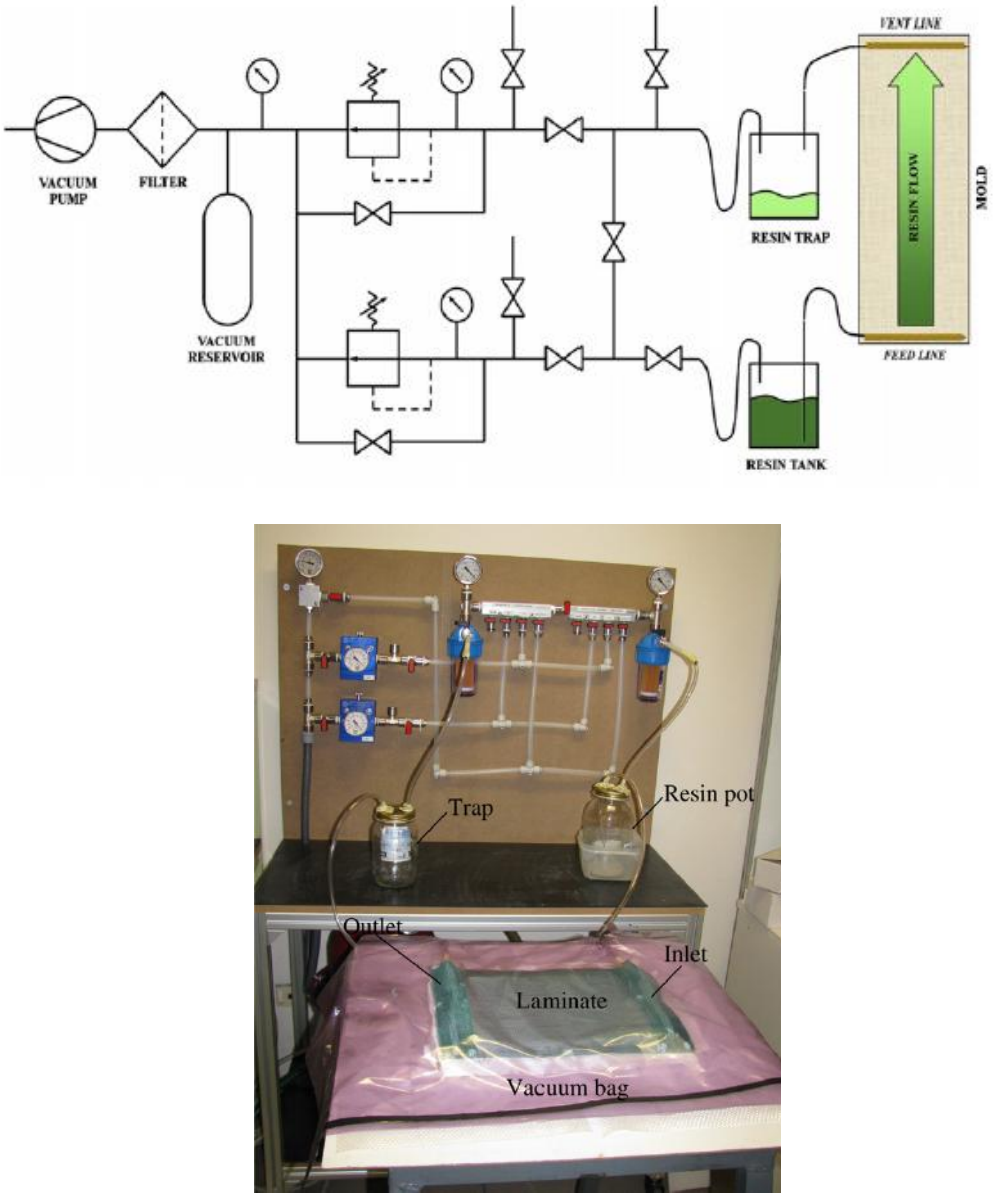

Figure 6.3. Schematic representation, (a), and picture, (b), of the infusion system (Quaresimin et al., 2012a).

the dimensions of the agglomerates seems comparable to the ones reported for 1%wt even if their content is more elevated while, in the RXG7000 case, the dispersion of the clay seems good even at 5wt%. As a general trend for all the clay contents under investigation, RXG7000 seems to be better dispersed than 30B. A different morphology for 30B and RXG7000 nanoclays was expected as they differ for the organic modifier. Similar morphologies have been reported by other authors (Kornmann 2001 and 2002, Zerda and Lesser, 2001, Becker et al., 2002).

In order to further investigate the morphology of the nanocomposite systems, a XRD analysis has been carried out with the help of Dr. Andrea Dorigato (University of Trento, Italy). The results are summarised in Table 6.2 and the XRD patterns of the nanocomposites containing 1 and 3 wt % of both 30B and RXG7000 clays are represented in Figure 6.7. For the 1 and 3 wt% 30B the reflection peaks are located at 2.62° (d-spacing: 33.7 Å) and at 2.57° (d-spacing: 34.3 Å) respectively. In the case of RXG7000, the reflection peaks of the 1 and 3 wt% specimens are located at 3.00° (d-spacing: 29.4 Å) and 2.91° (d-spacing: 30.3 Å) respectively.

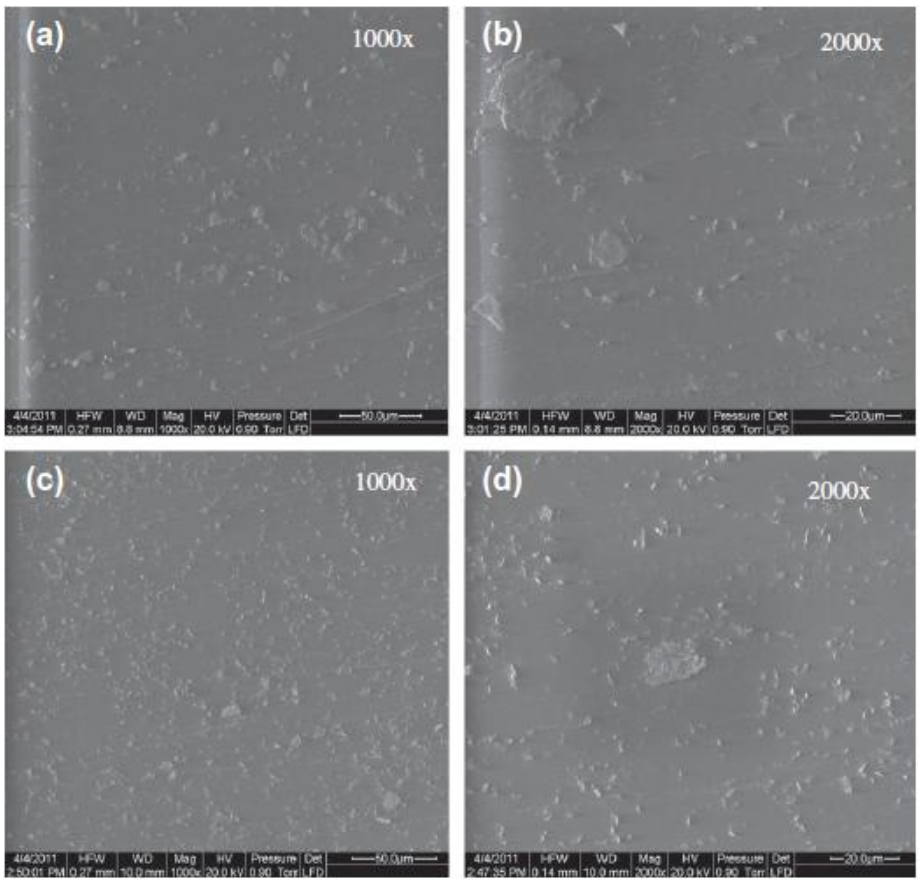

Figure 6.4. Scanning electron micrographs at different magnification of 1%wt clay-loaded resins. 30B nanoclays (a, b) and RXG7000 nanoclays (c, d) (Quaresimin et al., 2012a).

Considering that both the organoclays are sold by the manufacturer with a d-spacing of about 18.5 Å, these values indicate a rather good degree of intercalation of the nanofiller. It is worth noting that the level of intercalation does

not seem to be affected by the amount of organoclay either in the 30B or in the RXG7000 case. Moreover, the 30B shows a slightly more pronounced intercalation than the RXG7000 due to the greater hydrophilicity of its organo-modifier.

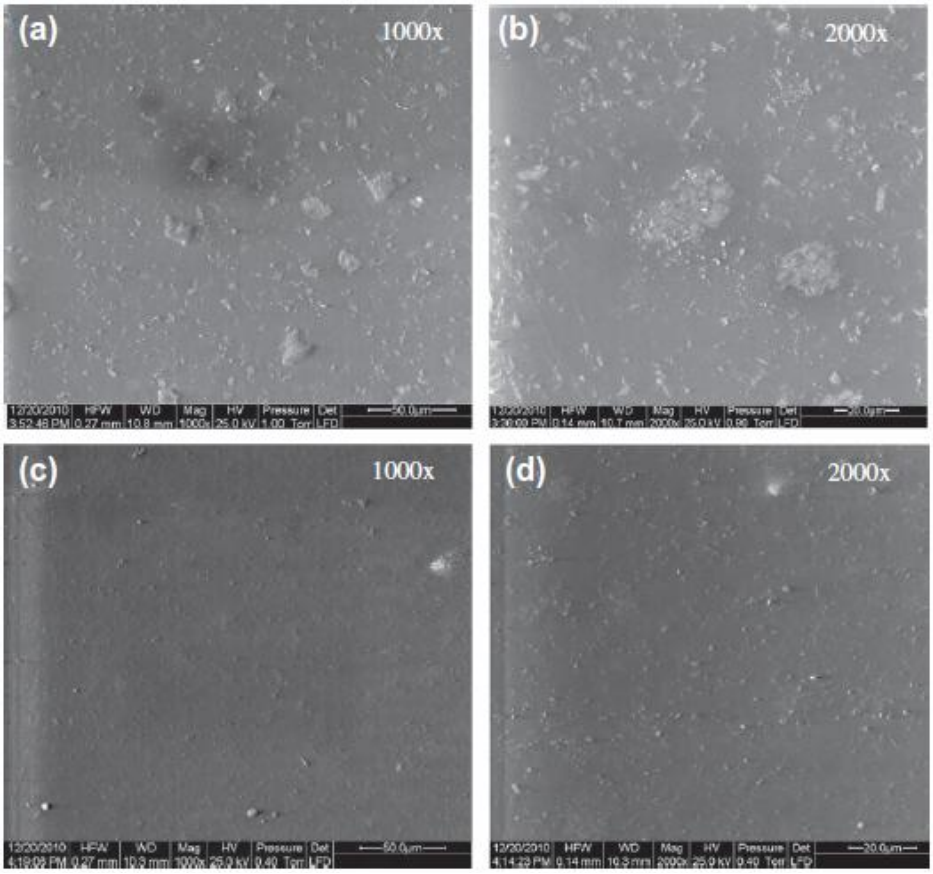

Figure 6.5. Scanning electron micrographs at different magnification of 3%wt clay-loaded resins. 30B nanoclays (a, b) and RXG7000 nanoclays (c, d) (Quaresimin et al., 2012a).

The results, on the one hand, indicate that a partial exfoliation and a good intercalation has been achieved with both the clays. On the other hand, the presence of large agglomerates does suggest the need of further investigations in order to optimise the manufacturing process and then, in turn, the material morphology.

A morphological analysis has been carried out also on nanomodified epoxy laminates with the aim to identify possible defects and voids due to the

manufacturing process and to analyse the nanofiller dispersion within the laminate layers.

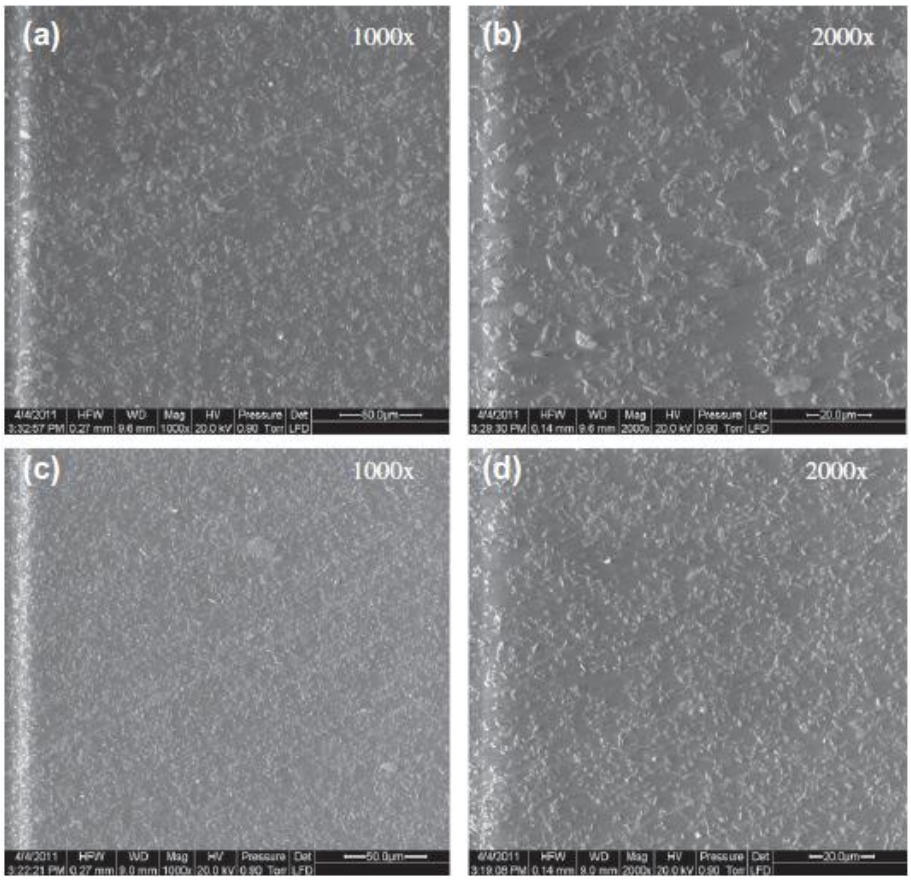

Figure 6.6. Scanning electron micrographs at different magnification of 5%wt clay-loaded resins. 30B nanoclays (a, b) and RXG7000 nanoclays (c, d) (Quaresimin et al., 2012a).

Optical microscopy images have been taken from the inlet and outlet of the infusion on both neat resin and nano-modified resin laminates revealing a good global quality and the absence of voids, as can be seen in Figure 6.8 a,b.

Specimen	2θ (°)	d (Å)
30B 1 wt.%	2.62	33.7
30B 3 wt.%	2.57	34.3
RXG7000 1 wt.%	3.00	29.4
RXG7000 3 wt.%	2.91	30.3

Table 6.2. d-spacing for different clays and weight contents (Quaresimin et al., 2012a).

Some SEM images of 3wt% nanomodified laminates have also been taken (see Figure 6.9), showing again the absence of voids and the emergence of clusters within the layers, whose size is comparable to that reported for the nanomodified resin at the same filler content.

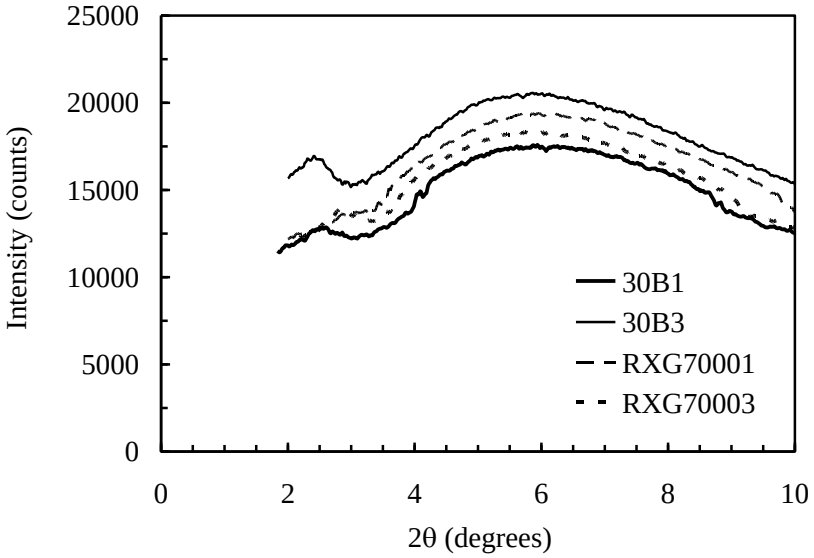

Figure 6.7. XRD patterns of nanocomposites containing different clay concentrations (Quaresimin et al., 2012a).

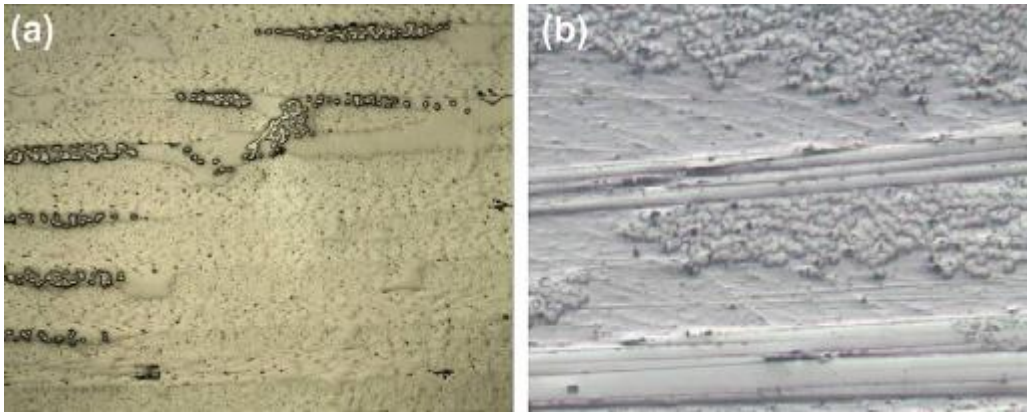

Figure 6.8. Micrographs of a typical neat epoxy laminate produced by vacuum infusion revealing a good overall quality and the absence of voids either in the inlet (a) or in the outlet (b) of the infusion (Quaresimin et al., 2012a).

In this situation it was considered non-essential to further investigate morphology using TEM analysis.

6.5 Experimental results and discussion

The experimental program included the following tests:

- tensile tests on the neat and nano-modified epoxy;
- mode I tests on the neat and nano-modified epoxy (CT specimens);
- mode I tests on neat and nano-modified epoxy laminates (DCB specimens);
- interlaminar shear tests on neat and nano-modified epoxy laminates;
- fatigue tests on the neat and nano-modified epoxy (CT specimens);
- preliminary fatigue tests on neat and nano-modified epoxy laminates (DCB specimens).

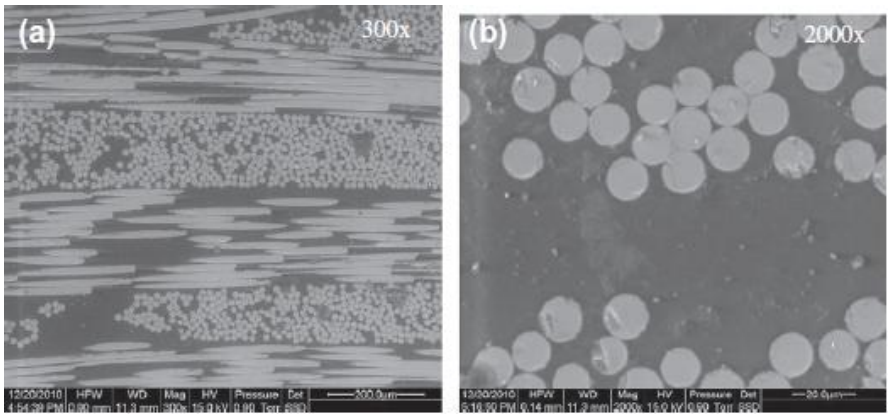

Figure 6.9. Scanning electron micrographs of a typical 3%wt epoxy laminate produced by vacuum infusion revealing a good overall quality and the absence of voids. The figures confirm the presence of agglomerates (size comparable to those identified in nanomodified resins) (Quaresimin et al., 2012a).

The experimental results for the neat and nanomodified epoxy and for the epoxy laminates are presented and discussed in the following sections.

All tests have been carried out by using a MTS 858 servo-hydraulic machine, equipped with a 1.5/15 kN load cell.

6.5.1 Nanomodified epoxy

Tensile test

Tensile tests have been carried out on dog-bone specimens (dimensions: 2x15x110 mm) by using a crosshead speed equal to 2 mm/min. An MTS 632.29F-30 extensometer was used for accurate strain measurements and for tensile

modulus calculation. Three specimens were tested for each material configuration. In all the performed tests failure took place in the centre of the specimen.

The effect of the weight content of Cloisite 30B® nano-additives upon the nanocomposite tensile properties is shown in Figures 6.10a-c.

In particular Figure 6.10a shows the tensile strength of the epoxy clays slightly decreasing with the increase of clay content; this result is in agreement with those of other researchers (Wang et al., 2005). A similar trend is exhibited also by the strain-to-failure (see Figure 6.10b).

It is the author's opinion that this limited reduction of the tensile strength due to nanomodification is not significant, the improvement of the polymer fracture toughness, shown later, being much more important.

Conversely Figure 6.10c shows that nanomodification resulted in a slight improvement of the elastic modulus of the modified resin with respect to the neat epoxy.

Fracture properties

In principle, the overall macroscopic properties of nanocomposites may be substantially affected by the amount of nanofiller and by processing conditions, as well. Then, with the aim to capture both these effects, in the present work, a parametric study has been carried out, by comparing the effect of the sonication process for different content (wt%) of nanofillers.

Figures 6.11a-b show the fracture toughness values versus the nanoclay content (wt%) for 30B- and RXG7000 nano-modified resin, with respect to the neat resin value. Experimental results exhibit a peak value of the fracture toughness for 1 wt% of both nanofillers, independently whether sonicated or not. In particular 30B nano-modified resin exhibits the highest fracture toughness, about a 40% higher than that of the neat resin. For higher nanofiller content, the 30B nano-modified resin is monotonically decreasing, while RXG7000 toughness increases again after 3 wt%.

The maximum value for 30B clay is about 10% higher than the RXG7000 one, either for sonicated or non-sonicated specimens. Surprisingly, the sonicated specimens show lower K_{Ic} values, except for 5 wt% RXG7000.

Usually, sonication is reported to improve properties of nanocomposites, however, opposite indications, in agreement with the results presented here, were reported in (Zunjarrao et al., 2006). This suggested us to carry out a deeper analysis to investigate the effect of sonication in terms of duty cycle or, equivalently, in terms of effective sonication time. Figure 6.12 shows that there is a detrimental effect of a duty cycle percentage increase on the measured fracture toughness, thus suggesting sonication could penalise the nanocomposite overall properties.

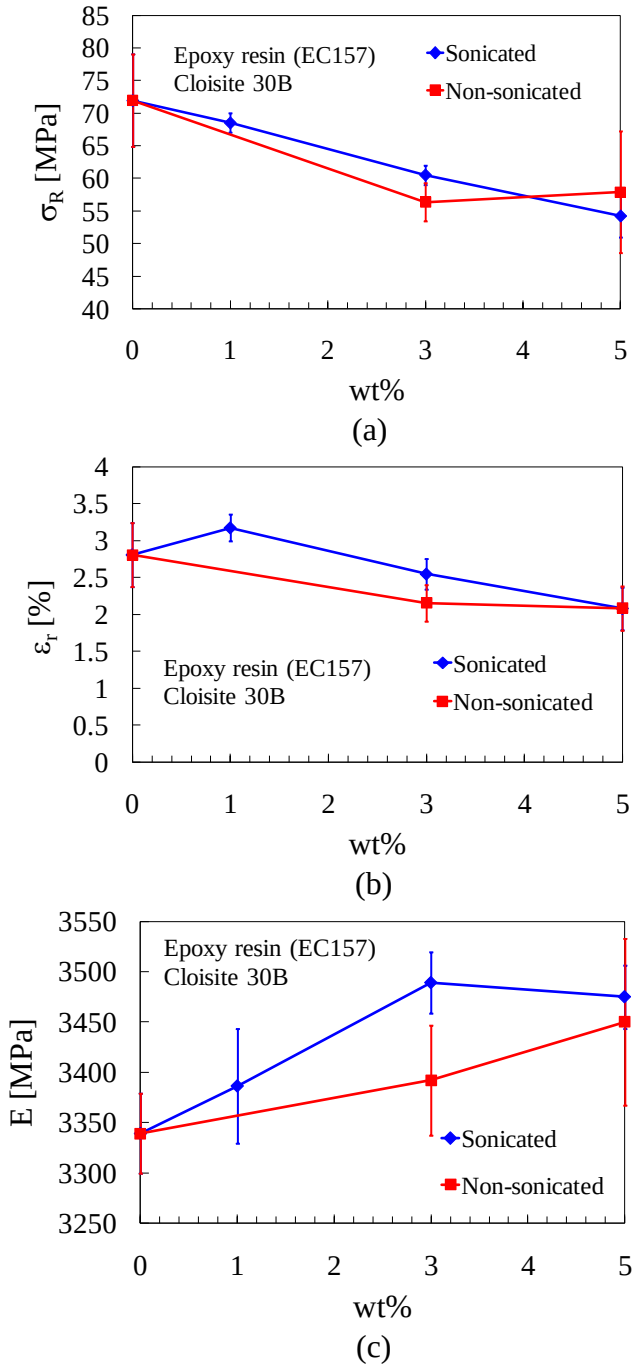

Figure 6.10. Results of tensile tests on neat and nanomodified epoxy resin.

On the other hand, XRD analyses carried out on sonicated and non-sonicated specimens showed the same d-spacing values of about 33 Å, revealing that this parameter, representative of the overall morphology, was not influenced by sonication. This apparently opposite trend, does suggest that some further investigations are needed, in order to better clarify the actual effect of the sonication process, both on the material morphology and on the overall strength properties.

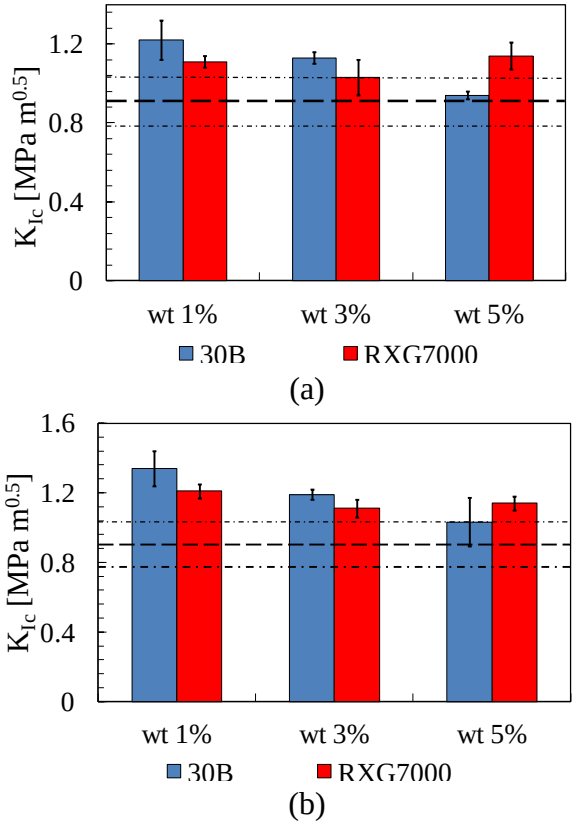

Figure 6.11. Fracture toughness versus nanoclay content (wt%) for 30B and RXG7000 modified resin sonicated (a) and non-sonicated (b) specimens. 3 tests per condition (The scatter band of the values for neat epoxy is given by the dashed line) (Quaresimin et al., 2012a).

Fatigue test results

Mode I fatigue tests on CT samples have also been carried out. Fatigue tests were performed according to procedures reported in the ASTM E 647-00. CT specimens (width 33 mm and thickness 5 mm) were pre-cracked by manual tapping using a razor blade. The length of the pre-crack was about 2 mm.

Tests were characterised by a nominal load ratio $R=F_{min}/F_{max}$, equal to 0.1, with a frequency of 20 Hz.

The crack tip area was magnified by means of a travelling microscope and then captured by means of a digital camera and an in-house-developed acquisition and analysis software (LabVIEW® enviroment). The crack growth was regularly detected and the crack length as a function of the number of cycles was reported. Figure 6.13 shows a typical a-N curve obtained.

The incremental polynomial method was implemented according to ASTM E 647-00 and used to evaluate the crack growth rate da/dN.

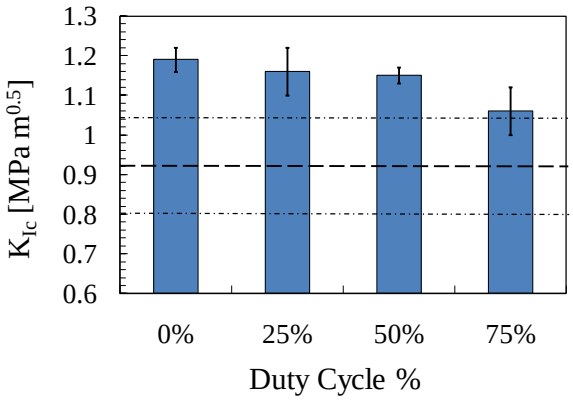

Figure 6.12. Fracture toughness versus duty cycle% for 3 wt% 30B specimens and comparison with neat resin. 0% duty cycle stands for no sonication. (3 tests per condition. The scatter band of the values for neat epoxy is given by the dashed line) (Quaresimin et al., 2012a).

In some cases the ΔK value chosen for the beginning of the test was such that the crack was already in the Paris regime, where the crack growth rate linearly increases with ΔK. Thus, the crack propagation threshold could not always be clearly detected.

Representative results, reported in Figure 14, show that the highest threshold value is exhibited by 1 %wt 30B nanomodified epoxy CT specimens, with a threshold value about 35 % higher than that of the neat resin. The better performances at low clay content suggest a more uniform and less agglomerated morphology for the 1%wt nanocomposites.

On the other hand, it can be observed that clay loading results in an improved crack propagation resistance. Again, this behaviour could be due to the presence

of slightly larger agglomerates with respect to the more finely dispersed clays, inducing a more significant crack path deflection and thus resulting in a higher resistance to crack propagation.

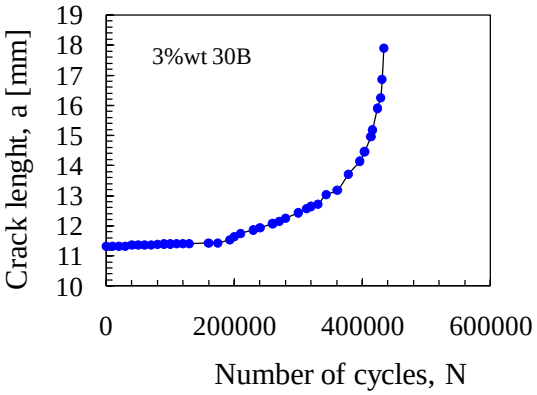

Figure 6.13. Crack growth for a 3%wt 30B loaded CT specimen (Quaresimin et al., 2012a).

A part from these speculations, generally speaking it can be said that all nanomodified epoxy CT specimens exhibit improved fatigue behaviour with respect to the neat resin. The same behaviour was reported also for other nanomodified systems (Battistella et al., 2008).

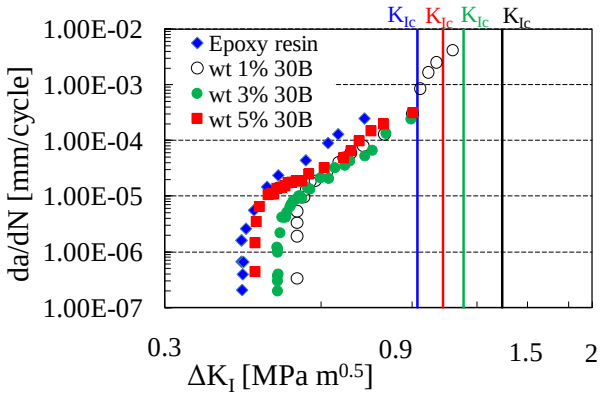

Figure 6.14. Comparison of the Paris curves for the neat and nanomodified epoxy CT specimens (Quaresimin et al., 2012a).

6.5.2 Clay modified epoxy laminates

Fracture properties

The manufacturing of vacuum infused nano-modified glass epoxy laminates is a solution of potential industrial interest provided, of course, that a suitable

compromise between production costs and performances enhancement is achieved.

For ternary laminates, matrix toughness improvement itself is the most interesting and promising result, the interlaminar fracture behaviour of traditional composites being a weak matrix dominated property. In the previous section it has been proved that 30B nanomodified epoxy resin exhibits higher fracture properties with respect to both the neat resin and to RXG7000 nanomodified epoxy resin. Research activities on laminates have been then mainly focused on 30B clay modified epoxy laminates. Tests have been carried out to evaluate the laminate interlaminar properties, by means of interlaminar shear (ILSS) tests, and mode I interlaminar fracture toughness with DCB quasi-static tests.

ILSS tests have been carried out, according to ASTM D2344. The crosshead speed was set at 1 mm/min and three specimens were tested for each material configuration. The specimen thickness was 4 mm and the span was 16 mm. During the interlaminar shear tests all the specimens failed by delamination.

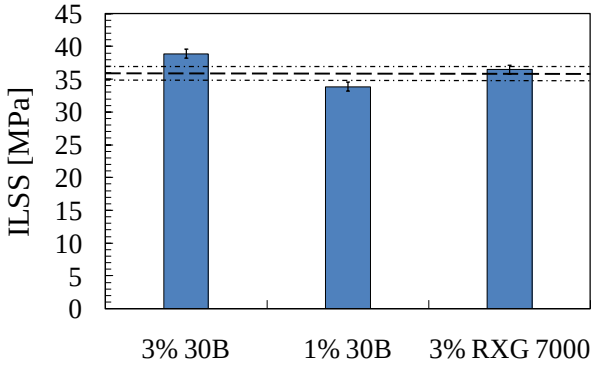

Figure 6.15. Comparison of interlaminar shear properties for neat and nano-modified epoxy laminates (the scatter band for neat epoxy laminates is given by the dashed line) (Quaresimin et al., 2012a).

Figure 6.15 shows a comparison between interlaminar shear strength of the neat, 1 wt% and 3 wt% 30B nano-modified epoxy laminates and 3 wt% RXG7000 nano-modified epoxy laminates. If one considers the actual scatter of the data it can be seen that 3 wt% 30B laminates exhibit a slightly improved interlaminar shear strength, while RXG7000 laminates does not exhibit a significant increment.

DCB quasi-static tests have been carried out, according to ASTM D5528. Three double cantilever beam (DCB) specimens for each material configuration were tested; the crack propagation was monitored by using a travelling microscope.

The crosshead speed was set at 0.5 mm/min. The reported G_{IC} values were calculated using the compliance calibration method (MCC) and the initiation values were determined by visual observation.

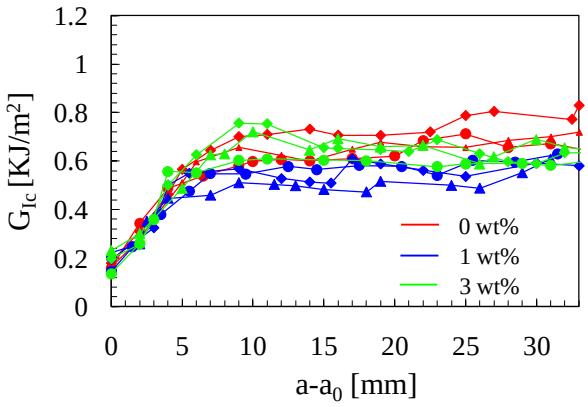

Figure 6.16. R-curves for neat and nano-modified epoxy laminate DCB specimens (30B only) (Quaresimin et al., 2012a).

Test results, shown in Figure 6.16, allow us to draw the following conclusions:

- Concerning the initiation values, there is no evident effect due to the nanoclay addition;
- Differently, a limited decrease is noticed for the propagation values in the case of nano-modified epoxy laminates. In more details, 1wt% seems to provide the lowest result, although it was the best percentage in the nano-modified epoxy system. The decrease is not significantly pronounced and further tests might be needed in order to clarify the obtained behaviour.

Fatigue test results

Besides the above described static tests, mode I fatigue tests on laminates have also been carried out, with a load ratio R = 0.1. Crack opening was monitored by means of the displacement transducer of the testing machine and the crack length was measured by means of a travelling optical microscope with a magnification of 40x. Preliminary results are shown in Figure 6.17. 3 wt% 30B nanomodified epoxy laminates exhibit a worse behaviour, both in terms of propagation and of

threshold value. However, only few tests have been carried out so far and this does not allow us to draw any significant conclusion in this direction.

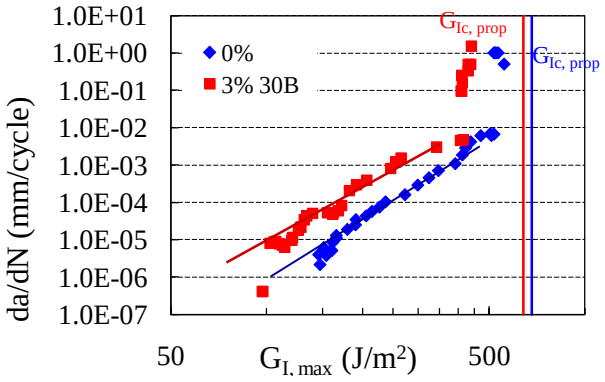

Figure 6.17. Comparison between the Paris curves for a neat and 3 wt% nanomodified epoxy laminate (Quaresimin et al., 2012a).

Fracture surface analyses

As an attempt to understand the reason for the above reported results, namely a comparable fracture toughness of the nano-modified epoxy laminates with respect to that of the neat ones and the worse behaviour under cyclic loading, SEM images of the fracture surfaces were taken.

Figure 6.18a shows a typical fracture surface for a neat resin laminate. The SEM image clearly shows a brittle fracture occurring at the matrix-fibre interface: the fibres appear very clean and no evident matrix damage has taken place. A similar situation is present in the fracture surface of 1%wt 30B laminates (see figure 6.18b).

Differently, Figure 6.18c shows the fracture surface of a 30B 3 wt% nano-modified epoxy laminate. Even if the governing mechanism seems to be, again, matrix-fibre interface failure, there is a different morphology of the matrix failure surface. These differences suggest an improved local energy dissipation for the nano-modified laminates. However this conclusion is not supported by the experimental results reported in the previous section, which do not show any increment in the fracture toughness due to the nano-modification of the matrix.

The improved matrix damage could be promoted by the clay presence and by the lower degree of cross-linking caused by the interactions between the nanoclays and the matrix (Bharadwaj et al., 2002). However, a possible, local deformation of

the matrix does not necessarily correspond to an increased interlaminar fracture strength. In facts, the dominant mechanism is proved to be matrix-fibre interface failure, so that the deformation of the matrix would not be as important as the interface toughness which, on the other hand, could be negatively affected by nanoclay addition.

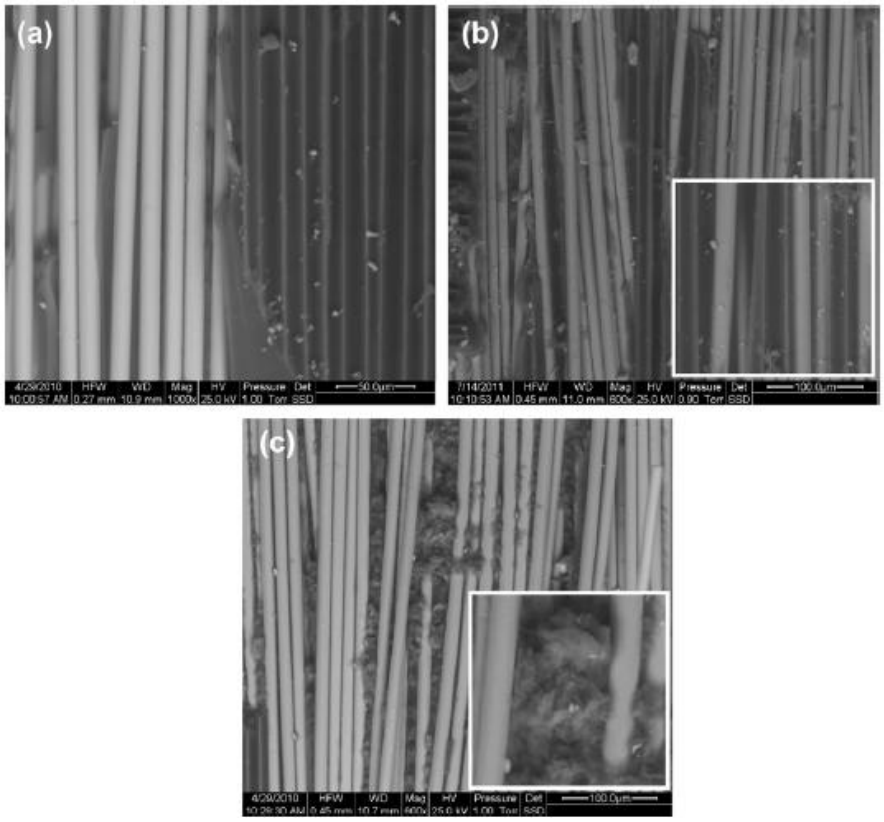

Figure 6.18. SEM images of fracture surfaces after DCB test for neat resin laminate, (a) and nano-modified epoxy laminate for different nanoclay loadings: 1 wt% 30B (b) and 3 wt% 30B (c) (Quaresimin et al., 2012a).

5.6 Discussion

In this work we have presented the results of the ongoing studies carried out by the author on the effect of nano-modification and its industrial potential by discussing the experimental results obtained on neat and nano-modified epoxy, as well as on neat and nano-modified epoxy laminates (ternary laminates).

As far as the nano-modified epoxy is concerned, the morphological analyses have made it evident the presence of clay agglomerates at least in the 30B case.

By the one hand, this result does suggest that some further investigations are needed, in order to optimise the manufacturing process, and then, in turn, the material morphology.

On the other hand experimental results provided in section 6.5.1 show that nanomodification of the resin results in improved fracture toughness, of about 40%, and an ameliorated fatigue behaviour, with a threshold value for the 1 %wt 30B loaded epoxy about 35 % higher than that of the neat resin. Therefore a finer distribution of at least intercalated clays must be present since the improvement in properties cannot be explained by assuming only micrometric size reinforcement at so low volume fraction.

The overall behaviour can be explained by arguing that even if, in principle, a full exfoliation of the clay platelets should maximise toughness improvements, sometimes a balance between an exfoliated and intercalated structure might be preferable as shown in (Zilg et al., 1997). Indeed, the presence of intercalated tactoids might promote toughening mechanisms such as crack deflection or crack pinning, which could not take place, by nature, at the very nanoscale.

Different from the clay-loaded epoxy, the effect of resin nanomodification on behaviour of clay-modified laminates was found to be weak, the results being almost comparable to or even worse than those for that of the neat epoxy laminates.

If, by one side, micrographics on both neat resin and nano-modified resin laminates revealed a good global quality and the absence of any void (Figure 6.8), the SEM images taken on 3wt% nanomodified laminates (Figure 6.9) show again the presence of clusters within the layers, whose size is comparable to that reported for the nanomodified resin at the same filler content.

The SEM analysis on the fracture surfaces of a neat resin laminate (Figure 6.18a) and nanomodified laminates 1%wt 30B (Figure 6.18b) show a brittle fracture occurring at the matrix-fibre interface. A similar behaviour is exhibited by the 30B 3 wt% nano-modified epoxy laminate (Figure 6.18c), where a different morphology of the matrix failure surface is also evident, suggesting an improved local energy dissipation.

The limited nanomodification-induced improvements of laminates properties could then be explained by the argument that the dominant fracture mechanism is matrix-fibre interface failure and that the interface toughness could be negatively affected by nanoclay addition.

For this reason future efforts should be made with the aim to improve the interface toughness.

In the authors' opinion this target can be achieved either through the optimisation of the dispersion process, to obtain a better dispersion and distribution of the nanofiller within the matrix, or improving fibre seizing. With particular reference to the last mentioned approach, the authors are investigating the chance to destroy the seizing on commercial fibres and to prepare an ad hoc seizing, which maximizes fibre-matrix adhesion. Preliminary results in this direction are very promising.

Differently, in order to detect the increasing improvements of nanofiller dispersion and distribution, it will necessary to carry out an extensive TEM investigation.

5.7 Conclusions

The preliminary experimental results of a project aiming to assess the benefits deriving from the matrix nano-modification of composite laminates made by vacuum infusion on woven glass fabrics have been presented.

The experimental program was aimed at investigating the following properties: mode I fracture toughness and crack propagation resistance for neat and clay-modified epoxy (CT test), interlaminar shear strength (ILSS test), delamination threshold and delamination resistance for base and clay-modified epoxy laminates (fatigue and quasi-static DCB test).

Available results indicate significant improvements in the fracture toughness and crack propagation threshold of clay modified epoxy.

On the other hand, the behaviour of clay-modified laminates is almost comparable to that of the neat epoxy laminates. This is assumed to be related to the nanofiller morphology and to the main failure mechanism in the laminates which was observed to be matrix-fibre interface failure.

In this situation, benefits deriving from matrix improved properties cannot be fully exploited.

Bibliography of chapter 6

Alexandre M, Dubois P. "Polymer-layered silicate nanocomposites: preparation, properties and uses of a new class of materials". *Mat Sci Eng R*, 28: 1–63, 2000.

Battistella M., Cascione M., Fiedler B., Wichmann M.H.G., Quaresimin M., Schulte K.. "Fracture behaviour of fumed silica/epoxy nanocomposites". *Compos: Part A*, 39: 1851–1858, 2008.

Becker O, Varley R, Simon G. "Morphology, thermal relaxations and mechanical properties of layered silicate nanocomposites based upon high-functionality epoxy resins". *Polymer*, 43: 4365–4373, 2002.

Bharadwaj RK, Mehrabi AR, C Hamilton, Trujillo C, Murgaa M, Fan R, Chavira A, Thompson AK. "Structure-property relationships in cross-linked polyester–clay nanocomposites". *Polymer*, 43 :3699–705, 2002.

Boo W.J., Liu J., Sue H.J. Fracture behaviour of nanoplatelet reinforced polymer nanocomposites. *Mat Sci Tech*, 22: 829–834, 2006.

Kornmann X, Lindberg H, Berglund LA. "Synthesis of epoxy-clay nanocomposites: influence of the nature of the curing agent on structure". *Polymer*, 42:4493–9, 2001.

Kornmann X, Thomann R, Mulhaupt R, Finter J, Berglund LA. "High performance epoxy-layered silicate nanocomposites". *Polym Eng Sci*, 42(9):1815–26, 2002.

Quaresimin M, Salviato M, Zappalorto M. "Fracture and interlaminar properties of clay-modified epoxies and their glass reinforced laminates". *Eng Fract Mech*, 81: 80-93, 2012a.

Quaresimin M., Varley R.J. "Understanding the effect of nanomodifier addition upon the properties of fibre reinforced laminates", *Comp Sci Tech*, 68: 718-726, 2008.

Quaresimin, M., Salviato, M., Zappalorto, M. "Strategies for the assessment of nanocomposite mechanical properties". *Compos. part B-Eng*. 43, 2290–97, 2012b.

Rice B.P., Chen C., Cloos L., Curliss D. "Carbon fibre composites: Organoclay-aerospace epoxy nanocomposites", Part I. *SAMPE J*, 37: 7–9, 2001.

Timmerman J.F., Hayes B.S., Seferis J.C. "Nanoclay reinforcement effects on the cryogenic microcracking of carbon fibre/epoxy composites". *Comp Sci Tech*, 62: 1249–1258, 2002.

Vaia R.A., Giannelis E.P. "Polymer melt intercalation in organicallymodified layered silicates: Model predictions and experiment". *Macromolecules*, 30: 8000–8009, 1997.

Wang K, Chen L, Wu J, Toh ML, He C, Yee AF. "Epoxy Nanocomposites with Highly Exfoliated Clay: Mechanical Properties and Fracture Mechanisms". *Macromolecules*, 38: 788-800, 2005.

Zerda AS, Lesser AJ. "Intercalated Clay Nanocomposites: Morphology, Mechanics, and Fracture Behavior". *J Polym Sci Pol Phys*, 39: 1137–1146, 2001.

Zilg C., Mulhaupt R., Finter J. "Morphology and toughness/stiffness balance of nanocomposites based upon anhydride-cured epoxy resins and layered silicates". *Macromolecules Chemistry and Physics*, 70: 661–670, 1999.

Zunjarrao S.C., Sriraman R., Singh R.P. "Effect of processing parameters and clay volume fraction on the mechanical properties of epoxy-clay nanocompoistes". *J Mater Sci*, 41: 2219-2228, 2006.

Conclusions

Throughout the last decades the subject of improving the mechanical properties of polymers by the addition of particle fillers has received a large attention. However, only recently nanotechnology has emerged providing very promising results in increasing the mechanical properties of polymers by the addition of nanosized fillers. This is the reason why nanocomposites have received a higher and higher interest by the scientific community, especially for the significant amelioration in terms of stiffness, strength and toughness which can be obtained at low nanofiller contents.

To effectively exploit the huge potential of nanocomposites it is of primary concern that with the experimental analysis, abundantly developed in the literature among the rest, comes an adequate modeling activity. Of course, the creation of models, either analytical or numerical, is a milestone for the comprehension and prediction of the mechanical behavior of this kind of materials and their successive application in engineering design.

As stated in this work, modelling nanocomposite mechanical properties there are some important issues that can but be taken into account. As a matter of facts, the reduction in filler length scale, on the one hand is the key of the extraordinary properties of nanocomposites thanks to which the exploitation of matter in its molecular state is possible, on the other hand takes to the limit many important drawbacks already known for traditional composites. The most important difficulties in modelling nanocomposites mechanical properties can be related to:

- *State of aggregation:* Mechanical properties of nanocomposites are strongly influenced by the *distribution* and the degree of *dispersion* of nanofillers. In facts, the huge amount of *SSA* of the single nanoreinforcement promotes the formation of *agglomerates* whose

dimensions belong to micro and not nano length scale cancelling out the "nano-effect".

- *Morphology:* It is broadly accepted that the interactions between nanofillers and the epoxy matrix depend on the fillers *surface structure*, *geometry* and *surface chemistry*.
- *Orientation*: When the nanofiller is not equiaxed, it presents an orientation distribution which is very important in determining the bulk nanocomposite mechanical properties (isotropic, transversely isotropic, anisotropic *etc*.).
- *Polymeric matrix/nanofiller interface:* the dimensions of the filler and the enormous SSA can enhance the creation of strong matrix/nanofiller interfaces. Being the reinforcement nearly at its molecular state, the correct modelling of the singular bonding is of cardinal importance.
- *Allignement:* Because of their small sizes, it is exceedingly difficult to align the nanotubes in a polymeric matrix material in a manner accomplished in traditional short fiber composites so that nanotubes frequently present *entangling* and *waviness*. The lack of control in orientation diminishes the effectiveness of nanotube reinforcement in nanocomposites, whether for structural or functional performance.
- *Defects:* Because of the production process or the functionalization treatment to improve the reinforcement dispersion, defects like atomic vacancy can occur. This can cause a detrimental drop of nanofiller mechanical performances.

Moreover, one of the most critical issues in modeling macro-mechanical properties of nanostructured materials is their *hierarachical structure* which spans from nano to macro length-scales. A good model should take into account the characteristic phenomena of each length-scale and bridge their effects from the "smaller" scale to the macroscale. As a consequence, a different way of thinking from traditional approaches is needed and a completely new class of models is required.

Most of available modelling strategies can be gathered, according to the scale used to address the problem (micro, nano, molecular), into three main groups:

- *Micromechanical strategies*
- *Nanostructural strategies*
- *Molecular strategies*

The micromechanical approach extends the continuity hypothesis to the polymeric chains length-scale so that, implicitly, the synergic change in the matrix and nanofiller properties is neglected. In this way, the model fails in explaining the "nano-effect" and it does not take into consideration the inherently hierarchical structure of the material. In nanostructural approaches, even if the continuity hypothesis is kept, there is an effort to take into account some characteristic aspects belonging to the nanoscale such as the wall thickness effect of carbon nanotubes, the grade of nanoclay exfoliation in PLS nanocomposites, the more pronounced tendency to agglomeration with respect to traditional composites at a given filler volume fraction or the possible presence of entangling and waviness. Then, Molecular approaches abandon the continuity hypothesis when the filler dimensions belong to the nanoscale. Continuum mechanics is substituted by discrete theories like molecular dynamics (MD) among the others.

In the author's opinion, provided of course that a robust multi-scale methodology is developed, the molecular approaches are required to address all the issues described above.

As previously stated, the interfacial interactions taking place at the nanoscale are an important issue that must be addressed in nanomechanics. Accordingly, in this work, a closed form expression for the nanoparticle detachment strength has been derived, using, contemporaneously, the Finite Fracture Mechanics approach and the Surface Elasticity theory and considering all constituents as isotropic materials. The solution accounts either for the emergence of an interphase zone around the nanoparticle or for surface stresses on the nanoparticle periphery.

It has been proved that the range of nanoparticle radii where interfacial effects do affect the solution is limited to the nanometer scale. In more details, considering the interphase and surface elastic properties used in the analysis, it has been found that for rigid particles with radius between 5 nm and 70 nm (silica, alumina and other metal oxide nanoparticles) the prominent role is played by the interphase

elastic properties. Surface elastic constants were found to have, instead, only a negligible effect.

The effects of the interphase have been later considered in Chapter 4 where a unique multiscale analytical procedure useful to evaluate the overall fracture toughness of a polymer/nanoparticle nanocomposite has been presented. The model integrates all the damaging models developed by the author (i.e. debonding, plastic yielding and shear banding) within a multi-scale, multi-mechanism approach. The model stems from the quantification of the energy absorbed at the nanoscale and accounts for the emergence of an interphase, created by the inter- and supra-molecular interactions arising at the nanoscale, with mechanical properties different from those of the matrix. It is proved that the interphase elastic properties highly affect the stress rising around particles, causing lower or higher energy dissipation at the nanoscale. Moreover it is proved that the particle size effects may be different depending on the elastic properties of the interphase.

In the present work, the results of some experimental investigations made by the author have been also presented. The effects of nanoclay addition on the fracture behaviour of an epoxy resin under mixed mode (I plus II) loadings have been studied by analysing the results from Single Edge Notch Bending (SENB) tests. The results allow to conclude that, for weight contents up to 5wt%, nanomodification significantly enhances the fracture toughness of the epoxy resin upon the entire range of mixed mode loadings, the improvements being dependent on the mode mixity ratio.

Experimental results have been compared to the theoretical predictions based three mixed mode fracture criteria for brittle homogeneous solids. The results from specimens made of pure epoxy are well predicted, almost independently of the approach used for the synthesis. Conversely, as far as the results from specimens made of nanomodified polymer are concerned, the agreement with theoretical predictions by one-parametrical approaches is worse. This can be thought of as linked to the emergence, due to nanomodification, of different damaging mechanisms depending on the mode mixity. Better predictions were obtained using Richard's criterion.

The experimental analysis has been later extended to nanomodified composite laminates manufactured by vacuum infusion. Mode I fracture toughness and crack propagation resistance for neat and clay-modified epoxy (CT test), interlaminar shear strength (ILSS test), delamination threshold and delamination resistance for base and clay-modified epoxy laminates (fatigue and quasi-static DCB test) have been investigated.

Available results indicate significant improvements in the fracture toughness and crack propagation threshold of clay modified epoxy. On the other hand, the behaviour of clay-modified laminates is almost comparable to that of the neat epoxy laminates. This is assumed to be related to the nanofiller morphology and to the main failure mechanism in the laminates which was observed to be matrix-fibre interface failure. In this situation, benefits deriving from matrix improved properties cannot be fully exploited.

List of publications

(a) INTERNATIONAL JOURNALS

[1] Zappalorto M., Salviato M., Quaresimin M. Assessment of Debonding-Induced Toughening in Nanocomposites. *Procedia Engineering*, Vol. 10, pp. 2973 – 2978, (2011).

[2] Salviato M., Zappalorto M., Quaresimin M. Plastic Yielding Around Nanovoids. *Procedia Engineering*, Vol. 10, pp. 3316 – 3321, (2011).

[3] Zappalorto M., Salviato M., Quaresimin M. Influence of the interphase zone on the nanoparticle debonding stress. *Composites Science and Technology*, 72, 48-55, (2011).

[4] Salviato M., Zappalorto M., Quaresimin M. The effect of surface stresses on the critical debonding stress around nanoparticles. *International Journal of Fracture*, 172:97-103, (2011).

[5] Quaresimin M., Salviato M., Zappalorto M., Fracture and interlaminar properties of clay-modified epoxies and their glass reinforced laminates. *Engineering Fracture Mechanics*, 81:80-93, (2012).

[6] Quaresimin M., Salviato M., Zappalorto M. Strategies for the assessment of nanocomposite mechanical properties. *Composites part B: Engineering*, 43, 2290-2297, (2012).

[7] Zappalorto M., Salviato M., Quaresimin M. Stress distributions around rigid nanoparticles. *International Journal of Fracture*, 176, 105-112, (2012).

[8] Zappalorto M., Salviato M., Quaresimin M. A multiscale model to describe nanocomposite fracture toughness enhancement by the plastic yielding of nanovoids. *Composites Science and Technology*, 72, 1683-1691, (2012).

[9] Salviato M., Zappalorto M., Quaresimin M.. Plastic shear bands and fracture toughness improvements of nanoparticle filled polymers: a multiscale analytical model. *In press*.

Moreover, **3** papers dealing with analytical models for nanocomposite toughness assessment and experimental analysis of mixed mode fracture toughness of nanocomposites are going to be submitted to International Journals with IF.

(b) INTERNATIONAL CONFERENCES

[10] Quaresimin M., Zappalorto M., Salviato M. Modelling strategies for nanocomposite toughening: a review, ETDCM9, 9th Experimental techniques and design in composite materials, Vicenza - Italy, September 30-October 2, 2009.

[11] Quaresimin M., Zappalorto M. Salviato M. On the prediction of nanocomposites mechanical properties. 14th European Conference on Composite Materials, Budapest, Hungary 7-9 June 2010.

[12] Carraro P., Quaresimin M., Salviato M., Zappalorto M. Interlaminar properties of clay-modified epoxy-glass reinforced laminates. 14th European Conference on Composite Materials, Budapest, Hungary, 7-9 June 2010.

[13] Quaresimin M., Zappalorto M. Salviato M. On the prediction of nanocomposites mechanical properties. 2nd International Conference on Nanomechanics and Nanocomposites, Beijing, China, 10-13 October 2010.

[14] Quaresimin M., Zappalorto M. Salviato M. Improvements of composite laminates properties by nanomodification. NanotechItaly, Venice, 20-22 October 2010.

[15] Zappalorto M., Salviato M., Quaresimin M. Assessment of Debonding-Induced Toughening in Nanocomposites. 11th International Congress on the Mechanical Behaviour of Materials, Como, Italy, 5-9 June 2011.

[16] Salviato M., Zappalorto M., Quaresimin M. Plastic Yielding Around Nanovoids. 11th International Congress on the Mechanical Behaviour of Materials, Como, Italy, 5-9 June 2011.

[17] Salviato M., Zappalorto M. Analytical study of the surface stress effects on the critical debonding stress around nanoparticles. 13th International Conference on Mesomechanics, Vicenza, 6-8 July 2011.

[18] Salviato M., Zappalorto M., Quaresimin M. The effect of the interphase zone and surface stresses on the critical debonding stress around nanoparticles. 4th ECNP Young Researchers Conference, Lyon, 7-10 November 2011.

[19] Zappalorto M., Salviato M., Quaresimin M. Fracture toughness enhancements in nanocomposites: a multiscale model. 15th European Conference on Composite Materials, Venice, Italy, 24-28 June 2012.

[20] Salviato M., Zappalorto M., Florio M., Dalla Via A., Quaresimin M. Mixed mode fracture toughness of cracked specimens made of nanomodified epoxy resin. 15th European Conference on Composite Materials, Venice, Italy, 24-28 June 2012.

[21] Salviato M., Pontefisso A., Zappalorto M., Santi M., De Rossi N., Quaresimin M. Fracture and interlaminar properties of clay-modified glass reinforced laminates. 15th European Conference on Composite Materials, Venice, Italy, 24-28 June 2012.

[22] Salviato M., Zappalorto M., Quaresimin M. Fracture toughness improvements due to plastic shear bands around nanoparticles. 15th European Conference on Composite Materials, Venice, Italy, 24-28 June 2012.

[23] Zappalorto M., Salviato M., Quaresimin M. Multiscale modelling of nanocomposite fracture toughness. The International Conference on Composite Interfaces, Kyoto, Japan, 6-8 August 2012.

(c) NATIONAL CONFERENCES

[24] Quaresimin M., Zappalorto M. Salviato M. Metodologie di modellazione delle proprietà meccaniche dei nanocompositi. XXXVIII Convegno AIAS, Torino , 9-11 settembre 2009.
[25] Quaresimin M., Zappalorto M. Salviato M. On the prediction of mechanical properties of nanocomposites, Workshop IGF, Forni di Sopra, 7-9 gennaio 2010.
[26] Salviato M., Zappalorto M. Modellazione nanostrutturale del meccanismo di debonding in nanocompositi a matrice polimerica. XXXIX Convegno AIAS, Maratea, 7-10 settembre 2010.
[27] Quaresimin M., Zappalorto M., Salviato M. Resistenza interlaminare di laminati in composito vetro/epossidica nanomodificati. XXXIX Convegno AIAS, Maratea, 7-10 settembre 2010.
[28] Zappalorto M., Salviato M., Quaresimin M. Modellazione dell'effetto tenacizzante indotto dalla plasticizzazione di nanovuoti. 40° Convegno Nazionale AIAS, Palermo, 7-10 settembre 2011.
[29] Salviato M., Zappalorto M., Quaresimin M. Studio del danneggiamento indotto dal debonding di nanoparticelle. 40° Convegno Nazionale AIAS, Palermo, 7-10 settembre 2011.
[30] Zappalorto M., Salviato M., Quaresimin M. Modellazione multiscala della tenacità a frattura di polimeri rinforzati con nanoparticelle. 41° Convegno Nazionale AIAS, Vicenza, 5-8 settembre 2012.
[31] Salviato M. Fracture toughness improvements of nanoparticle filled polymers due to plastic shear banding. 41° Convegno Nazionale AIAS, Vicenza, 5-8 settembre 2012.